Masters Theses   Graduate School

5-1991

Two Lithotectonic Boundaries In Western North Carolina: Geologic Interpretation of A Region Surrounding Sylva, Jackson County

Michael Joseph Quinn
University of Tennessee - Knoxville

To the Graduate Council:

I am submitting herewith a thesis written by Michael Joseph Quinn entitled "Two Lithotectonic Boundaries In Western North Carolina: Geologic Interpretation of A Region Surrounding Sylva, Jackson County." I have examined the final electronic copy of this thesis for form and content and recommend that it be accepted in partial fulfillment of the requirements for the degree of Master of Science, with a major in Geology.

Robert D. Hatcher, Jr., Major Professor

We have read this thesis and recommend its acceptance:

Harry Y. McSween, Steven G. Driese

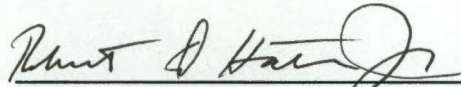Accepted for the Council:
<u>Carolyn R. Hodges</u>

Vice Provost and Dean of the Graduate School

(Original signatures are on file with official student records.)
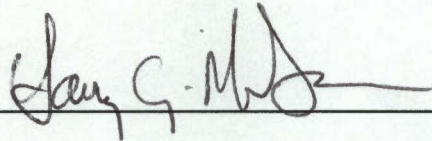
To the Graduate Council:

I am submitting herewith a thesis written by Michael Joseph Quinn entitled "Two Lithotectonic Boundaries in Western North Carolina: Geologic Interpretation of a Region Surrounding Sylva, Jackson County." I have examined the final copy of this thesis for form and content and recommend that it be accepted in partial fulfillment of the requrements for the degree of Master of Science, with a major in Geology.

_____
Robert D. Hatcher, Jr., Major Professor
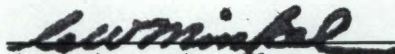
We have read this thesis
and recommend its acceptance:

_____

_____

Accepted for the Council:

_____
Associate Vice Chancellor
and Dean of The Graduate School

STATEMENT OF PERMISSION TO USE

In presenting this thesis in partial fulfillment of the requirements for a Master's degree at The Unitersity of Tennessee, Knoxville, I agree that the Library shall make it available to borrowers under rules of the Library. Brief quotations from this thesis are allowable without special permission, provided that accurate acknowledgment of the source is made.

Permission for extensive quotation from or reproduction of this thesis may be granted by my major professor, or in his absence, by the Head of Interlibrary Services when, in the opinion of either, the proposed use of the material is for scholoarly purposes. Any copying or use of the material in this thesis for financial gain shall not be allowed without my written permission.

Signature _Michael Joseph Quinn_

Date _April 25, 1991_

Two Lithotectonic Boundaries In Western North Carolina: Geologic Interpretation Of A Region Surrounding Sylva, Jackson County

A Thesis
Presented for the
Master of Science
Degree
The University of Tennessee, Knoxville

Michael Joseph Quinn
May, 1991

ACKNOWLEDGMENTS

ABSTRACT

Understanding the geology of any region begins with the construction of high-quality geologic maps. As maps for a specific region are revised in greater detail, geologic understanding is improved. This study involved detailed geologic mapping (at the scale of 1 : 24,000) of a portion of the southern Appalachian Blue Ridge that was previously only mapped by reconnaissance. It is hoped that the research herein will add to the present understanding of the Blue Ridge province and of the entire Appalachian orogenic belt.

During the course of field mapping, three lithotectonic units were divided, each separated from the others by a major fault. Unit 1, located in the northwesternmost portion of the study area, is part of the Great Smoky Group and is comprised of feldspathic metaquartzite and metagraywacke interlayered with subordinate aluminous schist. Unit 1 is bounded on the south by the Hayesville fault. Unit 2 occurs immediately south of the Hayesville fault and is composed of feldspathic metagraywacke, biotite gneiss, and interlayered amphibolite. This sequence is correlated with the Tallulah Falls Formation. In addition, Unit 2 contains large masses of amphibolite and ultramafic rock that are not considered part of the Tallulah Falls stratigraphic sequence. Unit 3 is the southeasternmost unit and consists of an assemblage of aluminous metagraywacke, feldspathic metaquartzite, aluminous schist, and interlayered amphibolite. These rocks are correlated with the Otto Formation which has been mapped directly along strike to the southwest. A small ultramafic body is also present in Unit 3. Unit 3 is separated from Unit 2 by the Soque River fault. Unit 2 is the hanging wall for both the Hayesville and Soque River faults.

The study area is structurally complex. Structural and metamorphic evidence indicates that all lithotectonic units were juxtaposed prior to the onset of metamorphism and early-stage deformation. Six separate fold generations have been recognized. Early-stage folding (F_1 and F_2) are isoclinal flowage folds, each of which involved transposition of a preexisting layering and development of a regionally penetrative foliation. The dominant foliation now present in the study area was designated S_2 because F_2 folds fold a preexisting foliation. Intermediate-stage folds are tight, passive flow to flexural flow folds. Intermediate-stage fold geometries indicate that rheologic contrasts developed and affected fold mechanics as the rocks cooled. Late-stage folds are open flexural flow and flexural slip buckle folds indicating that the rocks behave more rigidly and had cooled still further. Late stage deformation is responsible for the development of the "Webster-Addie dome", a

prominent doubly-plunging antiform in the study area. A window through Unit 2, exposing the underlying rocks of Unit 3, has developed in the core of the Webster-Addie dome.

One major regional metamorphism affected the rocks in the study area and is associated with the Taconic orogeny. Rocks in the study area underwent medium-pressure facies series metamorphism, ultimately attaining kyanite-sillimanite grade in the amphibolite facies. The sillimanite isograd has been domed in the study area exposing higher pressure (kyanite grade) rocks in the center. Textural relationships indicate that garnet growth continued well after the regional metamorphic peak. Thermobarometric calculations based on mineral equilibria indicate that perhaps closure temperatures varied between pelites, gneisses, and amphibolites. Maximum conditions for metamorphism (recorded by rocks with the highest closure temperature) were approximately 725°C and 9 kb. Metamorphic conditions recorded by rocks with the lowest closure temperature were 550°C and 5.5 kb. Retrograde metamorphism (chlorite-biotite zone) is evident in some samples and may be associated with Acadian regional metamorphism.

The geochemistry of amphibolites occurring in Units 2 and 3 indicates that they were mafic igneous rocks prior to metamorphic recrystallization. Trace element abundances indicate that amphibolites originated as ocean floor basalts. This suggests that Units 2 and 3 were deposited in a tectonic regime in which lavas from a depleted mantle source could be tapped and emplaced without significant crustal contamination.

TABLE OF CONTENTS

vi

LIST OF FIGURES

LIST OF TABLES

LIST OF PLATES

I. INTRODUCTION

Geologic elements exposed in the southern Appalachians have played an important role in guiding geologists toward an understanding of orogenic belts worldwide. From the folded and faulted sedimentary strata of the Valley and Ridge province to the onlap of the Coastal Plain, a remarkably informative erosional remnant of an asymmetric collisional orogen is exposed. Understanding the geology of this region began with the construction of high-quality geologic maps. Geologic maps covering localized areas of the southern Appalachians have been compiled over the past century, primarily by officers of the U.S. Geological Survey. Vast areas remain, however, that require either first-cycle geological mapping or detailed refinement of existing reconnaissance geologic maps. This thesis involves detailed geologic mapping of a portion of the southern Appalachian Blue Ridge that has previously only been investigated by reconnaissance studies (Keith, 1907; Hadley and Nelson, 1971). It is hoped that the research herein will add to the present understanding of the Blue Ridge province and of the entire Appalachian orogenic belt .

INTRODUCTION TO REGIONAL GEOLOGY

The southern Appalachian Blue Ridge is located east of the Valley and Ridge fold-thrust belt. The western boundary of the Blue Ridge has traditionally been drawn along the Great Smoky thrust fault (Fig. 1.1). From a structural standpoint, however, a more appropriate Blue Ridge–Valley and Ridge boundary is the Cartersville–Miller Cove fault. Unlike the Great Smoky thrust, this fault cuts across bedding in the hanging wall and marks the westernmost extension of cleaved and/or metamorphosed rocks. East of the Cartersville–Miller Cove thrust lies one of the largest composite crystalline thrust sheets in the world. This massive sheet was thrust westward on a major crustal detachment during the Alleghanian orogeny, in late Pennsylvanian to Permian time (Secor and others, 1986b; Hatcher, 1972, 1978, 1990). The eastern boundary of the Blue Ridge is considered to be the Brevard fault zone, a structural boundary separating the Blue Ridge and Piedmont geologic provinces (it is important to note that, in the southern Appalachians, geologic province boundaries do not necessarily coincide with geomorphologic province boundaries). The Brevard fault zone is a narrow region that has experienced significant strike-slip, and then dip-slip motion during the Alleghanian, but also may have a deformational history (primarily dip-slip) prior to this event (Hatcher, 1978; Edelman and others, 1987).

1
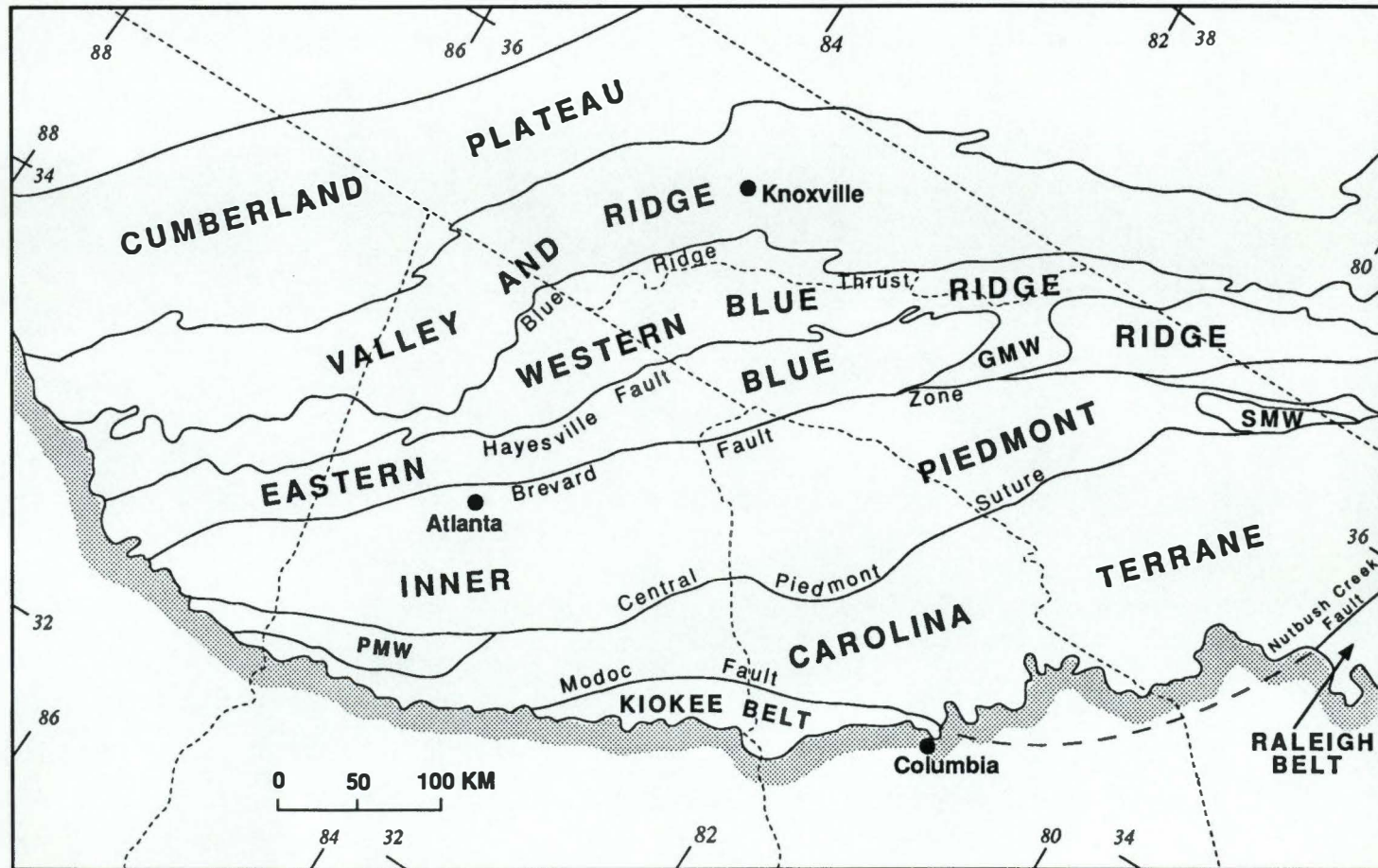
Figure 1.1: Tectonic map of the southern Appalachian orogen showing the major geologic province divisions and tectonic features. (GMW = Grandfather Mountain Window; SMW = Sauratown Mountains Window; PMW = Pine Mountain Window . Simplified after Hatcher, 1987.)

Over the past century a considerable amount of geologic reconnaissance mapping has been completed in the southern Appalachian Blue Ridge (Keith, 1895, 1904, 1907; Hadley and Nelson, 1971) but detailed geologic coverage for most areas is still lacking. This thesis involves detailed geologic mapping (at the scale of 1:24,000) and the primary focus of this research is to add accurate and informative data to the reserve of geologic knowledge for this region.

A very distinct and continuous boundary divides the Blue Ridge into two contrasting, longitudinal segments. These two segments are referred to as the western Blue Ridge and the eastern Blue Ridge and both have differing characteristics along the length of the entire orogen (Rankin,1975; Hatcher, 1978). Through the Blue Ridge of southwestern North Carolina this NE-SW trending boundary separates Ocoee Supergroup paragneisses and schists of the western Blue Ridge from layered paragneiss, schist, and associated mafic and ultramafic rocks of the eastern Blue Ridge. The boundary between these two sequences has been mapped as the Hayesville fault in southwestern North Carolina and northeastern Georgia (Hatcher, 1978; Hatcher and others, 1979; Eckert and others, 1989). In these studies, the Hayesville fault is described as a premetamorphic structure that juxtaposes two fundamentally different assemblages of rocks. The Hayesville, and correlative faults, may be traceable along the entire length of the Appalachians and is, therefore, a structure of significance for the entire orogen. Because it juxtaposes such contrasting packages of rock, many regard the Hayesville fault as a fundamental terrane boundary.

A primary goal of this thesis is to describe the nature and geometry of the western Blue Ridge-eastern Blue Ridge boundary in an area where the Hayesville fault has not been verified. Stratigraphic, petrologic, and structural treatment of the lithologic units on either side of this boundary will shed light on the tectonic significance of this portion of the Blue Ridge.

STUDY AREA

Given the primary goal of this project to map the boundary between the western and eastern Blue Ridge, the study area was strategically located to straddle this boundary as it occurs just north of the town of Sylva, in Jackson County, North Carolina (Fig. 1.2). The area under investigation includes approximately the southern half of the Sylva North 7 1/2 minute quadrangle and the northern half of the Sylva South 7 1/2 minute quadrangle. The northern boundary of the mapped area is entirely within Ocoee Supergroup rocks of the western Blue Ridge and extends to the crest of the Plott Balsam Range. The Plott Balsam

3
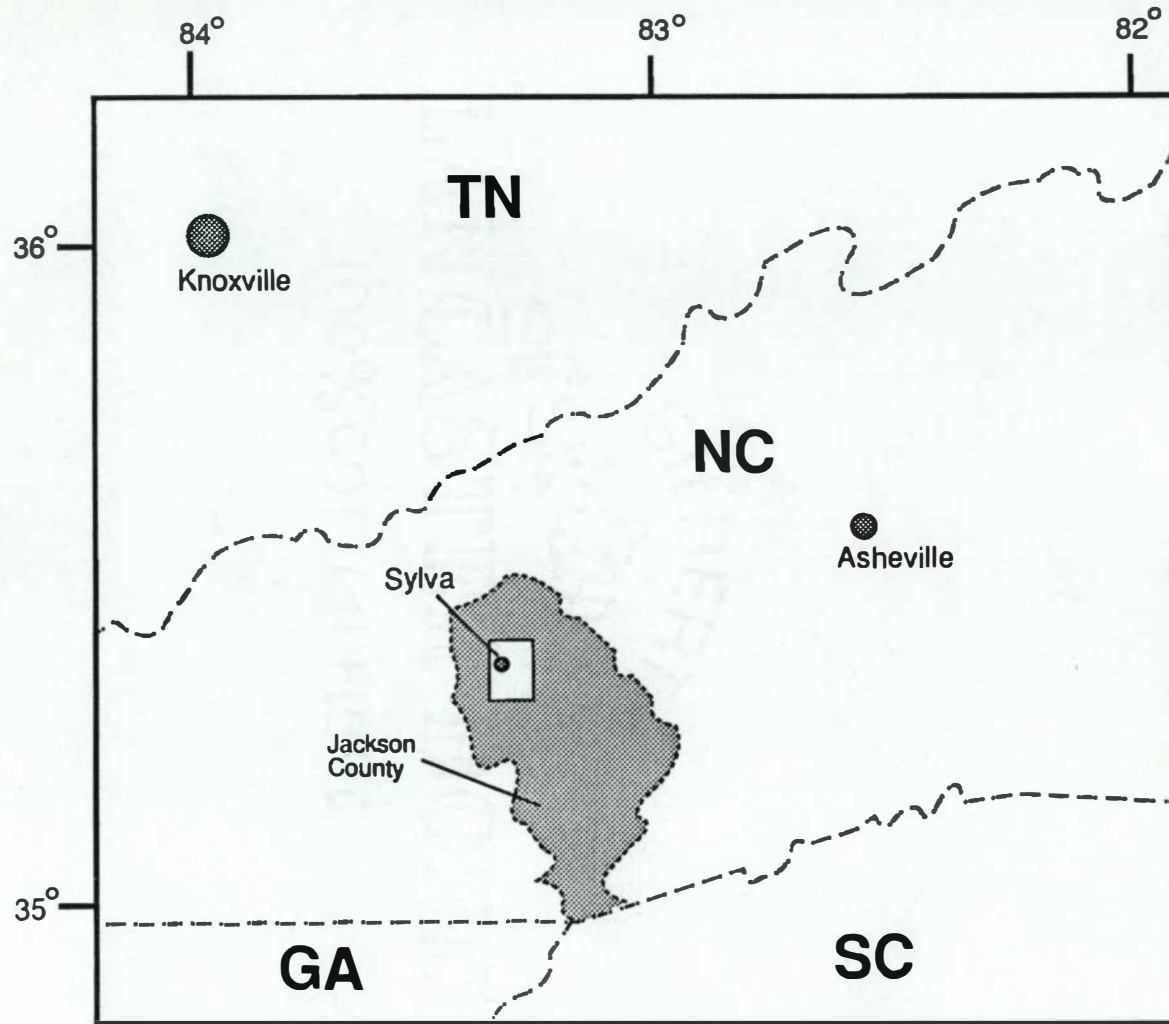
Figure 1.2: Location map showing the study area (highlighted rectangle within Jackson County, NC) and the surrounding geography.

Range provides 1,325 meters of local relief in this portion of the map area, exposing mostly massive metasandstone and well-foliated aluminous schist of the Great Smoky Group. Secondary ridges trend south from the range crest and descend into the Scott Creek and Tuckasegee River valleys. Relief is again significant along ridges east and southeast of Sylva where the best exposures of layered gneiss, amphibolite, and ultramafic rocks exist. The southern part of the study area includes a significant portion of the Otto Formation, which is separated from the Hayesville thrust sheet by the Soque River fault. The southern boundary of the map area was arbitrarily located just south of the town of Cullowhee so that significant portions of the Soque River fault and the Otto Formation were included. The entire area included for this study encompasses approximately 70 mi^2 (180 km^2).

GEOLOGIC SETTING AND PREVIOUS WORK

The western Blue Ridge assemblage is composed of Precambrian continental basement overlain by two units of the Late Proterozoic Ocoee Supergroup: the Great Smoky Group and the Snowbird Group. This geology was mapped in large part by Hadley and Goldsmith (1963) through the eastern portions of the Great Smoky Mountains National Park. In the eastern portions of the western Blue Ridge, the Great Smoky Group dominates in outcrop and is composed of immature to submature metasedimentary rocks (Hadley, 1970; Rast and Kohles, 1986). The Elkmont and Thunderhead Sandstone units of the Great Smoky Group are primarily thick-bedded to massive, coarse-grained metasandstone and metagraywacke. The metasandstones are commonly intercalated with dark, sulfidic and/or graphitic slate and schist that resemble descriptions given for the overlying Anakeesta Formation (King and others, 1958; Hadley and Goldsmith, 1963).

The Great Smoky and Snowbird Groups in this area are, in many places, in fault contact with Precambrian granitic basement gneiss over which they have been thrust along the Greenbrier fault (also a pre-metamorphic thrust). Granitic basement is well exposed as augen and flaser gneiss in three basement-cored windows: the Bryson City dome, the Ela dome, and the Ravensford anticline.

In contrast to the relatively homogeneous nature of the Great Smoky metasandstone and schist, the layered gneiss complex to the southeast (in the eastern Blue Ridge) contains more varied and very different lithologies. Sequences of interlayered biotite gneiss, biotite + hornblende gneiss, and amphibolite are most commonly observed. Bodies of ultramafic rocks also occur within this, as well as other eastern Blue Ridge units (Misra and Keller, 1978). The presence of abundant mafic and ultramafic rocks in the

5

eastern Blue Ridge is in stark contrast with the predominantly aluminous metasedimentary rocks to the west.

Eastern Blue Ridge rocks were first mapped and described by Keith (1895, 1904, 1907) who identified the entire sequence as "Carolina Gneiss." Keith considered the Carolina Gneiss to be of Archean age. Today, many geologists also support the idea that these rocks are part of a paragneiss basement complex, (Brewer, 1986; Merschat and Wiener, 1988) and consider them to be Middle Proterozoic. This interpretation is based upon recognition of relict features of the Grenville orogeny (structures, intrusions, and metamorphic assemblages) within the sequence to the northeast of the map area. Alternatively, similar rocks to the south (Tallulah Falls Formation) have been suggested as high-grade, time-stratigraphic equivalents of the Ocoee Supergroup that were deposited in a tectonic regime far to the east, presumably on transitional or oceanic crust (Hatcher, 1978). The eastern Blue Ridge rocks that lie immediately south of the Great Smoky Group assemblage in the study area are tentatively correlated with the Tallulah Falls Formation and the boundary separating them from the Great Smoky Group is interpreted as the Hayesville fault. It is possible that these rocks may be correlated with the Middle Proterozoic basement to the north, but no evidence of Grenville deformation or metamorphism has been observed to support this hypothesis. Correlations across broad regions of the eastern Blue Ridge is difficult because it is increasingly apparent that this province may be a complex amalgamation of thrust sheets and basement exposures.

Further south, another boundary separates the sequence of layered gneiss, amphibolite, and ultramafic rocks from a different assemblage of aluminous metasandstone and schist (aluminum silicate- and staurolite-bearing) with rare intercalations of amphibolite. This boundary is interpreted as the northeastern extension of the Soque River fault that has been mapped in northeast Georgia and southwestern North Carolina (Hopson and others, 1989). Rocks in the footwall of the Soque River fault have been correlated with similar lithologies mapped along strike to the south that have been formally designated the Otto Formation (Hatcher, 1988).

Rocks throughout the mapped area have undergone significant episodes of deformation and at least one prograde metamorphism to kyanite or sillimanite grade. Migmatization is observed in all rock units within the study area and is likely a function of the local availability of water during peak metamorphism. Original stratigraphic relationships of the sedimentary and volcanic protoliths have been virtually obliterated by transposition. Compositional layering and isolated occurrences of graded bedding in

6

metasandstones of the Great Smoky Group and Otto Formation may be the only original sedimentologic structures that have been preserved.

OBJECTIVES OF THIS STUDY

The primary objectives of this study are as follows:

(1)   To produce a quantitative, accurate, and detailed geologic map of the study area with accompanying cross sections. This map will add considerable detail to any that has been previously made for the area.

(2)   To provide detailed lithologic descriptions of all geologic units that have been separated. Internal stratigraphy of each of the three tectonic units recognized will be resolved to the degree that structural complexity permits.

(3)   To provide detailed structural descriptions of the three tectonic units in the area and of the boundaries that separate them. Structural relationships on the macroscopic and mesoscopic scales will be emphasized. In addition, fabric diagrams on equal-area stereonet projections will aid in the description of structural features.

(4)   To present petrologic and geochemical arguments as to the nature and tectonic origin of amphibolites collected from the eastern Blue Ridge units.

(5)   To interpret the depositional, metamorphic, and structural evolution of all lithologic units.

(6)   To correlate the stratigraphy contained within each tectonic unit with units that have been mapped elsewhere in the Blue Ridge and to place the geology of this small study area into a regional perspective.

METHODS

Detailed field mapping was conducted at the scale of 1 : 24,000 during the summer of 1989 and through the winter and spring of 1990. Numerous traverses were made to

7

provide dense coverage of the mapped area. Approximately 1600 data stations were recorded at which lithologies and structural features were noted and measured. All structural measurements were made using a Brunton compass. Final map compilation and cross-section construction was completed during the summer and autumn of 1990.

Structural analysis of mesoscopic deformational features has been completed by thorough descriptions, sketches, and by the use of equal-area (Schmidt lower hemisphere) projections. Structural elements of contrasting style and orientation were compiled and compared to highlight how deformational style varied over a long, episodic deformational history. Macroscopic deformational features were taken from large-scale map patterns and have been included in cross-section interpretations.

Petrographic descriptions of mineralogy, textures, and microstructures are added to outcrop and hand sample lithologic descriptions. Point counting was performed (>1000 points per slide) for a representative suite metasedimentary units to characterize their mineralogy and to highlight protolith differences between units.

Metamorphic mineral assemblages and textures have been identified and utilized to characterize the conditions and history of metamorphism. Field and petrographic identification of metamorphic mineral assemblages has provided a qualification of metamorphic grade and has allowed the sillimanite isograd to be delineated. Compositions of selected metamorphic mineral phases were obtained on a Cameca SX50 electron microprobe for a limited number of pelitic and amphibolite samples. With the microprobe data, various pressure and temperature exchange equilibria were applied to more precisely characterize the metamorphic conditions recorded by coexisting metamorphic phases.

Bulk rock chemistry of amphibolites was obtained through the use of X-ray fluorescence techniques. Data for major, minor, and trace element bulk rock abundances were gathered on an energy dispersive ORTEC X-ray fluorescence spectrometer. Trace element chemistry for the samples was compiled and used in tectonic discrimination diagrams (e.g., Pearce and Cann, 1973; Miyashiro and Shido, 1975) in order to characterize the origin and tectonic setting of the volcanic protoliths.

Lithologies in the study area were separated based upon combinations of texture, mineralogy, and on associations of various rock types. Establishing these criteria, and learning to recognize them in the field was the first step to enable accurate geologic mapping. The following chapter is a detailed treatment of lithologic descriptions and how each of the major lithotectonic units were separated based on these criteria.

II. TECTONIC UNITS AND LITHOLOGIES

Rocks in the study area can be divided into three major tectonic units separated by two major faults. The three tectonic units and their relationships are briefly introduced, followed by in-depth descriptions of the lithologies found within each unit.

INTRODUCTION OF MAJOR LITHOLOGIC DIVISIONS

UNIT 1

The northwesternmost lithologic unit is composed exclusively of rocks belonging to the Great Smoky Group. The Great Smoky Group is part of the Ocoee Supergroup, an extremely thick accumulation of immature to mature clastic sedimentary rocks and minor carbonate. Many studies have confirmed that the Ocoee Supergroup was deposited in fault-bounded rift basin(s) during Late Proterozoic extension and break-up of the Laurasian supercontinent (Hadley, 1970; Rankin, 1975; Wehr and Glover, 1985, Rast and Kohles, 1986). This formidable sedimentary sequence was subsequently metamorphosed during the Taconic orogeny in Middle to Late Ordovician time and now exhibits a classic Barrovian sequence prograding from west to east. Relatively unmetamorphosed to chlorite-grade rocks occur along the western margins of the outcrop belt and metamorphic grade culminates in the sillimanite zone along the eastern margins, near the study area. Ocoee Supergroup stratigraphy was defined by King and others (1958) who separated two different stratigraphic columns: a southeastern section above the Greenbrier fault and a northwestern section below the Greenbrier fault (Fig. 2.1). Only the southeastern stratigraphic section is pertinent for this study because the footwall of the Greenbrier fault was not encountered here. Near the study area, (e.g. in Cherokee, Ela, and Bryson City), the Great Smoky Group is faulted near the base and rests (in fault contact) on granitic gneiss that is part of the underlying basement complex. The Great Smoky Group and the underlying basement comprise the western Blue Ridge assemblage close to the study area.
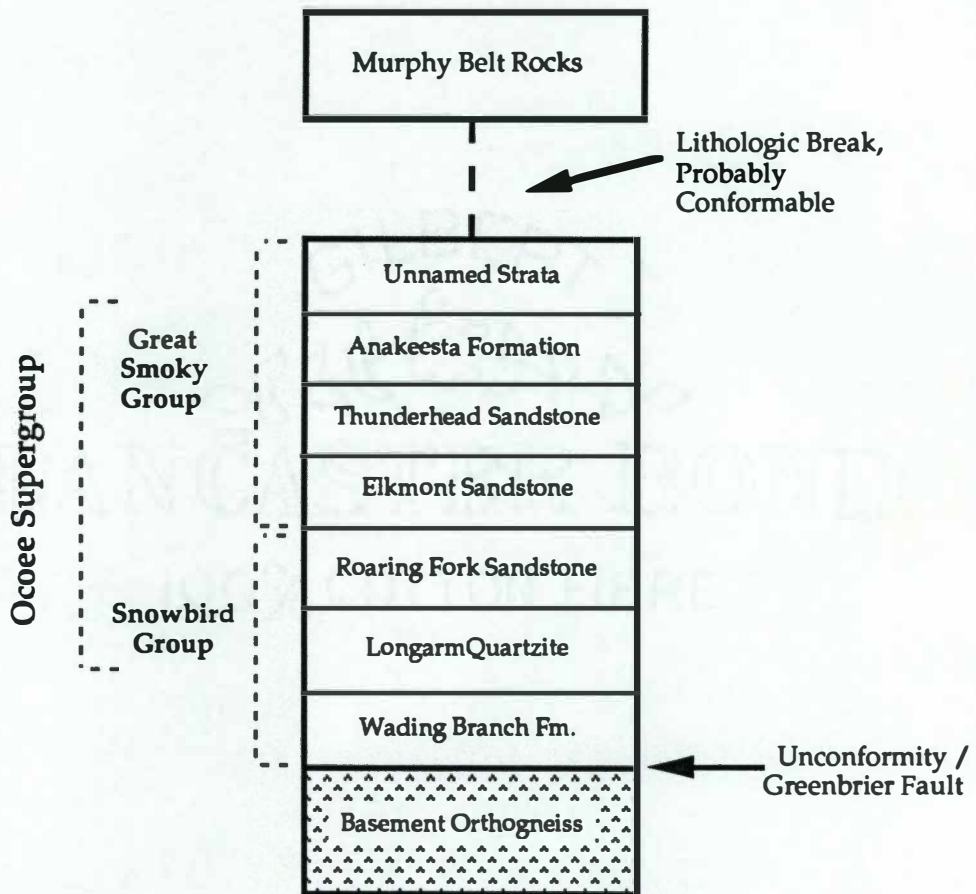
Figure 2.1: Stratigraphic column of the Ocoee Supergroup within the hanging wall of the Greenbrier fault. (After King and others, 1958.)

10

UNIT 2

The second lithotectonic unit is interpreted as a tectonic block that forms the hanging wall of both the Hayesville and Soque River faults. The Hayesville fault bounds the block on the northwest and the Soque River fault separates it from Unit 3 to the southeast. Unit 2 is a sequence of highly deformed, distinctly layered gneiss with abundant intercalations of amphibolite and rare occurrences of ultramafic rocks. These rocks appear to be a metamorphosed assemblage of texturally and mineralogically immature, clastic sedimentary rocks and/or intermediate volcanic tuffs interlayered with mafic volcanic rocks. Ultramafic rocks (mostly dunite) could be the olivine cumulate zone of a dismembered mafic intrusion, an origin analogous to the olivine zone of the Palisades sill (Walker, 1969). Alternatively, the ultramafic rocks could be part of a dismembered ophiolite sequence that was obducted during collapse of the Early Paleozoic continental margin during the Taconic orogeny.

Rocks in Unit 2 are notably more migmatitic in comparison with the other two lithologic units and metamorphic differentiation in the paragneisses is usually well developed. The contrasting appearance of this unit has led various geologists to different interpretations for its origin. Some (Merschat and Wiener, 1988, 1990) consider Unit 2 as basement paragneiss of Middle Proterozoic age, a situation that would associate Unit 2 with basement orthogneisses in the western Blue Ridge. Others (Hatcher and others, 1987) correlate Unit 2 with the Late Proterozoic Tallulah Falls Formation and the underlying Coweeta Group, cover units that comprise a tectonic block that was accreted to the continental margin during the Taconic orogeny.

If the first hypothesis is true, Unit 2 would initially have experienced Grenville (800-1,200 Ma), and later, Taconic (430-460 Ma) deformation and metamorphism. If the second hypothesis is true, then only Taconic features should be observed in Unit 2. In the Asheville area, rocks that lie immediately to the east of the Great Smoky Group in the Canton quadrangle contain granulite facies mineral assemblages relict of the Grenville orogeny that are overprinted by lower grade, Taconian metamorphic assemblages (Merschat and Wiener, 1988, 1990). This kind of overprinting relationship is not present in Unit 2 in the study area. No convincing evidence (neither structural nor metamorphic) is present that would suggest Unit 2 has a Grenville history. Structural and metamorphic features present in Unit 2 more closely resemble those observed in the Tallulah Falls Formation to the south. Unit 2 is consequently considered a cover sequence and is presently correlated with the Tallulah Falls Formation.

The Tallulah Falls Formation has been defined and mapped extensively in the Blue Ridge of northwestern Georgia, northwestern South Carolina, and southwestern North Carolina (Hatcher, 1971, 1973, 1979). If correlation of Unit 2 with the Tallulah Falls Formation is valid, the sedimentary and volcanic protoliths of this unit may be time-stratigraphic equivalents of the Ocoee Supergroup, deposited in an offshore environment on transitional or oceanic crust (Hatcher, 1978; Wehr and Glover, 1985).

UNIT 3

The southeasternmost lithologic unit in the study area is composed of massive to moderately-foliated metasandstone (with rare intercalations of amphibolite) that is interlayered with and overlain by aluminous two-mica schist. The close resemblance of these metasedimentary rocks to those of the Great Smoky Group suggest that the two metasedimentary packages may be genetically related, but Unit 3 contains appreciable amounts of interlayered amphibolite in contrast with the Great Smoky Group.

Rocks in Unit 3 closely resemble units mapped directly along strike in northwestern Georgia and southwestern North Carolina. Regional nomenclature of rocks correlative with Unit 3 is extremely varied and confusing. This unit is part of a narrow, but regionally extensive belt that is continuous from NE of Atlanta northward into western North Carolina. In northeastern Georgia, where the sequence contains abundant mafic and some ultramafic rocks, it was originally referred to as the "Dahlonega gold belt" (Yeates and others, 1896) and was later renamed the "Ashland-Wedowee belt" (Hurst, 1973). More recently, Nelson and Gillon (1985) termed this, and other eastern Blue Ridge sequences the "Helen Group". Equivalent rocks near Atlanta have also been termed the "New Georgia Group" (McConnell and Abrams, 1984). Others have subdivided the eastern Blue Ridge into different terranes, a scheme into which Unit 3 fits as the "Cullowhee Terrane" (Raymond and others, 1989). The name "Otto Formation" was introduced by Hatcher (1988) for extensive exposures of the sequence around the small town of Otto in southwestern North Carolina. Hopson and others (1989) correlated rocks in the Dahlonega gold belt in northeastern Georgia with the Otto Formation, extending it to the south, along the western margin of the Tallulah Falls dome. Regionally, the Soque River fault separates the Otto Formation from the Tallulah Falls Formation and Coweeta Group to the NW. The Tallulah Falls formation also occurs SE of the Otto Formation, but is separated from it there by the Chattahoochee fault (Hopson and others, 1989). This study is the first to document the continuity of the Otto Formation beyond Franklin, northeastward into western North

12

Carolina. Farther north, the Otto Formation may continue as either the Ashe or Alligator Back metamorphic suites or it may be terminated by a fault (Hadley and Nelson, 1971).

UNIT 1: GREAT SMOKY GROUP

FIELD OCCURRENCE AND MEGASCOPIC DESCRIPTION

Lithologies of the Great Smoky Group outcrop abundantly along the steep ridges and valleys of the Plott Balsam Range in the northern two-thirds of the Sylva North 7 1/2 minute quadrangle. Many high, steep cliffs in the Plott Balsam Range are held up by massive exposures of Great Smoky metasandstone. Some of the most accessible and best outcrops of Great Smoky Group rocks in and near the map area are along the Blue Ridge Parkway (between Soco Gap and mile post 446, several miles south of Waterrock Knob), and along U.S. 19 and 441 (just west of the interchange where U.S. 441 and 19 merge). These large road-cut exposures demonstrate the rusty, sulfidic weathering that is common to Great Smoky rocks throughout their outcrop belt.

Massive to thickly-bedded, feldspathic metasandstone is commonly interlayered with sulfidic, well-foliated (and often crenulated) two-mica schist. Estimation of the thickness of Unit 1 in this area is difficult because the base is faulted and the uppermost contact is not observed in the area. Hadley and Goldsmith (1963) estimated the thickness of the entire Great Smoky Group at 6,000-12,000 m. At the very least, the unit is approximately 2,000 m thick in the study area.

Interlayering of metasandstone and schist may be a reflection of original stratigraphic relationships, possibly involving a great number of stacked turbidite sequences within the Thunderhead Sandstone (King, 1964; De Windt, 1975). Additionally, interlayering of metasandstone and schist has been greatly enhanced in the map area by isoclinal folding and transposition of original bedding. Separation of metasandstone and schist into distinct map units proved to be impossible and the two lithologies have been combined into one map unit. In a general sense, however, schist increases in relative abundance in the northwestern portions of the map area.

Metasandstone is the most commonly observed lithology (approximately 65% field occurrence), but this includes many transitional lithologies between granular, mica-poor metasandstone and schist that, in the field, were referred to as micaceous metasandstone. The term "schist" was generally reserved for rocks that contained greater than 50%

13

micaceous material that exhibited well-defined schistosity. Most of the Great Smoky metasandstones encountered in the field were mica-rich (20-40% mica) and were probably graywackes prior to the metamorphic recrystallization that produced mica from detrital clay minerals.

Very minor occurrences of amphibolite occur within the Great Smoky Group in the map area. One relatively fresh outcrop and a few weathered float blocks of amphibolite were encountered during mapping. These rare occurrences of amphibolite are texturally similar to amphibolites in the eastern Blue Ridge and probably also originated as mafic dikes or sills.

Metasandstone

Great Smoky metasandstone is typically medium- to coarse-grained, massive to thickly bedded, and has a light- to medium-gray color when fresh. Mica content is variable and, when it is high, foliation is well-defined. Metasandstone is locally pebble-rich within narrow horizons that grade into medium- and fine-grained layers suggesting the presence of graded beds. Since the rocks are now thoroughly metamorphosed, graded bed sequences often culminate in thin zones of schist.

Hand-sample mineralogy in metasandstone includes quartz, feldspar, muscovite, biotite, and minor opaque minerals. Great Smoky metasandstone is more biotite-rich in the eastern portions of the map area (e.g., along the Blue Ridge Parkway) where it can be difficult to distinguish from Tallulah Falls Formation, especially if it is well-differentiated or migmatitic. Migmatization of Great Smoky metasandstone is rare but does occur close to the Hayesville fault.

Schist

In the map area, the abundant argillaceous layers that were an integral part of the Great Smoky Group sedimentary sequence were metamorphosed and have recrystallized into coarse-grained, two-mica aluminous schist. Biotite, garnet, and aluminum silicate are the major metamorphic index minerals that can be observed in hand samples of schist, and these are invariably accompanied by muscovite, quartz, feldspar, and small oxide and/or sulfide minerals. Schist of the Great Smoky Group is often highly weathered and has a yellowish-brown or rusty brown color due to the breakdown of accessory sulfide minerals. Other outcrops of Great Smoky schist are rich in graphite that produces a silvery-gray color in the rock.

14

Metasandstone

In thin section, Great Smoky metasandstone is granular, with an abundance of quartz and feldspar. Grains of plagioclase, microcline, and untwinned feldspar are often large (0.5 - 1mm) in comparison to quartz grains, which are mostly small (< 0.25 mm). Plagioclase composition ranges from An_{20} to An_{37} with an average of An_{27} (Michel-Levy technique). Where micas are relatively scarce, metasandstone has a uniform granoblastic texture. Foliation is apparent by alignment of muscovite and biotite porphyroblasts, becoming more distinct as modal concentrations of micas increase. As mica content increases, mica grains become coarser as well.

Garnet is sometimes observed in thin sections of metasandstone. Garnet grains in granoblastic metasandstone are sparse and have skeletal forms. Garnets are more euhedral and continuous in mica-rich lithologies. Typical accessory minerals observed in Great Smoky metasandstone are tourmaline, zircon, apatite, detrital sphene, detrital (?) garnet, and opaque minerals.

Schist

Pelitic schist of the Great Smoky Group is extremely mica-rich with a pronounced lepidoblastic texture. Quartz, plagioclase, and untwinned feldspar are present, but are clearly subordinate to abundant, coarse grains of biotite and muscovite. Porphyroblasts of garnet are usually present, are euhedral, and are relatively free of inclusions. Other porphyroblasts that may be observed are staurolite, kyanite, and fibrous mats of sillimanite depending on the composition and metamorphic grade of the rock. Opaque mineral grains (mostly ilmenite) are numerous in most samples of schist. Zircon and tourmaline are observed as accessory minerals in Great Smoky schist.

UNIT 2: TALLULAH FALLS FORMATION WITH ASSOCIATED MAFIC AND ULTRAMAFIC ROCKS

FIELD OCCURRENCE AND MEGASCOPIC DESCRIPTION

In general, Unit 2 is comprised of three main lithologies: biotite gneiss, amphibolite, and ultramafic rock (primarily dunite). Exposures of Unit 2 are abundant

immediately to the southeast of the Hayesville fault, along the lower ridges of the Plott Balsams, and along slopes to the southeast of the Scott Creek drainage (plate 1). Excellent and easily accessible exposures of gneiss/metagraywacke and interlayered amphibolite occur along a gorge excavated by Scott Creek between Cope Mountain and Willits-Ochre Hill on old U.S. 19 and 23 (southeastern edge of Sylva North quadrangle).

Amphibolite mostly occurs as small stringers and boudins interlayered with biotite gneiss. Occurrences of massive amphibolite, with subordinate intercalations of biotite gneiss, are concentrated along the eastern flank of the Webster-Addie dome, to the east and southeast of the Addie and Chestnut Gap dunite mines. Excellent road cut exposures of massive and variably migmatitic amphibolite outcrop along the new U.S. 19 and 23 (at the eastern margin of the Sylva North quadrangle and onto the western margin of the Hazelwood quadrangle).

Ultramafic rocks are part of the well-known Webster-Addie ultramafic body, one of the largest occurrences of ultramafic rock in the southern Appalachians, and an ideal example of an alpine peridotite (Hess, 1955). Ultramafic lithologies in the study area are mostly dunite, with subordinate amounts of harzburgite, talc, vermiculite, and chlorite+actinolite+talc schist. Most of these lithologies can be observed in two mines that have conveniently exposed the Webster-Addie body along its northeastern flank. The Chestnut Gap dunite mine, located several miles south on Blanton Branch Road, is smaller and less accessible than is the Addie mine. The best access to the Addie mine is along the secondary road that parallels Ochre Hill Creek (accessed via either new or old U.S. 19 and 23). In the mines, deep cuts have been made into massive ultramafic rock, exposing it in quarry walls and producing many float blocks. Ultramafic rock is also exposed in the town of Webster, but there it has not been commercially mined and exposures are deeply weathered.

An estimate of original stratigraphic thickness of Unit 2 is difficult because of the intensely deformed character and the fact that the base is faulted. The thickness of the Tallulah Falls unit in the study area is estimated to be between 2,000 to perhaps 5,000 m.

Biotite Gneiss/Metagraywacke

Biotite gneiss is the most common lithology in Unit 2. The most striking feature of this lithologic unit is a virtually ubiquitous layered and well-foliated appearance because of a high degree of metamorphic differentiation. Biotite gneiss is usually finely layered at hand-sample scale, with alternating mafic- and felsic-rich layers that range from 1mm to several cm in thickness. Primary foliation is normally coplanar with compositional

layering and is best defined by the lepidoblastic texture within micaceous layers. Occasionally, in areas where metamorphic differentiation is poorly developed, the appearance of biotite gneiss is more massive and foliation is less pronounced. This more homogeneous lithology is alternatively termed "metagraywacke" because gneissic banding is not apparent. In other areas, compositional layering in biotite gneiss is accentuated by partial melting (i.e., migmatization). In this process, felsic material has undergone melting and has segregated into relatively pure neosomal layers, leaving behind residual melanosomal layers of dark material, chiefly biotite.

Minerals that are conspicuous in hand samples of biotite gneiss or metagraywacke include quartz, feldspar, biotite, opaques, ± amphibole, ± garnet, ± aluminum silicate, ± white mica. Relative abundances of quartz, feldspar, and biotite vary significantly, particularly in the abundance of biotite relative to the other minerals. This modal variability suggests that sedimentary protoliths had a significant degree of compositional heterogeneity, particularly in the relative volume of detrital clay. Biotite + amphibole gneiss is usually found in close proximity to amphibolite bodies or occurs as zones within biotite gneiss that contains abundant intercalated amphibolite. Amphibole may be present due to an original mafic constituent in the sediments. Alternatively, amphibole may have crystallized in the paragneiss due to metasomatic interaction with nearby mafic rocks (now the associated amphibolites).

Grain sizes in Tallulah Falls biotite gneiss/metagraywacke are variable but generally range from medium to coarse. Larger grains appear to have been original detrital quartz and feldspar clasts.

Amphibolite

Amphibolite is common in most of the stratigraphic units in the eastern Blue Ridge and Piedmont of the southern Appalachians (Misra and McSween, 1984). This also holds true for Unit 2 in the study area. Amphibolite in Unit 2 is relatively uniform in appearance throughout the area but it has two basic modes of occurrence:

(1) as thin, discrete layers or small boudins within biotite gneiss or
     biotite + amphibole gneiss and,

(2) as large, outcrop- to map-scale bodies that are dominantly amphibolite, with
     subordinate amounts of intercalated gneiss/metagraywacke.

17

Most amphibolites in the study area are massive to poorly foliated. Compositional layering in amphibolites, however, may be enhanced by migmatization and is apparently coplanar with the primary foliation. Megascopic color of amphibolite is dark black because of the modal dominance of black to deep green amphibole. Biotite may also be a major constituent, which also contributes to the dark black color. Plagioclase is especially conspicuous in hand samples of coarse-grained amphibolites that may represent metamorphosed gabbro or coarse-grained diabase. Garnet is often present in amphibolites and may become large and numerous in certain areas. Garnet porphyroblasts are usually less than 2-3 mm across but some rare amphibolites have been observed in which garnets are up to 30 mm in diameter. Quartz can rarely be identified in hand sample.

The most common mode of occurrence for amphibolite in the map area is as thin layers or pods interlayered with biotite gneiss. These are invariably elongated in a plane that is concordant with the compositional layering and primary foliation of the surrounding gneiss. Thin amphibolite layers are commonly stretched out into discontinuous "stringers" and boudins (Fig. 2.2).

Much larger bodies of massive amphibolite are concentrated along the eastern portion of the map area, in the vicinity of Chestnut Gap and Willits-Ochre Hill. Outcrop- to map-scale amphibolite bodies are generally massive but may show irregular, migmatitic veining (Fig 2.3). Massive amphibolites are often coarser-grained than the smaller boudins or stringers. Large amphibolite bodies are not lithologically homogeneous and contain subordinate amounts of migmatitic biotite gneiss (right margin of Fig. 2.3).

Ultramafic Rocks

Ultramafic rocks in the study area are part of the well-known and extensively studied Webster-Addie ultramafic body (Pratt and Lewis, 1905; Miller, 1953; Condie and Madison, 1969; Greenberg, 1976; Cronin, 1983). Great interest in the Webster-Addie body has been generated over the years due to the economic potential of dunite, talc, chromite, and vermiculite associated with it.

The most common ultramafic lithology seen in the map area is dunite, composed almost entirely of olivine with minor amounts of pyroxene and chromite. Dunite weathers to a deep metallic brown color. Weathered surfaces highlight lamination in dunite that is less apparent in fresh exposures. Lamination appears to be coplanar with the primary foliation of the surrounding gneiss and amphibolite. Dunite is commonly broken along lamination-parallel joint surfaces that are covered with talc and serpentine. Joint

18

Figure 2.2: Photo of a small, boudinaged pod of amphibolite within biotite gneiss (Unit 2). (Outcrop located on Kings Mountain, north of Webster)

19
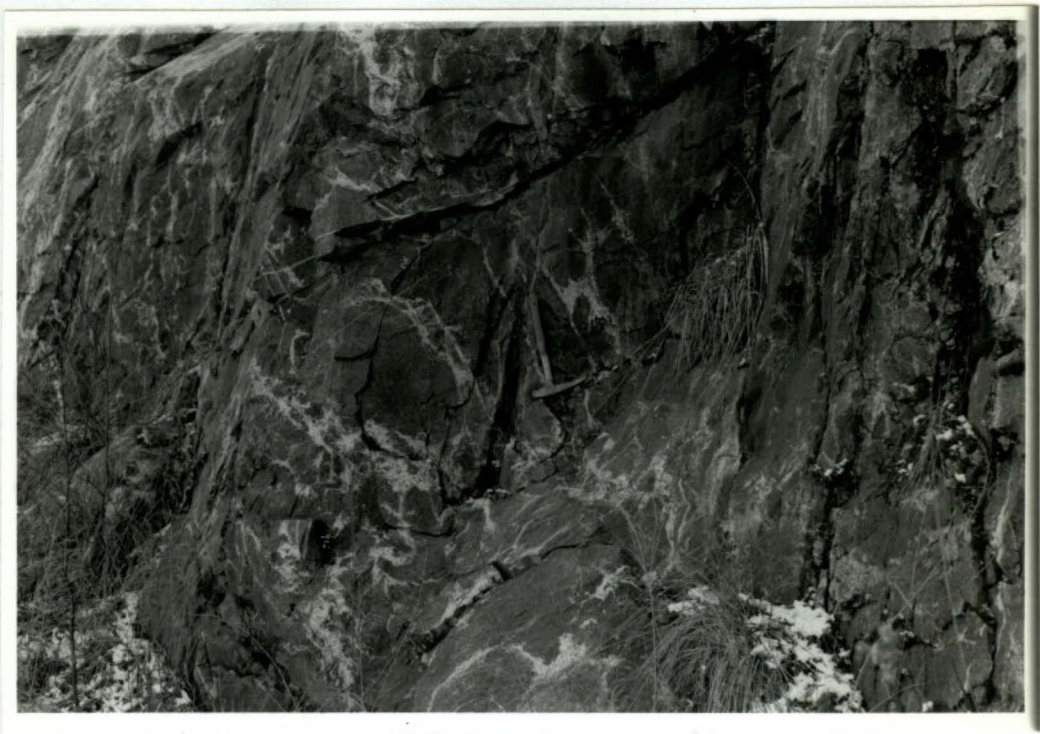
Figure 2.3: Photo illustrating irregular veining pattern in an outcrop of massive amphibolite (Unit 2). (Outcrop located on U.S. 19 & 23, south of Willits-Ochre Hill.)

surfaces may have been partings through which water migrated and retrograded the olivine to hydrous magnesian minerals. Also, along boundaries between ultramafic rock and the surrounding gneiss, dunite is commonly hydrated and altered to soapstone.

Pyroxenite has been reported from several localities in the Webster-Addie body and websterite (olivine + clinopyroxene) has been reported in ultramafic outcrops in Webster (the type locality) (Williams, 1891; Pratt and Lewis, 1905). No websterite was observed during the course of this study because of poor exposure and to removal of much of the lithology by over-enthusiastic rock collectors and mineralogists (S. Yurkovitch, pers. comm.). Pyroxene-bearing lithologies are best observed in piles of ultramafic rubble that have been left in the abandoned Addie mine. The Addie mine is the best locality to observe talc, chlorite, and actinolite in ultramafic schist, as well as hydrated zones that contain coarse vermiculite.

PETROGRAPHIC DESCRIPTION

Biotite Gneiss/Metagraywacke

Tallulah Falls metagraywacke is compositionally layered at the thin section scale with discrete, linear mafic and felsic zones. Layers dominated by quartz + plagioclase + microcline are separated by thinner layers, mainly composed of biotite ± epidote ± sphene, and accessory opaque minerals. Plagioclase composition ranges from An_{26} to An_{40} with an average of An_{34} (Michel-Levy technique). Alkali feldspar mostly occurs as microcline, identified by cross-hatch twinning patterns. Biotite usually exhibits a reddish brown to pale brown/yellow pleochroism. Biotite with a green pleochroic scheme is more infrequent, but is seen in several samples of biotite gneiss. Mafic layers in some cases are rich in epidote + sphene, or in hornblende + sphene in addition to biotite. These metamorphic assemblages indicate the bulk compositions of some rocks are rich in magnesium, iron, calcium, and titanium. Muscovite and aluminum silicate minerals are rare indicating that biotite gneiss is generally not peraluminous.

Most garnets present in Tallulah Falls gneiss/metagraywacke are small, anhedral to subhedral, with few inclusions. Garnets are mostly concentrated in micaceous layers in biotite gneiss. Some very small garnet grains are anhedral with rounded edges. These garnets perhaps have a detrital rather than metamorphic origin. Accessory zircon probably is also of detrital origin.

Thin biotite-rich layers best define the foliation of the rock, which mostly parallels the compositional layering. Quartz ribbons may be present and also parallel compositional

21

layering. Feldspars are typically large (up to 4 mm). Quartz sizes are variable with most quartz grains being small (< 0.5 mm). Biotite books may be large (1-3 mm long), especially where biotite is modally abundant.

Amphibolite

In thin section, amphibolites are commonly granoblastic with no obvious preferred orientations of amphibole crystals. Prismatic sections of amphibole are less common than prism cross-sections, however, indicating some degree of preferred orientation. All amphiboles were identified as common hornblende with maximum extinction angles of 19–31°. Most amphibole crystals show evidence of compositional zoning by a changing pleochroism from core to rim. Hornblende cores have a dark brown to olive brown to pale brown pleochroism, while narrow rim zones exhibit a light tan to pale green to blueish green pleochroic scheme. The largest hornblendes are up to a cm in length for prismatic sections.

Other minerals in amphibolites include plagioclase, quartz, opaques, microcline ± garnet ± sphene ± epidote ± biotite ± chlorite. Plagioclase is modally more abundant than quartz and microcline. Plagioclase composition ranges from An_{25} to An_{41}, with an average of An_{34} (Michel-Levy technique). Sphene is common in amphibolite, whereas epidote is more infrequent and occurs in lesser amounts. Garnet is often present and can be relatively large (3-4 mm across). Biotite and chlorite are rare.

Graphic intergrowth texture is common between various minerals in some amphibolite samples. Intergrowth occurs between quartz and plagioclase, amphibole and plagioclase, and amphibole and garnet (Fig. 2.4). This texture probably results from resorbtion reactions following peak metamorphic recrystallization.

Dunite

Three thin sections of ultramafic rock were made for this study and all of these were made from olivine-dominated lithologies. More numerous and more varied ultramafic lithologies from the Webster-Addie body were described by Cronin (1983, Appendix A), including varieties of dunite, harzburgite, websterite and pyroxenite.

Thin sections of dunite contain up to 95% olivine. Olivine composition in three dunite samples, determined from refractive indices (beta index), is approximately Fo_{86-95}. Orthopyroxene and accessory opaque minerals (probably mostly chromite) make up the remainder of the original mineralogy of unaltered dunite. Two of the three samples, however, are significantly altered and contain minerals produced by the hydration of

22
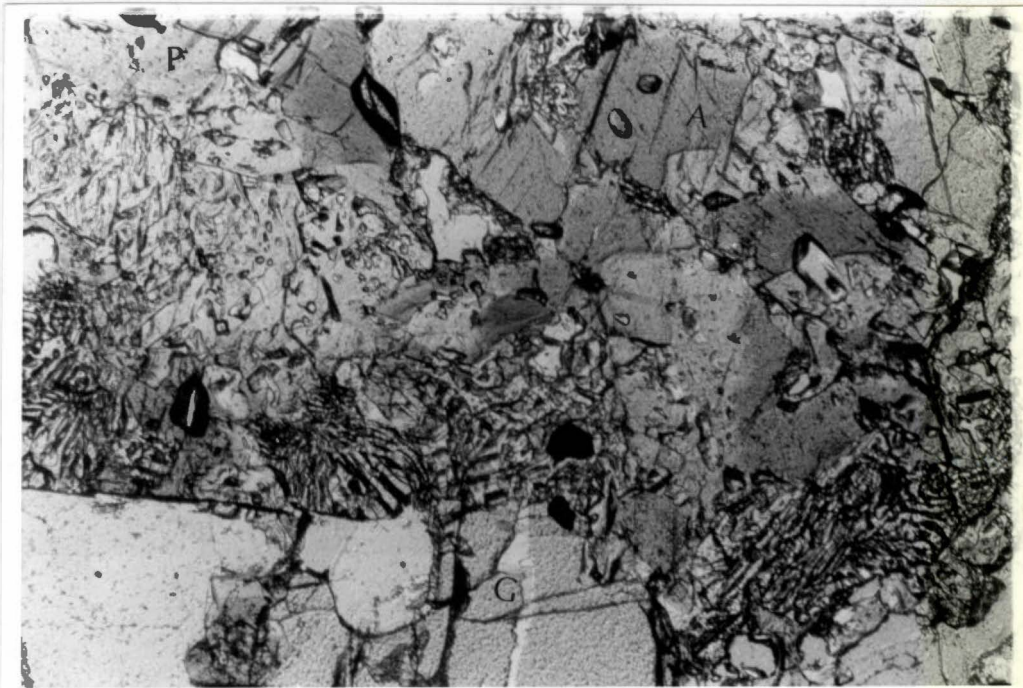
0.5mm

Figure 2.4: Thin section photo of a coarse-grained amphibolite illustrating graphic intergrowth texture between garnet (G), plagioclase (P), and amphibole (A). (Scale bar = 0.5 mm.)

23

olivine. Fibrous and asbestiform serpentine minerals such as antigorite have been produced by hydration reactions. In one sample, fibrous and frequently radiating aggregates of serpentine minerals have grown between olivine grains as fibrous mats. In another sample, serpentine minerals form an amorphous-looking matrix in which the residual olivine grains are suspended. Clearly, hydration has affected the original dunite mineralogy to varying degrees in different samples. Formation of serpentine is probably retrograde since its formation by the interaction of water and forsterite occurs only below 400°C (Deer and others, 1966).

UNIT 3: OTTO FORMATION

FIELD OCCURRENCE AND MEGASCOPIC DESCRIPTION

Unit 3 is composed primarily of aluminous metasedimentary rocks and for this reason, Hadley (1970) and Hadley and Nelson (1971) correlated this sequence with the Great Smoky Group to the northwest. A significant difference between the two, however, lies in the fact that interlayered amphibolite is abundant in Unit 3, while very scarce in the Great Smoky Group.

Exposures of Unit 3 can be observed in road cuts on U.S 107 (new) near Cullowhee and on U. S. 441 & 23, south of Sylva. These outcrops display the more amphibolite-rich and more gneissic variations of the unit. Examples of interlayered metasandstone and aluminous schist occur on the crest of Kings Mountain, immediately south of Sylva, and along Wayehutta Creek Road, east of Cullowhee.

Realistic thickness estimates for Unit 3 cannot be made because a lower contact was not observed and the top of the section is faulted. The unit certainly exceeds 2,000 m.

Metasandstone/Gneiss

Metasandstone is the most common lithology observed in Unit 3 in the study area. It is usually quartz-rich and feldspathic with variable amounts of biotite and muscovite. In comparison to gneisses in Unit 2, metasandstone of Unit 3 is generally less-differentiated, contains less migmatite, less amphibolite, and a significant amount of muscovite. In most areas the metasandstone is relatively homogeneous and poorly foliated. As mica content increases, foliation becomes more distinct. In other instances, metasandstone is compositionally layered with alternating layers of aluminous schist ± layer-parallel quartz

veins ± amphibolite ± calc-silicate quartzite. Metasandstone is the predominant lithology in compositionally layered outcrops.

Minerals that are readily identified in hand samples or outcrops of metasandstone are quartz, feldspar, biotite, muscovite, opaque oxides and sulfides ± garnet ± staurolite ± aluminum silicate. Grain sizes are usually medium to coarse with occasional pebble-sized material. Repeating sequences of alternating metasandstone and schist (Fig. 2.5) may suggest that the protolith contained graded beds.

Schist

Schist in Unit 3 is usually interlayered with metasandstone where it is a subordinate lithology. Relative frequency and volume of schist increases in outcrops that occur near the top of the section, closest to the Soque River fault. Schist is well-foliated and foliation parallels compositional layering. Schist in Unit 3 is frequently stained by a chalky yellow weathering color that is probably a product of the breakdown of biotite.

Mineralogy of the more aluminous schists is quite interesting because these bear easily identifiable, diagnostic index minerals that characterize the metamorphic grade. Kyanite and staurolite occur commonly with garnet and biotite in more aluminous schist samples. Sillimanite becomes the stable aluminum silicate phase in the extreme western and southern portions of the study area. Where schist is less aluminous, biotite and garnet are the only two index minerals present. Other minerals include fine-grained quartz, feldspar, muscovite, and tiny opaque oxide and/or sulfide minerals. In general, biotite surpasses muscovite in abundance in Otto Formation schist.

Amphibolite

Similar to amphibolites in Unit 2, those in Unit 3 mostly occur as small discontinuous stringers or boudins interlayered within metasandstone. Interlayered amphibolite is more infrequent in Unit 3 and is frequently weathered out as cobble-sized float blocks. Bodies of massive amphibolite are smaller and more rarely observed than those observed in Unit 2.

Amphibolite in Unit 3 generally lacks a well-developed foliation. Amphibole is the most abundant mineral with lesser amounts of biotite and plagioclase. Rare coarse-grained amphibolites have larger, more conspicuous plagioclase. Garnet porphyroblasts are often present in amphibolite.

Figure 2.5: Photo of interlayered metasandstone and schist in Unit 3. Compositional layering and foliation are coplanar and steeply dipping. (Outcrop located in Cox Cove, SW of Cullowhee.)

26

Altered Pyroxenite

A small body of altered ultramafic rock was encountered on the ridge to the northwest of Wayehutta creek. The ultramafic body here contains light green amphibole and orthopyroxene and appears to be an altered pyroxenite. The pyroxenite body is surrounded by a weathered chlorite schist.

PETROGRAPHIC DESCRIPTION

Metasandstone

In thin section, metasandstone from Unit 3 is granular, very micaceous, and generally has a compositional banding. Micas are oriented and define a primary foliation that is parallel to compositional layering. Biotite is the dominant mica and always exhibits reddish brown to pale brown pleochroism. Muscovite content is variable and is sometimes completely absent.

Other major constituents in metasandstone are quartz, plagioclase, microcline, and opaque minerals. Plagioclase compositions range from An_{20} to An_{38} with an average of An_{26} (Michel-Levy technique). Quartz grain sizes are variable while plagioclase and microcline grains tend to be mostly large. Garnet is common and is generally large (2-4 mm) and subhedral with abundant inclusions. Aluminum-rich varieties of metasandstone bear aluminum silicate (usually kyanite) and/or staurolite porphyroblasts. Accessory minerals observed in metasandstone were opaques, zircon, and rutile.

Schist

Thin sections of schist from Unit 3 exhibit much the same mineralogy as the more aluminous metasandstones, but with a higher percentage of mica. Muscovite in schist increases in abundance relative to biotite and both mica varieties are coarse grained. Abundant micas are well-aligned and define a distinct foliation. Porphyroblasts of garnet, aluminum silicate, and staurolite are larger and more euhedral than in metasandstone. Elongate porphyroblasts, such as kyanite or staurolite, are aligned with the foliation. Enclaves of quartz, plagioclase, and alkali feldspar are elongated parallel to the foliation.

In most samples of schist, the aluminum silicate phase is kyanite. Sillimanite becomes the stable aluminum silicate phase in the extreme western and southern margins of the map area. Sillimanite mostly occurs as fibrolite that has the form of aggregates of elongate, thin, and acicular crystals. Prismatic sillimanite occurs in several schist samples collected south of Cullowhee.

Amphibolite

In general, thin sections of amphibolite samples from Unit 3 appear to be modally and texturally very similar to amphibolite samples from Unit 2. Unit 3 amphibolites are granoblastic and are dominated by hornblende and plagioclase. All amphiboles were identified as common hornblende with maximum extinction angles of 18–26°. Most amphiboles exhibit pleochroic evidence of compositional zoning. Hornblendes are several mm long prismatic sections.

Other minerals in amphibolites include plagioclase, microcline, quartz, opaques ± garnet ± sphene ± epidote ± biotite ± chlorite. Plagioclase is modally more abundant than quartz and microcline. Plagioclase composition ranges from An_{28} to An_{44} with an average of An_{36} (Michel-Levy technique). One amphibolite sample (SS600) contains anomalously calcic plagioclase with a compositions around An_{65-67}. Sphene and epidote occur in variable amounts but sphene is more common and always more abundant. Garnets are euhedral and generally smaller in Unit 3 amphibolites than in Unit 2 amphibolites. Biotite and chlorite are rare.

Graphic intergrowth texture is also common in amphibolite samples from Unit 3. As described for some amphibolites in Unit 2, intergrowth occurs between quartz and plagioclase, amphibole and plagioclase, and amphibole and garnet .

Altered Pyroxenite

Sample SS191 taken from the ultramafic body contains pale green hornblende , orthopyroxene (bronzite), epidote, and plagioclase with minor opaques. Amphibole dominates over orthopyroxene and may represent altered clinopyroxene. The sample contains no apparent foliation as the grains are randomly oriented.

OTHER LITHOLOGIES

Calc-silicate

Calc-silicate quartzite rock is commonly intercalated as layers or pods in metasandstones/gneisses of all lithologic units. Calc-silicate in Unit 2 is less quartz-rich, coarser grained, and more commonly occurs as pods and boudins. Calc-silicate quartzites probably represent metamorphosed calcareous chert or quartzite beds that originally had calcareous cements. Fresh calc-silicate quartzite is massive and very hard with a waxy or

glassy appearance. Quartz is the dominant mineral with minor occurrences of feldspar, garnet, hornblende, epidote, and sphene.

Three samples of calc-silicate quartzite were thin sectioned for petrographic study; one from Unit 3 and two from Unit 1. In thin section, calc-silicate mineralogy is dominated by fine-grained quartz. Plagioclase is present in varying amounts but is always subordinate to quartz in modal abundance. Anorthite content in plagioclase is usually very high and averages about An_{62}. Sample SN127 plagioclases are considerably less calcic: An_{28-34}. Other calcareous minerals include epidote (or clinozoisite), sphene, and actinolite. Sample SN127 is anomalous in that it contains biotite and microcline and hornblende is absent. Accessory minerals include muscovite, apatite, and opaques.

Trondhjemite

Trondhjemite is a felsic variety of tonalite and contains predominantly plagioclase and quartz, with K-feldspar and biotite as minor constituents (Williams and others, 1954). Intrusive bodies of trondhjemite cross-cut all major units in the study area. Most are high-angle dikes that are no wider than 0.5 m. Some dikes are folded and others show brittle offsets indicative of some minor deformation after emplacement. Trondhjemite is very massive and generally lacks any distinct penetrative fabric. Where weathered to saprolite, trondhjemite has a chalky gray and white appearance and breaks apart easily.

No thin sections of felsic dike rocks were made for this study.

Pegmatite

Pegmatite bodies are scattered throughout the map area and have been mined within the last 70 years, primarily for micaceous minerals. Some pegmatites are foliated while others exhibit no obvious tectonic fabric. They are coarse grained, quartz- and feldspar-rich bodies. Plagioclase and K-feldspar are generally present as large, easily identifiable grains. Biotite and muscovite occur as large books and veins in pegmatite. Muscovite is usually the dominant mica. Pegmatite bodies have an igneous origin and probably represent crystallized aggregates of anatectic melts.

No thin sections of pegmatite were made for this study.

SEDIMENTARY PETROGRAPHY

Metasandstone and metagraywacke lithologies are common in all three of the major lithologic units in the study area. Point counting was performed on thin sectioned samples of metasandstone from each of the major lithologic units in an effort to quantify their modal mineralogy and to characterize the sedimentary protoliths. Seven metasandstone samples were selected from each of the three lithologic units. Greater than 1000 points were counted for each sample to provide a statistically significant representation of their mineralogy (Tables 2.1, 2.2, and 2.3). Confidence limits for mineral proportions are less than ±3.2% for major constituents (quartz, feldspar, and mica) and less than ±2% for minor constituents (van der Plas and Tobi, 1965).

Table 2.1 exhibits that samples from Unit 1 are quartz-rich (26-68%) with variable quartz : feldspar ratios. Plagioclase is significantly more abundant than alkali feldspar in all but one sample. Biotite is greater in abundance than muscovite and muscovite does not exceed 7% of the rock volume in all of the samples studied. Garnet and heavy minerals are rare, while opaque minerals are abundant, particularly in sample SN245.

Table 2.2 reveals that samples from Unit 2 are considerably rich in quartz and plagioclase. Plagioclase is consistently more abundant than alkali feldspar. Biotite is the only mica present in abundance except in sample SN722 where muscovite content nearly equals biotite. Sphene and/or epidote are often present in small amounts. Hornblende is relatively abundant in sample SS63 (a hornblende + biotite gneiss). Opaque and heavy minerals are present in minor amounts.

Table 2.3 exhibits that samples from Unit 3 are commonly very micaceous, with the exception of sample SS399, which is anomalously quartz-rich. Biotite is the dominant mica in some samples whereas muscovite dominates in others. Plagioclase exceeds alkali feldspar in most samples and total plagioclase is considerably variable. In comparison with the other units, samples from Unit 3 have much higher mica contents.

Metasandstone mineralogies are dominated by three constituents: quartz, feldspar, and mica (QFM). The relative proportions of the QFM constituents, although the minerals have undergone appreciable recrystallization during metamorphism, can be taken as reliable approximations of corresponding proportions of original detrital components: quartz, feldspar, and clay (respectively). This reasoning employs the assumptions that all detrital clay minerals have recrystallized as biotite or muscovite mica, and that quartz and feldspar constituents have retained their original proportions. Finally, if the QFM

30

Table 2.1: Point counting data for samples of metasandtone from Unit 1.

Raw Counts														
Sample	Qtz	Plg	A. F.	Bio	Musc	Gar	A. S.	Epi	Hbl	Sph	Chl	Opq	H. M.	Total
SN18	639	130	28	159	27	1	–	–	–	–	–	23	2	1009
SN62	577	169	50	141	68	2	–	–	–	1	–	4	1	1013
SN66	363	373	30	127	61	57	–	–	–	–	–	18	4	1033
SN245	523	53	63	248	44	19	–	–	–	–	–	65	4	1019
SN642	267	235	136	369	37	–	–	–	–	–	–	1	–	1045
SN662	710	116	50	124	42	–	–	–	–	–	–	1	3	1046
SN841	377	334	78	232	33	–	–	–	–	–	–	8	5	1067

Percentages														
Sample	Qtz	Plg	A. F.	Bio	Musc	Gar	A. S.	Epi	Hbl	Sph	Chl	Opq	H. M.	Total
SN18	63.3	12.9	2.8	15.8	2.7	0.10	–	–	–	–	–	2.28	0.20	100
SN62	57.0	16.7	4.9	13.9	6.7	0.20	–	–	–	0.10	–	0.39	0.10	100
SN66	35.1	36.1	2.9	12.3	5.9	5.52	–	–	–	–	–	1.74	0.39	100
SN245	51.3	5.2	6.2	24.3	4.3	1.86	–	–	–	–	–	6.38	0.39	100
SN642	25.6	22.5	13.0	35.3	3.5	–	–	–	–	–	–	0.10	–	100
SN662	67.9	11.1	4.8	11.9	4.0	–	–	–	–	–	–	0.10	0.29	100
SN841	35.3	31.3	7.3	21.7	3.1	–	–	–	–	–	–	0.75	0.47	100

Abbreviations			
Qtz = Quartz	Musc = Muscovite	Epi = Epidote	Opq = Opaques
Plg = Plagioclase	Gar = Garnet	Hbl = Hornblende	H. M. = Heavy
A. F. = Alkali Feldspar	A. S. = Aluminum	Sph = Sphene	Minerals
Bio = Biotite	Silicate	Chl = Chlorite	

31

Table 2.2: Point counting data for samples of gneiss/metagraywacke from Unit 2.

					Raw Counts									
Sample	Qtz	Plg	A. F.	Bio	Musc	Gar	A. S.	Epi	Hbl	Sph	Chl	Opq	H. M.	Total
SN1	436	214	73	255	–	–	–	41	–	8	–	7	4	1038
SN258	479	316	18	189	–	1	–	4	–	–	–	6	4	1017
SN419	466	253	108	176	7	–	–	21	–	–	–	–	5	1036
SN487	642	165	116	110	3	1	–	–	–	–	–	1	–	1038
SN722	509	178	41	153	119	6	–	–	–	–	–	10	4	1020
SS63	342	250	33	257	–	66	–	–	72	–	–	4	2	1026
SS81	370	294	100	256	–	–	–	–	–	9	–	–	3	1032

					Percentages									
Sample	Qtz	Plg	A. F.	Bio	Musc	Gar	A. S.	Epi	Hbl	Sph	Chl	Opq	H. M.	Total
SN1	42.0	20.6	7.0	24.6	–	–	–	3.9	–	0.8	–	0.7	0.4	100
SN258	47.1	31.1	1.8	18.6	–	0.1	–	0.4	–	–	–	0.6	0.4	100
SN419	45.0	24.4	10.4	17.0	0.7	–	–	2.0	–	–	–	–	0.5	100
SN487	61.8	15.9	11.2	10.6	0.3	0.1	–	–	–	–	–	0.1	–	100
SN722	49.9	17.5	4.0	15.0	11.7	0.6	–	–	–	–	–	1.0	0.4	100
SS63	33.3	24.4	3.2	25.0	–	6.4	–	–	7.0	–	–	0.4	0.2	100
SS81	35.9	28.5	9.7	24.8	–	–	–	–	–	0.9	–	–	0.3	100

Abbreviations

Qtz = Quartz	Musc = Muscovite	Epi = Epidote	Opq = Opaques
Plg = Plagioclase	Gar = Garnet	Hbl = Hornblende	H. M. = Heavy
A. F. = Alkali Feldspar	A. S. = Aluminum	Sph = Sphene	Minerals
Bio = Biotite	Silicate	Chl = Chlorite	

Table 2.3: Point counting data for samples of metagraywacke from Unit 3.

Raw Counts

Sample	Qtz	Plg	A. F.	Bio	Musc	Gar	A. S.	Epi	Sta	Sph	Chl	Opq	H. M.	Total
SS353	309	126	129	280	24	100	37	–	–	–	–	8	3	1016
SS360	169	61	12	275	368	132	–	–	–	–	2	23	–	1042
SS391	159	213	40	415	155	51	–	–	–	–	–	6	3	1042
SS399	618	136	26	182	–	51	6	–	–	–	1	–	1	1021
SS527	274	88	13	226	430	90	1	–	10	–	31	1	2	1166
SS556	279	81	19	344	325	78	–	–	–	–	–	24	2	1152
SS621	249	89	22	198	227	160	50	–	–	–	–	2	7	1004

Percentages

Sample	Qtz	Plg	A. F.	Bio	Musc	Gar	A. S.	Epi	Sta	Sph	Chl	Opq	H. M.	Total
SS353	30.4	12.4	12.7	27.6	2.4	9.8	3.6	–	–	–	–	0.8	0.3	100
SS360	16.2	5.9	1.2	26.4	35.3	12.7	–	–	–	–	0.2	2.2	–	100
SS391	15.3	20.4	3.8	39.8	14.9	4.9	–	–	–	–	–	0.6	0.3	100
SS399	60.5	13.3	2.5	17.8	–	5.0	0.6	–	–	–	0.1	–	0.1	100
SS527	23.5	7.5	1.1	19.4	36.9	7.7	0.1	–	0.9	–	2.7	0.1	0.2	100
SS556	24.2	7.0	1.6	29.9	28.2	6.8	–	–	–	–	–	2.1	0.2	100
SS621	24.8	8.9	2.2	19.7	22.6	15.9	5.0	–	–	–	–	0.2	0.7	100

Abbreviations

Qtz = Quartz	Musc = Muscovite	Epi = Epidote	Opq = Opaques
Plg = Plagioclase	Gar = Garnet	Sta = Staurolite	H. M. = Heavy
A. F. = Alkali Feldspar	A. S. = Aluminum	Sph = Sphene	Minerals
Bio = Biotite	Silicate	Chl = Chlorite	

Calcite

Zircon

proportions are considered approximately equal to detrital quartz-plagioclase-clay (QFC) proportions in the sedimentary protolith, the metasandstones can be classified on a QFC diagram. In the classification scheme of Pettijohn (1954), QFC proportions of sandstones are plotted on a ternary diagram that is subdivided to classify various types of clastic rocks. In this study, the same classification scheme is used but with QFM end-members (Fig 2.6a).

Samples containing significant amounts of garnet, aluminum silicate, staurolite, hornblende, sphene, or epidote were avoided as much as possible. This is because samples rich in minerals that are the products of discontinuous metamorphic reactions would have skewed QFM ratios relative to their original QFC proportions (Q, F, or M components may consumed as reactants in different proportions during metamorphic reactions).

Most samples studied plot in the graywacke field on the QFM ternary classification scheme (Fig. 2.6b, 2.6c, and 2.6d). Relative abundances of Q : F : M are variable, producing scatter, especially in Units 1 and 3. Scatter of samples from Unit 1 primarily results from variations in Q : F ratios (Fig 2.6b). Mica content is also variable, but to a lesser degree. The scatter of samples from Unit 1 indicates that the protolith was heterogeneous and ranged from graywacke to feldspathic quartzite.

Scatter of samples from Unit 3, on the other hand, results primarily from variations in Q : M ratios (Fig 2.6d). This suggests that the protolith was heterogeneous with respect to clay content and ranged from pelitic subgraywacke to graywacke to feldspathic quartzite.

Samples from Unit 2 are much less variable in composition than the other two groups. The samples cluster about the boundary separating the graywacke and arkose fields on the QFM diagram (Fig. 2.6c). The "clustering" of data points here indicates a relatively homogeneous, clay-deficient graywacke as a protolith.

Three major lithologic units now have been defined and described. Structural deformation and metamorphism is responsible for much of the observed textures and mineralogy seen in these rocks. Structural and metamorphic aspects will be addressed in the following two sections.
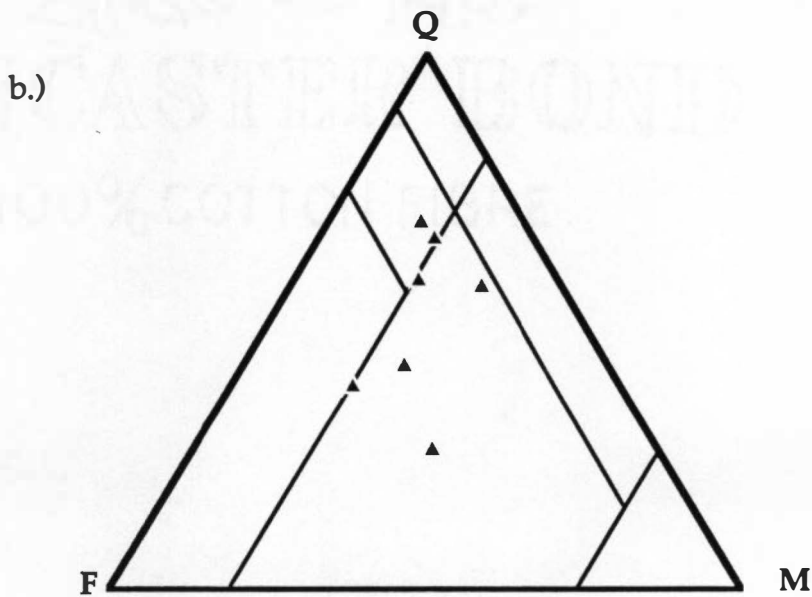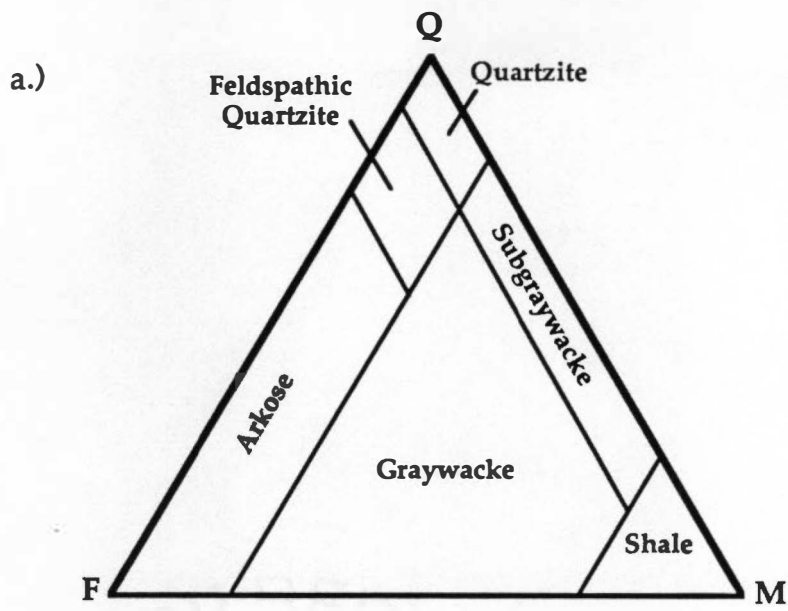
Figure 2.6: Classification of metasandstone on QFM ternary diagrams. (Based on the QFC sandstone classification scheme of Pettijohn, 1954.) a) Generalized form of the QFM ternary classification, b) samples from Unit 1, c) samples from Unit 2, d) samples from Unit 3.

35

c.)
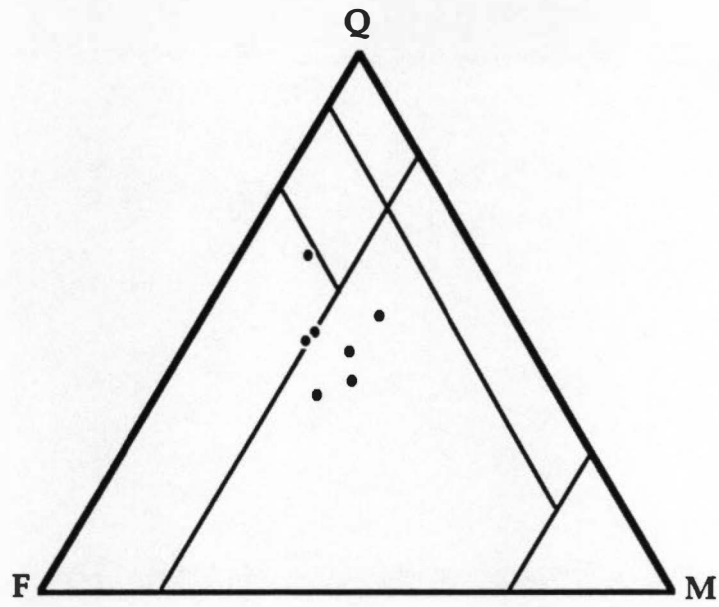
d.)
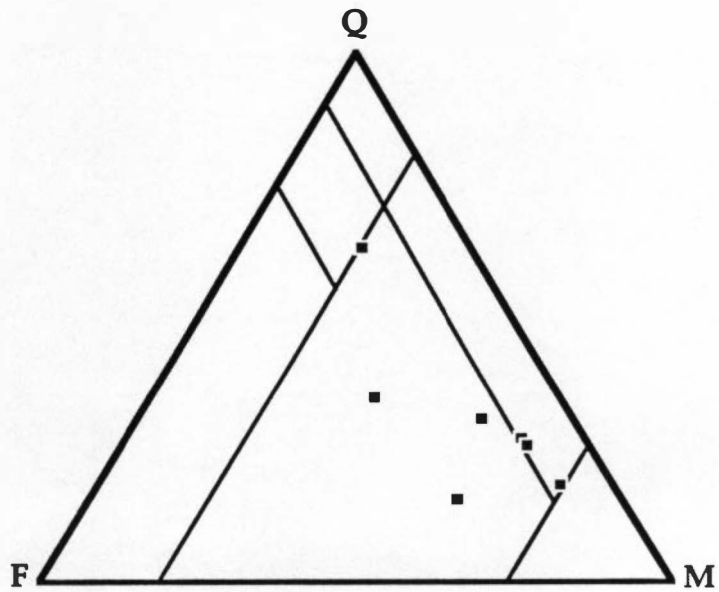
Figure 2.6 (continued)

III. STRUCTURAL GEOLOGY

Most rocks in the study area have undergone pervasive deformation and recrystallization. Structures observed here can be separated into different generations, indicating that deformation was most certainly diachronous. Crosscutting folds of contrasting style and orientation indicate that at least five separate folding events have affected the rocks. Compositional layering in all major lithologic units is the product of metamorphic differentiation and transposition. Transposition accompanied tight-to-isoclinal folding in the early stages of deformation, and at least two early isoclinal folding events are evident. Possibly four later folding episodes affected the the latest transposed layering. Scattered occurrences of mylonitic rocks indicate that localized, small-scale shearing has occurred. Evidence for large-scale faulting is not well-documented by mesoscopic structural features, but is more reliant on megascopic structural trends and on distinct lithologic contrasts across faults (see Chapter 2).

Structural complexity does not appear to vary between major lithotectonic units suggesting that deformational history may be consistent throughout the study area. Structural features observed in all lithotectonic units can, therefore, be discussed concurrently. The polyphase nature of deformation can be demonstrated at macroscopic, mesoscopic and microscopic scales. Each scale of observation provides somewhat different information and insight into the structural history of the region. Structural elements will be addressed from each of these perspectives in the following sections.

MESOSCOPIC FEATURES

FOLIATION, COMPOSITIONAL LAYERING, AND EARLY FOLDS

Compositional layering and coplanar primary foliation observed in the rocks of the study area is considered to be a product of transposition(s) during the earliest stages of deformation. Transposition is a process whereby a preexisting layering (primary bedding, or perhaps even an earlier transposed layering) is reoriented into parallelism with a newly developing foliation by folding or ductile shear (Hobbs and others, 1976; Hatcher, 1990). Metamorphic recrystallization and differentiation accompanied transposition during isoclinal F_1 flowage folding, producing a reoriented compositional layering parallel to S_1. Later, tight to isoclinal flowage folding (F_2) transposed the rocks again, refolding F_1 folds

and reorienting S_1 foliation into parallelism with a newly developed S_2 foliation. Primary stratigraphic layering (S_0, or bedding) has been effectively obscured or obliterated by transposition and metamorphic differentiation. Evidence for two transposition episodes during the early stages of deformation is twofold:

(1) the presence of intrafolial isoclines that have obviously been refolded during the formation of S_2 (Fig. 3.1), and

(2) gneissic banding (a preexisting, transposed compositional layering) is isoclinally folded by F_2 folds.

The primary foliation observed in the study area is axial planar to isoclinal F_2 folds, and is therefore designated S_2. Compositional layering produced by metamorphic differentiation may have developed prior to, or during, the formation of S_1 foliation. F_2 folding subsequently reoriented S_1 foliation and gneissic banding into parallelism with the axial surfaces of F_2 folds. Metamorphic differentiation probably continued during F_2 folding but not to the degree that F_2 fold hinges were completely obscured.

Migmatitic gneiss is present in all lithotectonic units in the study area but is more commonly encountered in Unit 2 than in Units 1 or 3. Migmatization appears to have increased the degree of differentiation and has enhanced compositional layering where it occurs. Leucocratic migmatite layers are mostly parallel to S_2, but sometimes crosscut S_2. Leucocratic migmatite layers are commonly folded by F_2 folds, suggesting that anatectic conditions prevailed prior to, or during, the development of S_2.

Approximately 1900 measurements of S_2 foliation were made during the course of this study. These data were separated into three groups, pertaining to their respective lithotectonic units. Poles to foliation were plotted and contoured on equal-area stereonet projections (Fig. 3.2). Because of later refolding events, S_2 foliation orientations are nonuniform. Contoured foliation data emphasize that S_2 foliations generally strike NE-SW. Dip of S_2 foliation is generally shallow in Unit 1, shallow to steep in Unit 2, and steep in Unit 3. "Girdles" (great circle-like bands produced by the contour pattern) are formed by the data from Units 1 and 2. These girdles indicate folding of the S_2 surfaces occurred about axes that plunge gently to the northeast (β on Fig. 3.2a, b). It is likely that this same fold set affected the rocks in Unit 3, but there, folding was tighter, producing steeper limbs and narrower hinge zones. Very tight folding would reduce the girdling effect on the data for Unit 3. Alternatively, S_2 in Unit 3 may not have been greatly perturbed by later folding if

F1?
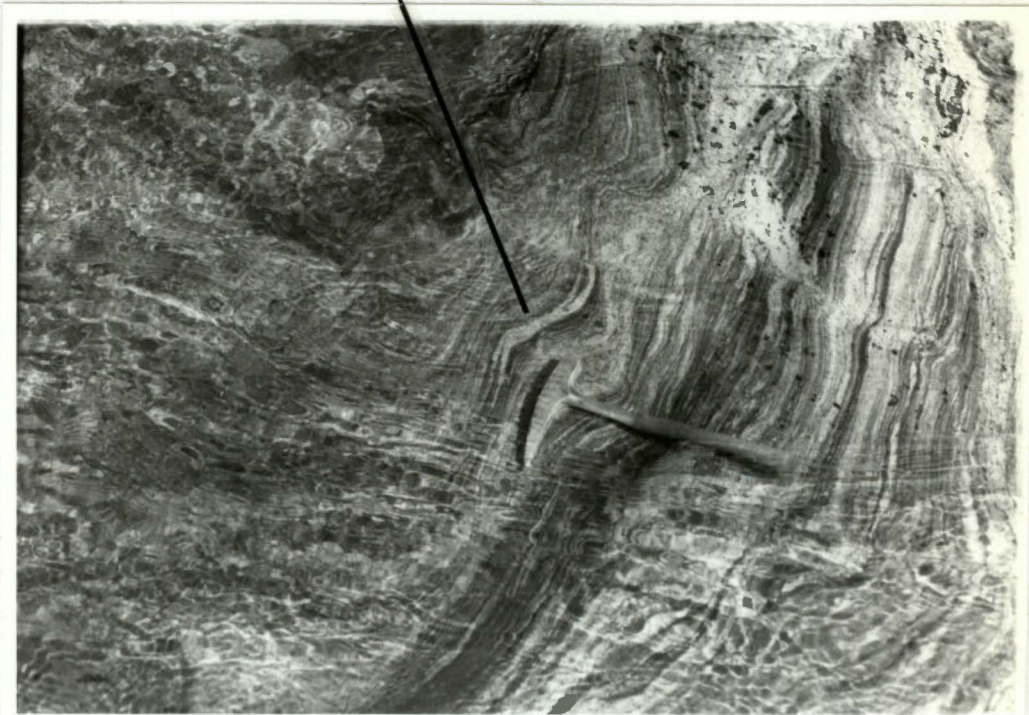
Figure 3.1: Photo of a refolded intrafolial fold in migmatitic gneiss of Unit 2. This structure is a probable F$_1$ fold that was transposed and is now intrafolial within S$_2$. (Outcrop located in Buff Creek.)

39
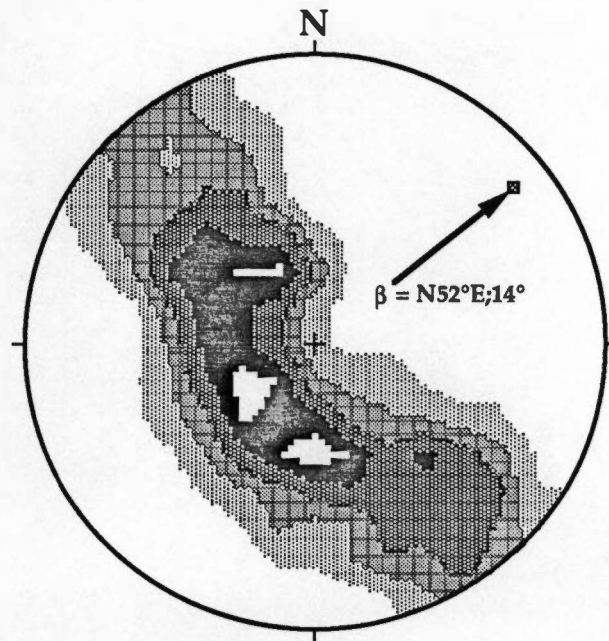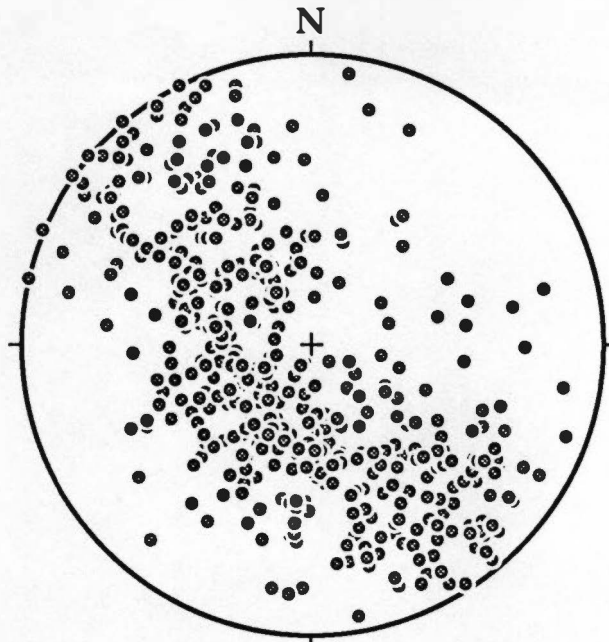
Figure 3.2: Equal-area plots of poles to S₂ foliation measured in each lithotectonic unit. Contoured data contoured using the Kamb (1959a) method. a) Unit 1 – Great Smoky Group, b) Unit 2 – Tallulah Falls Formation, c) Unit 3 – Otto Formation.

β = N44°E;32°
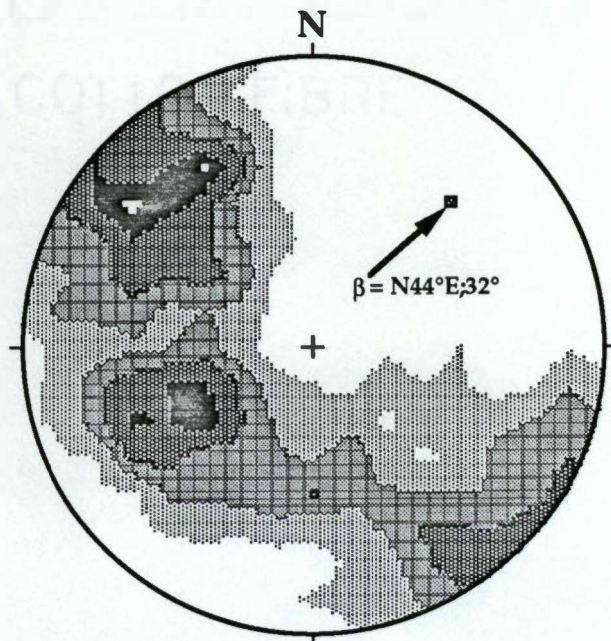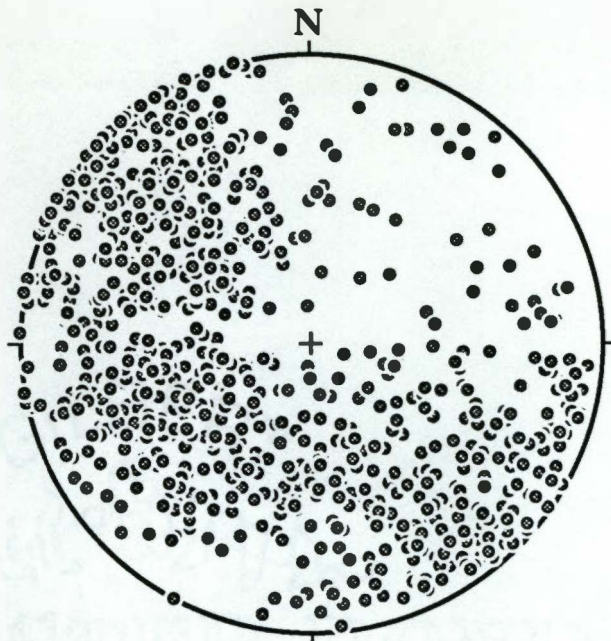
b.)

N = 875
C.I. = 2.0 sigma

Figure 3.2 (continued)

41

β = N48°E; 45°

N = 524
C.I. = 2.0 sigma

c.)

Figure 3.2 (continued)

the layering was oriented parallel to the axial surfaces of the later fold set.

Foliations that developed later than S_2 are generally weak and are rarely observed. Two superposed foliations are most easily recognized in schists where a second foliation is more apparent. A secondary foliation vaguely overprints the dominant S_2 foliation and is parallel to the axial surfaces of intermediate or late-generation folds. Secondary foliation was usually slightly oblique (10–20°) to S_2, suggesting that it was mostly observed on the limbs of tight to isoclinal (probably F_3) folds. Mesoscopic intermediate to late-stage folds rarely display a strong axial-planar cleavage or foliation.

FOLDS

Folds are quite common and readily observed in the study area. Crosscutting folds, intrafolial folds, and folds of contrasting style indicate that multiple folding episodes have affected the rocks over a long deformational history. Deformation has occurred through a wide range of environmental conditions, resulting in variations in the mechanics of folding through time. Hatcher and Butler (1979) separated six possible deformational events in the southern Appalachian Blue Ridge on the basis of crosscutting fold sets of contrasting style and orientation (Table 3.1). At least 5 fold generations were recognized in the study area and these appear to correlate reasonably well with the fold generations shown in Table 3.1.

Fold Geometry

Approximately 380 mesoscopic folds were measured. For most folds, both fold hinges and axial surfaces were measured if both features could be visualized three-dimensionally. These data were separated into three groups based on early, intermediate, and late-stage folds. Equal-area stereonet plots of fold hinges and poles to axial surfaces from these fold groups (Fig. 3.3) exhibit considerable scatter. Despite the variability in the data, generalized patterns can be recognized. Early stage folds have tight to isoclinal geometry and generally have ENE- to NE-trending hinges with shallow to moderate plunge. Poles to axial surfaces of early stage folds are nearly girdled, mimicking the pattern generated by the plots of poles to S_2 foliation, confirming that these two surfaces are coplanar. Intermediate-stage fold hinges have closed to tight geometry and generally trend NE with moderate to near vertical plunges. Poles to axial surfaces of intermediate folds indicate that they mostly verge to the NW, although some data indicate E to SE vergence. Late-stage folds have open geometry and most orientations are similar to those seen for

Table 3.1: Suggested fold generations, geometric characteristics, and foliation designations for the southern Appalachian Blue Ridge (after Hatcher and Butler, 1979).

Generation	Style	Orientation/Vergence	Deformation	Associated Foliation	Orogeny
F1	Isoclinal Recumbent	EW-NE N-NW vergent	D1	S1 (rare)	Taconic
F2	Isoclinal Recumbent	EW-NE N-NW vergent	D2	S2 (Dominant S surface)	Taconic
F3	Tight to isoclinal. Upright	NE NW vergent	D3	S3 (rare)	Taconic ?
F4	Crenulation cleavage	NE NW&SE vergent	D4	S4	Acadian ?
F5	Upright Open	NE NW vergent	D5		Alleghanian
F6	Upright Open	NW	D6		Alleghanian

44
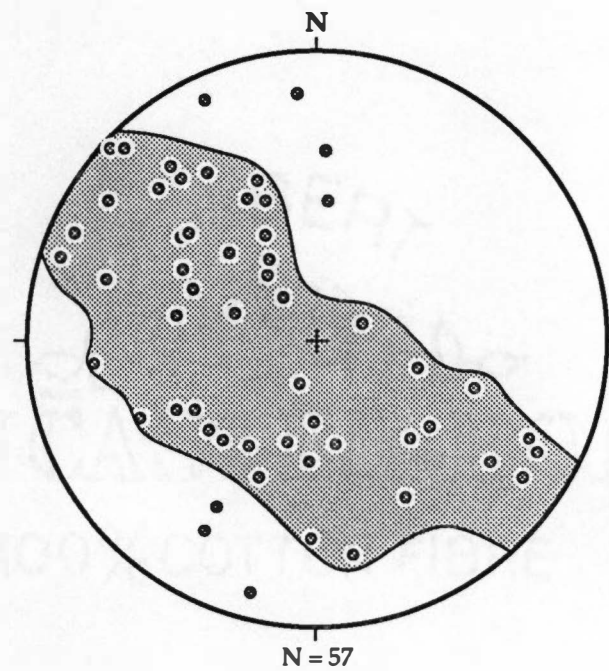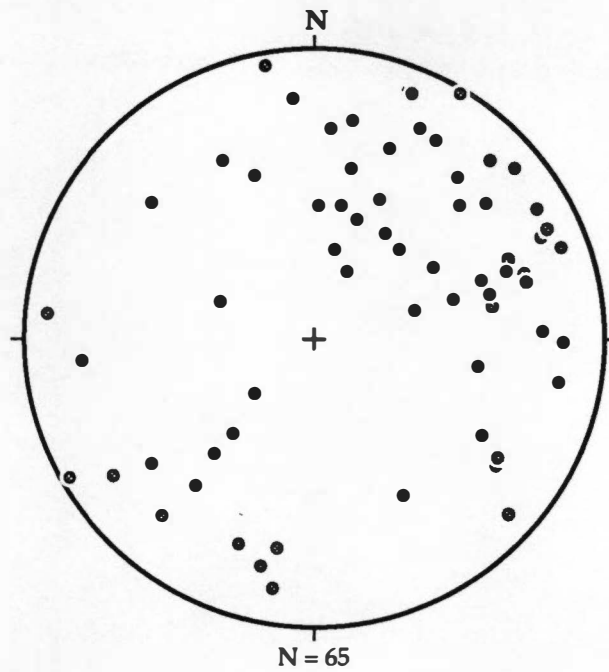
Figure 3.3: Equal-area stereonet plots of fold data. Data separated in terms of early-, intermediate-, and late-stage folds. (Upper nets are fold hinges, lower nets are poles to axial surfaces.) a.) Early stage (F_1, F_2) folds, b.) Intermediate-stage (F_3) folds, c.) Late-stage (F_4, F_5, F_6?) folds.

45

N = 153

N = 147
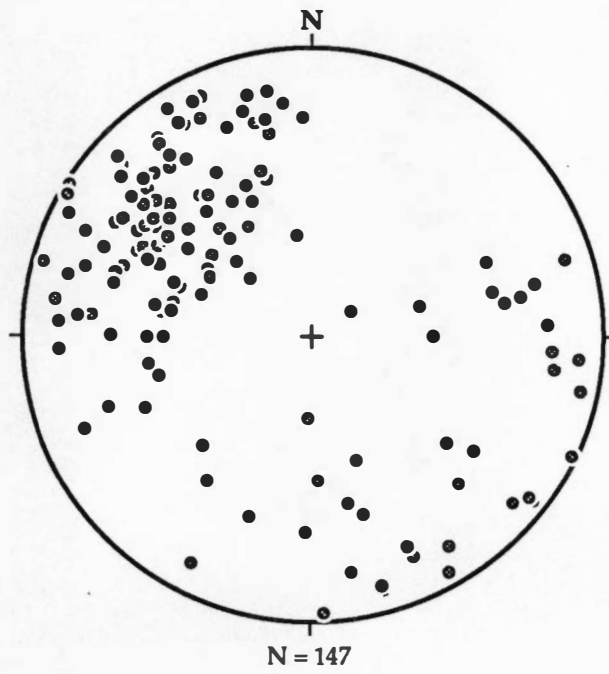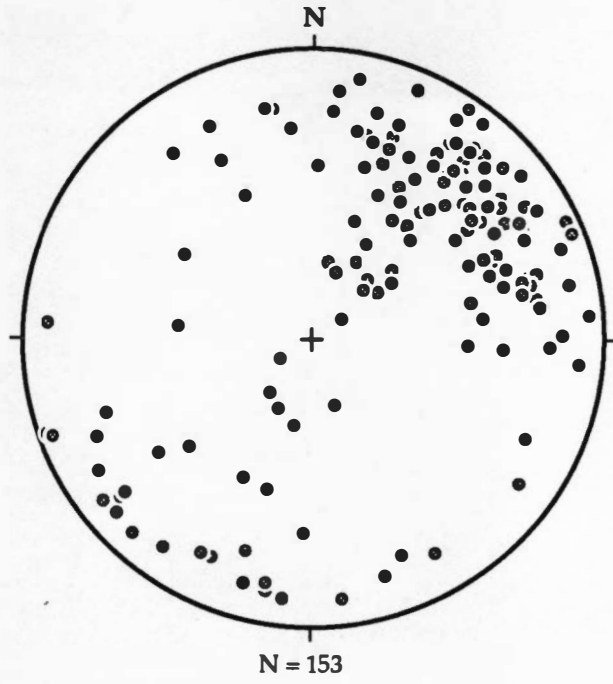
b.)

Figure 3.3 (continued)

46

N = 162

N = 147
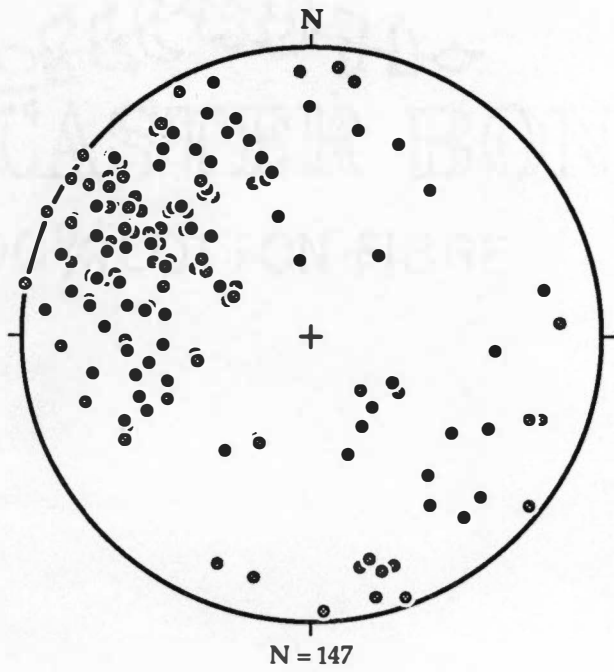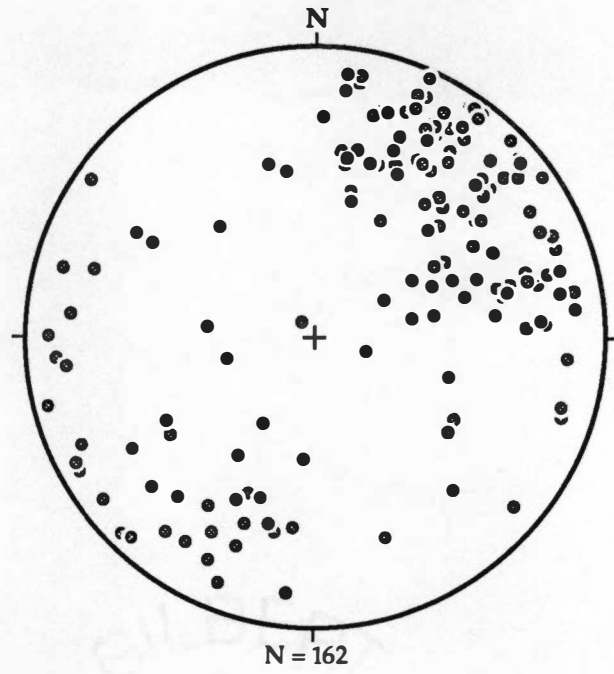
c.)

Figure 3.3 (continued)

intermediate-stage folds. Both intermediate- and late-stage fold sets are mostly upright with hinges plunging to the NE and vergence generally to the NW. The complex distribution of the data for all stages of deformation reflects how earlier structures are overprinted by later structures, and perhaps, how the presence of preexisting structures may affect the development of later structures.

Fold Mechanics

Early stage folds (F_1 and F_2) are rarely observed but are easily recognized by tight to isoclinal geometry and by the fact that axial surfaces are coplanar with the surrounding S_2 foliation (Fig. 3.4). Early-stage folds exhibit evidence of dominantly passive flow behavior (Donath and Parker, 1964) reflected by the fact that all layers change thickness through fold hinges into the limbs. During passive flow folding, rocks behave plastically and layering plays no mechanical role in the formation of the fold (Donath and Parker, 1964). Differentiated metamorphic layering was perhaps present prior to D_1, and certainly prior to D_2, yet rheologic anisotropy was apparently absent or at least inconsequential. Donath and Parker (1964) stated that passive flow folding is indicative of no ductility contrast between layers and a high average ductility. These are probably the conditions under which these rocks deformed during both F_1 and F_2 folding.

F_1 and F_2 folding resulted in extreme flattening perpendicular to the axial surfaces of these folds. Evidence for simultaneous extension in the plane of S_2 layering is typically exhibited by boudinage (pinch and swell structure) of more competent layers in gneisses. Boudinaged amphibolite layers are particularly common in Unit 2 and Unit 3.

F_3 folds are extremely difficult to distinguish from early stage folds because they also have tight to isoclinal geometry. Most parasitic folds with "S", "Z", and "M" geometry, as well as other tight similar folds, were associated with F_3. Mechanical behavior appears to have ranged from passive flow to flexural flow. Abundant parasitic folds (M, S, and Z forms) indicate that F_3 folds are polyharmonic, with smaller mesoscopic folds parasitic to larger, megascopic folds (Fig. 3.5). Polyharmonic folds result from compressional buckling of a multilayered package in which closely spaced layers vary in thickness and competence (Ramsay and Huber, 1987). Rheological contrasts between layers in the rocks, therefore, differed enough to affect the mechanics of folding and enabled the formation of polyharmonic folds during F_3 (Fig. 3.6).

Late-stage folds are crenulations (F_4?) and upright open folds (F_5, F_6?). Late-stage folds range from flexural flow to flexural slip behavior depending on layer thicknesses and competence contrasts present. Flexural flow behavior is particularly observed in outcrops

Figure 3.4: Photo of a biotite gneiss outcrop (Unit 2) containing isoclinal, early-stage flowage folds. (Outcrop located on ridge west of Monteith Branch.)

49

Polyharmonic Folding
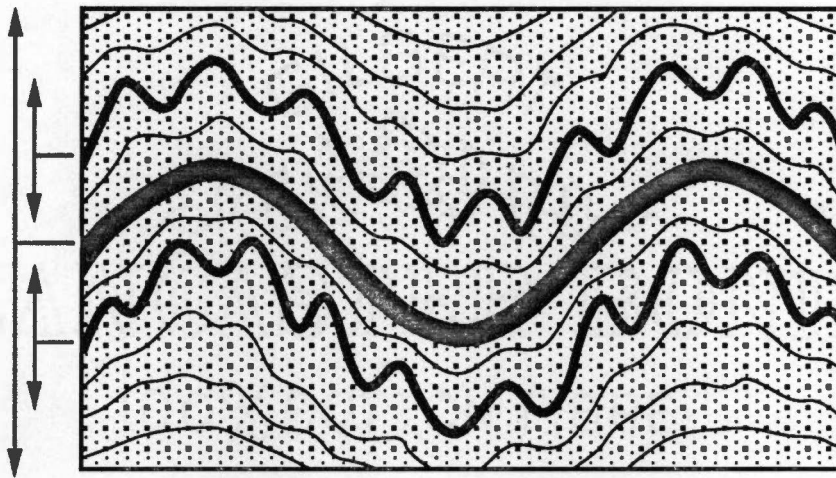
Figure 3.5: Illustration of polyharmonic folds developed by buckling a layered sequence of competent (black) and incompetent (stipled) material. (After Ramsay and Huber, 1987.)
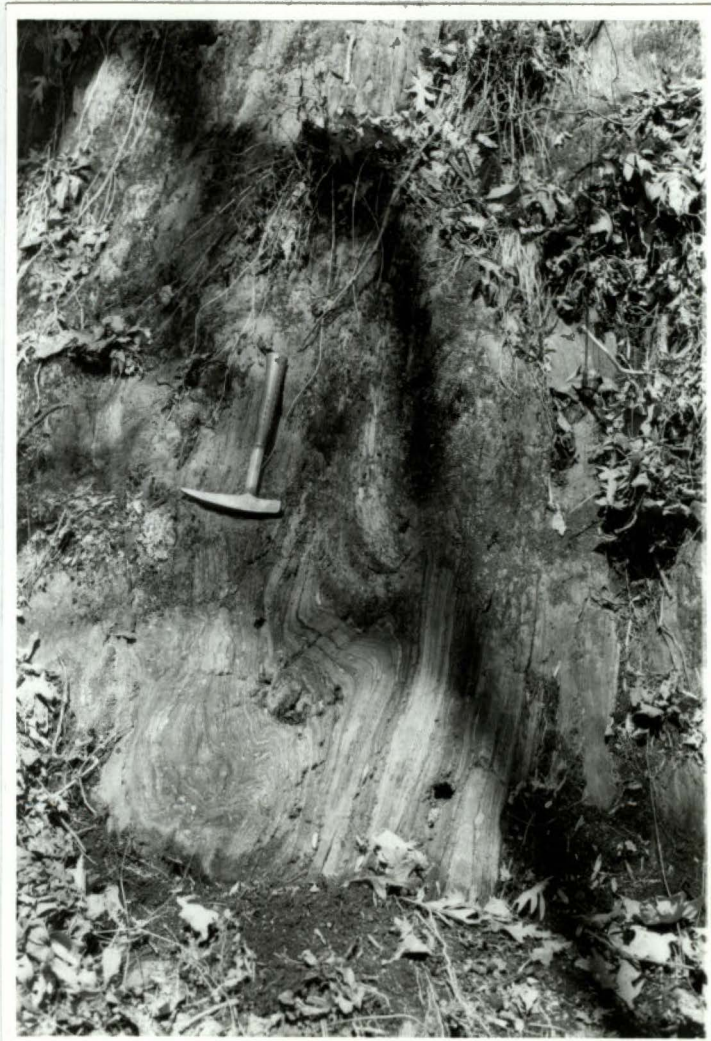
Figure 3.6: Photo of parasitic F3 fold in Unit 2 with S-form geometry. A more competent amphibolite layer is boudinaged and folded into the hinge of this parasitic S-fold. (Outcrop located on Kings Mountain near Webster.)

where interlayered schist and metasandstone are present (schist behaving as the incompetent material). Flexural slip behavior is common where there is little competence contrast between layers or where incompetent layers are comparatively thin, providing convenient slip surfaces. Where thin layers of schist are interlayered with metasandstone, slip between metasandstone layers is facilitated by the mechanical anisotropy of the intervening schist. Late-stage open folds generally have cylindrical forms (Fig. 3.7).

Both symmetrical and asymmetrical crenulations, or fine-scale microfolds, appear to be late-stage flexural-slip structures. Crenulations are rare and are mostly seen in schistose lithologies because of the fine-scaled layering required to form them (Ramsay and Huber, 1987). It may be that crenulations are parts of larger, polyharmonic folds, but more probably were formed as a separate, unique fold set (F_4?). Orientations of crenulation microfolds are relatively uniform (Fig. 3.8) and crenulation hinges and axial surfaces do not reveal whether they are part of a separate fold set or actually a polyharmonic subsidiary of another fold set (perhaps F_5). Crenulation axes plunge gently to the northeast and are mostly asymmetric with northwestward vergence. Crenulation cleavage is not strongly developed along axial planes of crenulation microfolds.

A summary of early-, intermediate-, and late-stage folds (Fig. 3.9) shows how fold styles and fold mehanics varied between deformational episodes that occurred under progressively changing environmental conditions.

LINEATIONS AND SHEAR STRUCTURES

Lineations measured in the field area (other than fold hinges) fall into two general categories: mineral lineations and intersection lineations. Mineral lineations are expressed by preferred orientation of elongate aggregates of minerals (primarily quartz and mica). Observed mineral lineations mostly have ENE orientations (Fig. 3.10) and were most often associated with sheared rocks. In these cases, the rocks exhibit independent evidence of simple shear by the presence of tailed porphyroclasts and other mylonitic textures. Lineation present on the dominant foliation surface apparently parallels the direction of shear. Lineations associated with these rocks suggest that mineral elongation was produced by ductile simple shear and, therefore, may be useful indicators of the orientation of shearing (Simpson, 1986).

Intersection lineations observed in the field area involve the intersection of a secondary foliation with the primary S_2 foliation, or the intersection of crenulation folds and the S_2 foliation surface. Intersection lineations are oriented NE or SW (Fig. 3.10).

Figure 3.7: Photo of cylindrical flexural slip fold in metasandstone (Unit 1). Thin interlayers of schist appear to have facilitated layer-parallel slip. (Outcrop located on ridge east of Bart Cove, north of Dillsboro.)

53
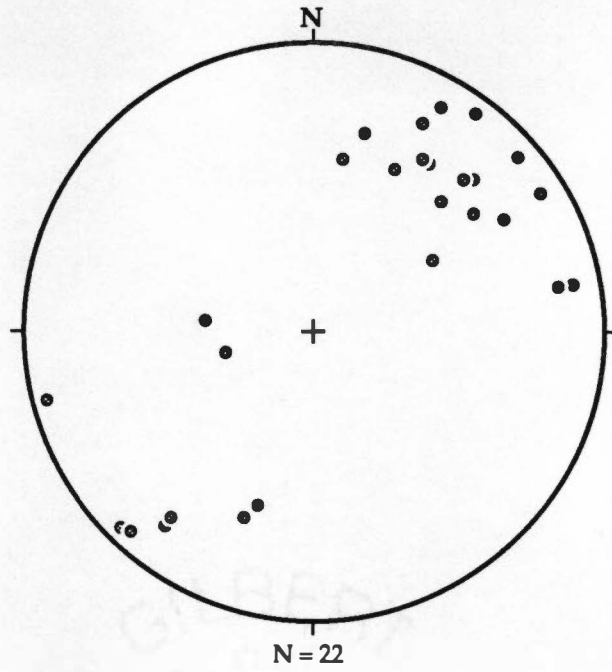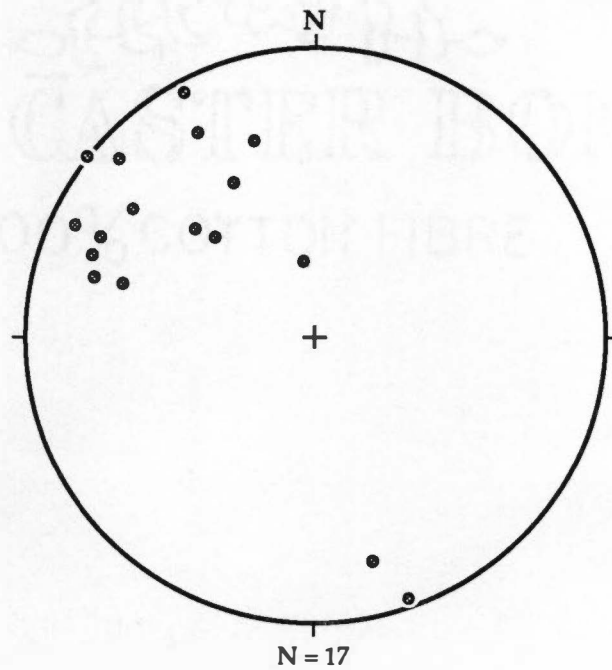
Figure 3.8: Stereonet plots of F$_4$? crenulation folds measured in the study area.
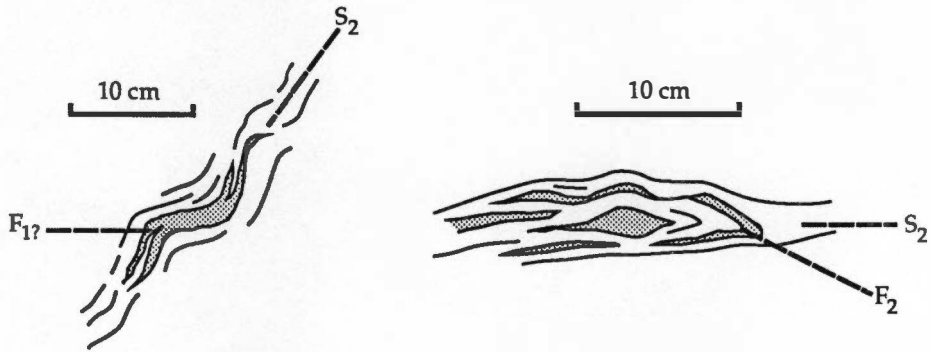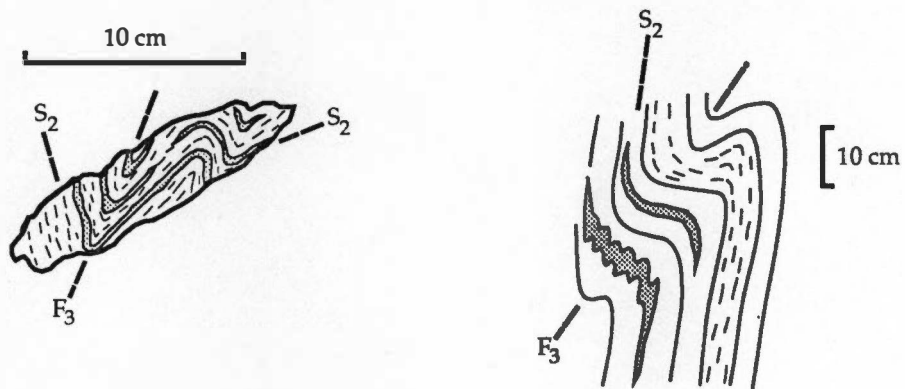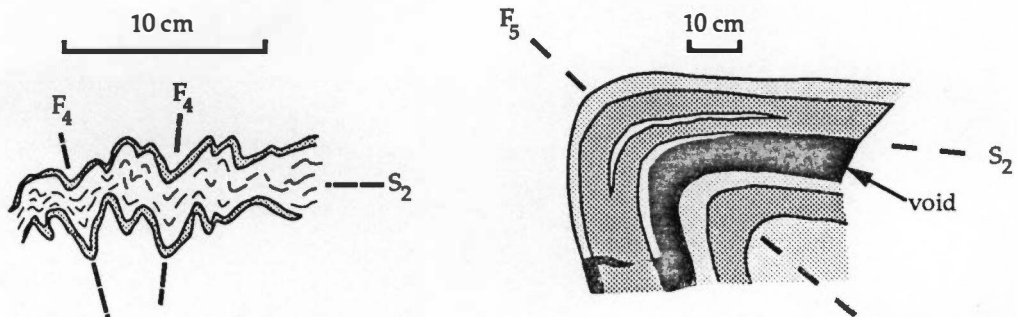
Figure 3.9: Illustrations of folds observed in the study area are classified as early-, intermediate-, or late-stage folds.
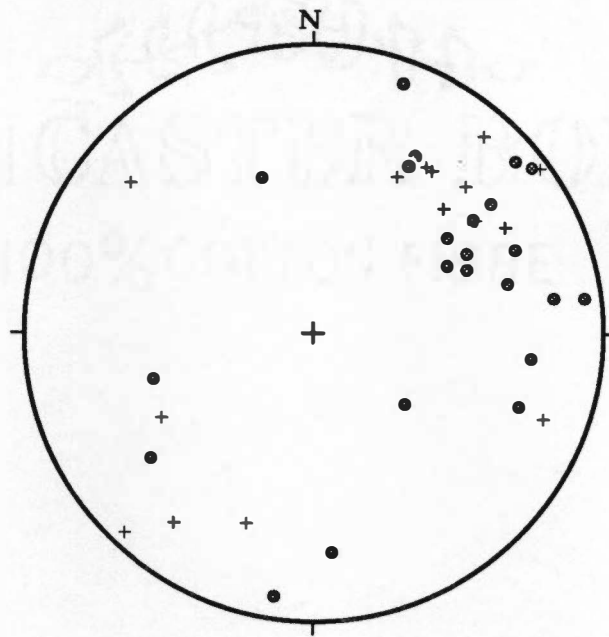
Figure 3.10: Stereonet plot of lineations measured in the study area. Dots represent mineral lineations, plus symbols represent intersection lineations.

Intersection lineation is useful for the identification of particularly subtile secondary foliations.

Mylonitic rocks, although sparse, occur over the entire field area indicating ductile shearing has affected all three lithotectonic units. Mylonites are most commonly located close to lithologic boundaries and faults (Fig. 3.11). Annealed mylonite occurring near the contacts of the Webster-Addie body indicates differential motion between the ultramafics and surrounding gneisses during early- and/or intermediate-stage deformation. Shear zones cannot be traced for very great distances indicating either that shearing was localized or that annealing has obscured the original continuity. Mylonitic layering is most commonly parallel to the surrounding foliation, but in some cases, mylonitic shear zones (probably late-stage) abruptly truncate the local S_2 foliation. Shear texture includes features such as ribbon quartz, asymmetric and symmetric augen (porphyroclasts), mica fish (buttons), and grain-size reduction (Fig. 3.12). Annealed mylonitic texture was observed in many, but not all, mylonites indicating that shearing episodes occurred at various times relative to the thermal-metamorphic peak.

MACROSCOPIC FEATURES

MAP PATTERNS

Lithologic identification and orientation of structural features were made at nearly all of the 1600 field stations recorded, enabling a detailed geologic map to be constructed (Plate 1). Observations made at map scale (1 : 24,000) provide a better appreciation for the spatial relationships of rocks and deformation. Complex interactions between rock units and deformation episodes become evident at this scale of observation.

S_2 Foliation

The dominant structural feature in the field area is the S_2 foliation. Nearly 1900 strike and dip measurements of S_2 were gathered at approximately 1600 field stations during the course of field work. Individual strike and dip symbols shown on Plate 1 illustrate the orientations of S_2 in great detail. Local individual foliation measurements vary appreciably, reflecting the complex patterns produced by deformation episodes that followed the formation of S_2.

A simplified map-scale representation of S_2 foliation is provided by a form-line map (Fig. 3.13) that shows more generalized trends of gneissic layering, ignoring the small-

57
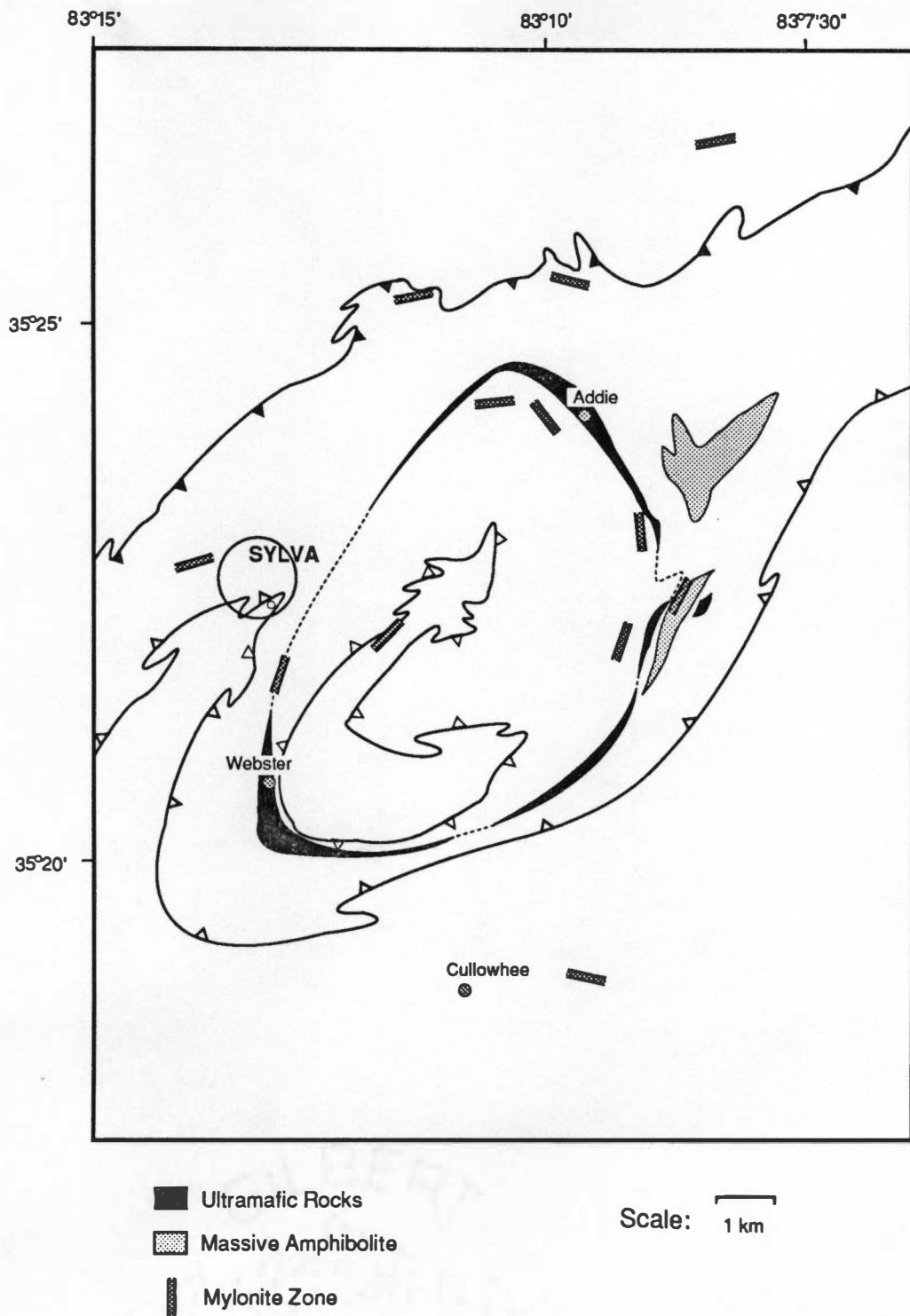
Figure 3.11: Map of the study area showing the locations and orientations of mylonite zones.

58

Figure 3.12: Photos representing the various types of mesoscopic shear structures in the field area. a.) SN20f (Unit 2): porphyroclasts suspended in fine-grained matrix produced by grain-size reduction (top to the left sense of shear). b.) SS522 (Unit 3): Type I S-C mylonite with augen-shaped porphyroclasts (top to the right sense of shear), c.) SN832 (Unit 1): mylonitic Great Smoky metasandstone with porphyroclasts and quartz ribbons (top to the left sense of shear), d.) SS397 (Unit 3): micaceous (Type II) S-C mylonite with mica fish and small porphyroclasts (top to the right sense of shear). e.) SN517 (Unit 2): annealed mylonite with symmetrical and asymmetrical porphyroclasts and recrystallized quartz ribbons (top to the right sense of shear).

a.)

b.)

c.)
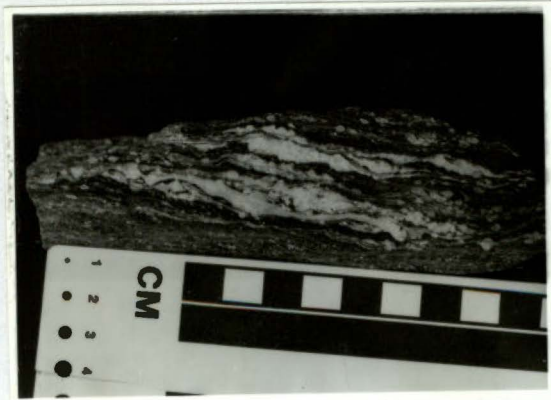
d.)
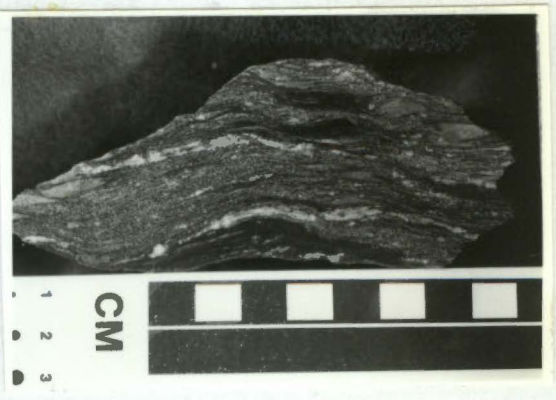
e.)
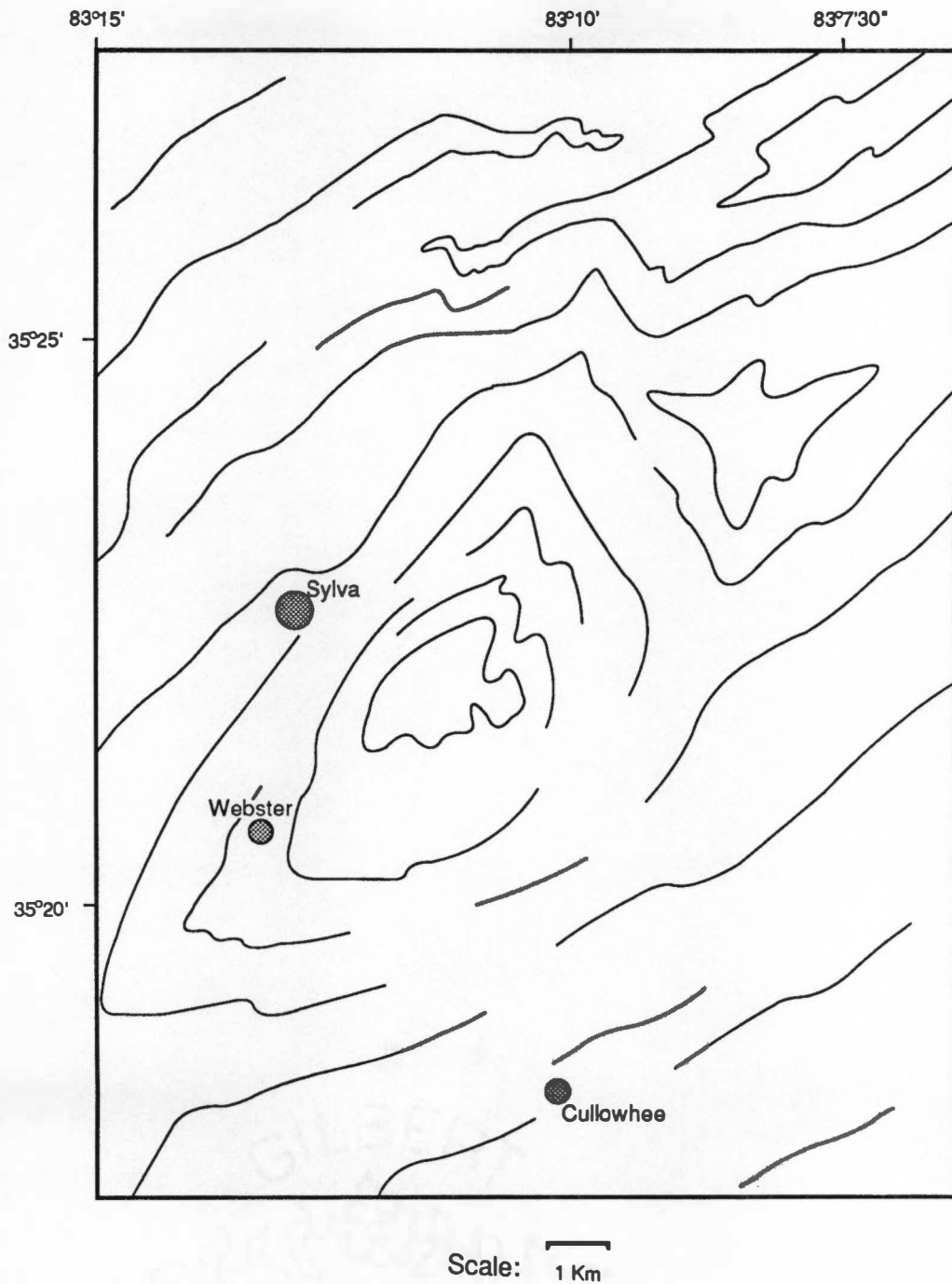
Figure 3.13: Form-line map showing the generalized trends of S$_2$ foliation throughout the study area.

scale perturbations. S_2 form lines strike predominantly NE-SW except in the hinge zones of large scale folds. Tight- to isoclinally- folded form lines in the northern portion of the map are interpreted from nearly parallel, but converging foliations, and may be macroscopic manifestations of early stage isoclinal folds. Form lines that show closure illustrate the presence of dome-and-basin (Type 1) refold patterns (Ramsay, 1967; Ramsay and Huber, 1987).

Folding

Folds are an abundant mesoscopic feature in the field area, but resolving fold traces at the map scale is more difficult. Several fold sets are apparent, however, and these exhibit various orientations and cross-cutting relationships (Fig. 3.14).

Evidence for early and intermediate stage folds is sparse since the hinge zones are difficult to identify at the map scale. Two possible F_2 folds are located in Unit 1, trending roughly ENE along the northern portion of the map area. These early fold traces, as well as faults, are folded by tight, NE-trending F_3 folds. Intermediate stage F_3 folds trend about N50°E and their axial traces are discordant with (but are not obviously folded by) NNE-trending late-stage (F_5) folds. Traces of F_5 folds have been gently folded as well, apparently by W- or WNW-trending (F_6?) folds.

The most prominent fold is an elliptical dome (a doubly plunging antiform) located in the center of the map area. This feature is very obvious because it has folded a layer of ultramafic rocks that, by the outcrop pattern, outlines the elliptical geometry of the dome. I suggest this prominent structure be called the Webster-Addie dome. Possibly a smaller companion basin is adjacent to the Webster-Addie dome along the northeastern flank. These large scale superposed fold structures are oriented NNE along slightly curving fold traces and probably involve the interference of F_5 and F_6 folds.

Faults

Two major thrust faults were mapped through the study area: the Hayesville fault and the Soque River fault. Both are large thrust faults that have been mapped farther south (Eckert, 1984; Hatcher and others, 1987; Eckert and others, 1989; Hopson and others, 1989) and have been correlated to this area using similar stratigraphic relationships.

The northernmost fault is the Hayesville fault, which places paragneisses of Unit 2, and perhaps the underlying rocks of Unit 3, on metasedimentary rocks of Unit 1 (see following section). An isograd (see Ch. 4), form lines, and F_3 (and perhaps earlier) folds transect the fault trace. These cross-cutting relationships indicate that the Hayesville fault is
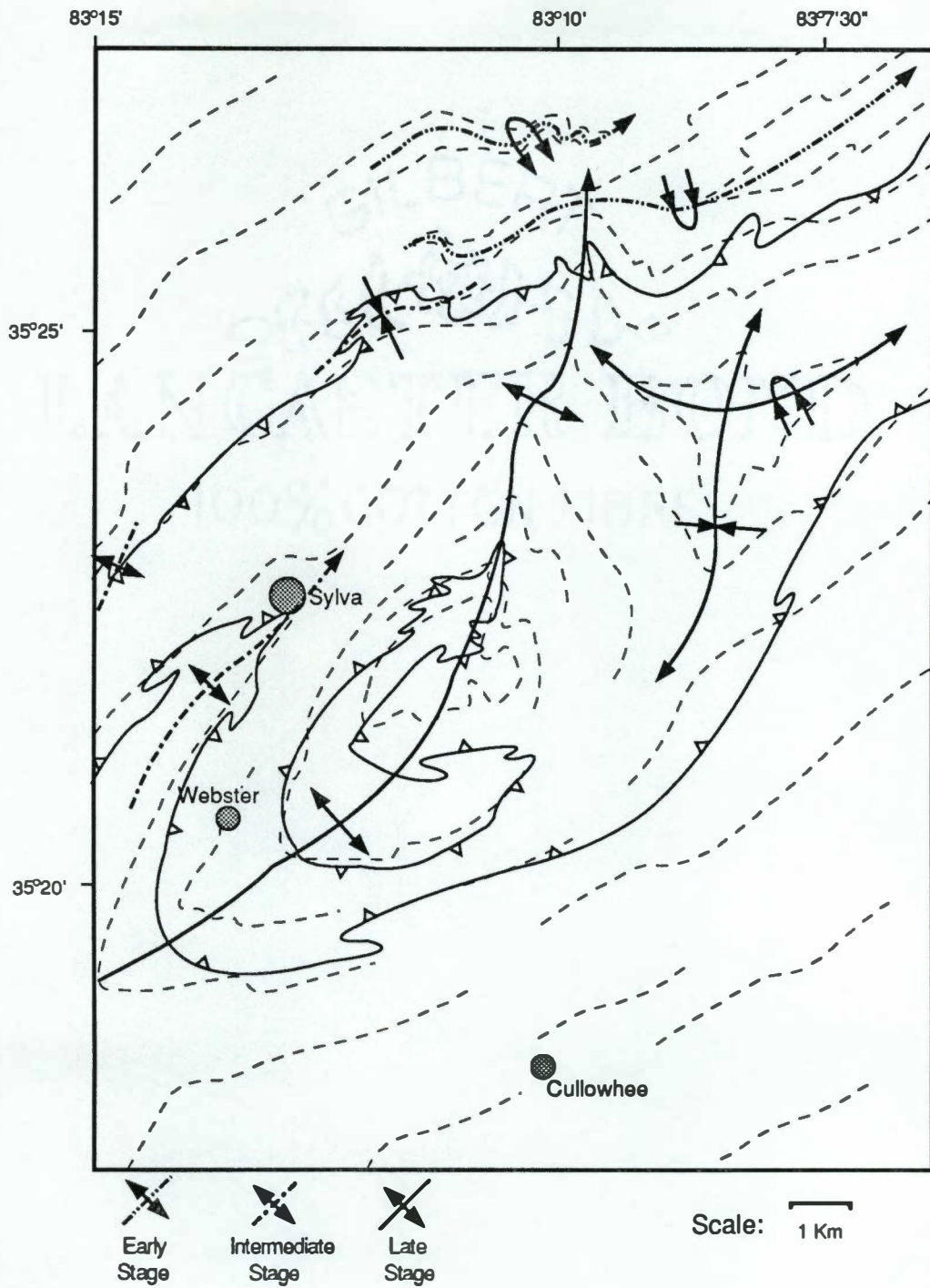
Figure 3.14: Fold traces of megascopic folds in the study area are superposed over S_2 form lines (dashed) and fault traces.

63

an early structure and that significant thrust displacement must have occurred prior to metamorphism and, at the latest, F3 deformation. The Hayesville fault has been tightly folded and, in some areas, the fault surface is overturned (dips to the NW).

Nearly everywhere it is exposed, the Soque River fault dips to the northwest. Thrust motion was toward the northwest, emplacing Unit 2 paragneisses over metasedimentary rocks and amphibolites of Unit 3. Folding and erosion of the fault plane has produced the odd relationship where the hanging wall is located NW of the footwall, with the fault plane dipping toward the direction of transport. Most of the hanging wall (Unit 2) of the Soque River fault has been removed by erosion and it is not exposed southeast of the fault trace in the study area. Further southeast, Unit 2 is encountered again as the hanging wall of the Chattahooche fault (Hopson and others, 1989).

Extremely tight folding (F3?) of the Soque River fault is displayed by the large, nearly isoclinal reentrant of the fault trace NW of Webster. Further evidence of the folded fault surface is the presence of a window through rocks of Unit 2 in the hanging wall, exposing Unit 3, roughly along the axis of the Webster-Addie dome.

Form lines, fold traces, and an isograd all transect the Soque River fault indicating that, it too, should be interpreted as an early, premetamorphic structure. This is contrary to the interpretations of others (Hatcher and others, 1987; Hopson and others, 1989) who regard at least some of the movement on the Soque River fault as post-metamorphic. Based on the evidence gathered for this study, post-metamorphic movement on the Soque River fault may have occurred, but must have been minimal and restricted to suitably oriented, planar segments.

Because both faults in the study area are premetamorphic structures, textural evidence of shearing along them has, in large part, been annealed by metamorphic recrystallization. Annealed mylonite zones were often observed near lithotectonic boundaries, but these tectonites may not be relicts of large-scale movement on the faults. Similar looking mylonites also occur far removed from lithotectonic boundaries and probably formed from relatively small-scale shearing.

CROSS SECTIONS

Three cross sections (Plate 2) were constructed along lines trending N45°W across the geologic map (Plate 1). The vertical scale of the cross sections is identical to the horizontal scale (1" = 2000') to avoid vertical exaggeration. Topographic and geologic features were rigorously transferred and projected onto each section. Dashed form lines

indicate interpreted geometries of foliation planes at depth projected from measurements at the surface.

Section A–A'

The southernmost cross section (A–A') transects the Hayesville fault, the reentrant of the Soque River fault, the southern portion of the Webster-Addie dome, and the Soque River fault again. Along this section line the folded nature of the Soque River fault is apparent. The emergence of the fault at the surface, in the vicinity of Kings Mountain is related to upright, moderately plunging, tight folding (probably F3). The emergence of the fault along the axis of the Webster-Addie dome is a product of gentler folding, perhaps by a fold generation later than F3. Folding along the Webster-Addie dome is probably later than F3 because of the open fold geometry. The Webster-Addie ultramafic body is also folded by this gentle antiform and the inferred original continuity is indicated by projecting the contacts above the surface.

The Hayesville fault is the deeper fault surface. The Hayesville and Soque River faults may merge at depth, beneath the northwestern limit of Unit 2. It is unclear which fault truncates the other at the branching point, as either one could conceivably be the older of the two. If the faulting history was "in-sequence", the Soque River fault would be the older fault. An alternate interpretation is that the Hayesville and Soque River faults are actually one continuous fault surface. This interpretation either assumes that Units 1 and 3 are stratigraphically equivalent or that some unexposed structure juxtaposes the two units at depth.

Neither of the above interpretations include the complexities raised the possibility of the Shope Fork fault and the underlying Coweeta Group rocks (Hatcher, 1988; McClellan, 1988) occurring at deeper levels. To the south, the Shope Fork fault places rocks of Unit 2 on rocks of the Coweeta Group (Plate 3). By down-plunge projection, the Shope Fork fault may occur at depth in the Sylva area. Based on the available data, however, it is assumed that the Shope Fork fault and the underlying Coweeta Group rocks have been cut out by the Soque River fault in the Sylva area.

Section B–B'

Cross section B–B' exhibits many of the same features that appear on A–A', with the exception of the northwestern emergence of the Soque River fault. The fault does not emerge at the surface here because the antiformal structure, by which it is upfolded, plunges northward. The antiform constructed at depth was projected down-plunge from where it

65

occurs at the surface to the south. Along this cross section line, the Webster-Addie dome is broader, and again, the same window is transected at the central axis of the dome. Because this cross-section line transects the widest portion of the Webster-Addie dome, more of the uppermost thrust sheet (Unit 2) is preserved here than in A–A'. The SE dip of the Soque River fault south of the dome was interpreted as a small perturbation or gentle fold occurring in the fold surface there.

Section C–C'

Cross section C–C' is the northernmost cross section and does not transect the lithologic expressions of the Webster-Addie dome. Tight folding of the fault surfaces at depth is required by foliation orientations at the surface. Rocks adjacent to the Hayesville fault dip shallowly to the SE but become vertical or dip steeply NW proceeding to the SW. The Soque River fault dips more shallowly to the NW in this cross section and foliations abruptly change orientation across the fault. Here, again, the Hayesville and Soque River fault surfaces merge at depth but, unlike the other two sections, the Soque River fault intersects the topographic surface only once.

The three cross sections on Plate 2 raise many questions about how the tectonic units were assembled and the order in which they were put together. If the faulting was in-sequence, then Unit 2 was initially thrust upon Unit 3 on the Soque River fault. Later faulting on the Hayesville thrust emplaced Units 2 and 3, probably as a composite tectonic block, onto Unit 1. Later deformation folded the contacts between the tectonic units and subsequent erosion has produced the map and cross section patterns seen today.

MICROSCOPIC FEATURES

Microstructural analysis of rocks in the field area is not a major focus of this study. Various microstructural features encountered in thin sectioned mylonitic rocks, however, are worthy of mention.

SIMPLE SHEAR STRUCTURES: MYLONITIC FABRICS

As discussed above, mesoscopic evidence for ductile shearing is present in all tectonic units in the study area. Microscopic investigation of mylonite samples further reveals simple shear structures that are present. Petrographic investigation is also an ideal

perspective from which to characterize post-shear recovery processes based on microtextures.

S–C Fabric

Lister and Snoke (1984) outlined two general types of S–C mylonites: Type I and Type II. Both of these mylonite types can be demonstrated in the study area. S–C mylonites display two foliations that develop as a result of progressive simple shear. Two mylonitic foliations (S and C) develop when ductile shearing produces non-coaxial laminar flow in developing mylonites, translating material planes parallel to stream lines (Lister and Snoke, 1984). S–surfaces are oblique to the shear-zone boundaries and are probably parallel to the X–Y plane of the finite strain ellipsoid (Fig. 3.15). C–surfaces, or shear bands, are parallel to shear-zone boundaries and are planes along which high shear strains are localized.

Type I S–C mylonites develop in coarse-grained quartzofeldspathic rocks that have a tendency to form tailed porphyroclasts or augen under progressive simple shear. Deformed porphyroclasts are common in mylonites collected in this study where quartz + feldspar aggregates preserved as porphyroclasts in a fine-grained matrix (Fig. 3.16a, b). Subtle foliations developed along the inclined (with respect to the dominant foliation) boundaries of porphyroclasts are S–surfaces. C–surfaces parallel the elongate tails of porphyroclasts and are the surfaces along which simple shear has been concentrated.

Type II S–C mylonites develop in micaceous rocks where large feldspar grains, that would potentially form tailed porphyroclasts, are lacking. In Type II S–C mylonites, mica grains are deformed into sigmoid shapes ("fish" or "buttons") by boudinage or microfaulting parallel to the [001] plane (Lister and Snoke, 1984). S–surfaces are better developed in Type II mylonites because the bulk of the mica fish are oriented parallel to S–surfaces. Most mylonitic rocks encountered in the study area contain appreciable mica and are, to varying degrees, Type II mylonites. Mica-rich mylonites in the study area also contain tailed porphyroclasts and are probably good examples of mylonites that are transitional between Types I and II (Fig. 3.16b, c, and d).

Annealed Fabrics

Not all mylonites in the study area are annealed to the same degree indicating that mylonitization occurred over a long history relative to the thermal-metamorphic peak. Mylonites that are least recovered have clearly preserved the effects of grain-size reduction
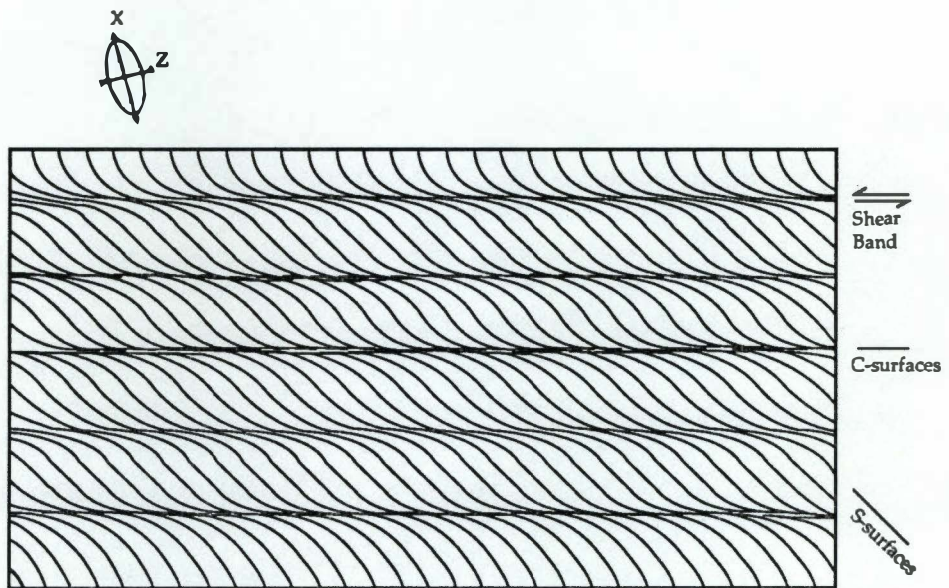
Figure 3.15: Illustration of S– and C–surface orientations in an S–C mylonite relative to the finite strain ellipse. (From Lister and Snoke, 1984.)

Figure 3.16: Photos of mylonitic textures in thin section. (Scale bars equal 0.5 mm.) a.) Sample SN20f (Unit 2): mylonite sample showing the effects of grain size reduction. Feldspar porphyroclasts are suspended in a fine-grained matrix. b.) Sample SS397 (Unit 3): tailed porphyroclasts are suspended in a fine, but recrystallized, micaceous matrix. c.) Sample SN682 (Unit 1): sheared schist from the Great Smoky Group with a well-developed S–C fabric defined both by porphyroclasts and mica fish (a hybrid of Type I and Type II S–C mylonites). d.) Sample SN682 (at higher magnification): sigmoidal aggregate of mica fish studded with euhedral garnets. e.) Sample SN517: coarse-grained, annealed mylonite with recrystallized quartz ribbons and euhedral garnets.
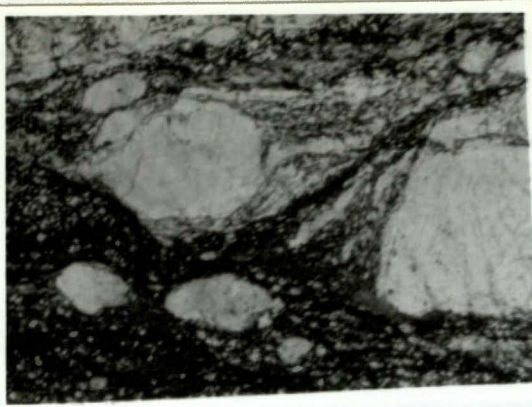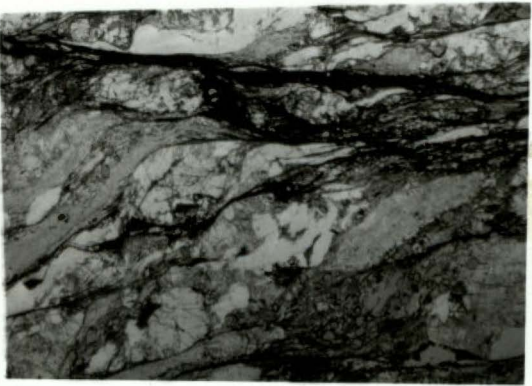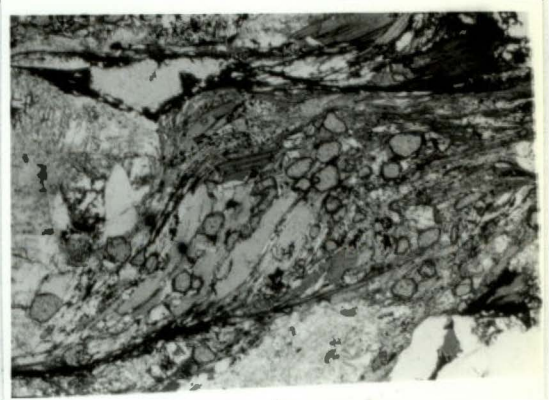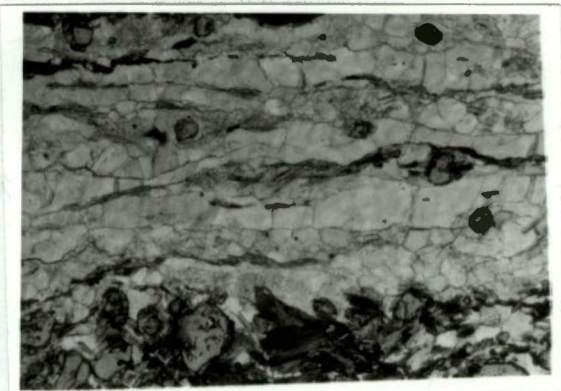
produced during mylonitization. In these samples, large porphyroclasts are suspended in an extremely fine-grained matrix (Fig. 3.16a). The preservation of fine-grained matrix implies that post-mylonitization temperatures were inadequate to recrystallize and anneal the fabric. Non-recrystallized mylonites often truncate the local S_2 foliation and these obviously represent the latest shearing events.

Most mylonites sampled, however, show signs of recovery or annealing in their microtextures. Recrystallized quartz ribbons (Fig. 3.16e), recrystallized matrix fabric (Fig. 3.16b and c), and euhedral metamorphic minerals (Fig. 3.16d) indicate that mylonite fabrics have been overprinted by varying degrees of recrystallization. Therefore, mylonitization probably occurred during widely spaced intervals during, and following, the thermal metamorphic peak.

The diachronous nature of structural features in the study area has been demonstrated on all scales of observation. Mesoscopic structures have helped define the geometry, style, and sequencing of features associated with separate deformational episodes. Macroscopic patterns and cross sections aided in defining tectonic units and the structural relationships between them. Microstructural analysis has emphasized that shearing episodes have occurred over a long history based on the relative degrees of annealing seen in sheared rocks.

Much of the deformation in the study area has occurred in conjunction with high grade regional metamorphism. The rocks have been taken through a range of environmental conditions along a P–T path that has produced rheologic changes in the rocks, which ultimately affected the mechanics of deformation over time. The following chapter will attempt to characterize the environmental conditions and progression of this thermal-metamorphic history.

IV. METAMORPHISM

In the study area, and in the surrounding Blue Ridge, regional metamorphism has produced a Barrovian sequence (Barrow, 1893) of prograde mineral assemblages present in pelitic rocks. Rocks of the Ocoee Supergroup are sub-chlorite grade along the northwestern margin of their outcrop belt in Tennessee. To the southeast, the rocks increase in grade through a medium pressure facies series, reaching sillimanite grade near the study area (Carpenter, 1970). Within the study area metamorphic grade has reached the kyanite and sillimanite zones. These zones are well constrained by abundant occurrences of pelitic rocks bearing index minerals. Garnet + andesine + hornblende assemblages in amphibolites interlayered with eastern Blue Ridge paragneisses indicate that metamorphic conditions in the study area were within the amphibolite facies (Eskola,1939).

In this section, mineral assemblages are used to characterize metamorphic conditions and reactions. Field and petrographic identification of index minerals have permitted delineation of the sillimanite isograd through pelite-bearing units. Microprobe analyses were performed to characterize mineral chemistry of various pelitic and mafic phases. Exchange equilibria between coexisting phases are used to estimate pressure and temperature conditions of pelitic rocks and garnet-bearing amphibolites.

TIMING OF METAMORPHISM

All rocks in the study area have been affected by regional metamorphism with the exception of the younger felsic intrusive rocks (trondhjemite and pegmatite dikes). Kish and others (1976) reported a Rb-Sr whole rock age of 440 ± 13 Ma for a pegmatite body from the Bryson City area and concluded that emplacement of the dike postdated peak metamorphism. This suggests that the peak metamorphism in the surrounding Blue Ridge occurred prior to ~450 Ma. All rocks in the study area are considered to be no older than Late Proterozoic because they do not appear to have recorded metamorphism associated with the Grenville orogeny (800-1200 Ma). Therefore, the maximum age of regional metamorphism must be Late Proterozoic.

The major prograde metamorphism that affected the southern Appalachian Blue Ridge can be associated with the Taconic orogeny. During the Taconic, sedimentary flysch sequences, now exposed in the southern Appalachian Valley and Ridge, were deposited in response to uplifted regions to the east . Stratigraphic sequences indicate that flysch

sedimentation commenced early in the Middle Ordovician when a major tectonic event caused a stable shelf to subside rapidly, creating a foredeep basin (Rodgers, 1971; Shanmugam and Lash, 1982). If the assumption is made that metamorphism was coeval with Taconic tectonism that produced the basin and the source areas to the east, an approximate date of ~480 Ma can be correlated to this metamorphic event.

Radiometric dating has further constrained the timing of Taconic metamorphism. Butler (1972) compiled regional radiometric data for much of the southern Appalachians and concluded that the main phase of Paleozoic regional metamorphism occurred at about 470 Ma. Dallmeyer (1975) used incremental gas release of Ar^{40}/Ar^{39} to date closure temperatures of biotite and hornblende in metamorphic rocks from the western Blue Ridge, close to the present study area. By assuming uplift and cooling rates, Dallmeyer placed the peak metamorphic pulse at 480 ± 30 Ma. These studies support the notion that metamorphism and Taconian tectonism were coeval.

Until recently, Acadian metamorphism in the southern Appalachians was regarded to have been much less intense and less pervasive than the Taconic orogeny (Glover and others, 1983). Recent radiometric studies, however, have raised the possibility that Acadian metamorphism may have played a significant role in the metamorphic evolution of the southern Appalachians. Dallmeyer (1988) reported $^{40}Ar/^{39}Ar$ mineral cooling ages (hornblende + biotite) from the eastern Blue Ridge in Georgia that suggest cooling from a Late Devonian thermal event. Additionally, Connelly and Dallmeyer (1991) obtained 340-350 Ma $^{40}Ar/^{39}Ar$ whole rock cooling ages for samples from the biotite and garnet zone, and 440-460 Ma ages for samples from the chlorite zone of the western Blue Ridge of in Tennessee and North Carolina. Connelly and Dallmeyer's results may indicate that a ~450 Ma thermal event was variably overprinted by a 350 Ma event. It is possible that rocks in the study area have experienced retrograde metamorphism associated with a metamorphic pulse during the Acadian orogeny (340-380 Ma) and this is supported by textural evidence in some samples.

Metamorphism associated with the Alleghanian orogeny (285-325 Ma) is apparently restricted to the the eastern Piedmont in the southern Appalachians. This thermal event reached amphibolite facies in the Kiokee and Raleigh belts and greenschist facies in the southeastern portion of the Carolina slate belt (Dallmeyer and others, 1986). It is nearly certain that this thermal event did not affect the rocks in the study area.

THE SILLIMANITE ISOGRAD

Mineral assemblages that are most indicative of metamorphic conditions are found in pelitic rocks because discontinuous reactions are common in them. The common pelitic assemblage in the study area includes quartz + muscovite + biotite + garnet ± staurolite ± aluminum silicate (kyanite or sillimanite). In some cases both kyanite and sillimanite coexist in the same rock. Occurrences of aluminum silicate are extremely common and the transition from kyanite to sillimanite was mapped with reasonable control. This transition marks the position of the sillimanite isograd in the study area (Fig. 4.1). No other isograds were recognized within the mapped area.

An isograd is an imaginary surface that constrains pressure and temperature conditions that prevailed during a specific discontinuous reaction. In this case, the discontinuous reaction involves the formation of sillimanite. In a regional sense, the Barrovian sequence of pelitic assemblages progrades NW to SE across the Blue Ridge. This progression reverses in the study area, however, where kyanite-bearing rocks are located southeast of the sillimanite zone. Sillimanite grade rocks are encountered again further to the south. Close observation of Fig. 4.1 reveals that the sillimanite isograd (a two dimensional surface) is folded and intersects the topographic surface to form a curved line in map view. The map pattern indicates that the isograd surface was folded upward along a broad, SW-plunging antiformal crest. With subsequent erosion, deeper rocks have been exposed at the surface in which kyanite is the stable aluminum silicate phase rather than sillimanite.

With the present resolution of field and petrographic data, the sillimanite isograd appears to traverse across both the Soque River and Hayesville faults without apparent offset or disruption. This implies that significant movement on both of these structures entirely preceded peak metamorphism.

MIGMATIZATION

Migmatites are particularly common in lithologic Unit 2, but are also seen in the Great Smoky Group and Otto Formation. There are four generally accepted modes for migmatite formation (Misch, 1968): (1) partial melting; (2) local subsolidus metamorphic differentiation; (3) injection of a granitic magma; and (4) metasomatism. Johannes (1983)
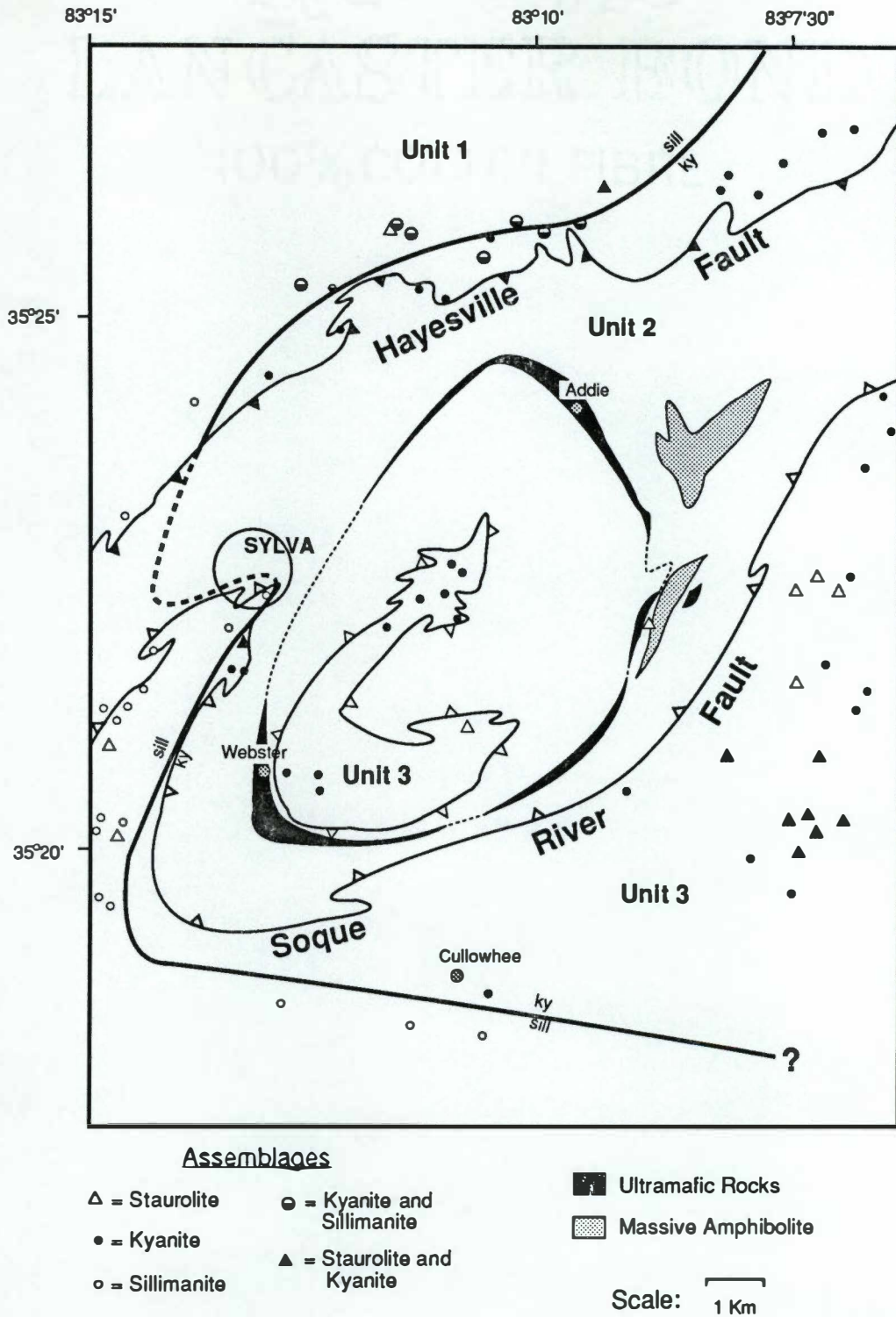
Figure 4.1: Geologic map of the Sylva area showing the position of the sillimanite isograd (dashed where approximated).

75

stated that most migmatites form in layered paragneisses where compositional layering is established prior to migmatization. During partial melting, fine grained quartz- and microcline-rich layers are transformed into leucosomes, while coarse-grained portions of the gneiss remain nearly unchanged, forming mesosome layers. Intervening mafic-rich selvages (melanosomes) form a thin border zone between gneiss layers of different composition and have migrated there by mass transfer from the leucocratic layers (Johannes, 1983).

Most migmatites in the study area display stromatic textures suggesting that they were produced by *in situ* partial melting of parental rock. These textures include phlebitic, folded, ptygmatic, and schlieren structures (terminology of Mehnert, 1968, p.10-11). No evidence was observed that would suggest that migmatites were derived from injection of externally-derived granitic material parallel to layering. For the purpose of this study, it is assumed that the migmatites were produced in a closed, isochemical system (Olsen, 1983) involving *in situ* segregation of neosomes and paleosomes.

Because migmatization probably occurred above the solidus for leucocratic minerals, some insight to the metamorphic conditions producing migmatites can be quantified. Anatexis of paragneisses of intermediate composition requires the presence of H_2O at standard high grade metamorphic temperatures (600-750°C). Winkler (1979) pointed out that temperatures at which partial melting occurs can be significantly lowered by increases in P_{H2O}. A P-T diagram that includes Winkler's melting curve of ab + or + qtz + H_2O = liq (Fig 4.2) illustrates the effect of increasing pressure ($P_{H2O} \approx P_{tot}$) on temperature of melting. Given the fact that most migmatites in the study area occur in the kyanite zone, a lower limit of metamorphic temperatures can be defined the the intersection of the ky–sill curve and the melting curve. This indicates that metamorphic temperatures that produced migmatite were above ~640° C and that P_{H2O} was greater than ~6 kb.

PELITIC ROCKS

ASSEMBLAGES AND TEXTURES

Pelitic lithologies are particularly common in Units 1 and 3, where interlayered muscovite+biotite schist and aluminous gneiss are major components of the units.
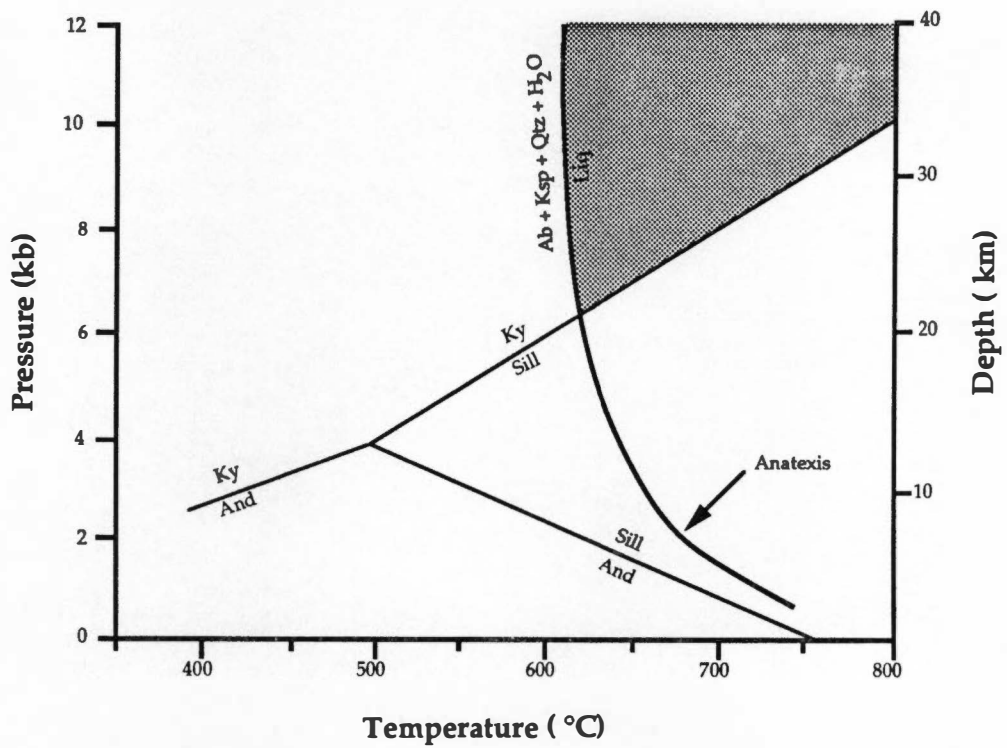
Figure 4.2: P-T diagram illustrating the environmental conditions under which migmatites can form in the kyanite zone. (Aluminum silicate phase relations from Holdaway, 1971; anatexis curve from Winkler, 1979.)

Metamorphic assemblages in pelites are remarkably similar between the two units, emphasizing their similarity in composition and metamorphic grade.

Garnet and biotite are two index minerals that are virtually ubiquitous in all samples of schist and aluminous metasandstone. Kyanite porphyroblasts, some up to several mm in length, are present in schist samples from the kyanite zone. Many samples located on, or in close proximity to the sillimanite isograd contain both bladed kyanite porphyroblasts and fibrolitic sillimanite. Prismatic sillimanite (rather than fibrolite) was observed in a few samples from Unit 3 in the southern portion of the map area, south and southwest of Cullowhee.

Staurolite is often present in many aluminous rocks from Units 1 and 3. Staurolite porphyroblasts are typically large, euhedral, optically continuous, and appear to be part of the prograde assemblage. Staurolite is particularly common in samples from Unit 3 in the southeast portion of the map area and its occurrence is more likely a function of bulk composition rather than metamorphic grade.

Both biotite and muscovite are present in samples of pelitic schist and biotite is usually the predominant mica. Chlorite is sometimes observed as a retrograde product of garnet or biotite. Occasionally chlorite occurs as well-formed porphyroblasts that do not appear to be of retrograde origin. The rarity of prograde chlorite is likely due to compositional constraints and to its nearly complete consumption as a reactant in the formation of other phases.

Textural relationships of metamorphic assemblages are simple and primarily reflect prograde reactions. Inclusion-rich garnets indicate that garnet growth was fairly rapid. A few samples contain garnets with inclusions of kyanite indicating that garnet growth continued beyond the formation of the aluminum silicate phases. Staurolite does not appear to consume kyanite or garnet but intergrowth with kyanite was observed. Textural evidence clearly indicates that staurolite is part of the prograde assemblage.

Pseudomorphic textures indicating retrograde consumption of preexisting phases are rare. Partial replacement of biotite grains by chlorite, of garnet by chlorite and quartz, of kyanite by white mica, or of micas and feldspars by sericite are the common retrograde relationships observed. Localization of retrograde effects in the study area could be a function of water migration and/or fluid concentration in fold hinges and other areas where stress gradients were low (Carpenter, 1968).

It is possible to suggest some metamorphic reactions that may have produced the observed metamorphic assemblages. The initial formation of biotite may have been produced at the expense of chlorite and recrystallized clays:

phengite + chlorite = biotite + Al-rich chlorite + quartz (Winkler, 1979).

As grade increased, biotite may have continued to form simultaneously with garnet by the relationship:

chlorite + muscovite + quartz = garnet + biotite + H_2O (Thompson and Norton, 1968).

Subsequent formation of staurolite may have occurred if chlorite was available by the reaction:

chlorite + muscovite = staurolite + biotite + quartz + H_2O (Winkler, 1979).

The latest discontinuous prograde reactions are those that have produced the highest grade assemblages, that is, those containing kyanite or sillimanite. Aluminum silicate formation involving the consumption of staurolite has been suggested:

staurolite + muscovite + quartz = garnet + biotite + Al_2SiO_5 + H_2O (Winkler, 1979),

but can be ruled out here on the basis of textural evidence. The textural appearance of staurolite and the apparently stable coexistence with aluminum silicate suggests that the staurolite-consuming reaction did not occur. A more likely Al_2SiO_5–producing reaction may have involved the consumption of chlorite:

chlorite + muscovite + quartz = biotite + Al_2SiO_5 + H_2O (Winkler, 1979).

The scarcity of prograde chlorite supports the notion that it was consumed during the formation of aluminum silicate and other phases.

MINERAL CHEMISTRY

Microprobe analyses of five samples of pelitic schist were performed on a Cameca SX50 electron microprobe using silicate and oxide mineral standards. Microprobe analyses have provided the chemical compositions of small portions of mineral phases (analysis points were 5 μm in diameter). Analytical conditions of these analyses and compiled

analyses are located in Appendix A. Minerals analyzed in pelitic rocks include biotite, garnet, and plagioclase.

Garnet

The composition of garnet in pelitic rocks is dominated by almandine. Fe and Mg, and Al contents are high, while Ca is a minor constituent. Mn content is relatively dilute ($X_{sp} < 0.06$ for Unit 1., $X_{sp} < 0.04$ for Unit 3.) and chromium content was below detection limits.

All garnets analyzed are essentially a solid-solution mixture of almandine, pyrope, and grossular end members. The proportions of these end members in a particular garnet can be effectively represented on a ternary diagram with Fe, Mg, and Ca as apexes (Fig. 4.3). Average compositions of garnet cores and rims are plotted for each sample of pelitic schist analyzed. This ternary plot reveals that garnets have lower Fe/Mg ratios in their cores than in their rims. Relative calcium content remains essentially constant from core to rim except in the sample from Unit 1 where garnet rims are Ca-enriched.

More detailed garnet zoning patterns were obtained by a traverse of analysis points across a grain from rim to core, or from rim to rim. Relative concentrations of Fe, Mg, Ca, and Mn in garnets reflect some interesting core-to-rim variations among the analyzed pelitic samples (Fig. 4.4). Samples from Unit 3 contain garnets that have zoning patterns where Fe/Mg ratios increase, and Ca steadily decreases, toward garnet rims. A Ca–decrease toward garnet rims may indicate growth occurred along a decompression path. Sample SS454 shows an abrupt Ca increase at the extreme rim of the garnet, which could be a product of garnet consumption rather than garnet growth. Mn zoning patterns in all samples are relatively flat. Small increases in Mn content at garnet rims may also indicate garnet consumption.

The garnet analyzed in sample SN125 (Unit 1) is anomalous in that it is quite small (0.6 mm in diameter) and becomes Ca-enriched toward the rim (with a corresponding decrease in Mg and Fe), while Mn content remains relatively uniform from core to rim. The Ca–enriched rims in these garnets may indicate that growth proceeded along a compressional path.

Biotite

Biotite is slightly more enriched in the phlogopite component relative to the annite component and Mg and Fe concentrations are within the ranges: Mg/(Mg + Fe) =
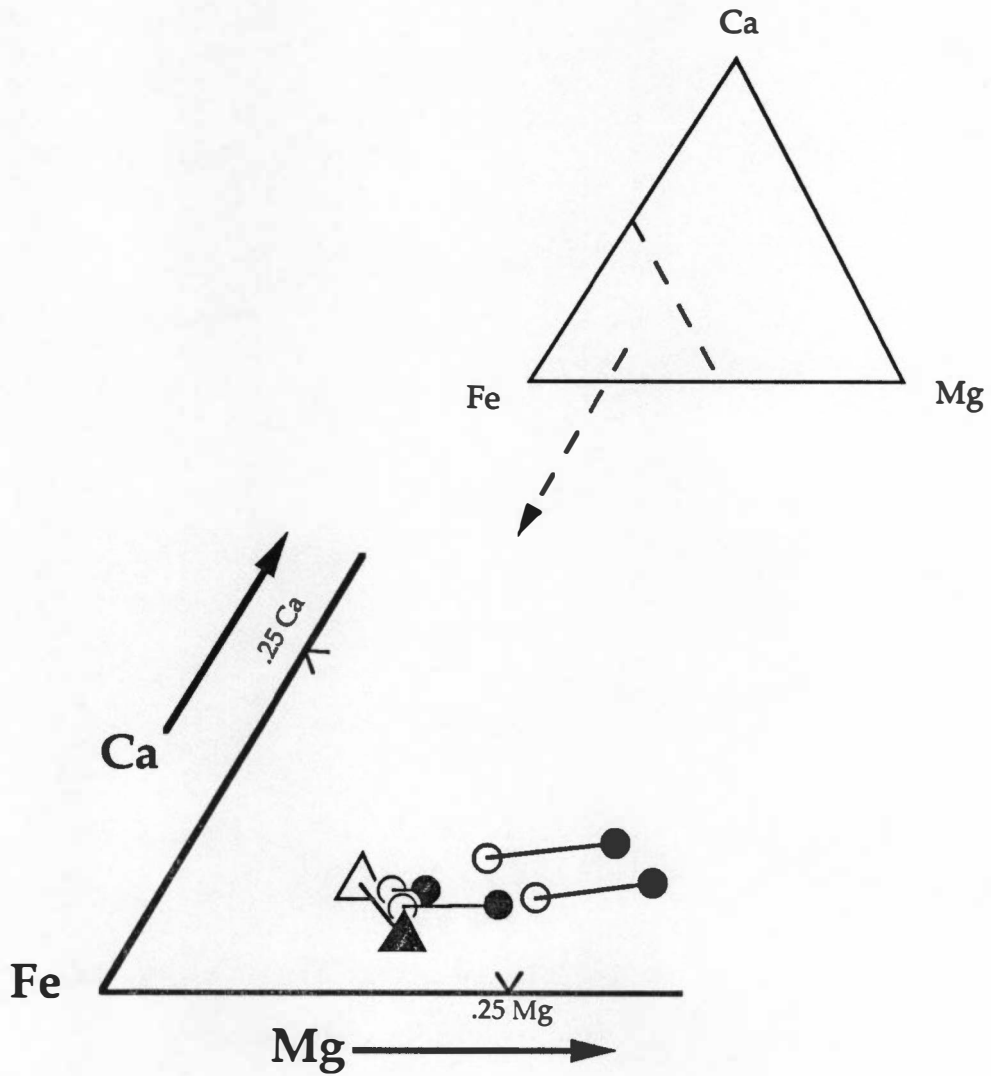
Figure 4.3: Ternary diagram showing pelitic garnet compositions between Fe, Ca, and Mg end-members. (Solid symbols are average core compositions, open symbols are average rim compositions. Circles represent garnets from Unit 3, triangles are garnets from Unit 1.)

Sample SS454
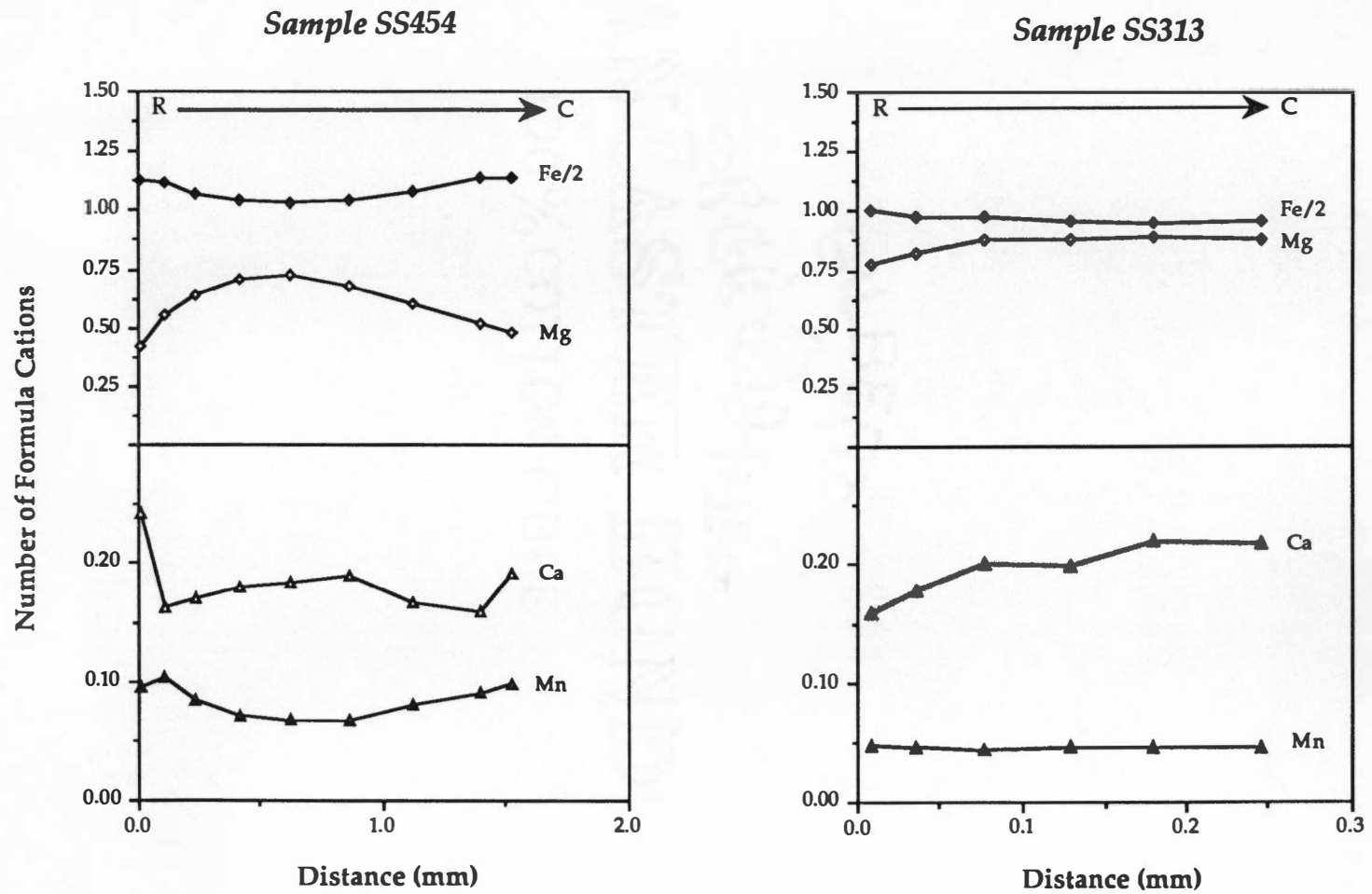
Sample SS313

Figure 4.4: Compositional profiles of analyzed garnets from pelitic rocks. (R = rim, C = core.)

Sample SS349

Sample SS287

Number of Formula Cations

Distance (mm)

Distance (mm)

Figure 4.4 (continued)

Sample SN125
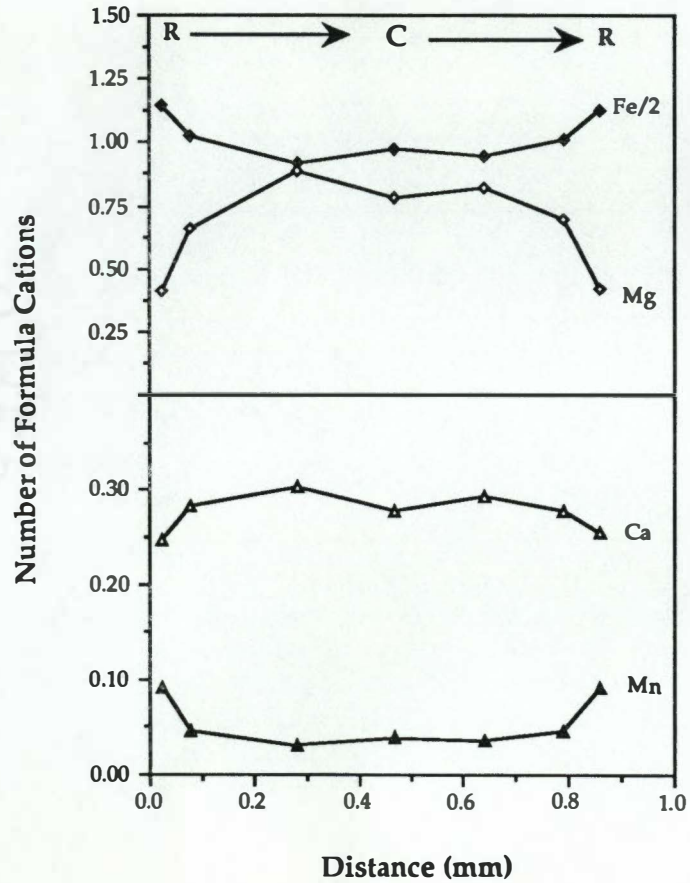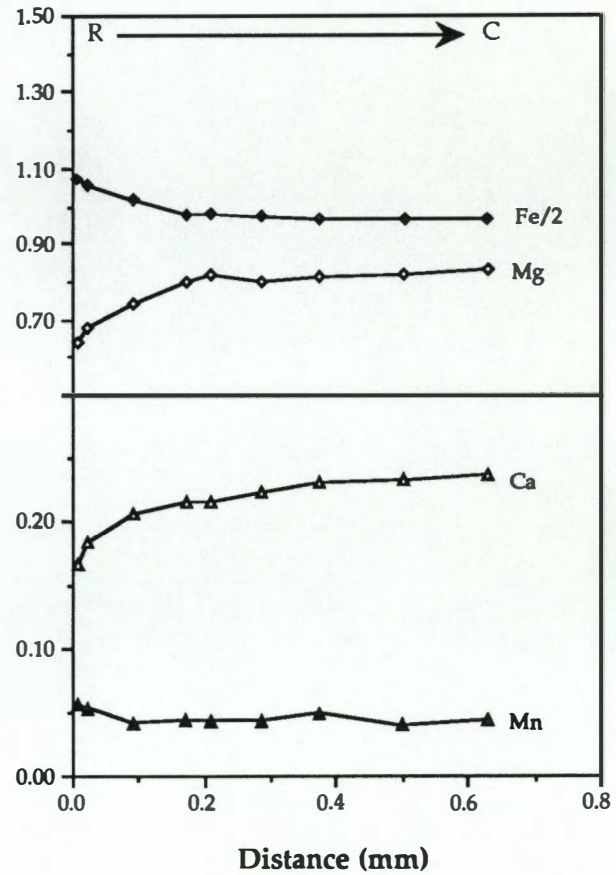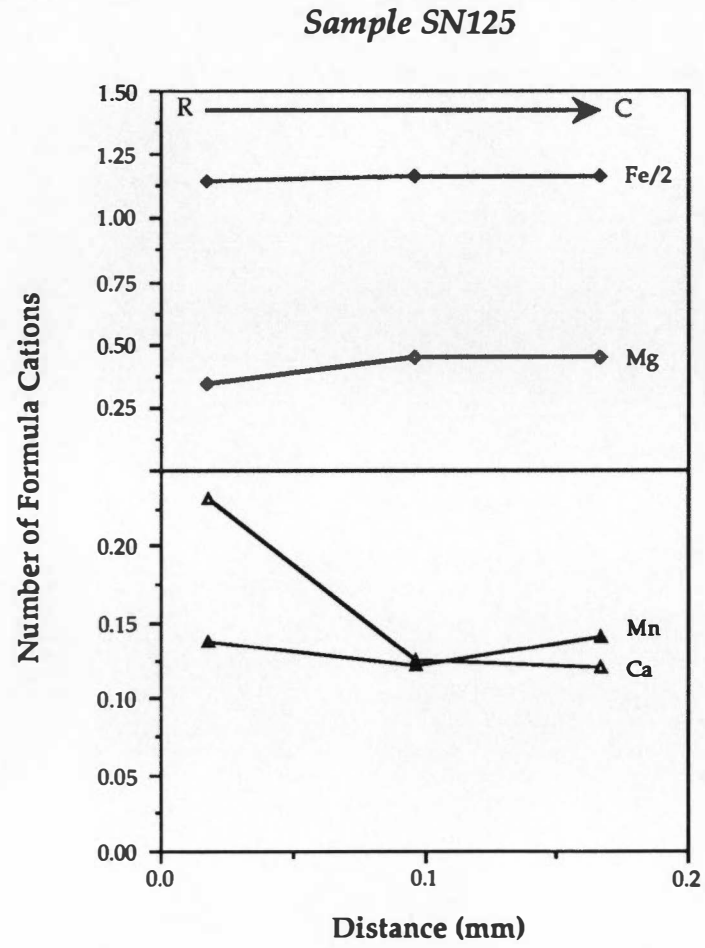
Figure 4.4 (continued)

0.55-0.65. Biotite inclusions in large garnets in sample SS454 have slightly higher Mg/Fe ratios: $Mg/(Mg + Fe) \approx 0.70$. Ti content of biotite ranges from 0.082–0.195 cations per three octahedral sites. In all cases, biotite coexists with at least one Ti-oxide phase (usually ilmenite) so they should be saturated with respect to Ti. Ti content in biotite is greater in samples that contain both rutile + ilmenite. Higher proportions of Ti in biotite may indicate the sample is of slightly higher metamorphic grade (Guidotti, 1984). Biotite inclusions in garnet (Sample SS454) have lower Ti content: 0.066–0.071 cations per three octahedral sites and were probably included and isolated from Ti exchange at a lower metamorphic grade. The sum of Na + K cations (per 1 interlayer site) are always less than one (0.81—0.95) indicating that there are vacancies in the interlayer site. Charge imbalance resulting from interlayer site vacancies is compensated by Ti^{+4} in the octahedral site.

Plagioclase

Plagioclase analyses reveal that these feldspars range in composition from oligoclase to andesine. Plagioclase in Unit 3 samples ranges from An_{28} to An_{42} with most analyses in the andesine field ($>An_{30}$). Plagioclase analyses for sample SN125 (Unit 1) have lower An–content and are all within the oligoclase field (An_{20}–An_{24}). Fe and K contents are extremely low for all plagioclase analyses (Fe < 0.011; K < 0.014 cations per 8 oxygens) K content in plagioclase from sample SS287 is slightly higher than for all other samples. Ba was not analyzed and the concentration in plagioclase is unknown.

AFM Projection

Figure 4.5 is a projection of mineral compositions that plot within the K_2O–FeO–MgO–Al_2O_3 tetrahedron. Points are projected from muscovite onto a triangular surface that extends from an apex at Al_2O_3-$3K_2O$ to infinity (toward K–feldspar). This AFM projection (after Thompson, 1957) is a useful way of representing pelitic assemblages containing muscovite, quartz, and other minerals within the composition limits of the system.

Each triangle in Figure 4.5 is formed by tie lines connecting average mineral compositions for each sample. Tie lines between garnet (rim averages) and biotite are closely parallel (with one exception) indicating that Fe–Mg partitioning between these two is consistent for most samples. Several samples contain stable staurolite but this phase was not analyzed by electron microprobe. Staurolite composition for a given sample, however, is limited by the tie line joining garnet and kyanite (pure Al_2SiO_5) which provides an
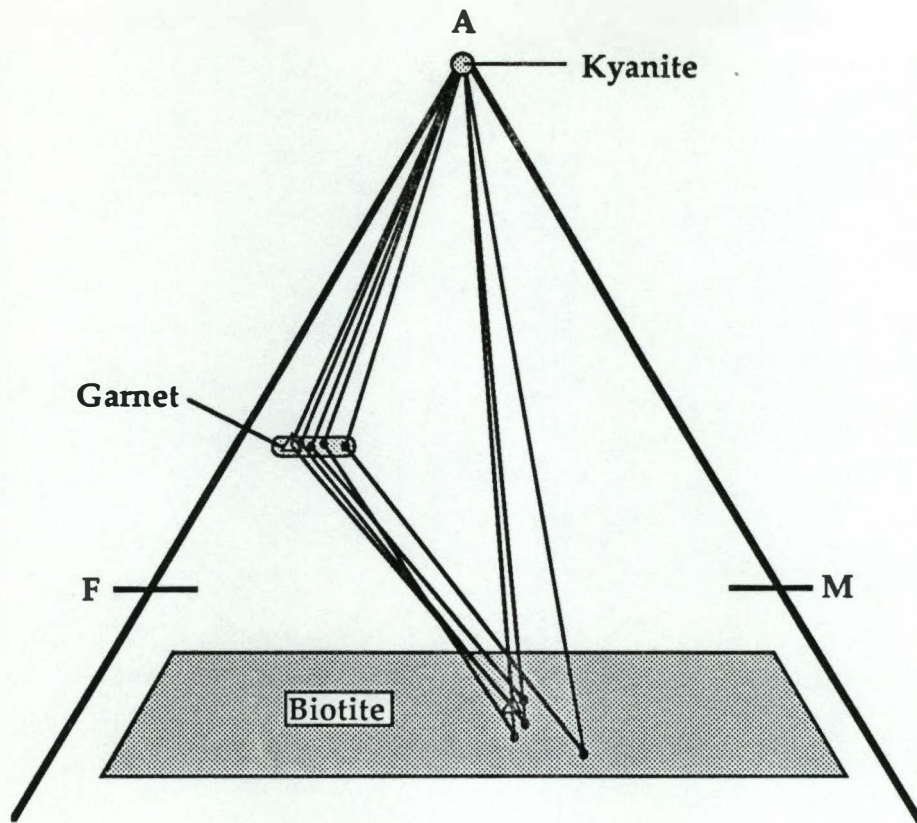
A = Al$_2$O$_3$ - 3 * K$_2$O
F = FeO
M = MgO

△ = Great Smoky Group
• = Otto Formation

+ Quartz
+ Muscovite
± Staurolite (not analyzed)
+ Ti oxide

Figure 4.5: AFM projection with compositions of analyzed minerals plotted. (Tie lines connect coexisting phases in each sample.)

Fe/Mg maximum for staurolite. Biotite compositions do not appear to vary in terms of the AFM end members, except for sample SS287 where biotite has a lower Fe/Mg ratio than the other samples.

THERMOBAROMETRY OF PELITES

Initial constraints on metamorphic pressure and temperature of pelitic rocks can be obtained from observing the mineral assemblages within them. Regions of mineral stability in pressure and temperature space are bounded by discontinuous reactions or polymorphic transitions that have been reliably determined by empirical and experimental determinations. P–T conditions for most samples are only generally constrained by the stability region of kyanite (Holdaway, 1971) and the stability field of staurolite (Spear and Cheney, 1989) (Fig. 4.6). Samples that contain sillimanite in lieu of kyanite formed at slightly lower pressure and/or higher temperature. The stability field extends into the sillimanite field to encompass these samples.

More precise determinations of metamorphic conditions can be obtained from thermodynamic relationships of coexisting mineral compositions. Various cation exchange equilibria that are sensitive only to temperature or to pressure have been calibrated and are useful tools for quantifying prevailing conditions that existed during exchange reactions. Fe and Mg exchange equilibria between garnet and biotite (GB thermometry) was used to estimate metamorphic temperatures. Metamorphic pressures were obtained using Ca exchange equilibria between garnet and plagioclase given the assemblage garnet + aluminum silicate + plagioclase + quartz (commonly known as the GASP geobarometer).

Geothermometry and Geobarometry

Selection criteria for samples to be analyzed required they contain the necessary mineral assemblages to apply both GB geothermometry and GASP geobarometry (garnet + biotite + plagioclase + quartz + aluminum silicate). Thermodynamic variables used in all formulations are defined in Table 4.1. Coexisting garnet, biotite, and plagioclase compositions were obtained by microprobe analysis and used to calculate temperatures and pressures using well-calibrated formulations that have been extensively used in recent petrologic studies.

Intercrystalline exchange of Fe and Mg between garnet and biotite has been shown to be primarily a temperature-sensitive process and various calibrations have been
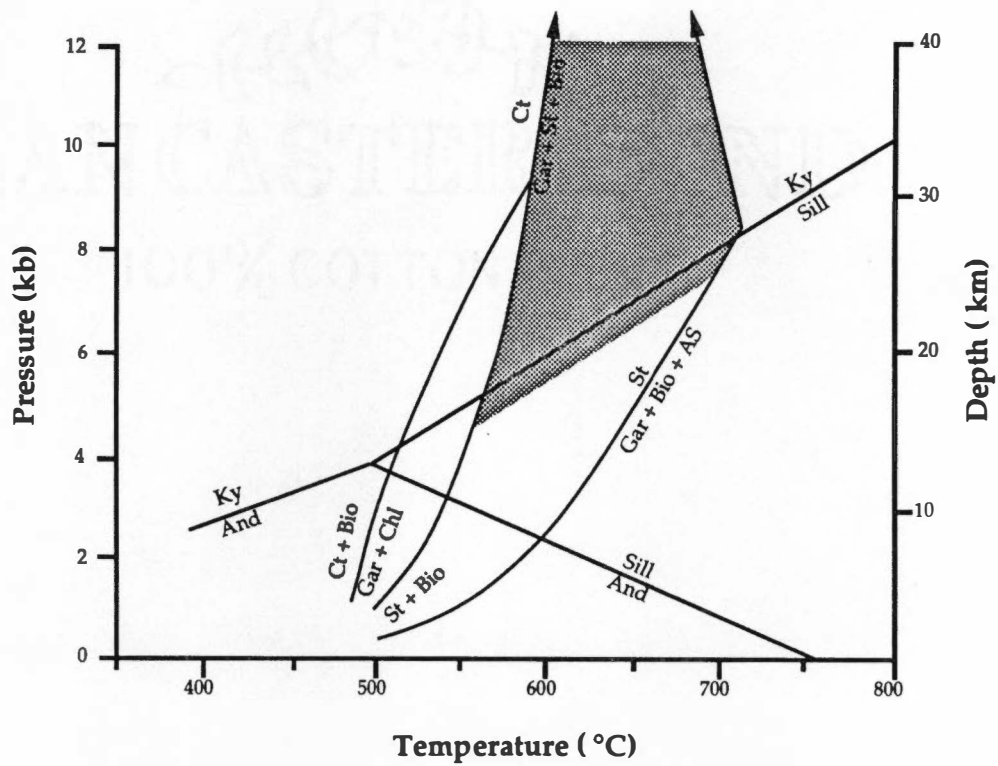
Figure 4.6: The region of stability in pressure-temperature space for pelites in the study area based on their mineral assemblages. (Aluminum silicate phase relations from Holdaway, 1971; other curves from Spear and Cheney, 1989.)

Table 4.1: Thermodynamic variables used in thermobarometric calculations.

K_D	Distribution coefficient
Keq	Equilibrium constant
X	Molar concentration
α	Chemical activity
γ	Activity coefficient
W	Mixing parameter
$\Delta V°$	Volume change at 273 °K and 1 bar
ΔV	Volume change at T and P
$\Delta G°$	Free energy change at 273 °K and 1 bar
ΔG	Free energy change at T and P
R	Universal gas constant (1.98717 cal/°K mol)

proposed for a garnet-biotite exchange geothermometer over the past decade and a half (Goldman and Albee, 1977; Ferry and Spear, 1978; Perchuk and Lavrent'eva, 1983). Both the Ferry and Spear and Perchuk and Lavrent'eva calibrations were used in geothermometry calculations. The Ferry and Spear formulation for the GB thermometer is:

$$\ln K_D = 4.662 \ T(^\circ K) - 0.057 \ P(bars) - 12,454 \quad (4\text{-}1)$$

$$\text{where} \ \ K_D = \frac{(Fe/Mg)^{Biot}}{(Fe/Mg)^{Gar}} \quad (4\text{-}2)$$

Perchuk and Lavrent'eva gave two formulations for the GB thermometer using two different values for the volume change of almandine versus pyrope (ΔVgar):

$$T(^\circ K) = \frac{[7843.7 - 0.0577 \ (P\text{-}6000)]}{R \ \ln K_D + 5.699} \quad (4\text{-}3)$$

$$T(^\circ K) = \frac{[7843.7 - 0.0246 \ (P\text{-}6000)]}{R \ \ln K_D + 5.699} \quad (4\text{-}4)$$

Compositions of coexisting garnet and biotite can be used to calculate temperatures at which cation exchange occurred. It is necessary to be confident that the paired analysis points from garnet and biotite are points that actually coexisted and that exchange between the two was feasible. Garnet–biotite point pairs were chosen from garnet rims and nearby matrix biotite to insure that this criterion was met. This has provided temperatures that postdate all but the final stages of garnet growth. Garnet rim–matrix biotite paired analysis points, then, may preserve either peak metamorphic temperature or some portion of the cooling path.

Garnet rim points were also paired with nearby matrix plagioclase to obtain estimates of pressure based on the pressure-sensitive net transfer reaction:

3Anorthite = Grossular + 2Aluminum Silicate + Quartz

(the GASP geobarometer). The best calibrations for this geobarometer have been published by Newton and Haselton (1981) and Koziol and Newton (1988). The Koziol and Newton (1988) calibration was used in this study because of the refined determination of the anorthite breakdown reaction they presented. The anorthite breakdown reaction that

involves kyanite as the Al_2SiO_5 phase (3 anorthite = grossular + 2 kyanite + quartz), as revised by Koziol and Newton has the form:

$$P = 22.80T - 1093 \quad (4\text{–}5).$$

This equation is used to calculate the pressure of the end-member reaction at the prevailing metamorphic temperature. $\Delta G°$ of the reaction is then calculated using the end-member equilibrium pressure and the volume change:

$$\Delta G° \approx -P\Delta V° \quad (4\text{–}6).$$

Molar volumes of end-member phases were taken from the thermodynamic data set of Holland and Powell (1990). Therefore, given the compositions of garnet and plagioclase, and a prevailing metamorphic temperature, the general equation for the GASP geobarometer can be applied:

$$\Delta G = RT \ln\left[\frac{\alpha_{gr}}{\alpha_{an}}\right]^3 + P\Delta V = 0 \quad (4\text{–}7)$$

Here, ΔV must be calculated using the partial molar volume of grossular, obtained by interpolation given the mole fraction of $Ca_3Al_2Si_3O_{12}$ (Newton and Haselton, 1981; Fig.1).

Activity models for garnet and plagioclase assume non-ideal mixing of grossular in garnet and anorthite in plagioclase. The activity-composition relationship for plagioclase given by Newton and Haselton (1981) is:

$$\alpha_{an} = \frac{X_{an}(1+X_{an})^2}{4} \exp\left\{\left[\frac{(1-X_{an})^2}{RT}\right][2050 + 9329X_{an}]\right\} \quad (4\text{–}8)$$

The latest revision of the grossular activity–composition relationship (Koziol and Newton, 1989) was used in the GASP geobarometer. The grossular activity coefficient, γ_{grs}, is given by:

$$RT \ln \gamma_{grs} = (1-X_{grs})^2 \left[W_{Ca} + 2X_{grs}(W_{FM} - W_{Ca})\right] \quad (4\text{–}9)$$

91

$$\text{where } W_{Ca} = -2060 + \left[3.57 \times 10^4 \, (Mg\#)\right] - \left[4.95 \times 10^4 \, (Mg\#)^2\right] \quad (4\text{-}10),$$
$$\text{and } W_{FM} = 3390 - \left[3.71 \times 10^4 \, (Mg\#)\right] + \left[6.49 \times 10^4 \, (Mg\#)^2\right] \quad (4\text{-}11).$$
$$[MG\# = Mg/[Mg + Fe)]$$

Note that the formulation for GB thermometry requires the analyst to assume a pressure before a temperature can be calculated. Similarly, an assumed temperature must be input into the GASP barometer formulation before a pressure can be calculated. These two intensive parameters can be solved for simultaneously, however, given the two equations and the compositions of garnet, biotite, and plagioclase coexisting in a given sample. Simultaneous solution of the two formulations was done by iteration, facilitated by P-T calculations constructed on the Macintosh™ computer using the Microsoft Excel™ spreadsheet application. Pressures were obtained by simultaneous solution with both Ferry and Spear (1978) and Perchuk and Lavrent'eva (1983) GB temperatures. Calculated temperatures and corresponding pressures are compiled in Table 4.2 for the five samples analyzed. Simultaneous solution of the Perchuk and Lavrent'eva GB thermometer and the Koziol and Newton GASP barometer appears to yield the most reasonable results based on observed assemblages.

Usage of interior garnet points and matrix biotite points to obtain estimates of earlier metamorphic temperatures is valid only if the matrix biotite has not changed composition appreciably during later stages of garnet growth through further exchange. This is possible when a sample contains significantly more biotite than garnet so that the additional growth of garnet does not greatly affect the overall biotite composition (Tracy and others, 1990). This approach is considered invalid for these pelites because most samples contained large and modally abundant garnet as well as abundant biotite (i.e., no drastic predominance of one phase over the other).

Interior garnet points *can* be paired with nearby biotite inclusions, however, and this strategy was applied to sample SS454. Garnets in SS454 appear ideal for constructing a P-T history because the grains are large and biotite and plagioclase inclusions are abundant. Pairing interior garnet points and nearby inclusions revealed no significant changes or variations in calculated temperature from those obtained from garnet rim–matrix biotite points. This may indicate the majority of garnet growth occurred during a period where temperature was constant. It is more likely, however, that equilibration has occurred between the inclusions and the surrounding garnet during the latter stages of garnet growth and that these points did not preserve an "early" metamorphic temperature.

Table 4.2: Results of simultaneous calculation of pressure and temperature. (FS = Ferry and Spear, 1978; PL = Perchuk and Lavrent'eva, 1983; KN = Koziol and Newton, 1988. Pressures were calculated in combination with both thermometry schemes. Several garnet–biotite-plagioclase pairs have beem used for each sample. Temperatures are given in °C, pressures in kbars.

Sample #	T (FS)	P (KN)	T1 (PL)	T2 (PL)	P (KN)
SS313	492	3.89	545	541	4.87
	480	3.58	539	535	4.63
	490	4.21	542	539	5.18
SS454	500	3.39	555	549	4.30
	528	4.37	565	561	5.02
	593	5.60	595	594	5.62
	597	5.86	595	594	5.81
SS349	504	4.55	548	546	5.38
	528	5.04	559	558	5.65
	519	5.33	551	551	5.98
	700	9.17	628	635	7.80
SS287	572	6.37	576	578	6.47
	629	7.40	602	606	6.90
SN125	486	6.10	524	527	7.02
	458	5.45	510	512	6.69
	463	5.16	516	517	6.36

BIOTITE GNEISS

ASSEMBLAGES AND TEXTURES

Metamorphic assemblages in biotite gneiss from Unit 2 are different than the pelitic assemblages observed in the adjacent units. Recrystallized metamorphic minerals include Fe-, Mg-, and Ca-rich phases that are concentrated in mafic layers of the gneiss. Recrystallized quartz and feldspar (mostly plagioclase) dominate felsic layers. More aluminous minerals such as aluminum silicate and staurolite are sparse and none were observed in thin section.

Biotite is the primary mica in all samples of biotite gneiss and it is often concentrated in narrow bands that clearly define the gneissic foliation. Metamorphic minerals associated with biotite in mafic layers are epidote ± sphene ± garnet ± hornblende ± chlorite. Of these, epidote is most commonly observed, is often complexly intergrown with biotite, and does not appear to be retrograde. The presence of epidote reflects the calcic and aluminous chemistry of the rocks. Sphene is also common indicating the presence of excess Ti that could not be accommodated by biotite. Hornblende occurs in biotite gneiss, mostly in close proximity to amphibolite, and its presence may be controlled by metasomatic exchange with a proximal mafic lithology. Sphene does not coexist in great abundance with hornblende in biotite gneiss samples. This may be due to the ability of hornblende to accommodate most of the Ti present, thereby preempting the formation of abundant sphene. The occurrence of garnet and its modal abundance seems to be related to the the amount of biotite in the rock. Garnet abundance, then, is greater in more micaceous samples that could provide the components for its growth. The coexistence of epidote + hornblende + oligoclase–andesine (petrographically determined plagioclase composition: An_{28-37}) indicates that the rocks recrystallized under amphibolite facies conditions (Eskola, 1939; Robinson and others, 1982).

MINERAL CHEMISTRY

Microprobe analyses were performed on several samples of biotite gneiss and biotite + hornblende gneiss. Minerals analyzed include biotite, garnet, plagioclase, and hornblende. Compiled analyses may be found in Appendix A.

Garnet

In general, garnets in samples of biotite gneiss are less abundant and less euhedral than garnets in more pelitic rocks. Garnet analyses indicate that they are enriched in almandine, but Fe/Mg and Fe/Ca ratios are variable (Fig 4.7). Sample SN34 contains garnet that is most enriched in almandine, while SN408 (a more mafic sample) contains garnet most enriched in pyrope. Garnet in samples SN487 and SS63 are intermediate in terms of the Fe/Mg ratio, but have a slightly higher Ca content. Mn content in all analyzed garnets is low ($Xsp < 0.084$). Average core and rim compositions for all garnets do not vary appreciably.

A traverse of probe points across garnet grains did not reveal much compositional zoning.(Fig. 4.8). Compositional profiles across garnet grains are relatively flat with only minor deflections at the rims for some samples. The compositional profile for the garnet from sample SS63 is most interesting because it shows the effect of a biotite inclusion on the local composition of the surrounding garnet. The probe point closest to the biotite inclusion indicates that the garnet composition there is anomalously high in Fe and Mn, and depleted in Mg, relative to the rest of the profile. It is unlikely that this compositional deflection was produced by growth zoning, but probably is a result of later reequilibration between the two phases following inclusion of the biotite. A higher Fe/Mg ratio indicates that this reequilibration occurred at a lower temperature than that at which the garnet formed (i.e., during cooling).

Biotite

Biotites in most samples of biotite gneiss are slightly enriched in annite (Mg/(Mg + Fe) = 0.380–0.493) except for sample SN408, which contains biotites that are enriched in phlogopite (Mg/(Mg + Fe) = 0.624–0.634). Ti content of biotite ranges from 0.087–0.241 cations per three octahedral sites. Ti content is highest in sample SN487, which contains rutile as well as ilmenite. The sum of Na + K cations (per 1 interlayer site) ranges between 0.81–0.98.

Hornblende

Microprobe analyses indicate that the amphibole species in amphibole + biotite gneiss is Al-rich hornblende. Amphibole analyses were normalized to 13 cations excluding Ca, K, and Na ($\Sigma13eCKN$) with the assumption that all iron was ferrous. Charge balance with 23 oxygens was then obtained by partitioning ferrous and ferric iron in the appropriate proportions (Robinson and others, 1982, Ch. 1). In this reformulation the T, M1, M2, M3

95
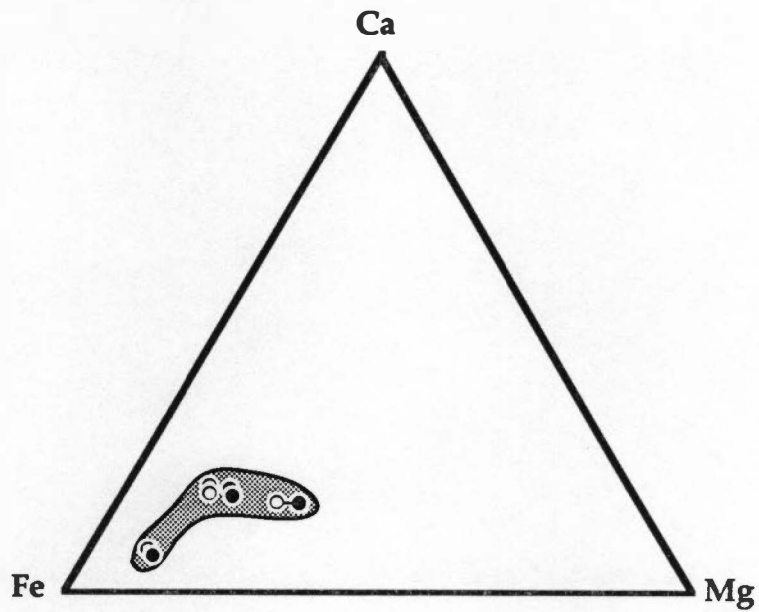
Figure 4.7: Ternary plot showing biotite gneiss garnet compositions between Fe, Ca, and Mg end-members. (Solid symbols represent average core compositions, open symbols indicate average rim compositions.)

96
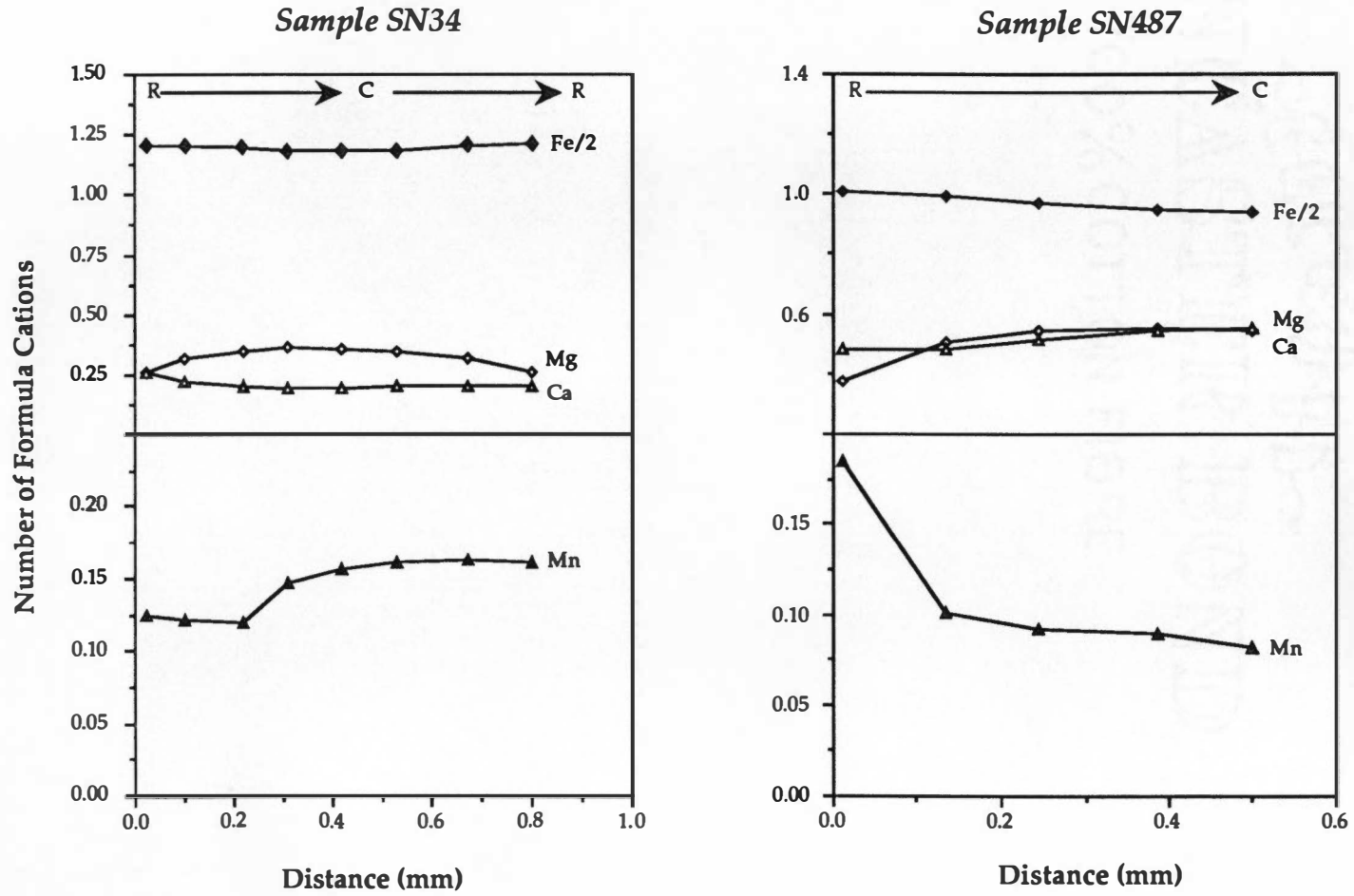
Figure 4.8: Compositional profiles of analyzed garnets from biotite gneiss (Unit 2). (R = rim, C = core.)
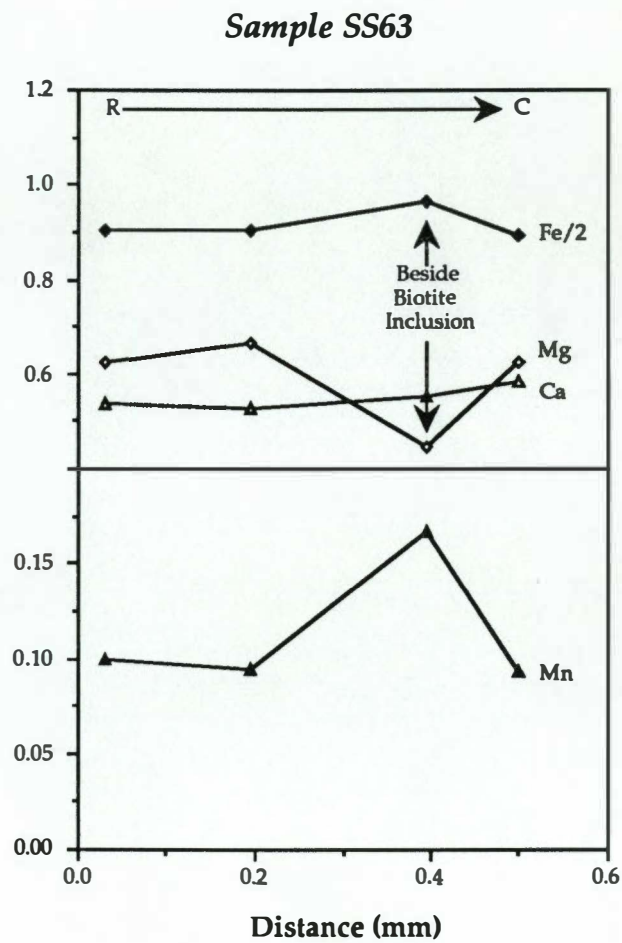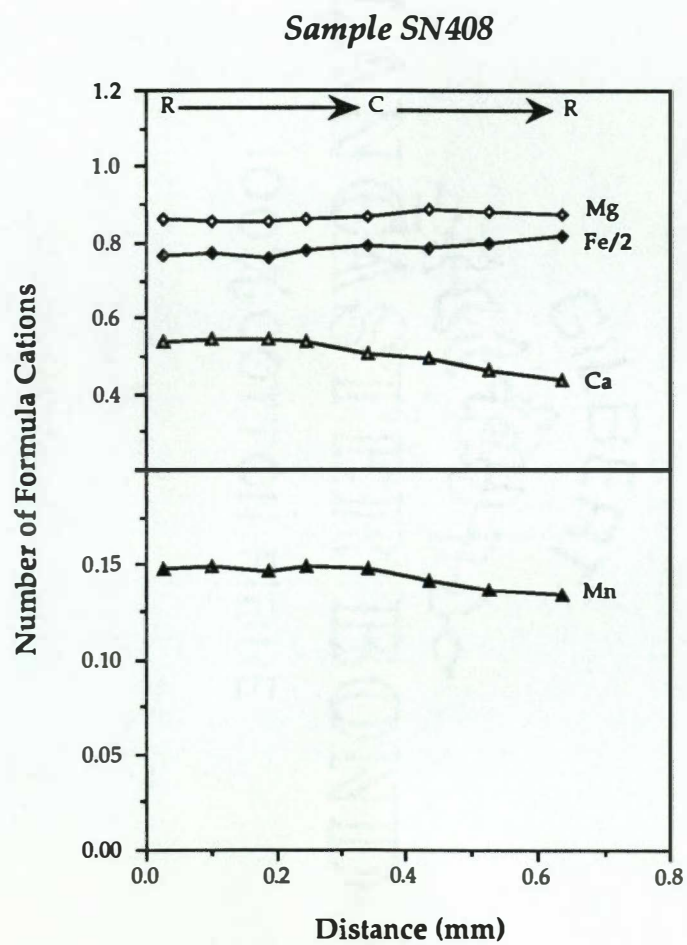
Figure 4.8 (continued)

and M4 sites are completely filled and vacancies occur only in the A site. Small amounts (0.121-0.219 cations) of Na were required to fill the M4 site. Approximately 1.5 cations of Al was required in the T site to fill it to 8 cations. Hornblende compositions are remarkably uniform.

All probe point analyses are plotted for each sample (Fig. 4.9) and the patterns exhibited for both are very similar. The majority of amphibole analyses plot as common hornblende, but occur close to the pargasite end member. No zoning patterns were evident between core and rim analyses.

Plagioclase

Plagioclase is abundant in samples of biotite gneiss and several grains were analyzed from each sample to characterize their composition. Plagioclase compositions range from oligoclase to andesine (An26 – An36). Two samples (SS63 and SN34) appear to contain only oligoclase, while the other two (SN487 and SN408) contain only andesine.

THERMOBAROMETRY OF BIOTITE GNEISS

There is a distinct paucity of diagnostic index minerals in most occurrences of biotite gneiss from Unit 2. Assemblages most often observed include biotite + quartz + plagioclase + K-feldspar + opaques ± garnet ± sphene ± epidote ± chlorite. Compositions of these gneisses were not adequately aluminous to produce abundant aluminum silicate minerals, except in rare and weathered schist layers. Consequently, a precise estimate of metamorphic conditions (both P and T) based on Al_2SiO_5-bearing assemblages were not obtained from these rocks.

Metamorphic temperature can be obtained, however, by applying known thermodynamic exchange equilibria between coexisting minerals. Garnet–biotite (GB) thermometry (Ferry and Spear, 1978; Perchuk and Lavrent'eva, 1983) and plagioclase–hornblende (PH) thermometry (Blundy and Holland, 1990) were used to obtain metamorphic temperature from samples of biotite gneiss and biotite + hornblende gneiss. Garnet–plagioclase–hornblende (GPH) barometry (Kohn and Spear, 1989, 1990) was used to obtain metamorphic pressure from hornblende-bearing samples. GB thermometry formulations were thoroughly explained in the section on the thermobarometry of pelites. PH thermometry and GPH barometry formulations are explained below.

99

Hornblende Compositions in Biotite and Amphibole Gneiss
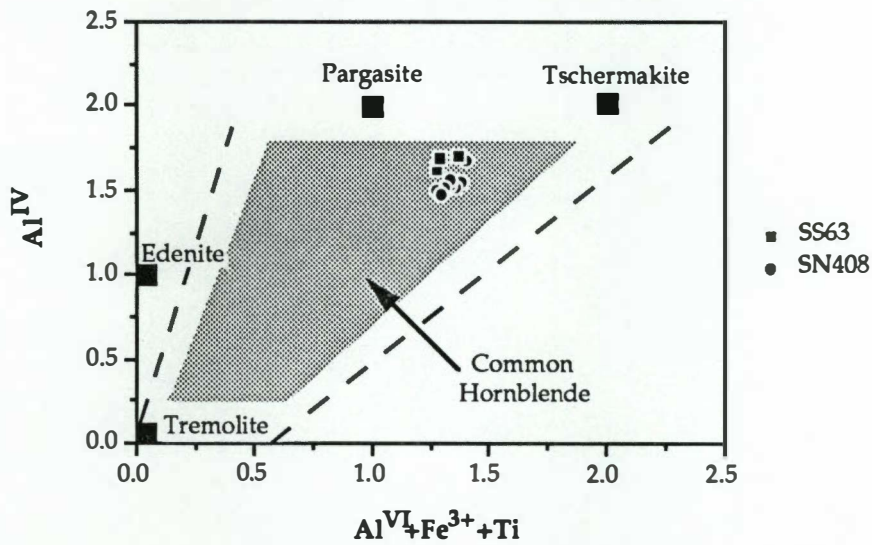
Figure 4.9: Compositions of hornblende from biotite + hornblende gneisses shown on an amphibole classification diagram of Al^{IV} versus $[Al^{VI} + Fe^{3+} + Ti]$. (After Deer and others, 1966.)

Although the thermodynamic mixing properties of amphibole are poorly understood, several thermometers, and recently two barometers, have been proposed that appear to be reliable (Spear, 1980; Graham and Powell, 1984; Blundy and Holland, 1990; Kohn and Spear, 1989, 1990). The PH thermometer (Blundy and Holland, 1990) was used for hornblende-bearing samples and involves edenite exchange (Na^A, Al^{IV}, $\square^A_1$, Si_{-1}) between hornblende and plagioclase. This thermometer has the form:

$$T\,(^\circ K) = \frac{0.677\,P(\text{bars}) - 48.98}{-0.0429 - 0.008314\,\ln K_D} \quad (4\text{--}12)$$

$$\text{where}\quad K_D = \frac{(Si - 4)}{(8 - Si)}\,X^{Plg}_{Ab} \quad (4\text{--}13)$$

Note that a metamorphic pressure must be known or assumed before a temperature can be calculated.

Two geobarometers recently proposed by Kohn and Spear (1990) involve intercrystalline exchange between hornblende, garnet, and plagioclase. The two geobarometers are very similar and differ only in the Mg and Fe end-members of garnet and hornblende:

(1) 6Plagioclase + 3Tremolite = 2Grossular + Pyrope + 3Tschermakite + 6Quartz,

(2) 6Plagioclase + 3Fe-Actinolite = 2Grossular + Almandine + 3Fe-Tschermakite + 6Quartz.

Pressure formulations vary slightly depending on the Mg-Fe end-member equations:

$$P_{Mg} = \frac{[79507 + T(29.14 + 8.3144\,\ln K_{eq})]}{10.988} \quad (4\text{--}14)$$

$$P_{Fe} = \frac{[35327 + T(56.09 + 8.3144\,\ln K_{eq})]}{11.906} \quad (4\text{--}15)$$

Activity models for garnet, plagioclase, and amphibole (Kohn and Spear, 1990) are outlined in Table 4.3. Differences between pressures calculated by each barometer for a given set of coexisting minerals are minimal. Note that a metamorphic temperature must be known or

Table 4.3: Activity models for the GPH barometers. (From Kohn and Spear, 1990)

Garnet and Plagioclase

$$\alpha_{py} = \left\{ X_{py} \, EXP\left[\frac{(13800 - 6.28T)\,(X_{gr}^2) + (X_{al}\,X_{gr}) + (X_{gr}\,X_{sp})}{RT} \right] \right\}^3$$

$$\alpha_{gr} = \left\{ X_{gr} \, EXP\left[\frac{(13800 - 6.28T)\,(X_{py}^2 + X_{al}\,X_{py} + X_{py}\,X_{sp})}{RT} \right] \right\}^3$$

$$\alpha_{al} = \left\{ X_{al} \, EXP\left[\frac{(13800 - 6.28T)\,(-X_{py}\,X_{gr})}{RT} \right] \right\}^3$$

$$\alpha_{an} = X_{an} \, EXP\left[\left\langle \frac{610.34}{T} \right\rangle - 0.3837 \right]$$

Amphibole

$$\alpha_{Tsch} = \left\langle \frac{256}{27} \right\rangle \langle X_{T1Al} \rangle \langle X_{T1Si} \rangle^3 \left[\frac{Mg}{Fe + Mg} \right]$$

$$\alpha_{Tr} = \langle X_{T1Si} \rangle^4 \left[\frac{Mg}{Fe + Mg} \right]^2$$

where: $X_{T1Si} = \dfrac{Si - 4}{4}$ and: $X_{T1Al} = \dfrac{8 - Si}{4}$

assumed before a pressure can be calculated. The PH thermometer and the GPH barometer were solved simultaneously to determine their intersection in P-T space.

Results of exchange equilibria for biotite gneiss samples are compiled in Table 4.4. GB temperatures obtained with the formulation of Perchuk and Lavrent'eva (1983) appear to be more reasonable than those obtained with the Ferry and Spear (1978) formulation. All samples have recorded a temperature of approximately 650-725°C, except for sample SN34, which yielded a temperature of about 550-600°C. Temperatures obtained by both GB and PH thermometry show relatively good agreement for the hornblende-bearing samples. Pressures between 8.0-9.5 kbars were obtained by GPH barometry.

AMPHIBOLITES

ASSEMBLAGES AND TEXTURES

Thin sectioned samples of amphibolite are dominated by hornblende (± biotite) which gives them a dark green color. The remaining mineralogy of amphibolites includes plagioclase + microcline + minor quartz + sphene + ilmenite ± garnet ± epidote ± chlorite. Textural evidence suggests that the rocks have been thoroughly recrystallized, resulting in a granoblastic texture.

Hornblende typically displays pleochroism from beige to pale brown. Pleochroism apparently defines zoning in hornblende where narrow bands near crystal rims have a pale brown to green pleochroic scheme. Hornblende crystals are well-formed, optically continuous, and show no evidence of retrograde replacement (although the pleochroic zoning may record retrograde cation exchange).

Plagioclase and microcline are much more abundant than quartz and tend to be much larger in size. Quartz and feldspar grains appear to have been thoroughly recrystallized. Graphic or myrmekitic intergrowth between feldspars and quartz or feldspar and hornblende is common. It is unclear whether this intergrowth texture is a product of metamorphic recrystallization or results from a post-crystallization diffusion process. Biotite and chlorite are sometimes observed in amphibolite but are not usually abundant in thin section.

Table 4.4: Results of temperature calculations from garnet-biotite and garnet-plagioclase equilibria for biotite gneiss and biotite + amphibole gneiss (Unit 2). (FS = Ferry and Spear, 1978; PL = Perchuk and Lavrent'eva,1983; BH = Blundy and Holland, 1990; KS = Kohn and Spear, 1990. Temperature ranges correlate to pressures between 5-10 kbars. Several garnet–biotite pairs have been used for each sample. Temperatures given in °C, pressures in kbar.)

Sample #	T (FS)	T (PL)	T (BH)	P(KS)
SN34	555 - 575	550 - 580		
	585 - 605	565 - 595		
	595 - 610	570 - 600		
SN408	855 - 885	690 - 720		
	875 - 900	700 - 730		
	840 - 865	685 - 720		
			720	8.00
SN487	974 - 1000	745 - 775		
	900 - 930	710 - 745		
	950 - 975	725 - 765		
SS63	750 - 775	645 - 680		
	900 - 930	705 - 745		
	710 - 730	625 - 660		
			718	9.60

Sphene is always observed in amphibolites and is usually a relatively abundant accessory mineral. During prograde transitions into the amphibolite facies, mafic rocks lose sphene, which reacts to produce more Ca- and Ti-rich amphibole, Ti-rich biotite, and ilmenite (Robinson and others, 1982). The persistence of sphene in these rocks indicates that they are rich in Ti. The inability of hornblende to accommodate excess Ti, and the scarcity of biotite, may have extended the stability of sphene in these lithologies. Epidote, more commonly seen in the greenschist-epidote amphibolite facies, has mostly reacted away in these rocks, and occurs infrequently as an accessory mineral. Opaque minerals could not be identified petrographically but are inferred to be ilmenite and magnetite.

MINERAL CHEMISTRY

Two garnet amphibolites were selected for microprobe analysis (Appendix A) to provide a quantification of mineral chemistry and to facilitate the application of garnet-plagioclase-hornblende thermobarometry. Analyzed samples are coarse grained, fresh, and are composed primarily of hornblende (zoned), garnet, and plagioclase. Hornblende, plagioclase, and garnet were the three phases analyzed.

Hornblende

Analyses of two amphibolite samples indicate that the amphibole species is Al-rich hornblende. Amphibole analyses were normalized to 13 cations excluding Ca, K, and Na (Σ13eCKN) with the assumption that all iron was ferrous (as explained for amphiboles analyzed in biotite + hornblende gneiss). Charge balance with 23 oxygens was then obtained by partitioning ferrous and ferric iron in the appropriate proportions (Robinson and others, 1982, Ch. 1). Small amounts (0.067-0.228 cations) of Na were required to fill the M4 site. About 1.5 cations of Al was required in the T site to fill it to 8 cations. Hornblende compositions are remarkably uniform except for more tschermakitic rim analyses.

All probe point analyses were plotted for each sample (Fig 4.10) and the patterns exhibited for both are very similar. The majority of amphibole analyses plot as pargasitic hornblende while a few points (rim analyses) trend farther toward the tschermakite end member. A similar amphibole classification scheme modified after Leake (1978) (Vyhnal, 1989) shows that the amphiboles in SN489 are more pargasitic than those in SN414 (Fig. 4.11). Here again, the amphibole compositional data are uniform for each sample, but with a few outlying points representing altered rim compositions.

105

Sample SN414

Sample SN489
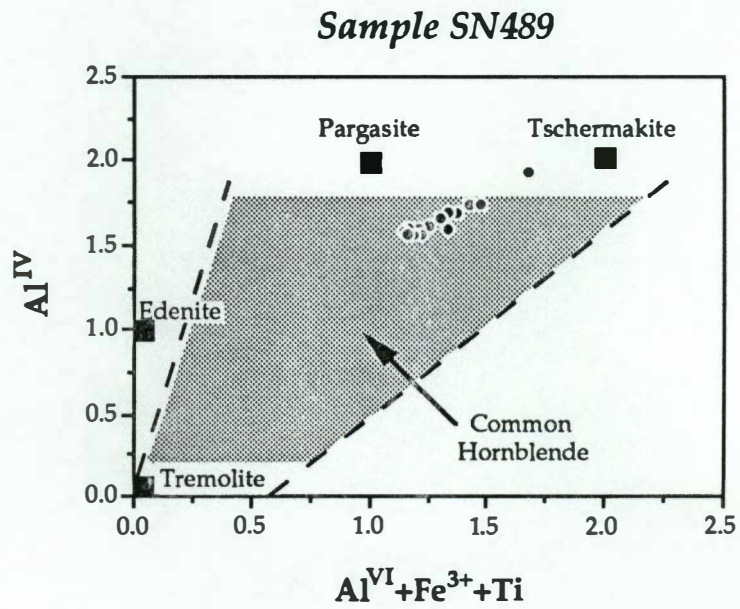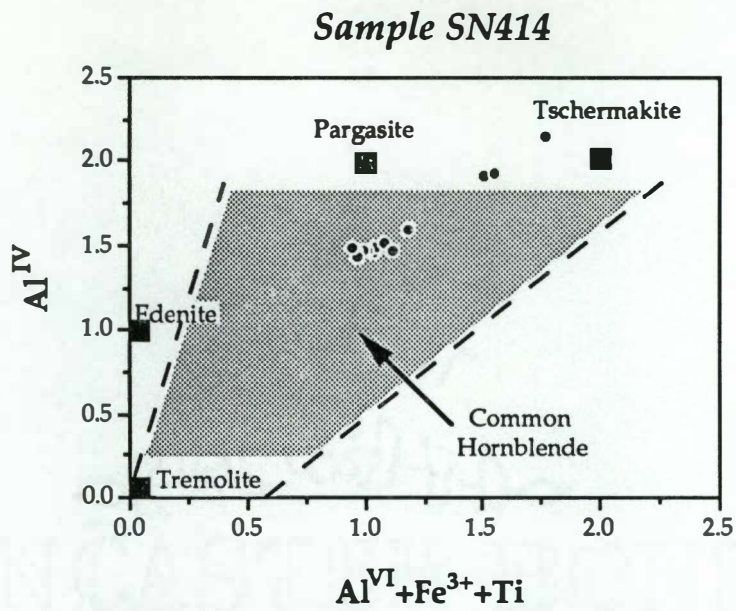
Figure 4.10: Compositions of hornblende from amphibolites shown on an amphibole classification diagram of Al^{IV} versus $[Al^{VI} + Fe^{3+} + Ti]$. (After Deer and others, 1966.)

106
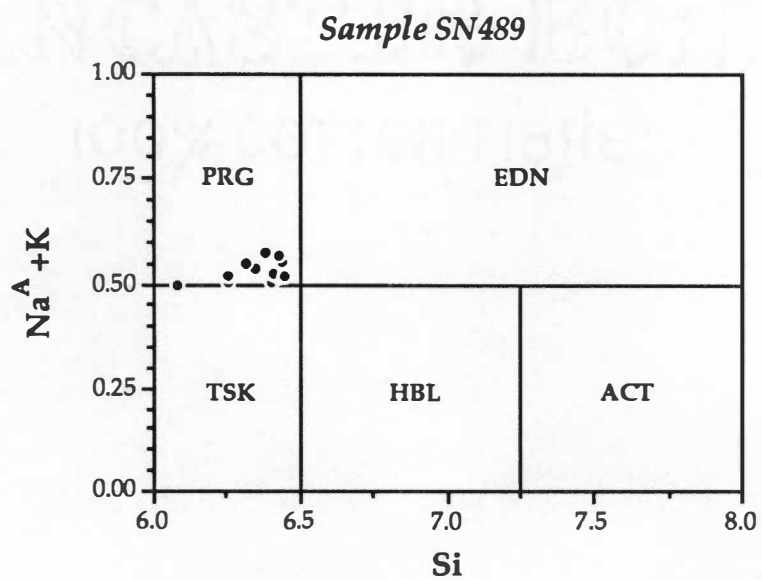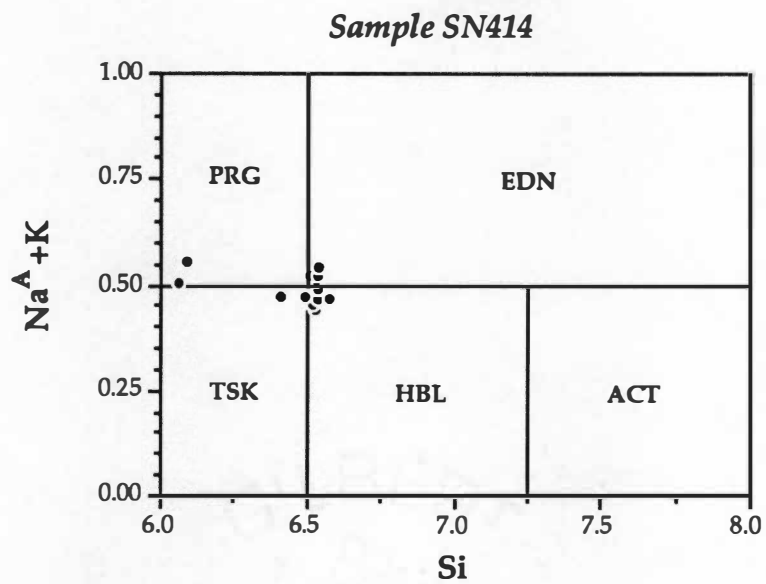
Figure 4.11: Composition and classification of hornblende from amphibolites on a classification diagram of Si versus Na + K. (After Leake, 1978.)

Zoning patterns of hornblende in amphibolites involve dominantly pargasitic crystals with narrow rims that are more tschermakitic. A corresponding increase in Na^A in zoned rims indicates involvement of the edenite substitution:

$$Na^A, Al^{IV}, \square^A_{-1}, Si_{-1}$$

Experimental studies by Blundy and Holland (1990) showed that the edenite substitution in amphiboles is a function of temperature Increased Al^{IV} and Na^A in hornblende rims, therefore, indicate that they record crystallization or reequilibration during elevated temperature. This relationship can be explained if a late thermal pulse affected these rocks and caused hornblende rims in the amphibolites to reequilibrate at higher temperature.

Garnet

Garnets are abundant and euhedral in the two samples of amphibolite analyzed and many contain inclusions (mostly plagioclase). Average core and rim compositions were plotted on a ternary plot with Fe, Ca, and Mg end members (Fig. 4.12). Garnet compositions are enriched in almandine, have higher concentrations of Ca and Mg than garnets from pelites, and are similar in composition to more pyrope- and grossular-rich garnets from biotite gneiss. Mn content in garnet is low ($Xsp < 0.047$) and Cr concentrations were mostly below detection limits. Compositional differences between garnet cores and rims are not very apparent in Fig 4.12.

Core to rim variations are best shown by garnet composition profiles obtained by a traverse of probe points across the grains (Fig. 4.13). It is apparent from garnet composition profiles that Ca and Mg concentrations inversely mirror one another while Fe concentration remains relatively constant. Mn concentration is higher in the garnet core in sample SN414, which is consistent with the high K_D of Mn in garnet (Hollister, 1966). The Mn increase close to the garnet rim in sample SN489 is not a normal growth-zoning pattern and perhaps indicates late-stage resorbtion of the garnet.

Plagioclase

Plagioclase is an abundant phase in amphibolites and several grains were analyzed per sample. Plagioclase compositions range throughout the andesine field (An_{30} – An_{49}), with a few analyses crossing into the labradorite field ($\geq An_{50}$). Fe and K contents in plagioclase are very low. Plagioclase in SN414 is much more calcic (An_{46} – An_{51}) than plagioclase in SN489 (An_{31} – An_{37}). Plagioclase compositions are well above the
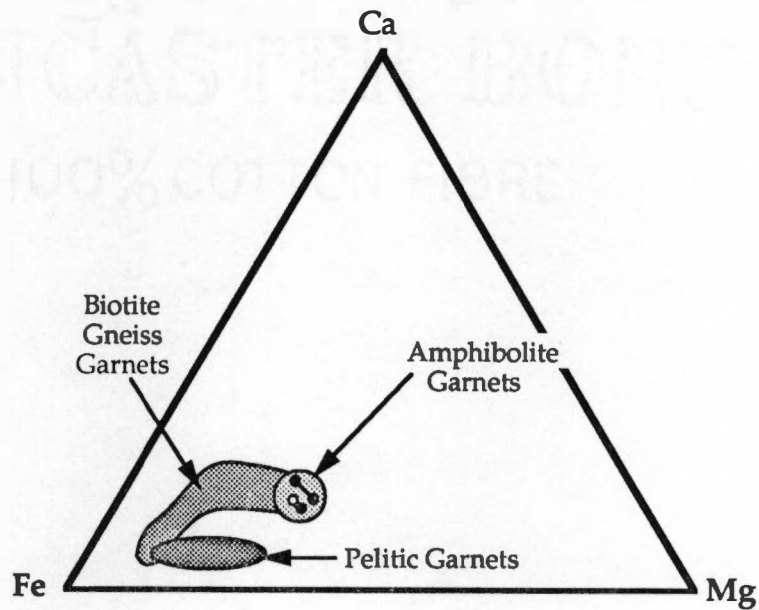
Figure 4.12: Ternary plot showing amphibolite garnet compositions between Fe, Ca, and Mg end-members. (Solid symbols represent average core compositions, open symbols indicate average rim compositions. Composition fields of garnet from pelitic rocks and biotite gneiss are shown for comparison.)
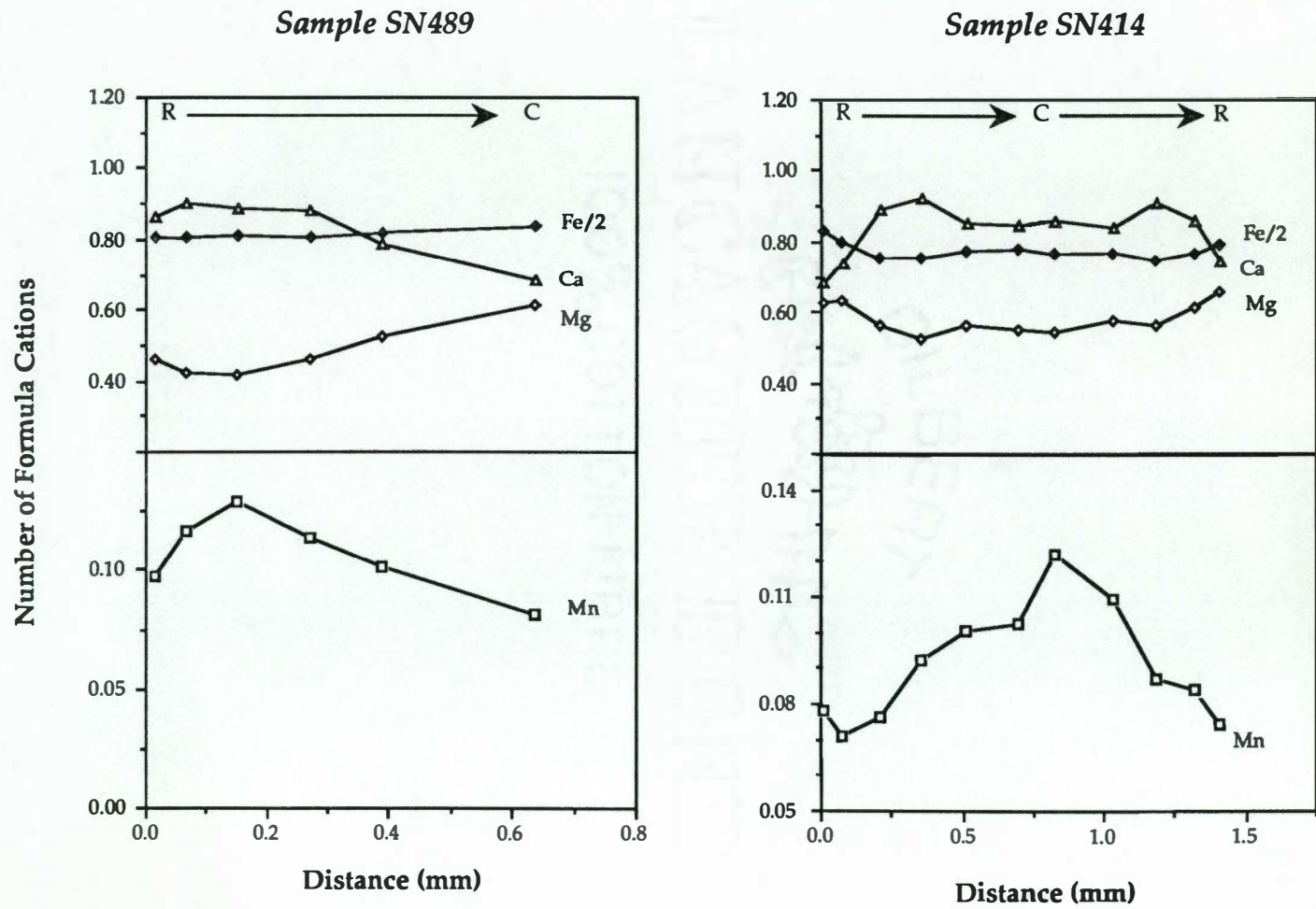
Figure 4.13: Compositional profiles of analyzed garnets from amphibolites. (R = rim, C = core.)

peristerite gap. Hornblende coexisting with oligoclase (or more calcic plagioclase) indicates metamorphism occurred in the amphibolite facies (Miyashiro, 1973; Laird, 1980; Robinson and others, 1982).

THERMOBAROMETRY OF AMPHIBOLITES

As discussed previously, many exchange equilibria between hornblende, plagioclase, and garnet have been developed for metamorphic rocks bearing amphibole (Spear, 1980; Graham and Powell, 1984; Blundy and Holland, 1990; Kohn and Spear, 1989, 1990). In addition to the plagioclase–hornblende (PH) thermometer used for samples of biotite + hornblende gneiss, the garnet-hornblende (GH) Fe, Mg_{-1} exchange thermometer (Graham and Powell, 1984) was also used for amphibolite samples. This thermometer is independent of pressure and has the form:

$$T(°K) = \frac{(2880 + 3280 \, X_{Ca,g})}{(\ln K_D + 2.426)} \quad (4-16)$$

$$\text{where} \quad K_D = \frac{(X_{Fe,g} / X_{Mg,g})}{(X_{Fe,hb} / X_{Mg,hb})} \quad (4-17)$$

This permits the calculation of a metamorphic temperature without an assumption of pressure. The Blundy and Holland PH formulation yields higher temperatures than does the Graham and Powell GH thermometer (Table 4.5). The garnet–hornblende–plagioclase barometer (Kohn and Spear, 1990) was used to calculate metamorphic pressure from the amphibolite samples using temperatures obtained from both thermometry schemes.

The PH thermometer and the Kohn and Spear barometer equations were solved simultaneously to obtain the intersection point of the two lines in P-T space. Since garnet and hornblende compositions are roughly between Fe, and Mg end-members, pressures obtained from each Kohn and Spear pressure formulation were averaged. Simultaneous solution with the Graham and Powell thermometer is not possible because it is completely independent of pressure. Temperatures and pressures do not vary significantly between the two sets of calculations. The temperatures obtained from amphibolite samples (Table 4.5) are comparable with those obtained from nearby biotite gneiss samples.

111

Table 4.5: Results of pressure and temperature calculations for two amphibolite samples. GP = Graham and Powell, 1984; BH = Blundy and Holland, 1990; KS = Kohn and Spear, 1990. Pressures were calculated using both temperature formulations. Temperatures are given in °C, pressures in kbar.

Sample #	T(GP)	P(KS)	T(BH)	P(KS)
SN414	764	9.23	742	9.11
	735	9.01	747	9.07
	738	8.88	748	8.93
	712	9.05	753	9.27
	707	8.32	761	8.51
SN489	626	10.05	698	10.57
	630	10.10	697	10.59
	663	9.28	733	9.71
	672	10.20	721	10.54
	689	10.11	708	10.24

IMPLICATIONS OF THERMOBAROMETRY

Temperatures and pressures obtained from pelites are generally lower than those obtained from biotite gneiss and amphibolites (Fig. 4.14). PT conditions calculated for all samples, however, agree with the PT constraints of observed assemblages (Fig 4.15).

Higher pressures and temperatures obtained from the unit that structurally overlies other units metamorphosed at lower pressures and temperatures presents a problem. This pattern perhaps indicates that the metamorphic evolution of Unit 2 is somehow different than for Units 1 and 3. An alternate interpretation could be that Unit 2 is actually a basement unit and it has preserved temperatures relict of an earlier metamorphism. Polymetamorphism has been suggested in recent studies (Shireman and others, 1985; Labotka and Shireman, 1991) for rocks in the study area, near Cullowhee, North Carolina. Polymetamorphism cannot explain the higher metamorphic conditions obtained in Unit 2, however, because all temperatures and pressures were calculated from garnet rim compositions. PT conditions calculated with garnet rim compositions should agree if all units were juxtaposed prior to the latest metamorphic pulse.

If higher metamorphic conditions in Unit 2 indicate that it has undergone a metamorphic evolution that is different than the surrounding units, then neither the Hayesville or Soque River faults can be premetamorphic structures. The cryptic nature of the fault boundaries and the apparent continuity of the sillimanite isograd across these boundaries, however, almost surely require them to be premetamorphic. I can only suggest that Unit 2 has somehow preserved metamorphic peak conditions whereas pelites in the surrounding units preserve conditions at some point along the cooling path. Resolving this paradox with the present data is difficult and, clearly, a more detailed petrologic study in this area is necessary.
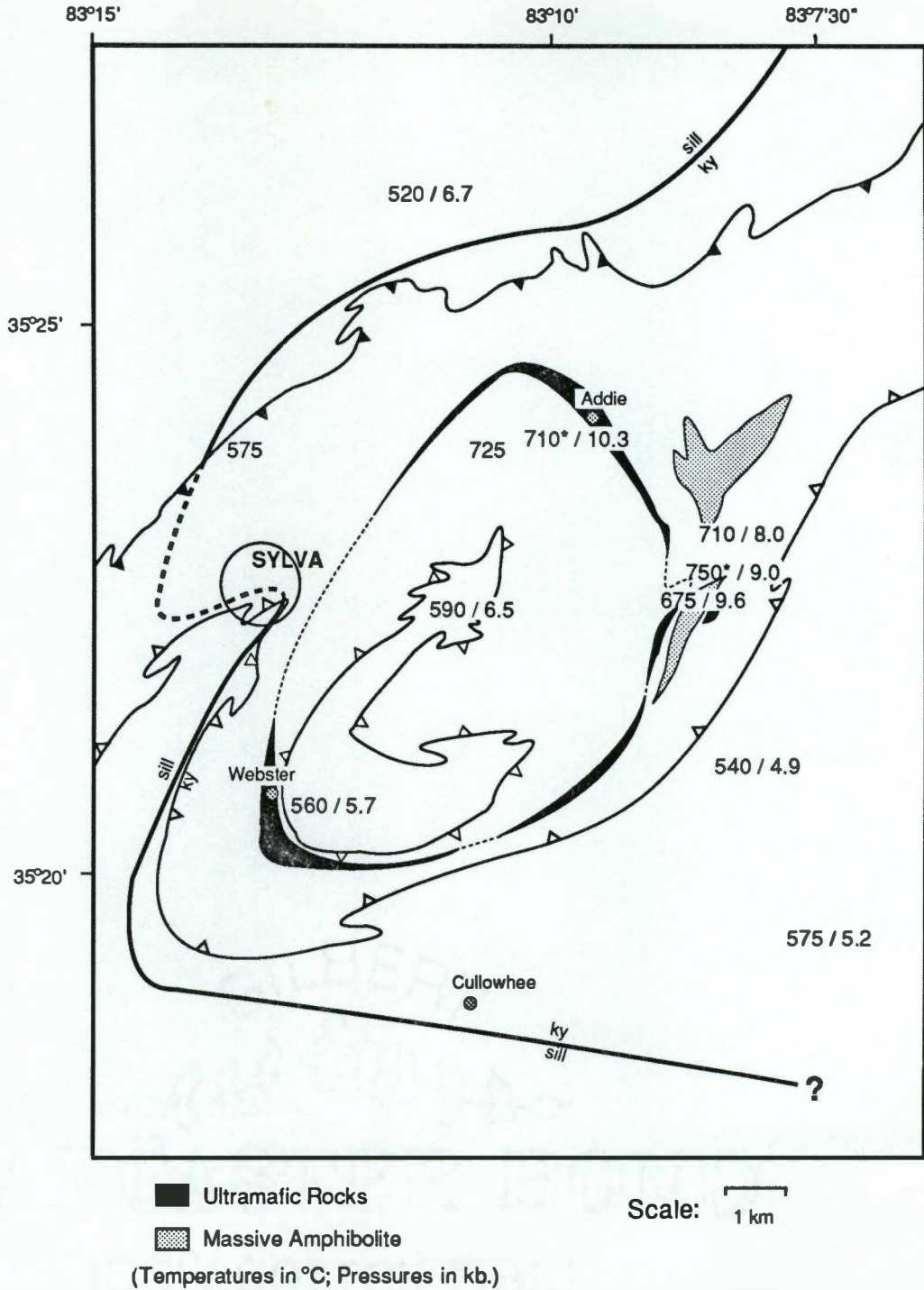
Figure 4.14: Map showing the areal distribution of metamorphic temperatures and pressures obtained from each analyzed sample. Temperatures were calculated with GB thermometry (Perchuk and Lavrent'eva, 1983) except those with an asterisk, which were obtained from amphibolites using PH thermometry (Blundy and Holland, 1990). Pressures were obtained using the GASP geobarometer (Koziol and Newton, 1988, 1989) except for samples in Unit 2, where pressures were obtained by PGH barometry (Kohn and Spear, 1990).

114
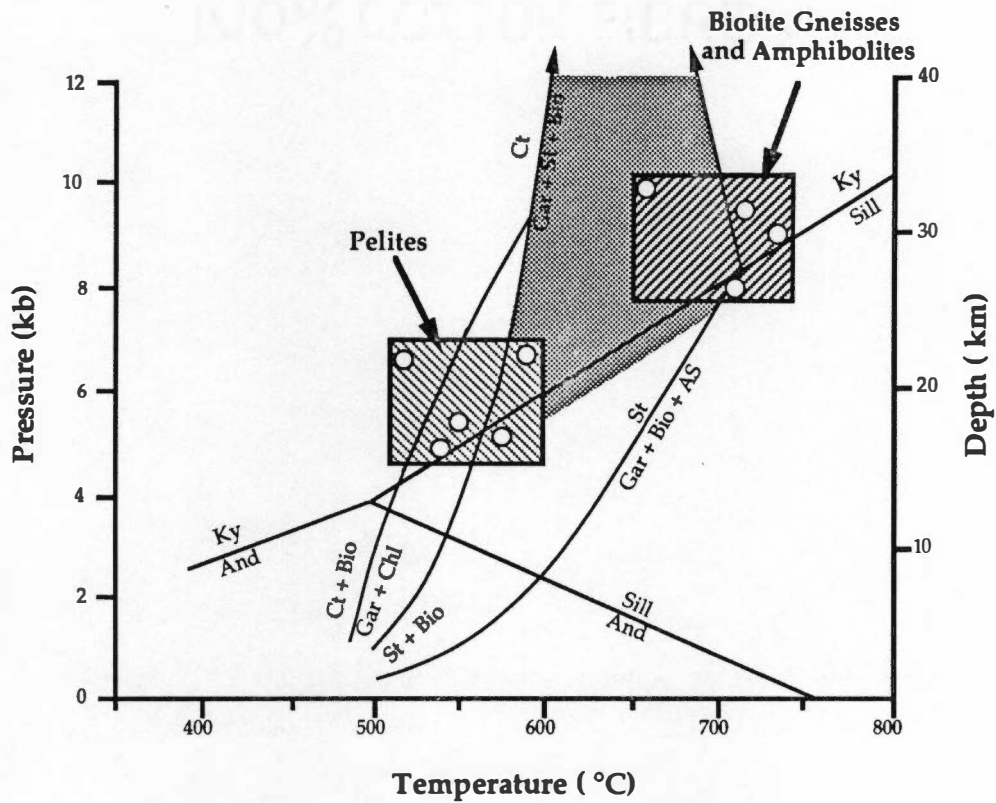
Figure 4.15: PT plot showing the agreement between calculated metamorphic conditions of analyzed samples and constraints imposed by the observed metamorphic assemblages. (Aluminum silicate phase relations from Holdaway, 1971; other curves from Spear and Cheney, 1989.)

115

V. AMPHIBOLITE GEOCHEMISTRY

During field mapping, amphibolite samples were collected at every station where the lithology was observed and deemed fresh enough for chemical analysis. As a result, 82 amphibolite samples were gathered, prepared, and analyzed on the EG&G ORTEC X-ray fluorescence spectrometer (EDS) at the University of Tennessee. Detailed descriptions of sample preparation and XRF procedures are included in Appendix A. Bulk rock chemistry was obtained using the IGROCK protocol that yielded weight percents for 10 major element oxides and 8 minor and trace elements. IGROCK was designed and calibrated for analyses of igneous rocks but is also appropriate for amphibolites and other metamorphic rocks with an igneous protolith. Individual amphibolite analyses may be found in Appendix B.

Amphibolites observed and collected in the study area were initially presumed to be metamorphosed mafic volcanic rocks based on textural appearance and mineralogy. Penetrative transposition and later deformational events, however, have obliterated possible stratigraphic and cross-cutting relationships that would confirm an igneous origin. Additionally, these rocks were thoroughly recrystallized under upper-amphibolite facies conditions, subjecting the assumption of an igneous protolith to uncertainty and skepticism. The possibility that these rocks could have originated as calcareous or dolomitic shale must be considered and tested. In a previous study, Nelson (1969) concluded that amphibolite in the eastern Blue Ridge of western North Carolina was ortho-amphibolite based on chemical data for six samples from scattered localities and on data from Wilcox and Poldervaart (1958). Two of Nelson's sample localities occur within and very close to the present study area.

The first objective of this section is to confirm that the amphibolites collected for this study are ortho-amphibolites based on more numerous analyses than have been performed in the past for this particular rock unit. Because chemical trends are, in some cases only vaguely igneous, a discussion of element mobility before and during metamorphism will follow. Finally, trace element geochemistry of the amphibolites will be applied to some standard tectonic discrimination diagrams. By using a number of these diagrams in combination, a tectonic regime in which the igneous protoliths were emplaced can be determined with a relatively high degree of certainty.

PROTOLITH

Because present field relations are inadequate to prove the origin of amphibolite in the map area, a geochemical signature or trend must be relied upon to distinguish ortho- from para-amphibolite. Leake (1964) noted that igneous and sedimentary trends of evolution differ considerably and can easily be distinguished on a ternary plot of Niggli values mg vs. c vs. al-alk ($mg = 100*[MgO/FeO+ MnO+ MgO]$; $c = CaO$; and al-$alk = [Al_2O_3]-[Na_2O+ K_2O]$). Fig. 5.1 is a plot of Niggli functions for all amphibolites analyzed for this study. Although there is considerable clustering of data points on this diagram, a clear igneous trend is apparent and is at a high angle to the sedimentary trends that are also shown.

To further substantiate that the amphibolites in the study area have an igneous origin, Harker diagrams (Cox and others,1979) have been used to highlight possible fractionation trends of the igneous precursors. The standard Harker diagram plots a fractionation index as the abscissa versus various elements or oxides to demonstrate igneous variations as fractionation proceeds. SiO_2 is most commonly used as the fractionation index. For this study, however, the use of SiO_2 produced scattered, nonlinear trends. I conclude that SiO_2 was a significantly mobile component during metamorphism and cannot be used to represent the original igneous signature of the rocks.

As an alternative to SiO_2, magnesium number ($Mg\# = MgO/FeO + MgO$) was used as a fractionation index where $Mg\#$ decreases as fractionation proceeds. Figure 5.2 plots $Mg\#$ against various major element oxides and minor elements. As Mg has a higher distribution coefficient than Fe, $Mg\#$ decreases as fractionating phases remove Mg (Note: fractionation increases toward the <u>left</u> on Figure 5.2 plots). Although there is considerable scatter, all plots exhibit igneous fractionation trends with varying degrees of clarity. The alkalis exhibit a general increase and CaO exhibits a moderate decrease with fractionation. No apparent change with fractionation was produced by alumina. More distinct trends were produced by minor elements because they were probably less mobile than major elements during metamorphism. As would be expected, the incompatible elements TiO_2 and Zr exhibit an increase with fractionation and a compatible element, Ni, exhibits a corresponding decrease.

Another useful fractionation index is the trace element Zr. Because Zr is incompatible, Zr concentration increases as fractionation proceeds. Figure 5.3 includes numerous Harker diagrams using Zr as a fractionation index. Of all the major element

117
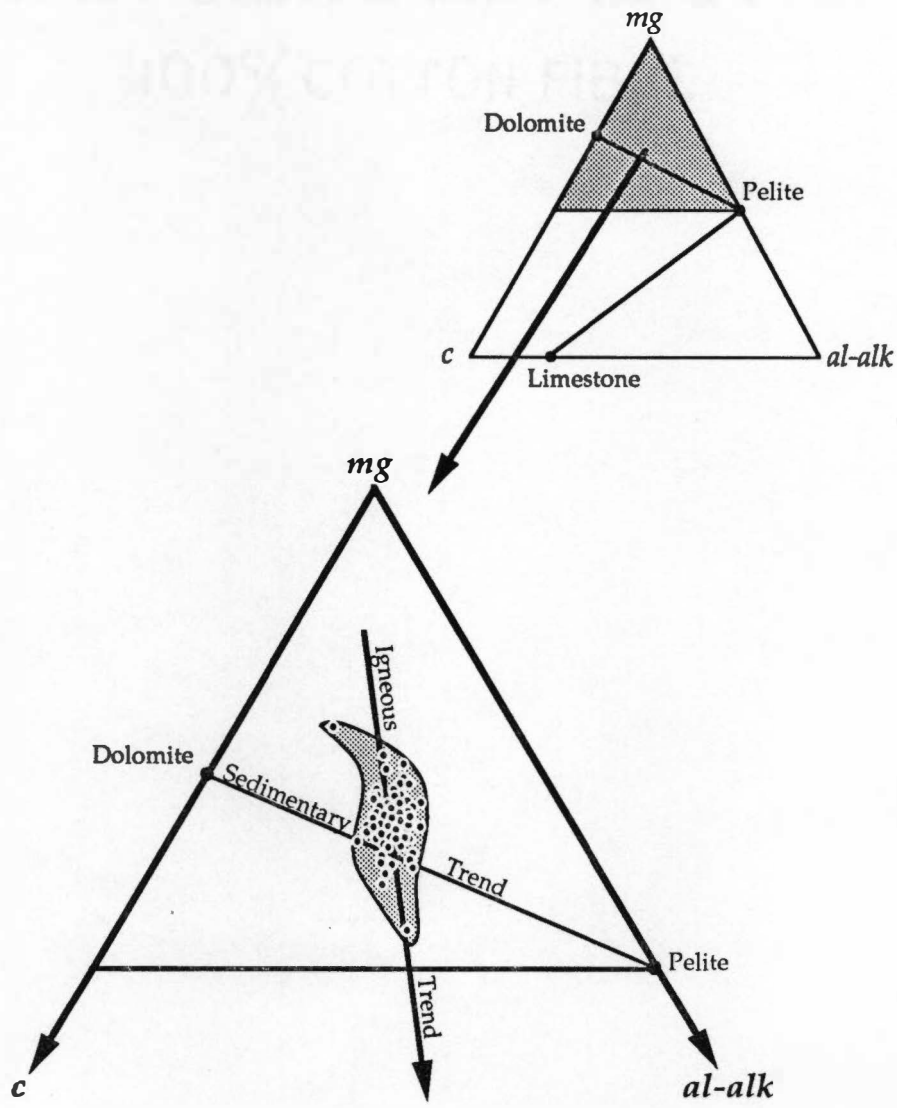
Figure 5.1: Niggli c vs mg vs $al\text{-}alk$ ternary plot demonstrating an igneous trend for amphibolites from Units 2 and 3. (mg =100* [MgO/FeO+MnO+ MgO], c = CaO, and $al\text{-}alk$ = [Al$_2$O$_3$]-[Na$_2$O+ K$_2$O]).
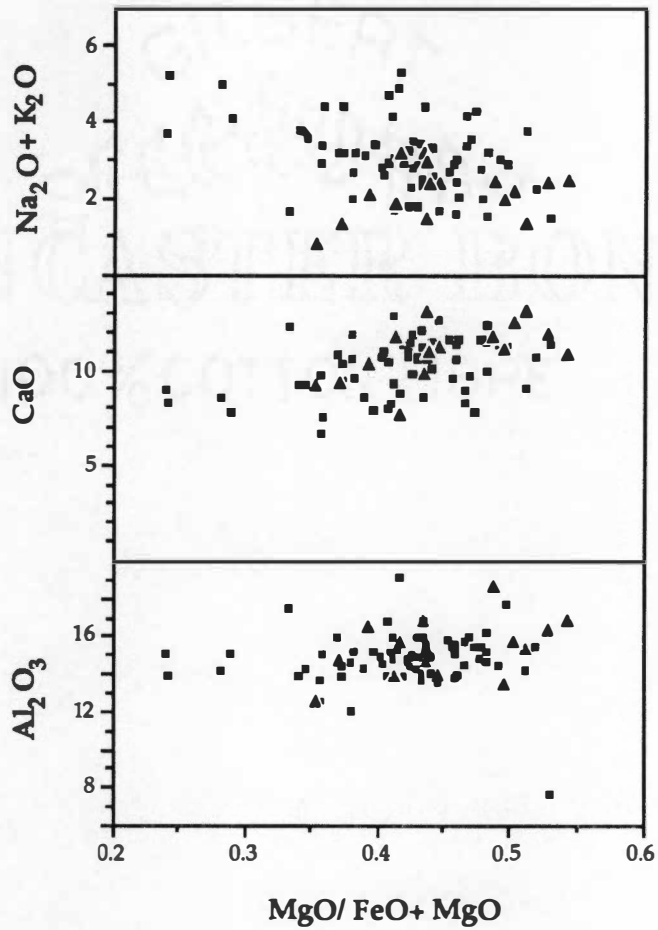
Figure 5.2: Harker diagrams plotting Mg# versus major an minor elements.
(Squares = Unit 2 amphibolites, triangles = Unit 3 amphibolites.) a.) Mg# vs. major
element oxides, b.) Mg# vs. minor elements.
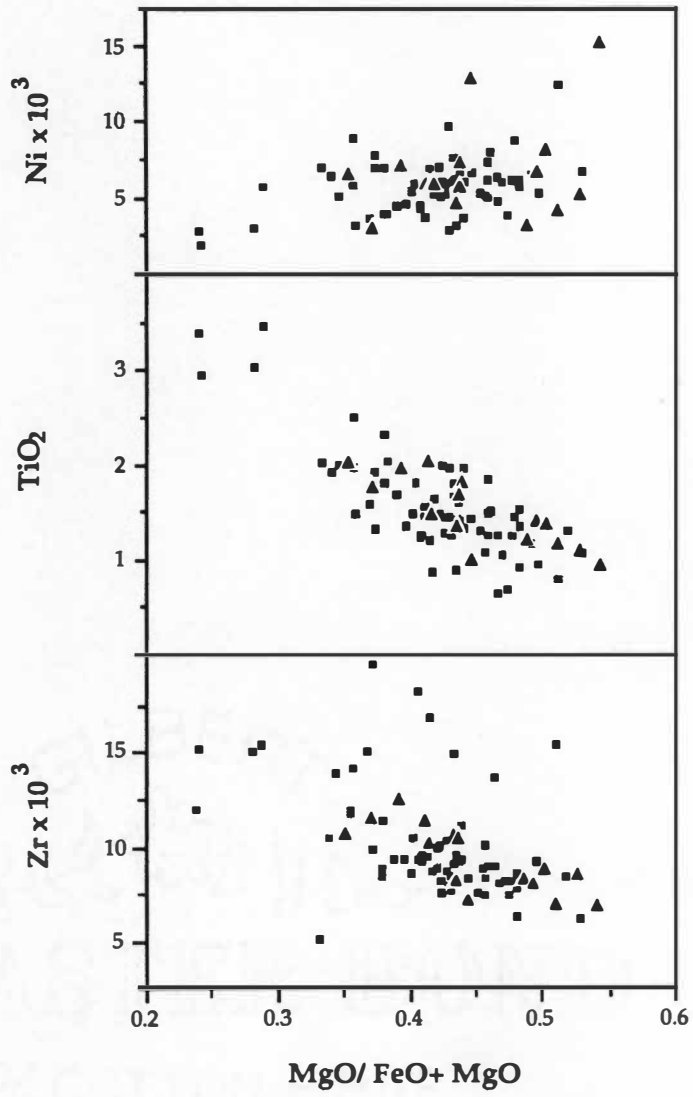
b)

Figure 5.2 (continued)
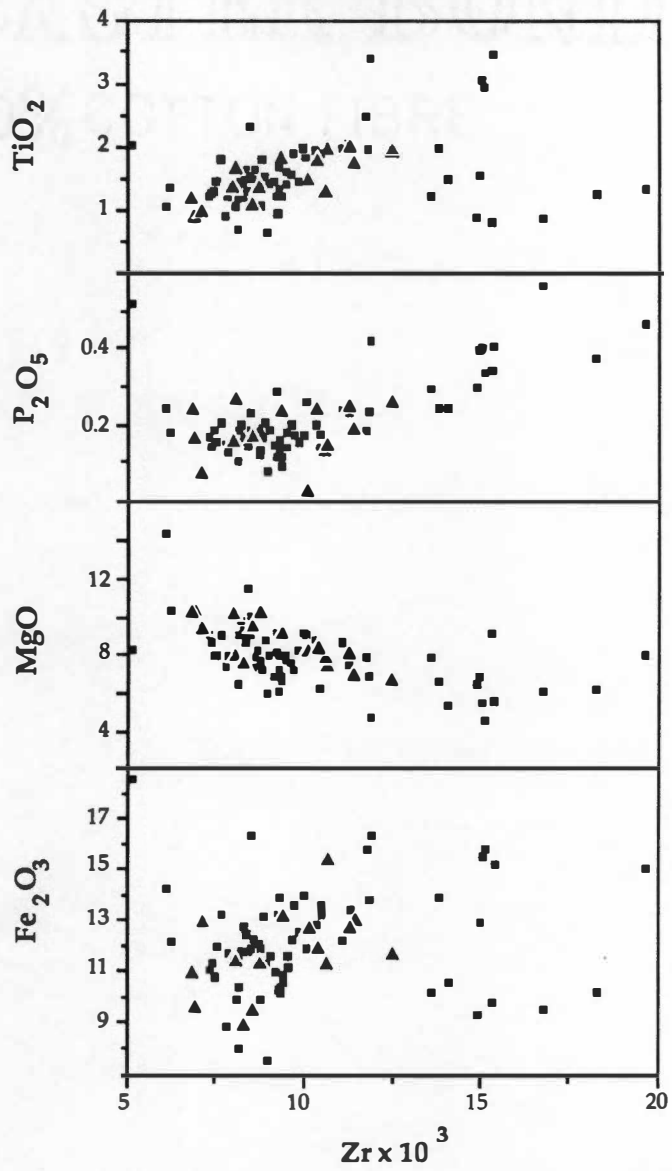
a)

Figure 5.3: Harker diagrams plotting Zr versus major and minor elements. (Squares = Unit 2 amphibolites, triangles = Unit 3 amphibolites.) a.) Zr vs. major element oxides, b.)Zr vs. minor and trace elements.

121
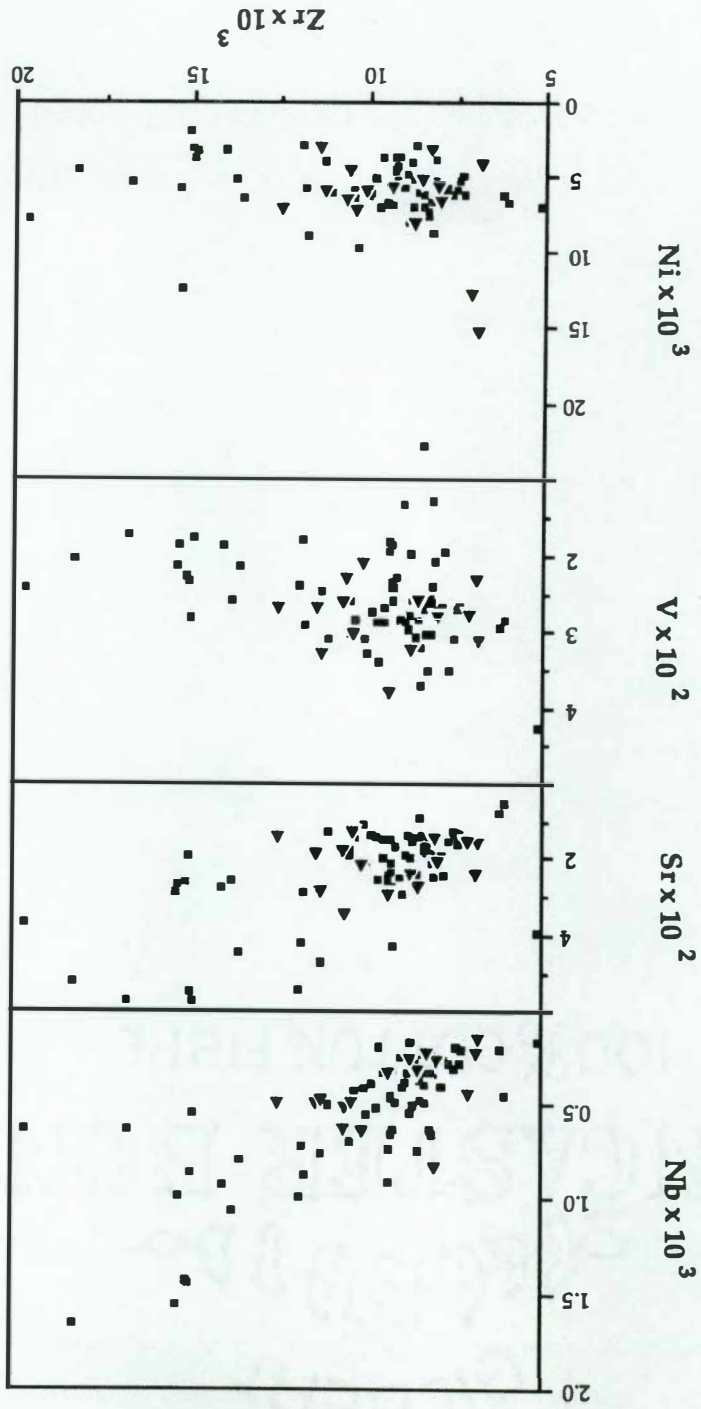
oxides, MgO and P_2O_5 produce the most distinct trends. P_2O_5 increases while MgO decreases. Trace and minor elements show only vague igneous trends using Zr as the fractionation index.

An interesting relationship exists for trends of Fe_2O_3 vs. Zr and TiO_2 vs. Zr. Initially they both undergo an increase, then seem to reach a maximum at approximately Zr = 0.0125, and finally undergo a sharp decrease with further fractionation. This relationship may be indicative of an igneous process in which these components initially have a relatively low distribution coefficient, but only until a phase such as ilmenite ($FeTiO_3$) or titanomagnetite (Fe_2TiO_4) begins to crystallize. An Fe- and Ti-bearing phase may have entered the fractionation sequence, at which point Fe and Ti suddenly become compatible and begin to be depleted. This scheme, albeit hypothetical, would reasonably account for the initial increase and following decrease in both Fe_2O_3 and TiO_2.

ELEMENT MOBILITY

From the considerable amount of scatter present on some of the Harker plots previously shown, it is clear that there has been varying degrees of element mobilization before and/or during metamorphic recrystallization of these rocks. If exposed on the sea floor, the initial basalts may have been altered by hydrothermal activity and converted to spilite. Spilitization tends to alter the amounts of SiO_2, FeO, CaO, Na_2O, Cu, Co, Ni, and H_2O from the original basaltic composition (Best, 1982).

The elements Ca, Na, and K are also mobile during low grade metamorphism (Pearce and others, 1977). It has been suggested that elements are most susceptible to mobilization below upper greenschist facies conditions. Element mobility beyond these conditions would be hampered because interstitial fluids would have been completely driven out of the system (Hatcher and others, 1984). As regional metamorphism above upper greenschist facies, element mobilization probably occurs at a much more reduced rate due to kinetic limitations imposed by the lack of H_2O.

Rock and others (1985) emphasized that there can be extensive chemical exchange between metabasalts and their host rocks. Chemical exchange between metabasalt and country rock could be a very important process for amphibolites from this study because they often occur as thin (typically 5-10 cm thick) layers, stringers, and boudins within a host of biotite gneiss or metasandstone. In these cases, the scale of exchange is small enough so that alteration of perhaps the entire lens of amphibolite is very possible.

123

Cations that are the least mobile during various alteration processes tend to be "high field-strength" cations (Shervais, 1982). High field-strength cations have a small ionic radius and a high charge/radius ratio. These elements (Zr, Hf, Ti, P, Nb, and Ta) tend to be strongly incompatible and relatively immobile. Of this group, only Zr, Ti, and P occur in high enough concentrations to be useful in discriminating between basalt types based on trace element geochemistry. Most of the tectonic discrimination diagrams in the following section rely on high field-strength elements to characterize original basalt types.

TECTONIC DISCRIMINATION OF METABASALTS

Chemical discrimination of basalt types has been developed and used extensively for nearly two decades (Miyashiro and Shido, 1975; Pearce, 1976; Pearce and Cann, 1973; Pearce and Norry, 1979; and Shervais, 1982). These discrimination schemes are, for the most part, based on empirical observation of clear chemical differences between modern, pristine basalts originating in known tectonic regimes. Tectonic discrimination diagrams have proven very useful for characterizing mafic volcanic rocks that are no longer in their original tectonic setting. This technique use has been successfully extrapolated to metamorphosed equivalents of basalt in the southern Appalachians (Petty, 1982; Eggers, 1983; Hatcher and others, 1984; Conte, 1986; Brewer, 1986). Several discrimination diagrams will be used here to characterize the tectonic origin of amphibolites observed in the study area.

Tectonic discrimination diagrams were developed for non-cumulative mafic lavas and should only be used for these types of rocks. Most discriminant schemes require that samples be within a compositional range of 12%< [CaO + MgO] >20% (Pearce and Cann, 1973; Pearce, 1976). This chemical screen is meant to remove metabasalt samples that contain a significant proportion of cumulate minerals. The [CaO + MgO] screen was applied to all amphibolite samples analyzed for this study and this screening process reduced the sample population from 90 to 51.

Pearce and others (1975) suggested the ternary plot of TiO_2 vs K_2O vs P_2O_5 as an effective discrimination diagram to distinguish oceanic from non-oceanic lavas. This diagram was used for amphibolite samples from both Unit 2 and Unit 3 (Fig. 5.4).
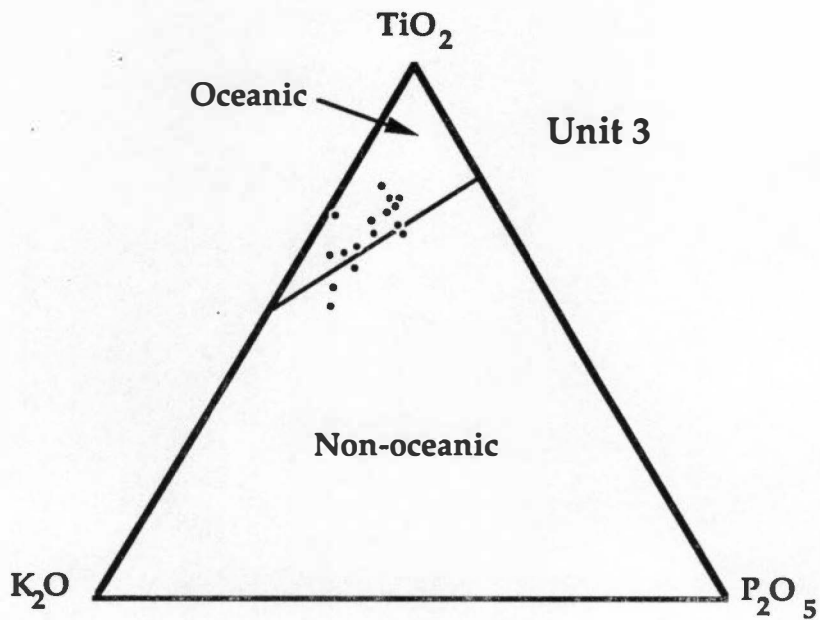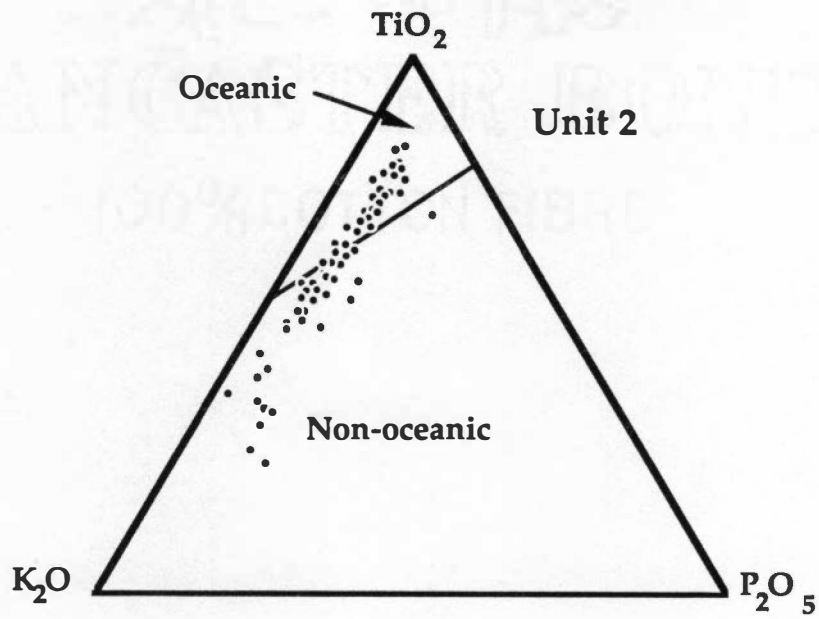
Figure 5.4: Ternary plot of K₂O vs. TiO₂ vs. P₂O₅ distinguishing oceanic from non-oceanic lavas. (After Pearce and others, 1975.)

Unfortunately, these data straddle the boundary between the oceanic and non-oceanic fields and indicate a trend toward K_2O enrichment. Pearce and others (1975) suggested that enrichment in K_2O accompanies metamorphism and warned against data points migrating out of the oceanic field toward the K_2O apex for metamorphosed samples. Rock and others (1985) also observed that metabasites enclosed in psammites and granite-gneisses undergo a K and Rb gain due to exchanges with these country rocks. Consequently, the TiO_2-K_2O-P_2O_5 diagram does not necessarily distinguish two groups (oceanic and non-oceanic) of metabasalts in the study area.

Another ternary tectonic discrimination diagram developed by Pearce and Cann (1973) plots values of Ti/100 vs Zr vs Y∗3 (Fig. 5.5). Here, again, Unit 2 and Unit 3 amphibolite samples are separated. All data from Unit 3, and the bulk of the data from Unit 2, plot in the ocean floor basalt fields. Some data from Unit 2 occur in the within-plate and calc-alkaline basalt fields (fields D and C, respectively).

A Cartesian coordinate plot of Ti vs Zr (ppm values) is another discrimination diagram developed by Pearce and Cann (1973) (Fig. 5.6). Here, amphibolite sample data from both Unit 2 and Unit 3 are superposed on the same plot with separate symbols distinguishing them. On this diagram the bulk of the amphibolites (including all samples from Unit 3) plot in the ocean floor basalt field. Another group of samples occur well within the calc-alkaline basalt field suggesting an apparent arc affinity. A significant group of samples from Unit 2 occur above all tectonic fields because they have very high Ti values (above 14,000 ppm).

A large group of samples plot as ocean floor basalts (MORB field) on a discriminant plot of Zr/Y vs Zr (Pearce and Norry, 1979) (Fig. 5.7). The IAT (island arc tholeiite) field significantly overlaps the MORB field here and no samples showing unequivocal arc affinity are separated. Only two samples that plot as WPBs here coincide with the within-plate group separated in Fig. 5.5. Interestingly, the remaining points from the within-plate group in Fig 5.7 plot as calc-alkaline basalts in Fig.5.5. The bulk of the samples, again, fall into the ocean floor basalt field, including all but one of the samples from Unit 3.

Finally, a discriminant diagram plotting the compatible element Cr against the FeO/ MgO ratio (Miyashiro and Shido, 1975) is shown in Fig. 5.8. Most of the samples are characterized here as ocean floor ("abyssal") tholeiites. A group of 12 samples are separated as arc basalts. Only three of this group coincide with the arc group in Fig. 5.5, and only two of these three are characterized as arc basalts in Fig. 5.6.

Most of the samples that fall in non-oceanic fields in the above tectonic discrimination diagrams do not show a consistent affinity for a specific tectonic regime in
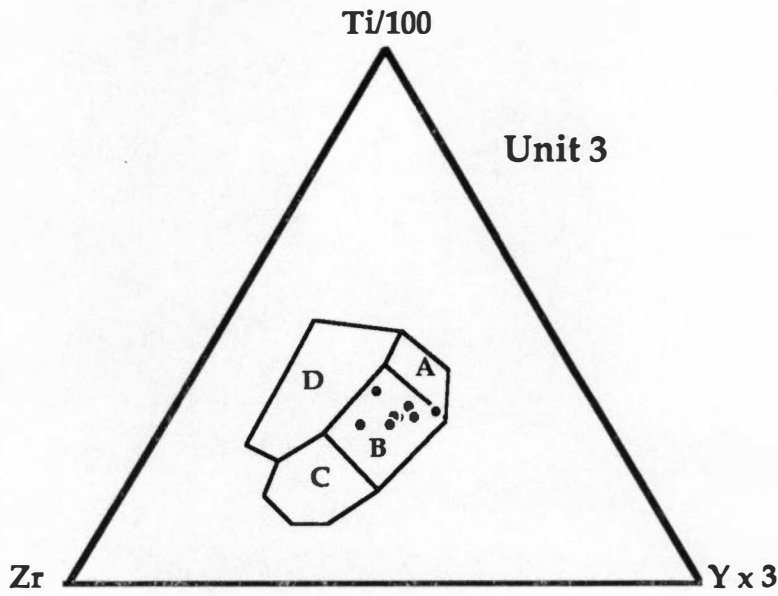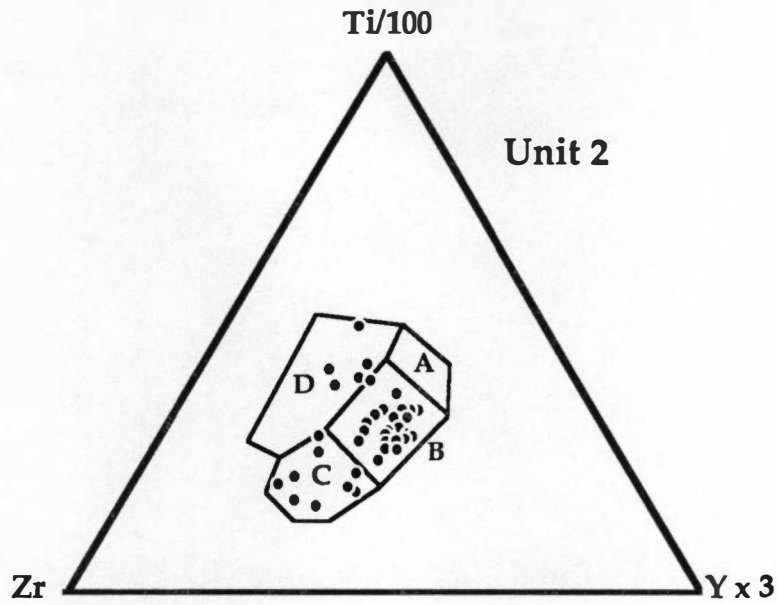
Figure 5.5: Ternary plot of Zr vs Ti/100 vs Y*3 distinguishing low-K tholeiites (field A), ocean floor basalts(field B), calc-alkaline basalts (field C), and within-plate basalts (field D). (After Pearce and Cann, 1973.)

127
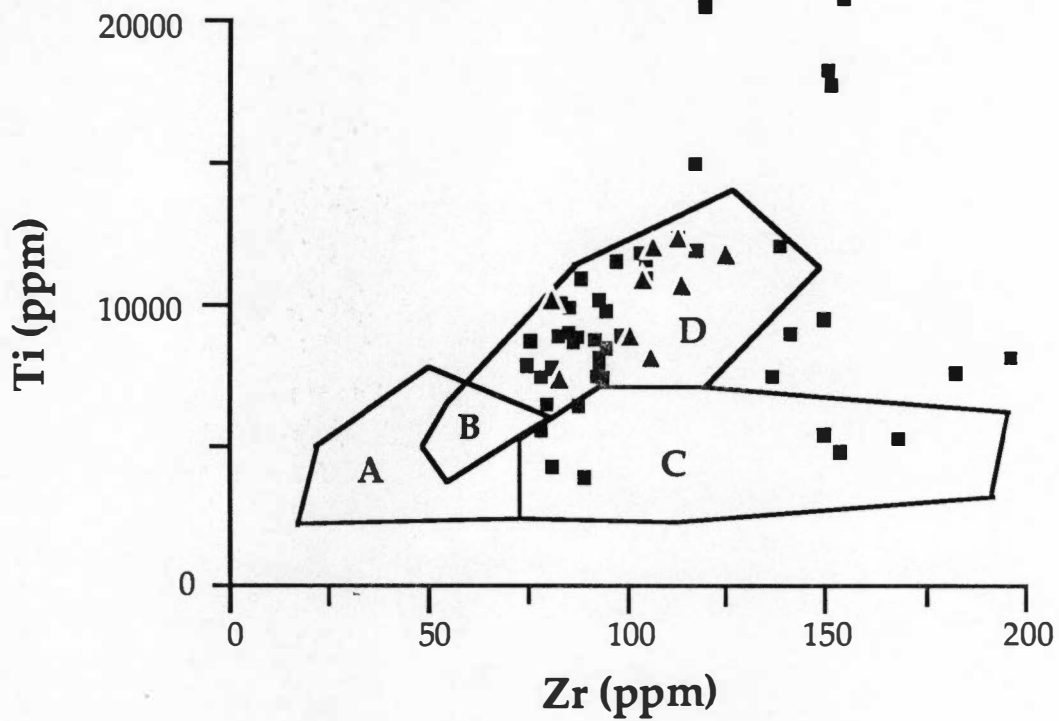
Figure 5.6: Tectonic discrimination diagram plotting Ti vs Zr. Fields A and B are low-K tholeiites, fields C and B are calc-alkaline basalts, and fields D and B are ocean floor basalts. (Squares = Unit 2 amphibolites, triangles = Unit 3 amphibolites. After Pearce and Cann, 1973.)

128
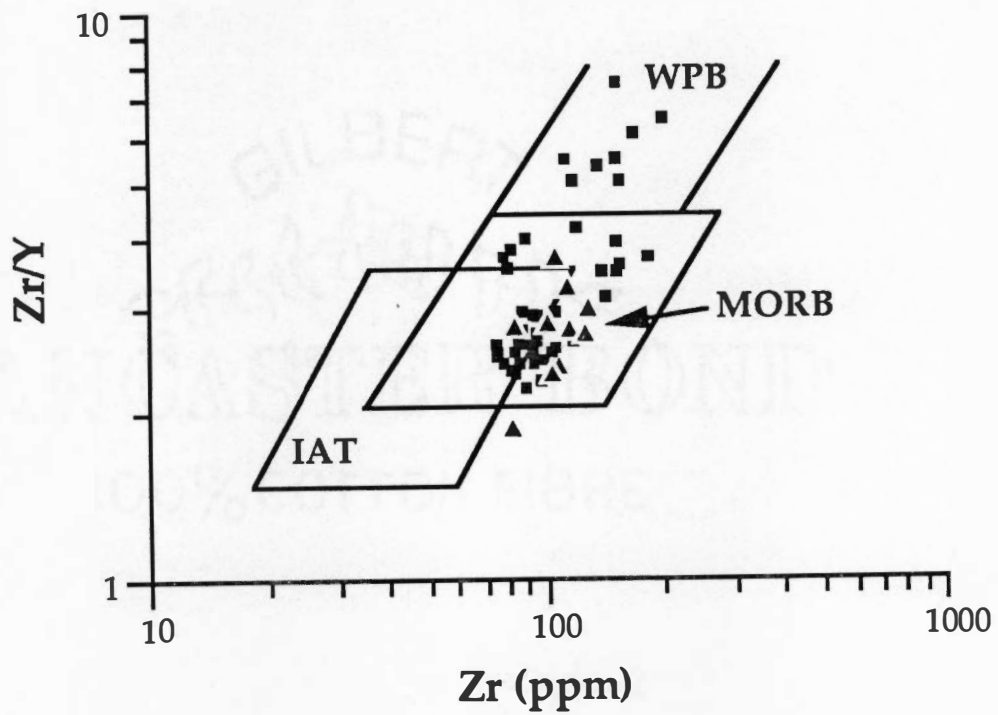
Figure 5.7: Plot of Zr/Y ratio vs Zr distinguishing between WBP (within plate basalts), MORB (mid-ocean ridge basalts), and IAT (island arc tholeiites). (Squares = Unit 2 amphibolites, triangles = Unit 3 amphibolites. After Pearce and Norry, 1979.)
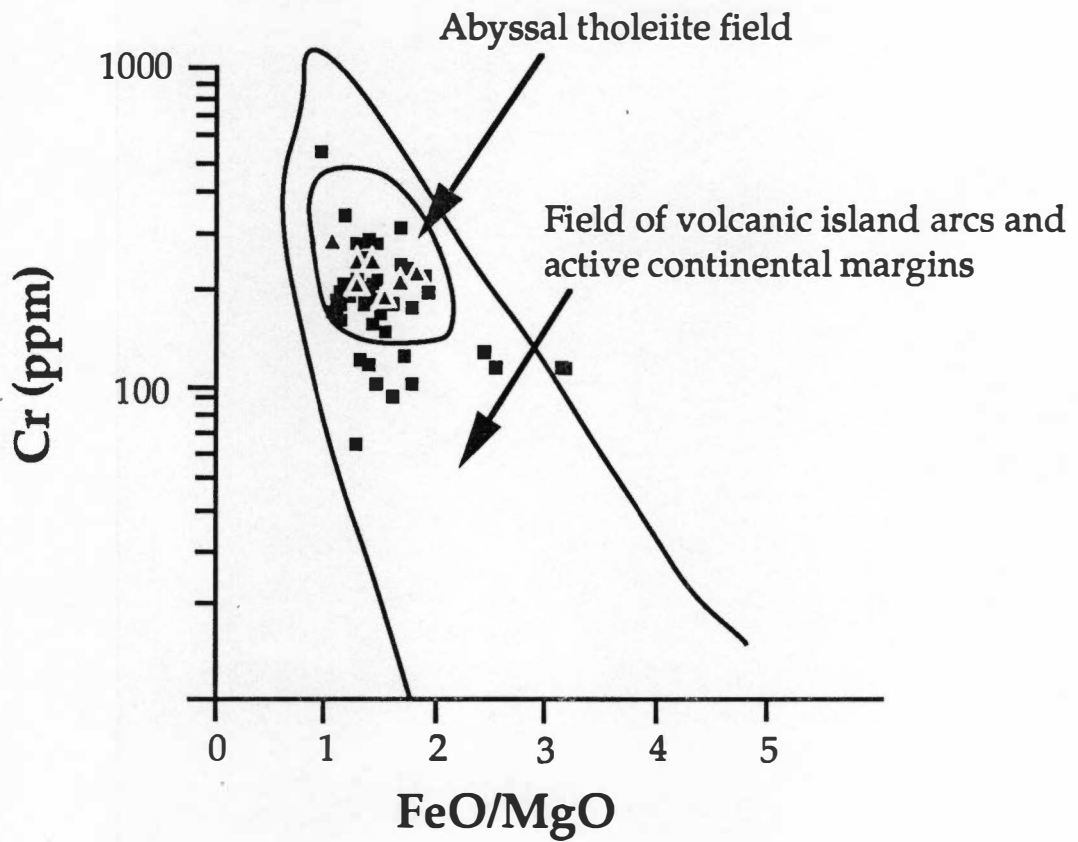
Figure 5.8: Plot of Cr vs the FeO/MgO ratio distinguishing between ocean floor (abyssal) tholeiites and arc/active margin basalts. (Squares = Unit 2 amphibolites, triangles = Unit 3 amphibolites. After Miyashiro and Shido, 1975.)

every discriminant plot used. Table 5.1 is a compilation of samples that consistently fall in non-oceanic basalt fields and clarifies in which field they fall for each of the corresponding diagrams. The occurrence of many samples in both arc and within-plate fields depending on the tectonic discrimination diagram used indicates a problem. Quite a few samples that are characterized as arc lavas by two or three diagrams often plot as within-plate basalts on Fig. 5.7. The lack of consistency leads me to conclude that many of these non-oceanic settings are not accurate characterizations. Many may, in fact *be* non-oceanic metabasalts, however, it is difficult to confidently place them in another category. It is also likely that this group of samples may have been altered to the degree that they were not accurately characterized by the discrimination diagrams. Additionally, no geographic correlation can be drawn from this group of non-oceanic metabasalts as the sample localities appear to be randomly scattered.

A significant majority of amphibolite samples are characterized by all tectonic discrimination diagrams as ocean floor basalts. Based on the preceding arguments, this is the only tectonic regime that can be unequivocally concluded from the set of amphibolite samples.

Table 5.1: A compilation of amphibolite samples that plot in fields other than "ocean floor basalt" fields in various tectonic discrimination diagrams. Decimal numbers refer to corresponding figure numbers.

OCCURRENCES IN NON-OCEANIC BASALT FIELDS

Sample Number	Arc Lavas	Within-Plate Basalts
SN1	5.8	
SN35	5.5	5.7
SN96A	5.5, 5.8	5.7
SN135A	5.8	
SN489A	5.8	5.5, 5.7
SN604	5.5, 5.6	
SN782	5.8	5.5
SN798	5.5, 5.6	5.7
SN802	5.5, 5.6, 5.8	5.7
SN811	5.5, 5.6, 5.8	
SN837	5.5, 5.6	
SN849	5.8	
SS5A	5.6	
SS63	5.8	5.5
SS67	5.8	
SS553	5.6	
SS548	5.5, 5.6, 5.8	5.7
GC4		5.5, 5.7
HZ33	5.5	5.7

VI. INTERPRETATIONS AND SYNTHESIS OF DATA

All data gathered for this study can be integrated into a comprehensive geologic history of the Sylva region. Many of the stratigraphic, structural, and tectonic ideas in this section have been influenced by previous work in the central and eastern Blue Ridge. For the most part, however, I have strived to develop my interpretations with a significant degree of objectivity.

STRATIGRAPHY AND REGIONAL CORRELATION OF LITHOTECTONIC UNITS

As detailed in Chapter 2, three lithotectonic units were recognized in the study area. All units are dominated by metasedimentary gneisses and schists and each unit is separated from the others by major faults. Stratigraphic and structural relationships are illustrated in Fig. 6.1.

UNIT 1

In the northern portion of the study area, massive to thickly bedded, feldspathic metasandstone is interlayered with sulfidic two-mica schist. Hadley and Goldsmith (1963) correlated similar rocks in the eastern portions of the Great Smoky Mountains National Park with the Great Smoky Group, a subordinate unit of the Ocoee Supergroup (King and others, 1958). Later geologic maps compiled for the region surrounding Sylva (North Carolina Geological Survey, 1985; Kish and others, 1975; Hadley and Nelson, 1971) have made the same correlation.

I agree with the previous correlations and have mapped Unit 1 as Great Smoky Group metasandstone and schist in the study area. Further subdivision of the Great Smoky Group into the subordinate components: Elkmont Sandstone, Thunderhead Sandstone, and Anakeesta Formation, was not possible due to structural complexity and transposition of the original stratigraphic relationships in the area. Unit 1 is most likely correlative mostly with the Thunderhead sandstone due to the predominance of metasandstone over schist. Although schist is commonly observed, it is not continuous or abundant enough to interpret the occurrence of the Anakeesta Formation within Unit 1. An alternative
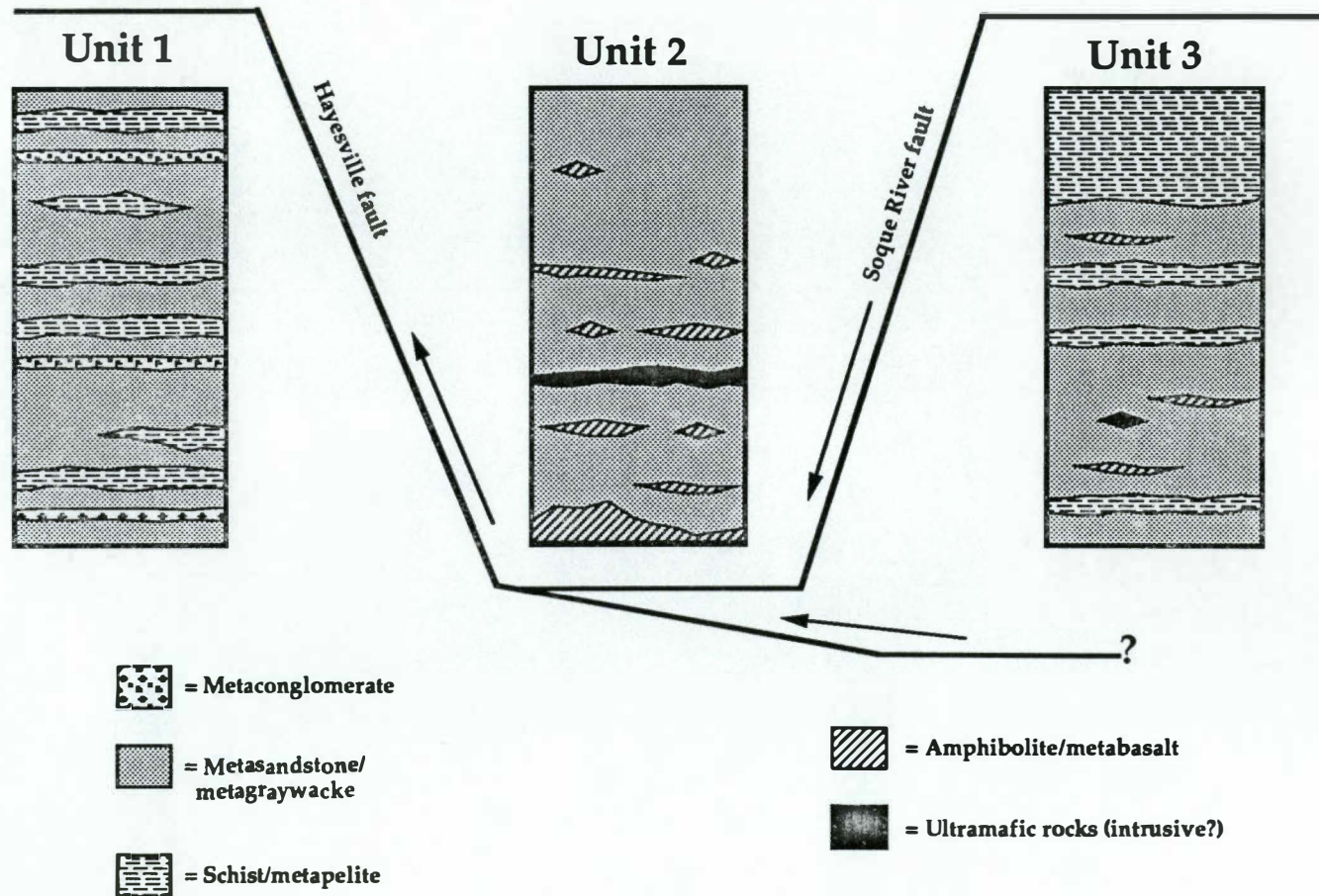
Figure 6.1: Simplified stratigraphic columns and structural relationships for the study area.

correlation for Unit 1 may be the Copperhill Formation that occurs to the south where the Great Smoky Group has been subdivided differently (Mohr, 1973).

Detailed petrographic analysis of Great Smoky metasandstone in the study area has indicated that protoliths ranged from graywacke to feldspathic quartzite (Fig 2.7b). This suggests that the sedimentary protolith was mostly a medium- to coarse-grained clastic sequence with variable proportions of clay-sized material. Fining-upward layers suggest the presence of turbidite sequences. Additionally, the abundant occurrence of schist as interlayers in the unit requires the presence of dominantly silt + clay beds in the original sedimentary sequence.

Infrequent occurrences of amphibolite in the Great Smoky sequence here indicate that it is not entirely a metasedimentary unit. One outcrop of amphibolite was observed in place, while other amphibolite occurrences were simply weathered float blocks. Fine-grained amphibolite interlayered in the metasedimentary sequence suggests that extrusive mafic flows (or shallow dikes and sills?) were included in the original depositional sequence prior to metamorphism. Since no chemistry was obtained from these deeply weathered amphibolites, a tectonic setting for the igneous precursors of Great Smoky amphibolite cannot be characterized.

UNIT 2

Unit 2, immediately southeast of the Great Smoky Group, is a heterogeneous assemblage of paragneiss including biotite gneiss, metagraywacke, amphibolite, and ultramafic rocks. The more mafic character starkly contrasts with the Great Smoky Group to the north and the Hayesville fault separates these two units. Unit 2 has been interpreted as either a basement paragneiss or a cover sequence. I have concluded, based on structural and metamorphic criteria, that Unit 2 is a cover sequence correlative with the Tallulah Falls Formation. The Tallulah Falls Formation has been mapped in the same structural and stratigraphic position to the south (Eckert and others, 1989; Hopson and others, 1989; McClellan, 1988; Hatcher and others, 1987).

Detailed petrographic analysis has determined that the protoliths for the metagraywacke units in the Tallulah Falls Formation here range from arkose to graywacke (Fig. 2.6c). The sedimentary classification of gneisses from Unit 2 (this study) is similar to modes obtained by Hatcher (1973) for the Tallulah Falls Formation in northeastern Georgia, northwestern South Carolina, and adjacent North Carolina (Fig. 6.2). Modal data for

135
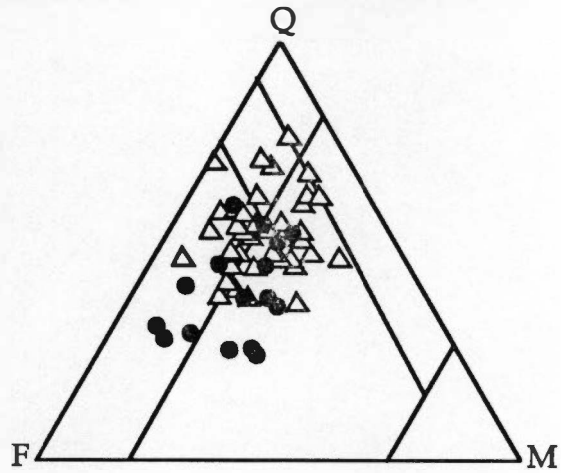
Δ = Moderate Grade Metasandstone

● = Migmatitic Biotite Gneiss

a.)
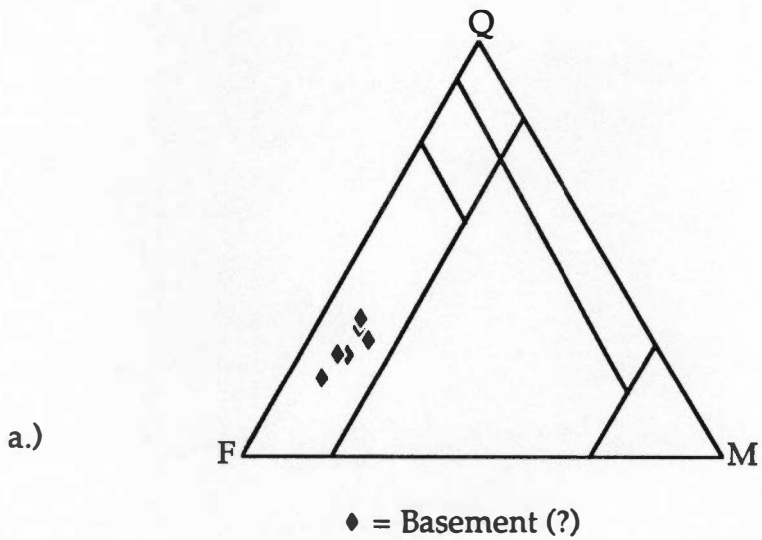
♦ = Basement (?)

Figure 6.2: Comparison of QFM modal mineralogy of Tallulah Falls Formation and basement (?) units with Unit 2. a.) Data from NE Georgia, NW South Carolina, and adjacent North Carolina (Hatcher, 1973); b.) Data from Unit 2 (this study). (Ternary boundaries after Pettijohn, 1954.)

136
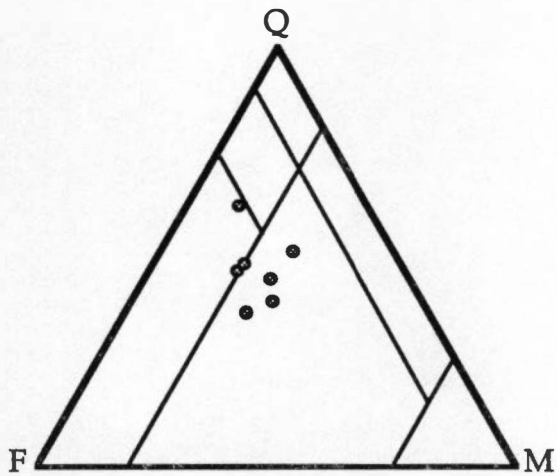
b.)

Figure 6.2 (continued)

Hatcher's "basement (?)" units are significantly more feldspathic than Tallulah Falls gneisses and metasandstones. The modal mineralogy of Unit 2 (this study) and Tallulah Falls Formation (Hatcher, 1973) is remarkably similar and is another line of evidence that correlation between the two is correct.

Abundant intercalated amphibolite occurs within the metasedimentary units of Unit 2. Amphibolite stringers, boudins, and pods are interpreted as mafic flows, dikes, and/or sills that were included in the sedimentary package prior to metamorphism and tectonic mobilization. Amphibolite geochemistry (see Chapter 5) has revealed that amphibolites from Unit 2 have trace element signatures indicative of oceanic basalts (MORBs). This fact suggests that Unit 2 was deposited on oceanic, or at least transitional, crust where lavas from a depleted mantle source were emplaced without significant crustal contamination.

More massive occurrences of amphibolite that are included in Unit 2 appear different than the thinner occurrences intercalated within biotite gneiss. Migmatitic veining patterns in these massive, map-scale amphibolites (Fig. 2.3) outline pillow-like amphibolite pods. This lithology has been interpreted by others as block-in-matrix mélange structures (part of the "Toe terrane" of Raymond and others, 1988). Raymond and others discussed a massive amphibolite exposure at Willits, North Carolina, (eastern edge of study area) as an example of a block-in-matrix mélange unit. There, the "matrix" appears to be mostly migmatitic gneiss and felsic leucosomes that surround the "blocks" of amphibolite. I believe that the podiform shapes of the amphibolite "blocks" are better interpreted as deformed mafic pillows indicative of submarine eruption of the protolith. In this interpretation, more massive amphibolite occurrences may represent slices of the upper portions of oceanic crust on which the Tallulah Falls Formation was deposited. Consequently, the massive amphibolite bodies are not considered to be mélange units.

The Webster-Addie ultramafic body has been interpreted as an originally tabular unit that has been folded by an open, upright, and doubly plunging antiform. The ultramafic body and the proximal bodies of massive amphibolite have been suggested as portions of a dismembered ophiolite (Quinn and Hatcher, 1990; Quinn, 1990). The Webster-Addie body could alternatively be interpreted as the cumulate basal layer of a layered mafic intrusion; but the lack of a contact metamorphic aureole at the margins raises serious doubts for this interpretation. The fact that the ultramafic rocks exhibit a distinct foliation (S_2-concordant) indicates that the body was present during regional metamorphism.

138

UNIT 3

The southeasternmost lithotectonic unit in the study area is mainly an assemblage of aluminous metasedimentary rocks with abundant intercalated amphibolite. Schist appears to increase in abundance at the top of the exposed section in the study area. Fining-upward sequences and monotonous repeating layers of metasandstone and schist suggest the presence of turbidite sequences. A small isolated ultramafic body was also discovered in Unit 3.

Unit 3 is similar to rocks mapped as the Otto Formation in southwestern North Carolina and northeastern Georgia (Hatcher, 1988) and I have correlated Unit 3 with the Otto Formation. The occurrence and contact relationships of the Otto Formation near Sylva, far northwest from where it was previously mapped (North Carolina Geological Survey, 1985; Hadley and Nelson, 1971) is perhaps one of the most significant discoveries of this study.

Petrographic analysis indicates that metasandstones in the Otto Formation have subgraywacke, graywacke, and feldspathic quartzite as protoliths (Fig. 2.7d). Modal variability for Otto Formation metasandstones may reflect variable proportions of argillaceous material in the original protoliths.

The presence of abundant amphibolite, and one occurrence of an ultramafic body, in the Otto Formation suggests deposition on oceanic or transitional crust. Trace element chemistry for Otto Formation amphibolites indicates that they have oceanic basalt signatures and were probably emplaced into the sedimentary package as flows, dikes or sills.

STRUCTURAL AND METAMORPHIC HISTORY

Evidence gathered for this study suggests that faulting on the Hayesville and Soque River faults preceded the metamorphic peak. It is postulated that all units were tectonically juxtaposed prior to or during the earliest stages of penetrative deformation and peak metamorphism.

DEFORMATION

The earliest stages of deformation recognized in the study area are recorded by ductile behavior and isoclinal flowage folding. Transposition of primary stratigraphic layering occurred to produce an S_1 foliation. This surface was later transposed again into

parallelism with F_2 isoclinal folds, producing S_2 foliation. During both D_1 and D_2, the rocks deformed plastically producing tight to isoclinal flexural flow folds. F_1 and F_2 folds mostly trend NE and are upright to recumbent. More competent amphibolite layers were stretched and boudined in the plane of foliation. Migmatitic layering is deformed by F_1 and F_2 folds, indicating the rocks were at or near their melting point prior to (or during) these deformational episodes.

Features developed during intermediate-stage deformation, unlike those developed in the early stages, begin to show the influence of rheologic contrasts between different layers in gneisses. This lead to the development of polyharmonic flexural flow folds and tight similar folds in addition to passive flow folds (F_3). F_3 folds trend NE, are generally upright, and have NW vergence. Boundinage of competent layers continued during intermediate-stage deformation.

Late-stage deformational features indicate that the rocks had a low mean ductility (i.e., the rocks were essentially rigid). Late-stage folds are dominantly tight crenulations (F_4) and open to gentle flexural slip and flexural flow folds (F_5 and F_6). Rheological contrasts between schist and metasandstone allowed for the development of flexural flow folds. Late-stage, open folds that trend W-NW may be F_6 folds. Doming of the Webster-Addie structure appears to have been late-stage, perhaps due to interference of F_5 and F_6 folds.

Evidence for large-scale faulting on major tectonic boundaries in the study are is not well-exhibited by mesoscopic structures. Variably annealed mylonites have been found close to lithologic and tectonic boundaries, but are also located in areas far removed from them (similar to observations of Merschat and Weiner, 1988). Since large-scale faulting preceded peak metamorphism and early-stage deformation, mylonites produced in the fault zones probably have not survived in great abundance. Mylonites observed in the study area are regarded as both products of localized shearing, and large-scale tectonic transport. Simple shearing episodes that produced mylonites occurred over a long history, which is reflected by different degrees of annealing.

The mechanisms of deformation have been traced through a progression of changes as deformational history of the area was worked out. Deformation mechanisms interpreted from the geometry of structures primarily reflect the prevailing temperature and how rheologies varied between layers of different composition. Mean ductility and ductility contrast decrease in each successive deformational stage indicating discrete deformational episodes recorded at different times during cooling from the metamorphic peak and possibly later deformation, associated with Alleghanian convergence and mobilization of the Blue Ridge-Piedmont crystalline thrust sheet.

METAMORPHISM

The thermal metamorphic peak probably coincided with migmatization because, at that time, the rocks were at or near the melting temperature of quartz + alkali feldspar (Fig. 4.2). Metamorphic intensity culminated in the kyanite and sillimanite zones in the study area. Different structural levels exposed in the study area control which metamorphic zone is exposed (i.e., deeper levels are kyanite zone, shallower levels are sillimanite zone)(Fig. 4.1).

Several samples from the Otto Formation show the textural relationship where kyanite is included in garnet. This indicates that garnet growth either continued beyond the metamorphic peak or that a later prograde metamorphic pulse overprinted the first. Compositional and textural evidence does not indicate that a second metamorphic pulse (as high as garnet grade) has occurred. I, therefore, conclude that garnet growth continued beyond the metamorphic peak. The presence of both kyanite and sillimanite Al_2SiO_5 polymorphs in many pelitic rocks is indicative of a clockwise P-T path, first through the kyanite zone, and then into the sillimanite zone (with the metastable persistence of kyanite) during regional metamorphism (Fig. 6.3). This hypothesis is also supported by another petrographic texture in a schist from the Otto Formation where kyanite is included in garnet and sillimanite occurs in the matrix.

Thermobarometric calculations have allowed me to quantify some of the conditions of metamorphism. Most P-T estimates were obtained using garnet rim compositions and, thermodynamically, these pressures and temperatures would be the most reliable when considering chemical exchange between garnet, matrix biotite, and matrix plagioclases. These P-T conditions, however, are probably not metamorphic peak conditions, but represent a later portion of the P-T path because garnets show retrograde zoning (higher Fe/Mg ratios) at their rims. P-T conditions calculated using garnet core compositions yield higher temperatures and pressures and may be used to approximate conditions of the metamorphic peak. If this is the case, then a portion of the P-T path (cooling from peak conditions) can be quantified using P-T conditions calculated from both garnet rims and cores (Fig. 6.3).

Unfortunately there is a significant difference in P-T estimates calculated for pelites in Units 1 and 3 and gneisses and amphibolites of Unit 2. It may be that rocks in Unit 2 have preserved metamorphic peak conditions while rocks in Units 1 and 3 have preserved retrograde conditions. A different metamorphic evolution for Unit 2 is highly unlikely since the faults in the study area are confidently regarded as premetamorphic structures.

141
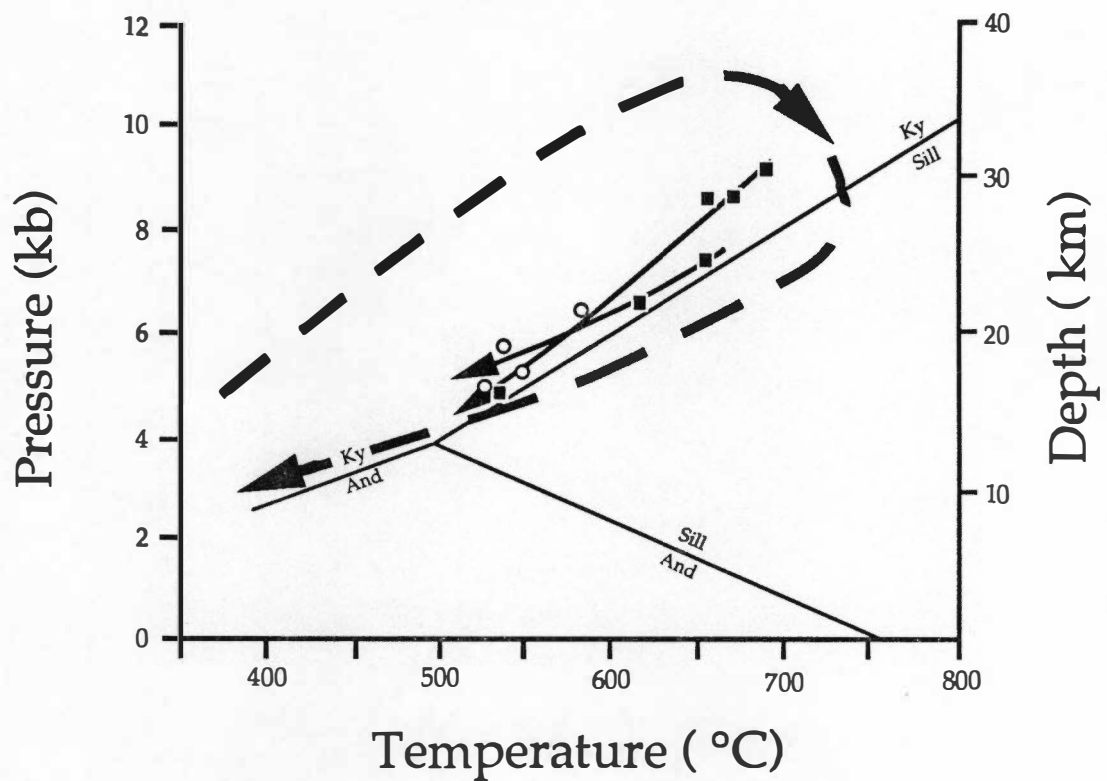
Figure 6.3: A clockwise loop in P-T space is interpreted from textures indicative of early kyanite followed by later sillimanite. Trajectories paralleling the down-temperature portion of the P-T loop are quantified by thermobarometry. Squares represent P-T conditions calculated using garnet core compositions, circles represent P-T conditions calculated using garnet rim compositions.

Late-stage retrograde metamorphism has also been recorded in some samples. Chlorite replacement of biotite and garnet and fractures filled with chlorite + biotite indicate retrograde metamorphism attained chlorite, and possibly biotite grade. This retrograde event could be associated with Acadian metamorphism.

TECTONIC SYNTHESIS

MIDDLE PROTEROZOIC
(1600-900 Ma)

(1) Grenville orogeny and amalgamation of the Laurasian supercontinent. Formation of Laurentian basement.

(2) Erosion and unroofing of high-grade Laurentian basement.

LATE PROTEROZOIC – EARLY PALEOZOIC
(750-500 Ma)

(3) Break-up of the Laurasian supercontinent and development of fault-bounded rift basins on Laurentian margin.

(4) Ocoee Supergroup sedimentation fills rift basins on continental shelf. Offshore sedimentation of the Otto Formation on transitional or oceanic crust. More distal sedimentation of the Tallulah Falls Formation on oceanic crust. Mafic igneous rocks are emplaced in greater abundance in more distal stratigraphic assemblages.

(5) Opening of the Iapetos ocean ceases and an oceanward-dipping subduction zone develops. Convergence and subduction begins to consume the Iapetan ocean basin.

TACONIC OROGENY
(500-400 Ma)

(6) Collision and accretion of eastern Blue Ridge-Piedmont terrane. Tallulah Falls Formation thrust onto Otto Formation and these, as a composite block, are thrust upon the continental margin.

(7) High grade metamorphism is coupled with early-stage ductile deformation in all units. Development of S_1 foliation, metamorphic differentiation, and migmatization produces a distinct compositional layering. This layering is later transposed to form S_2 foliation.

(8) Cooling from metamorphic peak. Intermediate stage deformation (?).

ACADIAN OROGENY
(400-300 Ma)

(9) Closure of the Iapetos ocean and docking of Avalon terrane to the east.

(10) Intermediate-stage (?) deformation. Regional metamorphism only attains chlorite-biotite grade for rocks in the study area.

ALLEGHANIAN OROGENY
(300-250 Ma)

(11) Closure of the Theic-Rheic ocean and collision of North America and Africa.

(12) Detachment of a massive composite crystalline thrust sheet (Type 5) (Hatcher and Williams, 1986) and cratonward tectonic transport over the continental shelf. Localized doming of the crystalline sheet occurs as underlying duplexes develop.

(13) Late stage deformation affects rocks in the study area.

(14) Mesozoic extension splits Pangea and North America and Africa separate. The Atlantic ocean basin forms.

144

(15) Tectonic stabilization and isostatic adjustment of eastern North America. Erosion of the Appalachian mountain chain.

VII. CONCLUSIONS

(1)

The study area has been divided into three lithotectonic units. Unit 1 is part of the Great Smoky Group (entirely Thunderhead Sandstone?) and is comprised of feldspathic metaquartzite and metagraywacke interlayered with subordinate aluminous schist. Unit 1 is bounded on the south by the Hayesville fault.

Unit 2, immediately south of the Hayesville fault, is correlated with the Tallulah Falls Formation, a sequence of feldspathic metagraywacke, biotite gneiss, and interlayered amphibolite. Unit 2 also contains large masses of amphibolite and ultramafic rock that are not considered part of the Tallulah Falls stratigraphic sequence.

Unit 3, to the south, is an assemblage of aluminous metagraywacke, feldspathic metaquartzite, aluminous schist, and interlayered amphibolite and these rocks are correlated with the Otto Formation. A minor ultramafic body is also present in Unit 3. Unit 3 is separated from Unit 2 by the Soque River fault.

(2)

Unit 1 was deposited in a Late Proterozoic rift basin as a thick clastic sequence of marine turbidites. Sediments were primarily derived from the Laurentian craton.

Unit 3 was also deposited as a sequence of marine turbidites, but in a more distal rift basin, on more attenuated crust. Sediments were mostly derived from the Laurentian craton. Mafic lava flows, dikes, and sills were deposited with, and intruded the sequence.

Unit 2 was deposited as a sequence of marine turbidites on transitional or oceanic crust. Sediments were probably derived from the Laurentian craton and from an oceanward arc or microcontinent. Mafic lava flows, dikes, and sills were deposited with, and intruded the sequence.

(3)

Faulting on both the Hayesville and Soque River faults was prior to peak Paleozoic metamorphism. The Soque River fault involves thrusting of Unit 2 over Unit 3. These units, as a composite block, were later thrust upon Unit 1 on the Hayesville fault.

(4)

The study area is structurally complex. Six separate fold generations were recognized. Early-stage folding (F_1 and F_2) are isoclinal flowage folds that involved

transposition of a preexisting layering and development of a regionally penetrative foliation. Intermediate-stage folds are tight passive flow to flexural flow folds indicating that rheologic contrasts developed as the rock masses cooled. Late-stage folds are open flexural flow and flexural slip buckle folds indicating that the rocks behave more rigidly and had cooled still further.

(5)

One major regional metamorphism affected the rocks in the study area and is associated with the Taconic orogeny. Rocks in the study area underwent medium-pressure facies series metamorphism, ultimately attaining kyanite-sillimanite grade in the amphibolite facies. The sillimanite isograd has been domed in the study area exposing higher pressure (kyanite grade) rocks in the center. Textural relationships indicate that garnet growth continued well after the regional metamorphic peak. In samples containing both kyanite and sillimanite, kyanite appears to be the earlier phase, indicating a clockwise PT path. Retrograde metamorphism in the chlorite-biotite zone may be associated with Acadian regional metamorphism.

(6)

Thermobarometric calculations using various published mineral equilibria indicate that Unit 2 has preserved more severe metamorphic conditions than those calculated for Units 1 and 3. Metamorphic conditions recorded by rocks from Unit 2 were 675–750°C and 8.5–9.5 kb. Metamorphic conditions recorded by rocks in Units 1 and 3 were 550–650°C and 5.0–6.5 kb.

(7)

Geochemistry of amphibolite rocks occurring in Units 2 and 3 indicates that they were originally mafic igneous rocks. Trace element abundances indicate that amphibolites originated as ocean floor basalts. This suggests that Units 2 and 3 were deposited in a tectonic regime in which lavas from a depleted mantle source could be tapped and emplaced without significant crustal contamination.

References Cited

Barrow, G., 1893, On an intrusion of biotite-muscovite gneiss in the south-east Highlands of Scotland and its accompanying metamorphism: Geological Society of London Quarterly Journal, v. 49, p. 330-358.

Best, M. G., 1982, Igneous and metamorphic petrology: New York, W. H. Freeman and Co., 630 p.

Blundy, J. D., and Holland, T. J. B., 1990, Calcic amphibole equilibria and a new amphibole-plagioclase geothermometer: Contributions to Mineralogy and Petrology, v. 104. p. 208-224.

Brewer, R., 1986, Structure and petrography of the basement complexes east of the Hot Springs Window, Blue Ridge province, western North Carolina: Unpublished M.S thesis, University of Tennessee, Knoxville, 196 p.

Butler, J. R., 1972, Age of Paleozoic regional metamorphism in the Carolinas, Georgia, and Tennessee southern Appalachians: American Journal of Science, v. 272, p. 319-333.

Carpenter, J. R., 1968, Apparent retrograde metamorphism: Another example of the influence of structural deformation on metamorphic differentiation: Contributions to Mineralogy and Petrology, v. 17, p 173-186.

Carpenter, R. H., 1970, Metamorphic history of the Blue Ridge Province of Tennessee and North Carolina: Geological Society of America Bulletin, v. 81, p. 749-762.

Condie, K. C., and Madison, J. A., 1969, Compositional and volume changes accompanying progressive serpentinization of dunites from the Webster-Addie ultramafic body, North Carolina: American Mineralogist, v. 54, p. 1173-1179.

Connelly, J. B., and Dallmeyer, R. D., 1991, Polymetamorphic evolution of the western Blue Ridge, Tennessee and North Carolina: Evidence from $^{40}Ar/^{39}Ar$ ages: Geological Society of America Abstracts with Programs, v. 23, p. 18.

Conte, J. A., 1986, Geochemistry and tectonic significance of amphibolites within the Precambrian Ashe Formation, northwestern North Carolina: Unpublished M.S thesis, University of Tennessee, Knoxville, 122 p.

Cox, K. G., Bell, J. D., and Pankhurst, R. J.,1979, The interpretation of igneous rocks: London, George Allen & Unwin Publishers Ltd., 450 p.

Cronin, T. P., 1883, Petrogenesis of the Webster-Addie ultramafic body, Jackson County, North Carolina: Unpublished MS thesis, University of Tennessee, Knoxville, 112 p.

Dallmeyer, R. D., 1975, Incremental $^{40}Ar/^{39}Ar$ ages of biotite and hornblende from retrograded basement gneisses of the Blue Ridge: Their bearing on the age of Paleozoic metamorphism: American Journal of Science, v. 275, p. 444-460.

Dallmeyer, R. D.,1988, Late Paleozoic tectonothermal evolution of the western Piedmont and eastern Blue Ridge, Georgia: Controls on the chronology of terrane accretion and transport in the southern Appalachian orogen: Geological Society of America Bulletin, v. 100, P. 702-713.

Dallmeyer, R. D., Wright, J. W., Secor, D. T., Jr., and Snoke, A. W., 1986, Character of the Alleghanian orogeny in the southern Appalachians: Part II. Geochronological constraints in the tectonothermal evolution of the eastern Piedmont in South Carolina: Geological Society of America Bulletin, v. 97, p. 1329-1344.

Deer, W. A., Howie, R. A., and Zussman, J., 1966, An introduction to the rock-forming minerals: New York, John Wiley & Sons, 528 p.

De Windt, J. T., 1975, Geology of the Great Smoky Mountains, Tennessee and North Carolina, with road log for field excursion, Knoxville-Clingman's Dome-Maryville: Compass, v. 52, p. 73-129.

Donath, F. A., and Parker, R. B., 1964, Folds and folding: Geological Society of America Bulletin, v. 75, p. 45-62.

Eckert, J. O., 1984, Stratigraphy, structure, and metamorphism in the east half of the Wayah Bald quadrangle, North Carolina: Key to Paleozoic granulite facies metamorphism in the southern Appalachians: Unpublished M.S. thesis, University of South Carolina, Columbia, South Carolina, 411 p.

Eckert, J. O., Hatcher, R. D., Jr., and Mohr, D. W., 1989, The Wayah granulite-facies metamorphic core, southwestern North Carolina: High-grade culmination of Taconic metamorphism in the southern Blue Ridge: Geological Society of America Bulletin, v. 101, p. 1434-1447.

Edelman, S. H., Liu, A., and Hatcher, R. D., Jr., 1987, The Brevard zone in South Carolina and adjacent areas: An Alleghanian orogen-scale dextral shear reactivated as a thrust fault: Journal of Geology, v. 95, p. 793-806.

Eggers, M. R., 1983, Petrology, structure, and geochemistry of the Kimsey Bald mafic complex, North Carolina: M.S. thesis, Florida State University, Tallahassee, 72 p.

Eskola, P., 1939, Die metamorphen Gesteine, "Die Entstehung der Gesteine": Berlin, Springer, p. 263-407.

Ferry, J. M., and Spear, F. S., 1978, Experimental calibration of the partitioning of Fe and Mg between biotite and garnet: Contributions to Mineralogy and Petrology, v. 66, p. 113-117.

Gillon, K. A., 1989, Geologic compilation of a portion of the western and eastern Blue Ridge tectonic province, Georgia and North Carolina: Georgia Geological Society Guidebook, v. 9, plate 1.

Glover, L., III, Speer, A., Russell, G., and Farrar, S. S., 1983, Ages of regional metamorphism and ductile deformation in the central and southern Appalachians: Lithos, v. 16, p. 223-245.

Goldman, D. S., and Albee, A. L., 1977, Correlation of Mg/Fe partitioning between garnet and biotite with O^{18}/O^{16} partitioning between quartz and magnetite: American Journal of Science, v. 277, p. 750-761.

Graham, C. M., and Powell, R., 1984, A garnet-hornblende geothermometer: Calibration, testing, and application to the Pelona Schist, Southern California: Journal of Metamorphic Geology, v. 2, p. 13-31.

Greenberg, J. K., 1976, The alpine ultramafic problem in the southern Appalachians: The Webster-Addie dunite: Geological Society of America Abstracts with Programs, v. 8, p. 185.

Guidotti, C. V., 1984, Micas in metamorphic rocks: Mineralogical Society of America Reviews in Mineralogy, v. 13, p. 357-456.

Hadley, J. B., 1970, The Ocoee Series and its possible correlatives, *in* Fisher, G. W., Pettijohn, F. J., Reed, J. C., Jr., and Weaver, K. N., eds., Studies of Appalachian geology: Central and southern: New York, Interscience, p. 274-259.

Hadley, J. B., and Goldsmith, R., 1963, Geology of the eastern Great Smoky Mountains, North Carolina and Tennessee: U. S. Geological Survey Professional Paper 349-B, 118 p.

Hadley, J. B., and Nelson, A. E., 1971, Geologic map of the Knoxville quadrangle, North Carolina, Tennessee, and South Carolina: U. S. Geological Survey Map, Miscellaneous Geologic Investigations, I-654, scale 1:250,000.

Hatcher, R. D., Jr., 1971, Geology of Rabun and Habersham Counties, Georgia: A reconnaissance study: Georgia Geological Survey Bulletin 83, 43 p.

——— 1972, Developmental model for the southern Appalachians: Geological Society of America Bulletin, v. 83, p. 2735-2760.

——— 1978, Tectonics of the western Piedmont and Blue Ridge, southern Appalachians: Review and speculation: American Journal of Science, v.278, p.276-304.

——— 1979, The Coweeta Group and Coweeta syncline: Major features of the North Carolina-Georgia Blue Ridge: Southeastern Geology, v. 21, P. 17-29.

——— 1987, Tectonics of the southern and central Appalachian internides: Annual Reviews of Earth and Planetary Science Letters, v. 15, p.337-362.

——— 1988, Bedrock geology and regional geologic setting of Coweeta Hydrologic Laboratory in the eastern Blue Ridge, *in* Swank, W. T., and Crossley, D. A., Jr., eds., Ecological Studies, v. 66: Forest Hydrology and Ecology at Coweeta: Springer-Verlag, p. 81-92.

——— 1989, Tectonic synthesis of the U.S. Appalachians, *in* Hatcher, R. D. Jr., Thomas, W. A., and Viele, G. W., eds., The Appalachian-Ouachita orogen in the United States: Boulder, Colorado, Geological Society of America, The geology of North America, v. F-2, p. 511-535.

——— 1990, Structural geology: Principles, concepts and problems: Columbus, Ohio, Charles E. Merrill, 531 p.

Hatcher, R. D., Jr., Acker, L. L., Bryan, J. G., and Godfrey, S. C., 1979, The Hayesville thrust of the central Blue Ridge of North Carolina and nearby Georgia: A pre-metamorphic, polydeformed thrust and cryptic suture within the Blue Ridge thrust sheet: Geological Society of America Abstracts with Programs, v. 11, p. 181.

Hatcher, R. D., Jr., and Butler, J. R., 1979, Guidebook for southern Appalachian field trip in the Carolinas, Tennessee and northeastern Georgia: International Geological Correlations Program -- Caledonides Project 27, University of North Carolina, Chapel Hill, 117 p.

Hatcher, R. D., Jr., Hooper, R. J., Petty, S. M., and Willis, J. D., 1984, Structure and petrology of three southern Appalachian mafic-ultramafic complexes and their bearing upon the tectonics of emplacement and origin of Appalachian ultramafic bodies: American Journal of Science, v. 284, p. 494-506.

151

Hatcher, R. D., Jr., Hopson, J. L., Edelman, S. H., Liu, A., McClellan, E. A., and Stieve, A. L., 1987, Geology of the Appalachian Ultradeep Core Hole (ADCOH) site area: Detailed map and cross sections of a major part of the crystalline southern Appalachians: Geological Society of America Abstracts with Programs, V. 19, p. 89.

Hatcher, R. D., Jr., and Williams, R. T., 1986, Mechanical model for single thrust sheets Part I: Taxonomy of crystalline thrust sheets and their relationships to the mechanical behavior of orogenic belts: Geological Society of America Bulletin, v. 97, p. 975-985.

Hatcher, R. D., Jr., Thomas, W.A., Geiser, P. A., Snoke, A. W., Mosher, S., and Wiltschko, B. V., 1989, Alleghanian orogen, *in* Hatcher, R. D. Jr., Thomas, W. A., and Viele, G. W., eds., The Appalachian-Ouachita orogen in the United States: Boulder, Colorado, Geological Society of America, The geology of North America, v. F-2, p. 233-318.

Hatcher, R. D., Jr., Osberg, P. H., Robinson, P., and Thomas, W.A., 1990, Tectonic map of the U.S. Appalachians: Geological Society of America Geology of North America, v. F-2, Plate 1, Scale: 1 : 2,112,000.

Hatcher, R D., Jr., Merschat C. E., Wiener, L. S., and Quinn, M. J., 1991, Basement-cover relationships in the Carolinas and Georgia Blue Ridge: Problems with contacts and correlations: Geological Society of America Abstracts with Programs, v. 23, p. 43.

Hess, H. H., 1955, Serpentines, orogeny, and epeirogeny: Geological Society of America Special Paper 62, p. 391-408.

Hobbs, B. E., Means, W. D., and Williams, P. F., 1976, An outline of structural geology: New York, Wiley and Sons, 571 p.

Holdaway, M. J., 1971, Stability of andalusite and the aluminum silicate phase diagram: American Journal of Science, v. 271, p. 97-131.

Holland, T. J. B., and Powell, R., 1990, An enlarged and updated internally consistent thermodynamic dataset with uncertainties and correlations: The system K_2O-Na_2O-CaO-MgO-MnO-FeO-Fe_2O_3-TiO_2-SiO_2-C-H_2-O_2: Journal of Metamorphic Geology, v. 8. p. 99-124.

Hollister, L. S., 1966, Garnet zoning: An interpretation based on the Rayleigh fractionation model: Science, v. 154, p. 1647-1651.

Hopson, J. L., Hatcher, R. D., Jr., and Stieve, A. L., 1989, Geology of the eastern Blue Ridge, northeastern Georgia and the adjacent Carolinas: Georgia Geological Society Guidebook, v. 9, p. 1-40.

Hurst, V. J., 1973, Geology of the southern Blue Ridge belt: American Journal of Science, v. 273, p. 643-670.

Johannes, W., 1983, On the origin of layered migmatites *in* Atherton, M. P., and Gribble, C. D., eds., Migmatites, melting, and metamorphism: Birkhauser Boston, Inc., p. 234-248.

Kamb, W. B., 1959, Theory of preferred orientation developed by crystallization under stress: Journal of Geology, v. 67, p. 153-170.

Keith, A., 1895, Description of the Knoxville sheet (Tennessee and North Carolina): U. S. Geological Survey Geologic Atlas, Folio 16, 6 p.

Keith, A., 1904, Description of the Asheville quadrangle (Tennessee and North Carolina): U. S. Geological Survey Geologic Atlas, Folio 116, 10 p.

———— 1907, Description of the Nantahala quadrangle (North Carolina and Tennessee): U. S. Geological Survey Geologic Atlas, Folio 143, 11 p

King, P. B., 1964, Geology of the central Great Smoky Mountains, Tennessee: U. S. Geological Survey Professional Paper 311, 36 p.

King, P. B., Hadley, J. B., Neuman, R. B., Hamilton, W., 1958, Stratigraphy of the Ocoee Series, Great Smoky Mountains, Tennessee and North Carolina: Geological Society of America Bulletin, v. 69, p. 947-966.

Kish, S. A., Merschat, C. E., Mohr,, D. W., and Wiener, L. S., 1975, Guide to the geology of the Blue Ridge south of the Great Smoky Mountains, North Carolina: Carolina Geological Society 1975 Field Trip Guidebook, 49 p.

Kish, S. A., Fullagar, P. D. and Dabbagh, A. E., 1979, Paleozoic plutonic activity in the Blue Ridge of North Carolina: Geological Society of America Abstracts with Programs v. 8, p 211-212.

Kohn, M. J., and Spear, F. S., 1989, Empirical calibration of geobarometers for the assemblage garnet + hornblende + plagioclase + quartz: American Mineralogist, v. 74, p. 77-84.

Kohn, M. J., and Spear, F. S., 1990, Two new geobarometers for garnet amphibolites, with applications to southeastern Vermont: American Mineralogist, v. 75, p. 89-96.

Koziol, A. M., and Newton, R. C., 1988, Redetermination of the anorthite breakdown reaction and improvement of the plagioclase-garnet-Al_2SiO_5-quartz geobarometer: American Mineralogist, v. 73, p. 216-223.

Koziol, A. M., and Newton, R. C., 1989, Grossular activity-composition relationships in ternary garnets determined by reversed displaced-equilibrium experiments: Contributions to Mineralogy and Petrology, v. 103, p. 423-433.

Labotka, T. C., and Shireman, J., 1991, Metamorphism in the Blue Ridge near Cullowhee, North Carolina: Geological Society of America Abstracts with Programs, v. 23, p. 55.

Laird, J., 1980, Phase equilibria in mafic schist from Vermont: Journal of Petrology, v. 21, p. 1-37.

Leake, B. E., 1964, The chemical distinction between ortho-and para-amphibolites: Journal of Petrology, v. 5, p. 238-254.

———— 1978, Nomenclature of amphiboles: Mineralogical Magazine, v. 42, p. 533-563.

Lister, G. S., and Snoke, A. W., 1984, S-C mylonites: Journal of Structural Geology, v. 6, p. 617-638.

Madison, J. A., 1968, Petrology and geochemistry of the Webster-Addie ultramafic body, Jackson County, North Carolina: unpublished Ph. D dissertation, Washington University, St. Louis, Missouri.

McClellan, E. A., 1988, Geologic history of a portion of the eastern Blue Ridge, southern Appalachians: Tray Mountain and Mecedonia 7 1/2' Quadrangles, Georgia: unpublished MS thesis, University of Tennessee, Knoxville, 179 p.

McConnell, K. I., and Abrams, C. E., 1984, Geology of the greater Atlanta region: Georgia Geologic Survey Bulletin, 96, 150 p.

Mehnert, K. R., 1968, Migmatites and the origin of granitic rocks: Amsterdam, Elsevier, 393 p.

Merschat, C. E., and Wiener, L. S., 1988, Geology of the Sandymush and Canton quadrangles, North Carolina: North Carolina Geological Survey Bulletin 90, 66 p.

Merschat, C. E., and Wiener, L. S., 1990, Geology of Grenville-age basement and younger cover rocks in the west central Blue Ridge, North Carolina: Carolina Geological Society Field Trip Guidebook, North Carolina Geological Survey, 42 p.

Miller, R. M., 1953, The Webster-Addie ultramafic ring, Jackson County, North Carolina, and secondary alteration of its chromite: American Mineralogist, v. 38, p. 1134-1147.

Misch, P., 1968, Plagioclase compositions and non-anatectic origin of migmatite gneisses in Northern Cascade Mountains of Washington State: Contributions to Mineralogy and Petrology, v. 17, p. 1-70.

Misra, K. C., and Keller, F. B., 1978, Ultramafic bodies in the southern Appalachians: A review: American Journal of Science, v. 278, p. 389-418.

Misra, K. C., and McSween, H. Y., Jr., 1984, Mafic rocks of the southern Appalachians: A review: American Journal of Science, v. 284, p. 294-318.

Miyashiro, A., 1973, Metamorphism and metamorphic belts: New York, John Wiley and Sons, 492 p.

Miyashiro, A., and Shido, F., 1975, Tholeiitic and calc-alkaline series in relation to the behaviors of titanium, vanadium, chromium, and nickel: American Journal of Science, v.275, p. 265-277.

Mohr, D. W., 1973, Stratigraphy and structure of the Great Smoky and Murphy Belt Groups, western North Carolina: American Journal of Science, v. 273-A, p. 41-71.

Nelson, A. E., 1969, Origin of some amphibolites in western North Carolina: U. S. Geological Survey Professional Paper 650-B, p. B1-B7.

Nelson, A. E., and Gillon, K. A., 1985, Stratigraphic nomenclature in the Richard Russell and Helen thrust sheets, Georgia and North Carolina: U. S. Geological Survey Bulletin 1605-A, p. A59-A62.

Newton, R. C., and Haselton, H. T., 1981, Thermodynamics of the garnet-plagioclase-Al_2SiO_5-quartz geobarometer, in Newton, R. C., Navrotsky, A., and Wood, B. J., eds., Thermodynamics of minerals and melts: New York, Springer-Verlag, p. 131-147.

Olsen, S. N., 1983, A quantitative approach to local mass balance in migmatites, in Atherton, M. P., and Gribble, C. D., eds., Migmatites, melting, and metamorphism: Birkhauser Boston, Inc., p. 201-233.

Pearce, J. A., 1976, Statistical analysis of major element patterns in basalts: Journal of Petrology, v. 17, p. 15-43.

Pearce, J. A., and Cann, J. R., 1973, Tectonic setting of basic volcanic rocks determined using trace element analyses: Earth and Planetary Science Letters, v. 19, p. 290-300.

154

Pearce, J. A., and Norry, M. J., 1979, Petrogenetic implications of Ti, Zr, Y, and Nb variations in volcanic rocks: Contributions to Mineralogy and Petrology, v. 69, p. 33-47.

Pearce, T. H., Gorman, B. E., and Birkett, T. C., 1975, The TiO_2-K_2O-P_2O_5 diagram: A method of discriminating between oceanic and non-oceanic basalts: Earth and Planetary Science Letters, v. 24, p. 419-426.

Pearce, T. H., Gorman, B. E., and Birkett, T. C., 1977, The relationship between major element chemistry and tectonic environment of basic and intermediate volcanic rocks: Earth and Planetary Science Letters, v. 36, p. 121-132.

Perchuk, L. L., and Lavrent'eva, I. V., 1983, Experimental investigation of exchange equilibria in the system cordierite-garnet-biotite, *in* Saxena, S. K., ed., Kinetics and equilibrium in mineral reactions: Springer-Verlag, p. 199-239.

Pettijohn, F. J., 1954, Classification of sandstones: Journal of Geology, v. 62, p. 360-365.

Pratt, J. H., and Lewis, J. V., 1905, Corundum and the peridotites of western North Carolina: North Carolina Geological Survey Bulletin 1, 440 p.

Quinn, M. J., 1990, Stratigraphy, structure and geochemistry across two lithotectonic boundaries in western North Carolina: Geologic interpretation of an area surrounding Sylva, Jackson County: Geological Society of America Abstracts with Programs, Vol. 22, No. 7.

Quinn, M.J., and Hatcher, R. D., Jr., 1990, Structural, stratigraphic,and petrologic dissimilarities across the Hayesville fault in western North Carolina: Preliminary report: Geological Society of America Abstracts with Programs, Vol. 22, No. 4.

Ramsay, J. G., 1967, Folding and fracturing of rocks: New York, McGraw-Hill, 568 p.

Ramsay, J. G., and Huber, M., I., 1987, The techniques of modern structural geology, vol. 2: Folds and fractures: London, Academic Press Ltd., p. 309-700.

Rankin, D. W, 1975, The continental margin of eastern North America in the southern Appalachians: The opening and closing of the Proto-Atlantic Ocean: American Journal of Science, v. 275-A, p. 298-336.

Rast, N., and Kohles, K. M., 1986, The origin of the Ocoee Supergroup: American Journal of Science, v. 286, p. 593-616.

Raymond, L. A., Yurkovitch, S. P., and McKinney, M., 1989, Block-in-matrix structures in the North Carolina Blue Ridge belt and their significance for the tectonic history of the southern Appalachian orogen: Geological Society of America Special Paper 228, p. 195-215.

Robinson, P., Spear, F. S., Schumacher, J. C., Laird, J., Klein, C., Evans, B. W., and Doolan, B. L., 1982, Phase relations of metamorphic amphiboles: Natural occurrences and theory: Mineralogical Society of America Reviews in Mineralogy, v. 9B, p. 1-227.

Rock, N. M. S., MacDonald, R., Walker, B. H., May, F., Peacock, J. D., and Scott, P., 1985, Intrusive metabasite belts within the Moine assemblage, west of Loch Ness, Scotland: Evidence for metabasite modification by country rock interactions: Journal of the Geological Society of London, v. 142, p. 643-661.

Rodgers, J., 1971, The Taconic orogeny: Geological Society of America Bulletin, v. 82, p. 1141-1178.

Secor, D. T., Snoke, A. W., and Dallmeyer, R. D., 1986b, Character of the Alleghanian orogeny in the southern Appalachians: Part III, Regional tectonic relations: Geological Society of America Bulletin, v. 97, p. 1345-1353.

Shanmugam, G., and Lash, G. G., 1982, Analogous tectonic evolution of the Ordovician foredeeps, southern and central Appalachians: Geology, v. 10, p. 562-566.

Shervais, J. W., 1982, Ti-V plots and the petrogenesis of modern and ophiolitic lavas: Earth and Planetary Science Letters, v. 59, p. 101-118.

Shireman, J., Labotka, T. C., and Knapp, S., 1985, Metamorphic history of a portion of the North Carolina Blue Ridge: Geological Society of America Abstracts with Programs, v. 17, p. 135.

Simpson, C., 1986, Determination of movement sense in mylonites: Journal of Geological Education, v. 34, p. 246.

Spear, F. S., 1980, NaSi = CaAl exchange equilibrium between plagioclase and amphibole: An empirical model: Contributions to Mineralogy and Petrology, v. 72, p. 33-41.

Spear, F. S., and Cheney, J. T., 1989, A petrogenetic grid for pelitic schists in the system SiO_2-Al_2O_3-FeO-MgO-K_2O-H_2O: Contributions to Mineralogy and Petrology, v. 101, p. 149-164.

Thompson, J. B., 1957, The graphical analysis of mineral assemblages in pelitic schists: American Mineralogist, v. 42, p. 842-858.

Thompson, J. B., and Norton, S. S., 1968, Paleozoic regional metamorphism in New England and adjacent areas, in Zen, E-An, White, W. S., Hadley, J. B., and Thompson, J. B., eds., Studies of Appalachian Geology; New York, Interscience Publisher (John Wiley & Sons), 475 p.

Tracy, R. J, Miller, S. J., and Armstrong, T. R., 1990, Selection of garnet and biotite compositions for garnet-biotite thermometry in amphibolite facies metapelites: Geological Society of America Abstracts with Programs, v. 22, p. A29.

Vyhnal, C. R., 1989, Hornblende chemistry in southern Appalachian granitoids: Implications for aluminum-hornblende barometry and Alleghanian tectonics: Unpublished MS thesis, University of Tennessee, Knoxville, 145 p.

Walker, K. R., 1969, The Palisades sill, New Jersey: A reinvestigation: Geological Society of America Special Paper, No. 111.

Wehr, F. and Glover, L., III, 1985, Stratigraphy and tectonics of the Virginia-North Carolina Blue Ridge: Evolution of a late Proterozoic-early Paleozoic hinge zone: Geological Society of America Bulletin, v. 96, p. 285-295.

Wilcox, R. E., and Poldervaart, A., 1958, Metadolerite dike swarm in Bakersville-Roan Mountain area, North Carolina: Geological Society of America Bulletin, v. 69, p. 1323-1367.

Williams, G. H., 1890, The non-feldspathic intrusive rocks of Maryland and the course of their alteration: American Geologist, v. 6, p. 35-49.

Williams, H., Turner, F. J., and Gilbert, C. M., 1954, Petrography: An introduction to the study of rocks in thin sections: Second Edition, W. H. Freeman and Company, 626 p.

⌐ Winkler, H. G. F., 1979, Petrogenesis of metamorphic rocks, 5th Edition: New York, Springer-Verlag, 348 p.

Yeates, W. S., McCallie, S. W., and King, F. P., 1896, A preliminary report on a part of the gold deposits of Georgia: Georgia Geologic Survey Bulletin 4-A, 535 p.

APPENDICES

APPENDIX A

Microprobe Analyses

Conditions of Microprobe Analysis

Instrument:	Cameca SX 50 WDS electron microprobe
Accelerating Voltage:	15 keV
Current:	20-30 nA
Spectrometer Crystals:	LIF, TAP, TAP, PET

Calibration Standards Used

Na_2O:	Albite		CaO:	Wollastonite
MgO:	Spinel		TiO_2:	Rutile
Al_2O_3:	Spinel		Cr_2O_3:	Chromium metal
SiO_2:	Wollastonite		MnO:	Spessartine
K_2O:	Orthoclase		Fe_2O_3:	Hematite

Garnet Analyses

	SS454 PT 1.1	SS454 PT 1.2	SS454 PT 1.3	SS454 PT 1.4	SS454 PT 1.5	SS454 PT 1.6	SS454 PT 1.7	SS454 PT 1.8	SS454 PT 1.9	SS454 PT 1.10
SiO2	37.0730	36.8593	37.1503	38.0703	37.8720	38.0981	37.8072	37.7293	37.4899	37.4739
TiO2	0.0000	bd	0.0273	bd	0.0326	0.0239	bd	bd	bd	0.0289
Al2O3	21.0368	20.9842	21.0111	21.3371	21.2326	21.3057	21.4834	21.1719	21.2087	21.0443
Cr2O3	0.0000	bd	bd	0.0000	bd	0.0000	bd	bd	bd	bd
MgO	3.4002	3.8504	3.9586	4.9420	4.9103	5.3470	5.1268	4.7695	3.4835	4.0371
CaO	3.1100	1.6690	1.6139	1.9872	1.9301	1.9427	1.8699	1.7832	2.8750	1.9049
MnO	1.3424	1.6496	1.6972	1.1911	1.1224	1.0992	1.1740	1.4549	1.4824	1.6493
FeO	33.6719	34.9193	34.2634	33.3369	33.0156	32.3059	32.8760	33.2326	33.7827	34.3662
Total	99.6343	99.9318	99.7218	100.8646	100.1156	100.1225	100.3373	100.1414	100.3222	100.5046
Si	2.985	2.970	2.988	3.000	3.004	3.009	2.990	3.000	2.994	2.990
Ti	0.000	bd	0.002	bd	0.002	0.001	bd	bd	bd	0.002
Al	1.997	1.993	1.992	1.983	1.985	1.984	2.003	1.984	1.997	1.979
Cr	0.000	bd	bd	0.000	bd	0.000	bd	bd	bd	bd
Mg	0.408	0.462	0.475	0.580	0.580	0.630	0.605	0.565	0.414	0.480
Ca	0.268	0.144	0.139	0.168	0.164	0.164	0.158	0.152	0.246	0.162
Mn	0.091	0.113	0.116	0.079	0.075	0.074	0.078	0.098	0.100	0.112
Fe2+	2.267	2.353	2.304	2.197	2.191	2.134	2.175	2.210	2.256	2.294
Total	8.017	8.034	8.015	8.008	8.002	7.997	8.009	8.008	8.008	8.019

bd= Below limits of detection

162

	SS454 PT 1.11	SS454 PT 3.1	SS454 PT 3.2	SS454 PT 3.3	SS454 PT 3.4	SS454 PT 3.5	SS454 PT 3.6	SS454 PT 3.7	SS454 PT 3.8	SS454 PT 3.9
SiO2	37.6772	37.1471	37.3892	37.3334	37.5363	37.3834	37.7375	37.9572	38.0093	37.9347
TiO2	bd	bd	bd	bd	bd	0.0392	bd	bd	0.0000	bd
Al2O3	21.3987	21.1618	21.0389	21.0250	21.0531	21.0154	21.2728	21.4373	21.5821	21.4948
Cr2O3	bd	bd	bd	bd	bd	bd	0.0000	0.0000	0.0000	0.0000
MgO	5.0264	3.4710	3.5095	3.7529	3.5155	4.6785	5.4082	6.0145	6.2375	5.7871
CaO	1.7378	2.8384	2.7892	2.1379	2.8245	1.9109	2.0098	2.1191	2.1818	2.2539
MnO	1.1650	1.4532	1.3034	1.3961	1.4090	1.5314	1.2559	1.0615	0.9906	0.9904
FeO	33.2399	33.5674	33.5205	34.1008	33.6094	33.3763	32.1287	31.5648	31.4422	31.6167
Total	100.2450	99.6389	99.5507	99.7461	99.9478	99.9351	99.8129	100.1544	100.4435	100.0776
Si	2.987	2.987	3.004	2.998	3.006	2.986	2.994	2.990	2.982	2.991
Ti	bd	bd	bd	bd	bd	0.002	bd	bd	bd	bd
Al	2.000	2.006	1.993	1.991	1.987	1.980	1.990	1.991	1.996	1.998
Cr	bd	bd	bd	bd	bd	bd	0.000	0.000	0.000	0.000
Mg	0.594	0.416	0.420	0.449	0.420	0.557	0.640	0.705	0.730	0.680
Ca	0.148	0.245	0.240	0.184	0.242	0.163	0.171	0.179	0.183	0.190
Mn	0.079	0.099	0.088	0.095	0.096	0.104	0.085	0.071	0.066	0.066
Fe2+	2.204	2.258	2.253	2.290	2.251	2.230	2.132	2.079	2.063	2.085
Total	8.012	8.010	7.999	8.007	8.001	8.022	8.011	8.015	8.020	8.010

163

	SS454 PT 3.10	SS454 PT 3.11	SS454 PT 3.12	SS454 PT 3.13	SS313 Pt. 1.1	SS313 Pt. 1.2	SS313 Pt. 1.3	SS313 Pt. 1.4	SS313 Pt. 1.5	SS313 Pt. 1.6
SiO2	37.7063	37.3802	37.2696	37.7430	37.3331	37.3893	37.3587	37.2610	37.2433	37.4793
TiO2	bd	bd	0.0336	0.0000	bd	bd	bd	bd	bd	bd
Al2O3	21.4016	21.2122	21.1516	21.1358	20.8255	21.0161	20.9346	20.8939	20.9363	20.7853
Cr2O3	0.0000	0.0000	bd	bd	0.0674	bd	bd	bd	bd	0.0601
MgO	5.1175	4.3512	3.9708	5.3456	3.5709	3.6120	3.5837	3.6515	3.5679	3.6131
CaO	1.9503	1.8508	2.2341	1.8358	2.0725	1.9129	1.8617	1.8835	1.9816	1.9526
MnO	1.1864	1.3181	1.4511	1.1802	1.0901	1.3149	1.2157	1.2414	1.2762	1.2439
FeO	32.6926	34.0288	34.0462	32.4630	35.0968	35.1265	35.2550	34.8093	34.5692	35.1924
Total	100.0547	100.1413	100.1570	99.7034	100.0563	100.3717	100.2094	99.7406	99.5745	100.3267
Si	2.990	2.984	2.982	3.000	2.998	2.994	2.997	2.999	3.000	3.003
Ti	bd	bd	0.002	0.000	bd	bd	bd	bd	bd	bd
Al	2.001	1.996	1.995	1.981	1.973	1.984	1.980	1.982	1.989	1.964
Cr	0.000	0.000	bd	bd	0.004	bd	bd	bd	bd	0.004
Mg	0.605	0.518	0.473	0.634	0.427	0.431	0.428	0.438	0.429	0.431
Ca	0.166	0.158	0.191	0.157	0.178	0.164	0.160	0.162	0.171	0.167
Mn	0.080	0.089	0.098	0.079	0.074	0.089	0.083	0.085	0.087	0.084
Fe2+	2.168	2.272	2.278	2.158	2.358	2.352	2.366	2.343	2.329	2.358
Total	8.009	8.018	8.019	8.009	8.012	8.014	8.014	8.009	8.005	8.011

164

	SS313 Pt. 1.7	SS313 Pt. 1.8	SS313 Pt. 1.9	SS313 Pt. 1.10	SS313 Pt. 1.11	SS313 Pt. 1.12	SS313 Pt. 4.1	SS313 Pt. 4.2	SS313 Pt. 4.3	SS313 Pt. 4.4
SiO2	37.4126	37.4910	37.4100	37.2919	37.4901	37.4872	37.4094	37.0647	36.8502	37.1346
TiO2	bd	bd	bd	bd	0.0245	bd	bd	bd	bd	0.0248
Al2O3	21.0240	21.0632	21.0091	20.7657	20.9165	20.9928	20.8673	20.4673	20.2244	20.7463
Cr2O3	bd	bd	bd	bd	bd	bd	bd	bd	bd	0.0513
MgO	3.4239	3.3161	3.2801	3.2301	3.3360	3.4880	3.2368	3.3746	3.2794	3.4974
CaO	2.0650	2.2299	2.2267	2.2994	2.2954	2.2919	2.2415	2.2440	2.2571	1.9840
MnO	1.0715	1.1191	1.1488	1.0341	1.1847	1.1923	1.1648	1.1378	1.0811	1.1221
FeO	35.0564	35.1448	35.2743	35.1996	34.6415	34.3827	35.0467	34.6854	34.9555	34.6576
Total	100.0534	100.3641	100.3490	99.8208	99.8887	99.8349	99.9665	98.9738	98.6477	99.2181
Si	3.002	3.001	2.998	3.005	3.011	3.009	3.008	3.011	3.010	3.004
Ti	bd	bd	bd	bd	0.001	bd	bd	bd	bd	0.001
Al	1.989	1.988	1.985	1.973	1.981	1.986	1.978	1.960	1.947	1.979
Cr	bd	bd	bd	bd	bd	bd	bd	bd	bd	0.003
Mg	0.409	0.396	0.392	0.388	0.400	0.417	0.388	0.408	0.399	0.422
Ca	0.178	0.191	0.192	0.199	0.198	0.197	0.193	0.195	0.198	0.172
Mn	0.073	0.076	0.078	0.070	0.080	0.081	0.079	0.078	0.075	0.077
Fe2+	2.353	2.353	2.364	2.373	2.327	2.308	2.357	2.357	2.388	2.345
Total	8.004	8.005	8.009	8.008	7.998	7.998	8.003	8.009	8.017	8.003

	SS349 PT 1.1	SS349 PT 1.2	SS349 PT 1.3	SS349 PT 1.4	SS349 PT 1.5	SS349 PT 1.6	SS349 PT 1.7	SS349 PT 1.8	SS349 PT 1.9	SS349 PT 1.10
SiO2	37.5599	37.9995	38.6504	38.1970	38.5044	38.0749	37.1758	37.2100	37.2753	37.6857
TiO2	bd	bd	0.0265	bd	0.0272	bd	bd	0.0275	0.0404	bd
Al2O3	21.0614	21.3575	21.6547	21.4580	21.6742	21.4739	20.9820	20.9693	21.1697	21.3714
Cr2O3	bd	bd	bd	0.0000	bd	bd	0.0000	0.0059	bd	bd
MgO	3.4810	5.6562	7.6703	6.7310	7.1074	5.9548	3.5397	3.4384	3.5993	5.2510
CaO	2.8844	3.3472	3.6708	3.3030	3.5202	3.2951	2.9695	2.7596	3.1835	3.9997
MnO	1.3518	0.6975	0.4810	0.5746	0.5424	0.6754	1.3385	1.2832	1.3245	0.7549
FeO	34.3339	31.0843	28.2179	29.8435	28.9989	30.8259	33.5030	34.2680	33.6258	30.9413
Total	100.6724	100.1422	100.3716	100.1071	100.3747	100.3000	99.5085	99.9619	100.2185	100.0040
Si	2.995	2.992	2.992	2.989	2.991	2.988	2.993	2.989	2.981	2.980
Ti	bd	bd	0.002	bd	0.002	bd	bd	0.002	0.002	bd
Al	1.980	1.983	1.976	1.980	1.985	1.987	1.991	1.986	1.996	1.992
Cr	bd	bd	bd	0.000	bd	bd	0.000	0.001	bd	bd
Mg	0.414	0.664	0.885	0.785	0.823	0.696	0.425	0.412	0.429	0.619
Ca	0.246	0.283	0.304	0.277	0.293	0.278	0.256	0.238	0.272	0.339
Mn	0.091	0.047	0.031	0.038	0.036	0.045	0.091	0.087	0.089	0.050
Fe2+	2.289	2.047	1.827	1.953	1.884	2.024	2.255	2.302	2.249	2.046
Total	8.015	8.016	8.018	8.021	8.014	8.018	8.012	8.016	8.019	8.025

	SS349 PT 1.11	SS349 PT 1.12	SS349 PT 1.13	SS349 PT 2.1	SS349 PT 2.2	SS349 PT 2.3	SS349 PT 2.4	SS349 PT 2.5	SS349 PT 2.6	SS349 PT 2.7
SiO_2	37.1542	37.2963	37.8856	37.4153	37.7557	37.8290	38.0962	38.2068	38.5218	38.3594
TiO_2	bd	0.0286	bd	0.0331	bd	0.0489	bd	0.0617	0.0383	0.5447
Al_2O_3	21.0748	20.9869	21.3337	20.9262	21.3824	21.4210	21.7035	21.5706	21.7059	21.4950
Cr_2O_3	bd	0.0000	0.0000	bd	bd	0.0000	bd	bd	0.0000	bd
MgO	3.2145	3.3352	6.0613	3.6254	5.3109	5.8909	6.5485	6.6697	6.7291	7.0009
CaO	3.0592	2.8995	3.1561	2.9842	3.2448	3.2329	3.3206	3.6128	3.8282	4.2532
MnO	1.2734	1.2695	0.6077	1.3630	0.7915	0.5875	0.5495	0.4743	0.6159	0.5071
FeO	34.2114	34.5366	30.8209	33.7104	31.4434	31.2103	30.1080	29.6174	29.0507	27.9764
Total	99.9875	100.3526	99.8653	100.0576	99.9287	100.2205	100.3263	100.2133	100.4899	100.1367
Si	2.986	2.988	2.987	2.997	2.987	2.978	2.978	2.985	2.993	2.982
Ti	bd	0.002	bd	0.002	bd	0.003	bd	0.004	0.002	0.032
Al	1.996	1.982	1.983	1.976	1.994	1.988	1.999	1.986	1.989	1.970
Cr	bd	0.000	0.000	bd	bd	0.000	bd	bd	0.000	bd
Mg	0.384	0.399	0.712	0.433	0.626	0.691	0.763	0.776	0.779	0.811
Ca	0.264	0.249	0.267	0.256	0.275	0.272	0.278	0.302	0.319	0.354
Mn	0.086	0.086	0.041	0.092	0.053	0.039	0.036	0.031	0.041	0.034
Fe^{2+}	2.299	2.314	2.032	2.258	2.080	2.055	1.968	1.935	1.888	1.819
Total	8.016	8.019	8.022	8.013	8.016	8.026	8.023	8.019	8.010	8.001

	SS349 PT 2.8	SS349 PT 2.9	SS349 PT 2.10	SS349 PT 2.11	SS349 PT 2.12	SS349 PT 2.13	SS287 Pt. 2.1	SS287 Pt. 2.2	SS287 Pt. 2.3	SS287 Pt. 2.4
SiO2	37.1515	37.6650	38.1241	37.3032	38.3724	37.9588	37.6343	38.3588	37.8928	37.8515
TiO2	0.0000	bd	0.0388	0.0393	0.0000	0.1041	bd	bd	0.0348	0.0144
Al2O3	20.9713	21.2428	21.2760	21.1851	21.7828	21.4501	21.3890	21.5437	21.6812	21.7376
Cr2O3	0.0531	bd	bd	bd	0.0000	0.0000	0.0000	0.0508	bd	bd
MgO	3.6599	3.8019	5.5356	3.4856	7.3159	5.7597	6.6743	7.0840	7.5120	7.5501
CaO	2.7419	3.0095	3.1992	2.9250	4.3945	3.1604	1.8972	2.1168	2.3847	2.3520
MnO	1.4059	1.3205	0.6454	1.3384	0.5104	0.8499	0.7179	0.6889	0.6524	0.6901
FeO	34.0325	33.4796	31.6234	33.6995	27.3426	30.7218	30.7400	29.8452	29.6028	29.1713
Total	100.0161	100.5193	100.4425	99.9761	99.7186	100.0048	99.0527	99.6882	99.7607	99.3670
Si	2.982	2.995	2.997	2.988	2.987	2.989	2.947	3.004	2.968	2.970
Ti	0.000	bd	0.002	0.002	0.000	0.006	bd	bd	0.002	0.001
Al	1.985	1.991	1.973	2.001	1.999	1.991	1.975	1.989	2.002	2.011
Cr	0.003	bd	bd	bd	0.000	0.000	0.000	0.003	bd	bd
Mg	0.438	0.450	0.649	0.417	0.849	0.676	0.778	0.826	0.877	0.883
Ca	0.236	0.256	0.270	0.252	0.252	0.366	0.267	0.159	0.178	0.200	0.198
Mn	0.096	0.089	0.043	0.091	0.034	0.057	0.048	0.046	0.043	0.046
Fe2+	2.285	2.227	2.079	2.258	1.780	2.023	2.013	1.955	1.939	1.915
Total	8.024	8.009	8.014	8.009	8.014	8.009	7.920	8.001	8.031	8.024

168

	SS287 Pt. 2.5	SS287 Pt. 2.6	SS287 Pt. 2.7	SS287 Pt. 2.8	SS287 Pt. 2.9	SS287 Pt. 2.10	SS287 Pt. 2.11	SS287 Pt. 2.12	SS287 Pt. 2.13	SS287 Pt. 1.1
SiO2	37.7647	37.6844	37.3486	37.3520	37.3592	37.9782	37.9310	38.0374	37.9325	38.1334
TiO2	bd	bd	bd	bd	0.0426	bd	0.0258	0.0263	bd	0.0357
Al2O3	21.7767	21.8226	21.4094	21.4588	21.7462	21.6887	21.7801	21.7307	21.7735	21.3416
Cr2O3	bd	bd	0.0000	bd	bd	0.0566	bd	bd	bd	0.0000
MgO	7.6077	7.5141	4.4332	5.2188	5.9308	6.7734	7.4604	7.5121	7.5357	5.4245
CaO	2.6017	2.5754	2.2461	2.3711	2.4517	2.3518	2.3970	2.5973	2.6276	1.9710
MnO	0.6784	0.6890	1.1084	0.9702	0.7879	0.6709	0.6447	0.7054	0.7184	0.8541
FeO	28.8364	29.1251	33.3782	32.4476	31.2270	30.6271	29.9952	29.1277	29.1964	32.5628
Total	99.2656	99.4106	99.9239	99.8185	99.5454	100.1467	100.2342	99.7369	99.7841	100.3231
Si	2.964	2.958	2.979	2.970	2.959	2.975	2.961	2.974	2.966	3.006
Ti	bd	bd	bd	bd	0.002	bd	0.002	0.002	bd	0.002
Al	2.016	2.020	2.013	2.012	2.031	2.003	2.004	2.003	2.007	1.984
Cr	bd	bd	0.000	bd	bd	0.004	bd	bd	bd	0.000
Mg	0.890	0.879	0.527	0.619	0.700	0.790	0.868	0.875	0.879	0.637
Ca	0.219	0.217	0.192	0.202	0.208	0.197	0.201	0.218	0.220	0.166
Mn	0.045	0.046	0.075	0.065	0.053	0.044	0.042	0.047	0.048	0.057
Fe2+	1.893	1.913	2.227	2.158	2.069	2.007	1.958	1.905	1.910	2.147
Total	8.027	8.033	8.013	8.026	8.022	8.020	8.036	8.024	8.030	7.999

	SS287 Pt. 1.2	SS287 Pt. 1.3	SS287 Pt. 1.4	SS287 Pt. 1.5	SS287 Pt. 1.6	SS287 Pt. 1.7	SS287 Pt. 1.8	SS287 Pt. 1.9	SS287 Pt. 1.10	SS287 Pt. 1.11
SiO2	37.9553	38.0766	38.2267	38.4818	38.4098	38.4499	38.4313	38.4331	38.2321	38.3562
TiO2	bd	0.0594	bd	0.0207	0.0207	0.0292	bd	bd	bd	bd
Al2O3	21.2585	21.4770	21.5719	21.3679	21.4502	21.3889	21.3831	21.2719	21.3489	21.2964
Cr2O3	0.0000	0.0000	0.0000	0.0000	bd	bd	bd	bd	bd	bd
MgO	5.7426	6.3367	6.8323	7.0349	6.8668	6.9672	7.0032	7.1091	6.7860	6.7152
CaO	2.1748	2.4525	2.5748	2.5749	2.6689	2.7476	2.7938	2.8200	2.8975	2.7395
MnO	0.7867	0.6305	0.6539	0.6669	0.6555	0.7374	0.6151	0.6580	0.6451	0.6815
FeO	31.7991	30.9569	29.7936	29.8550	29.5723	29.4825	29.4008	29.5037	29.5468	29.3754
Total	99.7170	99.9896	99.6532	100.0021	99.6442	99.8027	99.6273	99.7958	99.4564	99.1642
Si	3.004	2.992	2.998	3.007	3.009	3.008	3.010	3.008	3.004	3.019
Ti	bd	0.004	bd	0.001	0.001	0.002	bd	bd	bd	bd
Al	1.983	1.990	1.994	1.969	1.981	1.973	1.974	1.963	1.978	1.976
Cr	0.000	0.000	0.000	0.000	bd	bd	bd	bd	bd	bd
Mg	0.677	0.742	0.798	0.819	0.802	0.813	0.817	0.829	0.795	0.788
Ca	0.184	0.206	0.216	0.215	0.224	0.231	0.234	0.236	0.244	0.231
Mn	0.053	0.042	0.043	0.044	0.044	0.049	0.041	0.044	0.043	0.045
Fe2+	2.104	2.034	1.954	1.952	1.937	1.929	1.926	1.931	1.942	1.934
Total	8.005	8.010	8.003	8.007	7.998	8.005	8.002	8.011	8.006	7.993

	SS287	SS287	SS287	SS287	SS287	SS287	SN125	SN125	SN125	SN125
	Pt. 1.12	Pt. 1.13	Pt. 1.14	Pt. 1.15	Pt. 1.16	Pt. 1.17	PT 2.1	PT 2.2	PT2.3	PT 2.4
SiO2	37.8652	37.7982	37.7417	37.6328	37.7311	37.4786	37.2231	37.2508	37.4470	37.2181
TiO2	0.0503	0.0254	0.0342	bd	bd	0.0257	bd	0.0629	bd	0.0234
Al2O3	20.9224	21.0195	21.1151	21.1500	21.1397	21.0290	20.6851	20.5881	20.8111	20.7092
Cr2O3	bd	bd	bd	bd	bd	bd	0.0000	0.0662	bd	bd
MgO	4.6222	4.5016	4.3623	5.3526	5.5930	4.7643	2.6878	2.5099	2.8377	3.7294
CaO	2.6399	2.1178	2.0689	1.9611	1.9571	2.4721	2.5071	2.3608	2.7000	1.4583
MnO	0.9327	1.0520	1.0219	0.8551	0.8642	1.0102	2.3820	2.5925	2.0198	1.7907
FeO	32.6352	33.0892	33.5728	32.7527	32.2966	32.8349	34.6565	34.2057	33.9544	34.5476
Total	99.6679	99.6037	99.9169	99.7043	99.5817	99.6148	100.1416	99.6369	99.7700	99.4767
Si	3.017	3.017	3.009	2.993	2.998	2.993	3.003	3.017	3.018	3.005
Ti	0.003	0.002	0.002	bd	bd	0.002	bd	0.004	bd	0.001
Al	1.965	1.978	1.985	1.983	1.980	1.980	1.968	1.966	1.977	1.971
Cr	bd	bd	bd	bd	bd	bd	0.000	0.004	bd	bd
Mg	0.549	0.535	0.518	0.634	0.662	0.567	0.323	0.303	0.341	0.449
Ca	0.225	0.181	0.177	0.167	0.167	0.211	0.217	0.205	0.233	0.126
Mn	0.063	0.071	0.069	0.058	0.058	0.068	0.163	0.178	0.138	0.122
Fe2+	2.175	2.209	2.238	2.179	2.147	2.193	2.339	2.317	2.288	2.333
Total	7.997	7.993	7.998	8.014	8.012	8.014	8.013	7.994	7.994	8.008

	SN125	SN34	SN34	SN34	SN34	SN34	SN34	SN34	SN34	SN34
	PT 2.5	PT 1.1	PT 1.2	PT 1.3	PT 1.4	PT 1.5	PT 1.6	PT 1.7	PT 1.8	PT 1.9
SiO2	37.1828	37.0312	37.0198	37.0465	36.5377	36.6879	36.6927	36.8082	36.5768	36.6432
TiO2	bd	bd	bd	bd	bd	bd	bd	0.0280	bd	bd
Al2O3	20.8880	20.5702	20.8023	21.0052	20.9799	20.9943	20.8977	20.8846	21.0228	20.7721
Cr2O3	bd	0.0000	bd	bd	bd	bd	bd	bd	bd	bd
MgO	3.7611	2.3464	3.0786	3.1285	2.2918	2.7197	2.3865	2.9125	2.4607	2.0963
CaO	1.4027	2.6662	2.1279	2.1253	2.3382	2.2627	2.1750	1.9989	2.2145	2.3183
MnO	2.0791	1.7999	1.9273	2.1914	1.9801	1.6790	2.1998	2.2101	1.8618	2.2526
FeO	34.5915	35.2299	35.3362	34.2912	35.6683	35.8995	35.3695	35.2959	36.0475	35.6645
Total	99.9052	99.6438	100.2921	99.7881	99.7960	100.2431	99.7212	100.1382	100.1841	99.7470
Si	2.992	3.007	2.984	2.989	2.971	2.966	2.981	2.975	2.964	2.984
Ti	bd	bd	bd	bd	bd	bd	0.000	0.002	bd	bd
Al	1.982	1.969	1.976	1.998	2.011	2.001	2.002	1.990	2.008	1.994
Cr	bd	0.000	bd	bd	bd	bd	0.000	bd	bd	bd
Mg	0.451	0.284	0.370	0.376	0.277	0.328	0.289	0.351	0.297	0.255
Ca	0.121	0.232	0.184	0.184	0.204	0.196	0.190	0.173	0.192	0.202
Mn	0.142	0.124	0.132	0.150	0.136	0.115	0.151	0.151	0.128	0.155
Fe2+	2.328	2.392	2.382	2.314	2.425	2.427	2.404	2.386	2.443	2.429
Total	8.016	8.009	8.028	8.012	8.024	8.033	8.018	8.028	8.032	8.019

	SN34 PT 2.1	SN34 PT 2.2	SN34 PT 2.3	SN34 PT 2.4	SN34 PT 2.5	SN34 PT 2.6	SN34 PT 2.7	SN34 PT 2.8	SN34 PT 2.9	SN408 PT 2.1
SiO2	36.5236	36.5371	36.4703	36.7478	36.5702	36.7085	36.6971	36.4841	36.5237	38.4662
TiO2	bd	bd	bd	0.0000	0.0000	bd	bd	bd	bd	bd
Al2O3	20.8499	20.9332	21.0826	21.0542	20.9807	20.7918	20.7794	20.7348	21.0253	21.9079
Cr2O3	0.0000	0.0000	0.0000	0.0000	0.0000	bd	bd	bd	bd	0.0000
MgO	2.1513	2.6251	2.8391	3.0059	2.9551	2.8422	2.6209	2.0964	2.1271	7.5138
CaO	2.9629	2.5265	2.2983	2.2550	2.1993	2.2499	2.2608	2.2367	2.8548	6.4735
MnO	1.8119	1.7565	1.7447	2.1504	2.2683	2.3411	2.3819	2.3321	1.9419	2.2680
FeO	35.2487	35.3806	34.9999	35.0415	34.9903	34.8182	35.5246	35.6460	35.5213	23.7233
Total	99.5483	99.7590	99.4349	100.2548	99.9639	99.7517	100.2647	99.5301	99.9941	100.3527
Si	2.975	2.967	2.964	2.965	2.961	2.978	2.972	2.979	2.965	2.967
Ti	bd	bd	bd	0.000	0.000	bd	bd	bd	bd	bd
Al	2.002	2.003	2.020	2.002	2.003	1.988	1.984	1.996	2.013	1.992
Cr	0.000	0.000	0.000	0.000	0.000	bd	bd	bd	bd	0.000
Mg	0.261	0.318	0.344	0.362	0.357	0.343	0.316	0.256	0.258	0.863
Ca	0.258	0.220	0.200	0.195	0.191	0.196	0.196	0.196	0.248	0.535
Mn	0.125	0.121	0.120	0.147	0.156	0.161	0.163	0.161	0.133	0.148
Fe2+	2.402	2.402	2.379	2.364	2.370	2.362	2.405	2.435	2.412	1.530
Total	8.024	8.032	8.026	8.035	8.037	8.028	8.036	8.023	8.029	8.036

	SN408 PT 2.2	SN408 PT 2.3	SN408 PT 2.4	SN408 PT 2.5	SN408 PT 2.6	SN408 PT 2.7	SN408 PT 2.8	SN408 PT 2.9	SN408 PT 2.10	SN408 PT 1.1
SiO2	38.3369	38.3581	37.5578	38.0926	38.3062	38.4300	38.1761	38.2973	38.3250	38.2584
TiO2	bd	0.0465	0.0249	bd	0.0328	0.0393	bd	bd	0.0236	0.0000
Al2O3	21.9047	21.8856	21.2964	21.5588	21.5765	21.6435	21.7304	21.5555	21.6326	21.5623
Cr2O3	0.0000	0.0940	0.1119	0.0988	0.3185	0.1501	0.0625	0.2035	0.0834	0.1586
MgO	7.4526	7.4619	5.7295	6.9057	7.4942	7.5708	7.6677	7.6287	7.5674	7.3970
CaO	6.6201	6.5998	5.2760	5.2969	6.4657	6.0955	5.9621	5.5734	5.2560	5.7805
MnO	2.2812	2.2267	2.7170	2.1061	2.2777	2.2598	2.1620	2.0739	2.0351	2.1751
FeO	24.0270	23.6315	26.6295	26.4364	24.1631	24.5285	24.3520	24.6255	25.1416	25.1689
Total	100.6225	100.3041	99.3430	100.4953	100.6347	100.7175	100.1128	99.9578	100.0647	100.5008
Si	2.956	2.961	2.971	2.962	2.958	2.963	2.958	2.972	2.973	2.963
Ti	bd	0.003	0.001	bd	0.002	0.002	bd	bd	0.001	0.000
Al	1.991	1.992	1.986	1.977	1.964	1.967	1.985	1.972	1.978	1.968
Cr	0.000	0.005	0.007	0.006	0.020	0.009	0.004	0.012	0.005	0.010
Mg	0.856	0.858	0.675	0.801	0.862	0.870	0.886	0.882	0.875	0.854
Ca	0.547	0.546	0.447	0.442	0.535	0.504	0.495	0.463	0.437	0.480
Mn	0.149	0.146	0.182	0.139	0.149	0.148	0.142	0.136	0.134	0.143
Fe2+	1.550	1.526	1.762	1.720	1.560	1.582	1.578	1.598	1.631	1.630
Total	8.048	8.037	8.032	8.046	8.049	8.046	8.047	8.036	8.034	8.048

174

	SN408 PT 1.2	SN408 PT 1.3	SN408 PT 1.4	SN408 PT 1.5	SN487 PT 1.1	SN487 PT 1.2	SN487 PT 1.3	SN487 PT 1.4	SN487 PT 1.5	SN487 PT 1.6
SiO2	38.2295	38.6612	38.3975	37.7269	37.1260	37.5987	37.6567	37.5727	37.6172	37.6017
TiO2	0.0291	0.0000	0.0000	bd	0.0000	bd	0.0255	0.0742	0.1247	0.1792
Al2O3	21.6372	21.5821	21.5142	21.0910	20.9141	21.3066	21.1962	21.2637	21.1725	21.1790
Cr2O3	0.0684	bd	0.0859	0.1541	0.0510	bd	0.1065	0.1196	0.0896	0.0823
MgO	7.4783	7.3173	7.2908	5.5398	3.1261	4.2913	4.5974	4.6577	4.6051	4.2766
CaO	5.9927	6.3504	5.3490	4.9972	5.6355	5.7135	6.0757	6.4459	6.5348	6.4176
MnO	2.2009	2.1986	2.1931	3.8763	2.7152	1.5001	1.3745	1.3343	1.2218	1.3702
FeO	24.3874	24.0795	25.0134	26.6776	30.0914	30.0734	29.3695	28.7877	28.5293	29.1886
Total	100.0235	100.1891	99.8439	100.0629	99.6593	100.4836	100.4020	100.2558	99.8950	100.2952
Si	2.966	2.989	2.986	2.976	2.981	2.972	2.972	2.965	2.975	2.971
Ti	0.002	0.000	0.000	bd	0.000	bd	0.002	0.004	0.007	0.011
Al	1.979	1.967	1.972	1.961	1.979	1.986	1.972	1.978	1.974	1.973
Cr	0.004	bd	0.006	0.009	0.003	bd	0.007	0.007	0.006	0.005
Mg	0.865	0.844	0.845	0.651	0.374	0.505	0.541	0.548	0.543	0.504
Ca	0.498	0.526	0.446	0.423	0.485	0.484	0.514	0.545	0.553	0.544
Mn	0.145	0.144	0.144	0.259	0.185	0.100	0.092	0.089	0.082	0.092
Fe2+	1.582	1.557	1.627	1.760	2.020	1.988	1.938	1.900	1.887	1.929
Total	8.041	8.027	8.025	8.039	8.028	8.035	8.037	8.038	8.028	8.029

	SN487 PT 1.7	SN487 PT 1.8	SN487 PT 1.9	SN487 PT 1.10	SS63 PT 1.1	SS63 PT 1.2	SS63 PT 1.3	SS63 PT 1.4	SS63 PT 1.5	SS63 PT 1.6
SiO2	37.1973	37.2787	37.6271	37.5763	37.2233	37.8981	37.5770	37.8405	37.7993	36.7752
TiO2	0.0739	0.0296	0.0285	0.0837	0.0580	0.0650	0.0544	0.0398	0.0283	bd
Al2O3	21.0708	21.1497	21.3866	21.1939	20.7190	21.0095	20.8813	21.2664	21.1561	20.8780
Cr2O3	0.1043	0.0514	0.0558	0.0735	0.2531	0.3074	0.2353	bd	0.2057	0.0933
MgO	3.9069	3.1383	4.1047	4.3579	3.7477	5.3118	3.9071	5.6670	5.3282	1.8373
CaO	6.7979	6.8912	7.8019	6.1829	6.4373	6.9257	6.2275	6.2729	6.3945	7.1530
MnO	1.5628	1.9872	1.1323	1.3260	2.4592	1.4029	2.2960	1.4217	1.4896	5.4652
FeO	28.8029	29.6296	28.0873	29.4912	28.8265	27.2369	29.0374	27.5854	27.3752	27.4667
Total	99.5168	100.1557	100.2242	100.2854	99.7241	100.1573	100.2160	100.0937	99.7769	99.6687
Si	2.968	2.971	2.968	2.972	2.975	2.978	2.983	2.972	2.979	2.970
Ti	0.004	0.002	0.002	0.005	0.004	0.004	0.003	0.002	0.002	bd
Al	1.982	1.987	1.989	1.976	1.952	1.946	1.954	1.969	1.966	1.988
Cr	0.006	0.003	0.004	0.004	0.016	0.019	0.015	bd	0.013	0.006
Mg	0.465	0.373	0.482	0.514	0.447	0.622	0.463	0.664	0.626	0.221
Ca	0.581	0.588	0.659	0.524	0.551	0.583	0.530	0.528	0.540	0.619
Mn	0.105	0.134	0.076	0.089	0.167	0.093	0.155	0.094	0.099	0.374
Fe2+	1.922	1.975	1.853	1.950	1.927	1.790	1.928	1.812	1.805	1.855
Total	8.034	8.033	8.033	8.033	8.038	8.035	8.030	8.041	8.030	8.033

	SS63 PT 1.7	SS63 PT 2.1	SS63 PT 2.2	SS63 PT 2.3	SS63 PT 2.4	SS63 PT 2.5	SS63 PT 2.6	SS63 PT 2.7	SS63 PT 2.8	SS63 PT 2.9
SiO2	37.3460	36.8174	37.2277	36.8970	36.8092	37.2099	36.6445	37.3310	36.8352	37.6717
TiO2	0.0430	0.0611	bd	0.0378	0.0452	0.0284	0.0702	0.0326	0.0338	0.0535
Al2O3	20.9563	20.9967	21.0586	21.0981	21.1120	21.1108	20.9374	21.2288	20.9455	21.3042
Cr2O3	0.1982	0.0988	0.0576	bd	bd	0.0752	0.1166	0.0535	0.0826	bd
MgO	3.7905	3.1058	4.1469	2.8592	3.3882	4.3093	2.8224	5.0266	2.3032	5.2931
CaO	6.2522	6.2282	6.0061	6.4249	6.3880	5.9757	6.1023	5.9018	6.3722	6.0797
MnO	2.2760	2.7576	1.6434	3.4100	2.6483	1.8300	3.4560	1.4436	4.5244	1.4093
FeO	29.2440	29.5507	29.6156	28.4152	29.3157	29.0547	29.0123	27.8139	28.2403	27.7570
Total	100.1062	99.6163	99.7559	99.1422	99.7066	99.5940	99.1617	98.8318	99.3372	99.5685
Si	2.972	2.958	2.967	2.972	2.951	2.966	2.961	2.974	2.976	2.976
Ti	0.002	0.004	bd	0.002	0.003	0.002	0.004	0.002	0.002	0.003
Al	1.966	1.989	1.979	2.004	1.995	1.983	1.995	1.994	1.995	1.984
Cr	0.013	0.006	0.004	bd	bd	0.005	0.008	0.003	0.005	bd
Mg	0.449	0.372	0.493	0.343	0.405	0.512	0.340	0.597	0.277	0.623
Ca	0.533	0.536	0.513	0.554	0.549	0.511	0.528	0.504	0.551	0.515
Mn	0.154	0.188	0.111	0.233	0.180	0.124	0.237	0.097	0.309	0.094
Fe2+	1.946	1.986	1.974	1.915	1.966	1.936	1.961	1.853	1.908	1.834
Total	8.036	8.040	8.041	8.023	8.049	8.038	8.033	8.025	8.023	8.029

	SS63	SS63	SN414	SN414	SN414	SN414	SN414	SN414	SN414	SN414
	PT 2.10	PT 2.11	PT 1.1	PT 1.2	PT 1.3	PT 1.4	PT 1.5	PT 1.6	PT 1.7	PT 1.8
SiO2	36.7302	37.4517	37.9199	38.4423	38.3491	38.2964	38.0794	38.4086	38.2033	38.1802
TiO2	0.0299	0.0466	0.0596	0.0441	0.0657	0.0649	0.0456	0.0744	0.0634	0.0710
Al2O3	20.9105	21.187	21.6461	21.6287	21.5661	21.3974	21.4496	21.4071	21.4826	21.4558
Cr2O3	0.0520	0.0833	bd	bd	bd	bd	bd	bd	bd	bd
MgO	1.5634	4.0325	5.3437	5.4872	4.8571	4.4796	4.8041	4.7487	4.6846	4.9284
CaO	7.9974	6.1112	8.1222	8.8603	10.6446	10.9492	10.0876	10.0922	10.2618	10.0138
MnO	4.4270	1.7755	1.1701	1.0773	1.1547	1.3900	1.5036	1.5434	1.8515	1.6440
FeO	27.4404	29.1568	25.3558	24.5938	23.0314	23.1500	23.6852	23.9127	23.4036	23.5593
Total	99.1508	99.8446	99.6174	100.1337	99.6687	99.7275	99.6551	100.1871	99.9508	99.8525
Si	2.975	2.976	2.973	2.989	2.992	2.994	2.982	2.993	2.985	2.983
Ti	0.002	0.003	0.004	0.002	0.004	0.004	0.003	0.004	0.004	0.004
Al	1.997	1.985	2.001	1.983	1.984	1.973	1.981	1.967	1.979	1.977
Cr	0.003	0.005	bd	bd	bd	bd	bd	bd	bd	bd
Mg	0.188	0.477	0.624	0.636	0.565	0.522	0.560	0.552	0.545	0.574
Ca	0.694	0.520	0.682	0.738	0.889	0.917	0.847	0.843	0.859	0.838
Mn	0.304	0.120	0.078	0.071	0.076	0.092	0.100	0.102	0.122	0.109
Fe2+	1.859	1.938	1.663	1.599	1.503	1.514	1.552	1.558	1.529	1.540
Total	8.023	8.025	8.023	8.02	8.012	8.016	8.024	8.019	8.022	8.024

	SN414 PT 1.9	SN414 PT 1.10	SN414 PT 1.11	SN414 PT 2.1	SN414 PT 2.2	SN414 PT 2.3	SN414 PT 2.4	SN414 PT 2.5	SN414 PT 2.6	SN414 PT 2.7
SiO2	38.1715	37.7270	38.0433	38.3816	38.2164	38.3216	38.4456	37.9186	38.2466	38.3008
TiO2	0.0854	0.0740	0.0529	0.0595	0.0719	0.0928	0.1364	0.1303	0.0611	0.0477
Al2O3	21.5674	21.4873	21.5406	21.6641	21.5365	21.6539	21.4795	21.3709	21.6115	21.6223
Cr2O3	bd	bd	bd	0.0721	0.0679	0.0000	bd	bd	bd	bd
MgO	4.8101	5.2362	5.6292	5.4256	5.2065	4.0373	3.5338	3.6575	4.4729	5.0099
CaO	10.8814	10.2113	8.8505	8.3952	9.5551	12.2112	12.5826	12.4273	10.9400	9.8935
MnO	1.3161	1.2671	1.1159	1.0946	1.0613	0.9867	1.1321	1.0605	1.1092	1.2081
FeO	22.9281	23.3364	24.3145	25.3370	24.2981	22.5766	23.2295	23.3914	23.3605	24.1857
Total	99.7600	99.3393	99.5469	100.4297	100.0137	99.8801	100.5395	99.9565	99.8018	100.2680
Si	2.979	2.961	2.976	2.982	2.979	2.988	2.992	2.973	2.987	2.980
Ti	0.005	0.004	0.003	0.004	0.004	0.005	0.008	0.008	0.004	0.003
Al	1.985	1.988	1.987	1.984	1.979	1.990	1.970	1.975	1.990	1.983
Cr	bd	bd	bd	0.004	0.004	0.000	bd	bd	bd	bd
Mg	0.560	0.613	0.656	0.629	0.605	0.470	0.409	0.428	0.520	0.581
Ca	0.910	0.859	0.742	0.699	0.798	1.020	1.049	1.044	0.915	0.825
Mn	0.087	0.084	0.074	0.072	0.070	0.065	0.074	0.070	0.073	0.080
Fe2+	1.497	1.532	1.590	1.647	1.584	1.473	1.512	1.534	1.526	1.574
Total	8.023	8.041	8.028	8.020	8.025	8.011	8.015	8.032	8.015	8.025

	SN414	SN414	SN489	SN489	SN489	SN489	SN489	SN489	SN489	SN489
	PT 2.8	PT 2.9	PT 1.1	PT 1.2	PT 1.3	PT 1.4	PT 1.5	PT 1.6	PT 1.7	PT 1.8
SiO2	38.2011	38.2408	38.0609	38.0217	38.1193	37.8617	37.9570	38.1025	38.0621	37.9975
TiO2	0.0778	0.1108	0.0888	0.1103	0.0813	0.0914	0.0832	0.0493	0.0873	0.0941
Al2O3	21.6081	21.5069	21.4147	21.4003	21.3979	21.3963	21.3907	21.6335	21.4465	21.1976
Cr2O3	bd	0.0000	bd	bd	bd	bd	bd	bd	bd	bd
MgO	4.5761	5.3200	3.9349	3.6273	3.5474	3.9330	4.5007	5.2825	3.7418	3.4530
CaO	11.2600	9.9860	10.2478	10.6833	10.5307	10.4421	9.3501	8.1679	10.4094	10.5883
MnO	1.0263	1.0694	1.4557	1.7563	1.9504	1.7228	1.5177	1.2180	1.9608	2.0445
FeO	22.9103	23.5448	24.4760	24.4872	24.6668	24.5706	24.8936	25.6369	24.4970	24.3632
Total	99.6597	99.7787	99.6788	100.0864	100.2938	100.0179	99.6930	100.0906	100.2049	99.7382
Si	2.983	2.981	2.992	2.984	2.989	2.974	2.983	2.976	2.984	2.996
Ti	0.005	0.006	0.005	0.006	0.005	0.005	0.005	0.003	0.005	0.005
Al	1.990	1.977	1.984	1.980	1.978	1.982	1.982	1.992	1.983	1.970
Cr	bd	0.000	bd	bd	bd	bd	bd	bd	bd	bd
Mg	0.533	0.618	0.460	0.425	0.415	0.460	0.527	0.615	0.437	0.405
Ca	0.942	0.835	0.863	0.898	0.885	0.879	0.787	0.684	0.874	0.895
Mn	0.068	0.071	0.097	0.117	0.129	0.114	0.101	0.081	0.130	0.136
Fe2+	1.496	1.535	1.609	1.608	1.618	1.614	1.636	1.675	1.606	1.606
Total	8.017	8.023	8.011	8.019	8.018	8.029	8.021	8.025	8.020	8.014

	SN489 PT 1.9	SN489 PT 2.1	SN489 PT 2.2	SN489 PT 2.3	SN489 PT 2.4
SiO2	37.9469	38.4729	38.3953	38.2509	38.4494
TiO2	0.0903	0.0959	0.0960	0.1163	0.1062
Al2O3	21.3381	21.4110	21.3525	21.3727	21.6337
Cr2O3	bd	bd	bd	bd	bd
MgO	3.5381	4.1641	3.9722	4.3646	4.0867
CaO	10.6398	10.6842	10.9819	10.5450	11.0454
MnO	2.1398	0.5355	0.3941	0.6359	0.3081
FeO	24.4849	24.7133	24.9029	24.7001	24.7795
Total	100.1779	100.0769	100.0949	99.9855	100.4090
Si	2.982	3.003	3.001	2.991	2.991
Ti	0.005	0.006	0.006	0.007	0.006
Al	1.977	1.970	1.967	1.970	1.984
Cr	bd	bd	bd	bd	bd
Mg	0.415	0.484	0.462	0.508	0.474
Ca	0.896	0.893	0.919	0.884	0.921
Mn	0.142	0.036	0.026	0.042	0.020
Fe2+	1.609	1.613	1.628	1.615	1.612
Total	8.025	8.006	8.009	8.017	8.010

Biotite Analyses

	SS454 Pt 1.1	SS454 Pt 1.2	SS454 Pt 1.3	SS454 Pt 1.5	SS454 Pt 1.6	SS454 Pt 1.7	SS454 Pt 1.8	SS454 Pt 1.9	SS454 Pt 1.10	SS454 Pt 3.1
SiO_2	37.6554	37.1927	37.7171	38.1779	37.9459	36.7574	36.5527	36.7863	36.6808	37.3319
TiO_2	1.2535	1.2670	1.2461	1.2039	1.2009	2.6208	2.6760	2.3876	1.7141	1.5889
Al_2O_3	18.8196	18.8261	19.0547	19.5841	19.3961	19.1875	18.9881	19.0348	18.4856	18.7311
MgO	14.7803	14.7549	15.2049	15.2605	15.2565	11.7129	12.0515	11.9298	12.1310	13.4499
CaO	0.1414	0.1113	bd	bd	0.0220	bd	bd	0.0293	0.0554	bd
MnO	0.0000	0.0000	0.0000	0.0000	bd	0.0000	0.0000	0.0504	0.0525	0.0747
FeO	13.1752	13.4160	12.2294	11.9099	11.8566	15.2977	15.0339	15.2727	15.8341	14.4396
Na_2O	0.4282	0.4309	0.3640	0.3879	0.3720	0.3855	0.3321	0.3409	0.3649	0.4158
K_2O	7.7434	7.4952	9.1830	8.6008	8.5839	9.0860	9.2785	9.2718	8.7809	9.0256
Total	93.9970	93.4941	94.9992	95.1250	94.6339	95.0478	94.9128	95.1036	94.0993	95.0575
Si	2.780	2.762	2.764	2.775	2.773	2.735	2.726	2.740	2.764	2.765
Ti	0.069	0.071	0.069	0.066	0.066	0.147	0.150	0.134	0.097	0.089
Al	1.638	1.649	1.646	1.678	1.671	1.684	1.670	1.671	1.642	1.635
Mg	1.626	1.633	1.660	1.653	1.662	1.299	1.339	1.324	1.362	1.485
Ca	0.011	0.009	bd	bd	0.002	bd	bd	0.002	0.005	bd
Mn	0.000	0.000	0.000	0.000	bd	0.000	0.000	0.003	0.003	0.004
Fe	0.814	0.834	0.750	0.724	0.725	0.952	0.938	0.951	0.997	0.894
Na	0.062	0.062	0.051	0.055	0.052	0.056	0.048	0.049	0.053	0.060
K	0.729	0.711	0.858	0.797	0.800	0.863	0.883	0.881	0.844	0.853
Total	7.727	7.729	7.798	7.747	7.751	7.736	7.754	7.756	7.767	7.786

bd= Below limits of detection
na= Element not analyzed

183

	SS454 Pt 3.2	SS454 Pt 3.4	SS454 Pt 3.5	SS454 Pt 3.6	SS454 Pt 3.7	SS454 Pt 3.8	SS313 Pt 1.1	SS313 Pt 1.2	SS313 Pt 1.3	SS313 Pt 1.4
SiO_2	36.9583	37.5788	36.8335	36.2264	36.7064	36.5418	36.2941	36.7828	36.9117	36.5952
TiO_2	1.5936	1.2316	2.1318	1.7351	1.5842	1.7716	1.4585	1.6386	1.5651	1.5404
Al_2O_3	18.9135	19.1606	18.9067	18.8599	19.0391	19.0143	19.0050	19.1751	19.0565	19.0555
MgO	13.1681	15.9688	11.9431	12.2093	12.4382	12.1727	12.1297	12.2155	12.3313	12.1458
CaO	bd	0.0575	0.0235	0.0880	bd	0.0597	0.0788	0.0724	0.0323	0.1127
MnO	bd	0.0000	0.0000	0.0484	bd	bd	bd	bd	bd	bd
FeO	14.6313	11.8378	15.8062	16.0484	15.9426	15.7086	16.4011	15.8270	16.2645	15.9798
Na_2O	0.3547	0.4244	0.3200	0.3591	0.3641	0.3468	0.3045	0.3719	0.3212	0.3151
K_2O	8.9947	8.5327	9.3344	8.9049	9.2334	9.1088	8.6048	9.0971	9.1233	8.8515
Total	94.6142	94.7922	95.2992	94.4795	95.3080	94.7243	94.2765	95.1804	95.6059	94.5960
Si	2.753	2.747	2.745	2.726	2.736	2.737	2.733	2.740	2.743	2.743
Ti	0.089	0.068	0.119	0.098	0.089	0.100	0.083	0.092	0.088	0.087
Al	1.660	1.651	1.661	1.673	1.673	1.679	1.688	1.685	1.670	1.684
Mg	1.462	1.739	1.326	1.369	1.382	1.359	1.362	1.357	1.366	1.357
Ca	bd	0.005	0.002	0.007	bd	0.005	0.006	0.006	0.002	0.009
Mn	bd	0.000	0.000	0.003	bd	bd	bd	bd	bd	bd
Fe	0.911	0.724	0.985	1.010	0.994	0.984	1.033	0.986	1.011	1.002
Na	0.051	0.060	0.046	0.053	0.052	0.051	0.044	0.053	0.046	0.047
K	0.854	0.795	0.887	0.854	0.878	0.871	0.826	0.865	0.865	0.846
Total	7.780	7.788	7.772	7.793	7.803	7.785	7.775	7.785	7.790	7.774

	SS313 Pt 1.7	SS313 Pt 1.8	SS313 Pt 1.9	SS313 Pt 1.10	SS313 Pt 4.1	SS313 Pt 4.2	SS313 Pt 4.3	SS313 Pt 4.4	SS313 Pt 4.5	SS349 Pt 1.1
SiO2	36.7085	36.2671	36.7565	36.1280	36.2194	36.6787	35.9531	36.0159	36.5934	36.3928
TiO2	1.5518	1.6343	1.7229	1.5026	1.4326	1.6492	1.5237	1.5689	1.5050	2.2805
Al2O3	18.9625	19.0832	18.9895	19.1659	18.6556	19.3700	18.6586	18.8458	18.7173	18.8173
MgO	12.1657	12.0240	12.4071	11.9739	12.0284	12.2091	11.9952	11.8765	12.4837	11.6953
CaO	0.0978	0.0323	0.0492	0.2543	0.4422	0.2027	0.3151	0.4686	0.1033	0.0276
MnO	bd	bd	bd	0.0480	bd	bd	bd	bd	bd	0.0422
FeO	15.3928	15.8082	15.7030	15.7888	15.3150	15.7453	16.0379	15.6383	16.6142	16.5366
Na2O	0.3267	0.3238	0.3231	0.3280	0.3160	0.3214	0.2932	0.3005	0.3616	0.2163
K2O	8.6330	9.0466	9.1368	8.7413	7.9450	8.4980	8.3883	7.8159	8.8341	9.2507
Total	93.8388	94.2195	95.0881	93.9308	92.3542	94.6744	93.1651	92.5304	95.2126	95.2593
Si	2.762	2.733	2.741	2.728	2.763	2.737	2.737	2.746	2.736	2.724
Ti	0.088	0.092	0.096	0.085	0.082	0.093	0.087	0.090	0.085	0.128
Al	1.682	1.695	1.670	1.707	1.678	1.704	1.675	1.694	1.650	1.661
Mg	1.364	1.350	1.379	1.347	1.368	1.358	1.362	1.350	1.391	1.305
Ca	0.008	0.002	0.004	0.020	0.036	0.016	0.026	0.038	0.008	0.002
Mn	bd	bd	bd	0.003	bd	bd	bd	bd	bd	0.003
Fe	0.968	0.996	0.979	0.997	0.977	0.983	1.021	0.997	1.039	1.036
Na	0.048	0.047	0.046	0.048	0.047	0.046	0.043	0.044	0.052	0.032
K	0.828	0.870	0.870	0.842	0.774	0.809	0.815	0.761	0.842	0.883
Total	7.748	7.786	7.785	7.778	7.726	7.746	7.767	7.720	7.802	7.775

	SS349 Pt 1.2	SS349 Pt 1.3	SS349 Pt 1.4	SS349 Pt 1.5	SS349 Pt 2.1	SS349 Pt 2.2	SS349 Pt 2.3	SS349 Pt 2.4	SS287 Pt 2.2	SS287 Pt 2.3
SiO_2	36.3167	35.9662	36.1112	36.3921	36.2591	36.2801	36.1799	35.9984	37.4499	37.2681
TiO_2	2.0120	2.0614	2.1843	2.1792	2.4678	2.5459	1.8210	1.8692	2.4474	2.9979
Al_2O_3	18.7432	18.2027	18.9175	18.9145	18.6403	18.4879	18.6224	18.5825	18.5086	18.8372
MgO	11.7499	11.6515	11.8714	11.7530	11.7118	11.7964	11.9861	11.9452	13.8953	13.2027
CaO	bd	0.0796	bd	bd	bd	bd	bd	bd	na	na
MnO	bd	0.0100	bd	0.0000	0.0000	bd	bd	bd	bd	bd
FeO	16.4261	16.4512	16.2455	16.1371	16.5200	16.2922	16.0942	16.3926	12.5557	12.4092
Na_2O	0.2392	0.1876	0.2326	0.2536	0.2777	0.2362	0.2460	0.2362	na	na
K_2O	9.4542	8.9571	9.3864	9.3396	9.3637	9.5208	9.3743	9.2827	10.0912	9.5651
Total	94.9413	93.5673	94.9489	94.9691	95.2404	95.1595	94.3239	94.3068	94.9481	94.2802
Si	2.731	2.741	2.712	2.728	2.719	2.722	2.734	2.725	2.765	2.760
Ti	0.114	0.118	0.123	0.123	0.139	0.144	0.103	0.106	0.136	0.167
Al	1.661	1.635	1.675	1.672	1.648	1.636	1.659	1.658	1.611	1.645
Mg	1.316	1.323	1.329	1.313	1.309	1.319	1.350	1.348	1.530	1.457
Ca	bd	0.007	bd	bd	bd	bd	bd	bd	na	na
Mn	bd	0.001	bd	0.000	0.000	bd	bd	bd	bd	bd
Fe	1.033	1.048	1.021	1.012	1.036	1.022	1.017	1.037	0.776	0.769
Na	0.035	0.028	0.033	0.036	0.041	0.035	0.037	0.035	na	na
K	0.906	0.871	0.900	0.893	0.895	0.911	0.903	0.896	0.951	0.904
Total	7.796	7.773	7.794	7.778	7.786	7.789	7.803	7.806	7.768	7.702

	SS287 Pt 2.5	SS287 Pt 2.6	SS287 Pt 2.7	SS287 Pt 2.8	SS287 Pt 2.9	SS287 Pt 1.1	SS287 Pt 1.2	SS287 Pt 1.3	SS287 Pt 1.4	SS287 Pt 1.5
SiO2	36.8683	36.5834	37.1777	37.2272	36.9595	37.1893	37.4040	37.1706	37.1736	37.4692
TiO2	2.9588	2.9352	3.1917	3.4796	3.0596	2.8012	2.8417	2.7997	2.1273	2.8180
Al2O3	18.7458	18.9024	18.7735	18.0499	18.1774	19.0021	19.0561	18.0637	19.1691	18.2248
MgO	13.0819	13.1119	13.0410	12.3894	12.5857	13.2770	12.7773	13.1843	13.9945	13.4706
CaO	0.0828	0.0806	0.0600	0.0855	0.1301	na	na	na	na	0.0950
MnO	bd	bd	bd	bd	bd	0.0000	bd	bd	0.0524	0.0804
FeO	12.3375	13.4102	12.6884	13.7975	13.5521	12.5993	12.4751	13.1839	12.7998	13.1098
Na2O	0.0978	0.0952	0.0960	0.0622	0.0846	na	na	na	na	0.1093
K2O	8.9190	9.2042	9.8509	9.2270	9.5283	9.3479	9.3062	9.7164	9.6798	9.4799
Total	93.0919	94.3231	94.8792	94.3183	94.0773	94.2168	93.8604	94.1186	94.9965	94.8570
Si	2.758	2.722	2.748	2.773	2.765	2.755	2.776	2.775	2.740	2.771
Ti	0.167	0.165	0.177	0.195	0.172	0.156	0.159	0.157	0.118	0.157
Al	1.654	1.658	1.635	1.585	1.603	1.659	1.668	1.589	1.666	1.588
Mg	1.458	1.454	1.436	1.376	1.403	1.466	1.414	1.466	1.537	1.484
Ca	0.006	0.006	0.005	0.007	0.010	na	na	na	na	0.008
Mn	bd	bd	bd	bd	bd	0.000	bd	bd	0.003	0.005
Fe	0.772	0.835	0.784	0.860	0.848	0.781	0.775	0.823	0.789	0.811
Na	0.015	0.014	0.014	0.009	0.012	na	na	na	na	0.016
K	0.851	0.873	0.929	0.877	0.909	0.884	0.882	0.926	0.910	0.894
Total	7.681	7.728	7.729	7.682	7.722	7.701	7.672	7.736	7.764	7.734

187

	SS287 Pt 1.6	SN125 Pt 2.1	SN125 Pt 2.2	SN125 Pt 2.3	SN125 Pt 2.4	SN125 Pt 2.5	SN34 Pt 1.1	SN34 Pt 1.2	SN34 Pt 1.3	SN34 Pt 1.4
SiO_2	37.9717	35.9407	36.5022	36.0200	36.4250	36.3227	35.1120	35.2480	34.9179	34.8299
TiO_2	2.8848	1.6327	1.5206	1.4993	1.4879	1.4688	2.0192	1.8117	1.6596	1.8934
Al_2O_3	18.4190	18.5979	18.9084	18.2607	18.8761	18.8340	18.3539	18.3153	18.5586	19.2319
MgO	13.3028	11.5573	11.8828	12.2607	12.1732	12.1726	9.5464	9.6752	9.6730	9.7183
CaO	0.0871	0.0472	0.0478	0.0685	0.0266	0.0839	bd	0.0000	bd	0.1471
MnO	0.0543	0.0000	0.0442	bd	0.0663	0.0623	0.0000	bd	bd	0.0434
FeO	13.0601	17.8387	16.6053	16.9570	16.4696	16.4994	20.4466	20.6047	20.7348	19.1459
Na_2O	0.1118	0.2020	0.2421	0.2408	0.2901	0.2371	0.2084	0.2102	0.2028	0.2190
K_2O	9.5682	8.7826	8.7217	8.4398	9.0497	8.7922	9.1116	9.2145	9.1680	7.9330
Total	95.4598	94.5991	94.4751	93.7468	94.8645	94.4730	94.7981	95.0796	94.9147	93.1619
Si	2.786	2.722	2.746	2.738	2.735	2.735	2.700	2.705	2.687	2.689
Ti	0.159	0.093	0.086	0.086	0.084	0.083	0.117	0.104	0.096	0.110
Al	1.593	1.661	1.677	1.636	1.671	1.672	1.663	1.657	1.684	1.750
Mg	1.454	1.305	1.332	1.389	1.361	1.366	1.094	1.107	1.109	1.118
Ca	0.007	0.004	0.004	0.006	0.002	0.006	bd	0.000	bd	0.012
Mn	0.003	0.000	0.003	bd	0.004	0.004	0.000	bd	bd	0.003
Fe	0.801	1.130	1.045	1.078	1.034	1.039	1.315	1.322	1.334	1.236
Na	0.016	0.029	0.035	0.035	0.042	0.035	0.031	0.031	0.030	0.033
K	0.896	0.848	0.837	0.818	0.867	0.845	0.894	0.902	0.900	0.781
Total	7.715	7.793	7.765	7.786	7.800	7.785	7.814	7.828	7.840	7.733

	SN34 Pt 1.5	SN34 Pt 1.6	SN34 Pt 1.7	SN34 Pt 2.1	SN34 Pt 2.2	SN34 Pt 2.3	SN34 Pt 2.4	SN487 Pt 1.1	SN487 Pt 1.2	SN487 Pt 1.3
SiO2	35.5446	35.2843	35.2652	35.0844	34.9385	35.4665	35.2490	34.1439	35.0135	34.9516
TiO2	1.7675	1.8186	1.9486	1.8731	1.7916	1.7304	1.7437	2.9296	3.1271	4.1523
Al2O3	19.4905	18.7022	18.2566	18.1782	18.4311	18.6673	18.7078	17.5224	17.5920	17.4118
MgO	9.5335	9.6130	9.6500	9.2472	9.2962	9.6096	9.4946	7.7935	8.1033	7.6824
CaO	0.0676	0.0238	0.0464	bd	bd	bd	0.0000	0.0480	0.0413	bd
MnO	0.0490	0.0000	0.0677	bd	bd	0.0414	0.0000	0.2194	0.1793	0.2861
FeO	19.3769	20.1766	20.5205	21.0885	20.8190	20.4504	20.8630	22.6483	21.5598	21.1553
Na2O	0.2115	0.2151	0.2284	0.2133	0.2297	0.2272	0.2334	0.0583	0.0775	0.0705
K2O	8.6653	9.3098	9.0783	9.0261	9.2395	9.3582	9.3030	9.2142	9.3920	9.6438
Total	94.7064	95.1434	95.0617	94.7108	94.7456	95.5510	95.5945	94.5776	95.0858	95.3538
Si	2.706	2.700	2.705	2.708	2.696	2.706	2.694	2.675	2.708	2.697
Ti	0.101	0.105	0.112	0.109	0.104	0.099	0.100	0.173	0.182	0.241
Al	1.749	1.687	1.651	1.654	1.677	1.679	1.686	1.618	1.604	1.584
Mg	1.081	1.096	1.103	1.064	1.069	1.092	1.081	0.910	0.934	0.883
Ca	0.006	0.002	0.004	bd	bd	bd	bd	0.004	0.003	bd
Mn	0.003	0.000	0.005	bd	bd	0.003	bd	0.015	0.012	0.019
Fe	1.234	1.292	1.316	1.361	1.344	1.305	1.333	1.484	1.395	1.366
Na	0.031	0.033	0.034	0.031	0.034	0.034	0.034	0.009	0.012	0.010
K	0.842	0.909	0.888	0.889	0.910	0.911	0.907	0.921	0.927	0.949
Total	7.754	7.823	7.819	7.817	7.834	7.828	7.834	7.808	7.777	7.750

	SN487 Pt 1.4	SN487 Pt 1.5	SN487 Pt 1.6	SN487 Pt 1.7	SN408 Pt 2.1	SN408 Pt 2.2	SN408 Pt 2.3	SN408 Pt 2.4	SN408 Pt 2.5	SN408 Pt 2.6
SiO2	34.9530	35.1398	34.9773	35.0933	37.1486	37.2470	37.0466	37.2066	36.8634	36.8610
TiO2	3.5764	3.1828	3.1170	3.4064	1.7549	1.7470	1.7663	1.8330	1.6484	1.5436
Al2O3	17.6076	17.7259	17.3995	17.5813	16.9400	17.2047	16.8584	17.1931	16.7660	16.7818
MgO	7.9461	8.1654	8.1253	7.8287	13.9920	13.8488	14.2271	13.9483	14.1227	14.1124
CaO	0.0373	bd	bd	bd	0.0249	0.0508	bd	bd	bd	bd
MnO	0.1951	0.2161	0.1339	0.1740	0.1897	0.2534	0.2419	0.2052	0.2399	0.2400
FeO	20.9028	20.9625	21.2302	21.4016	14.7791	14.8849	14.8336	14.3419	14.7839	14.7185
Na2O	0.0728	0.0595	0.0633	0.0690	0.1065	0.1387	0.1393	0.1537	0.1052	0.0825
K2O	9.6054	9.6186	9.6100	9.7998	9.9212	9.6725	9.7644	10.0018	9.9219	10.0237
Total	94.8965	95.0706	94.6565	95.3541	94.8569	95.0478	94.8776	94.8836	94.4514	94.3635
Si	2.704	2.713	2.718	2.710	2.785	2.784	2.777	2.783	2.779	2.782
Ti	0.208	0.185	0.182	0.198	0.099	0.098	0.100	0.103	0.094	0.087
Al	1.606	1.613	1.594	1.601	1.497	1.515	1.490	1.516	1.491	1.493
Mg	0.917	0.940	0.941	0.901	1.563	1.542	1.590	1.555	1.587	1.587
Ca	0.003	bd	bd	bd	0.002	0.004	bd	bd	bd	bd
Mn	0.013	0.014	0.009	0.011	0.012	0.016	0.015	0.013	0.015	0.015
Fe	1.352	1.353	1.379	1.382	0.927	0.930	0.930	0.897	0.932	0.929
Na	0.011	0.009	0.009	0.010	0.016	0.020	0.020	0.022	0.016	0.012
K	0.949	0.947	0.952	0.966	0.949	0.922	0.933	0.954	0.954	0.965
Total	7.764	7.774	7.784	7.780	7.850	7.832	7.855	7.844	7.867	7.872

	SS63 Pt 1.1	SS63 Pt 1.2	SS63 Pt 1.3	SS63 Pt 1.4	SS63 Pt 1.5	SS63 Pt 1.6	SS63 Pt 1.7	SS63 Pt 2.1	SS63 Pt 2.2	SS63 Pt 2.3
SiO2	36.1555	35.9672	35.5976	35.4285	35.7701	35.4267	35.3854	35.7017	35.5886	35.6910
TiO2	2.4321	2.3689	2.5190	2.8910	2.9011	2.7089	2.4841	2.2768	2.3194	2.4849
Al2O3	15.8211	16.4146	16.6873	17.0029	16.3464	16.5358	16.5506	16.4106	16.3338	16.2635
MgO	10.8770	10.6550	10.2460	9.4678	10.2488	10.4669	10.5610	10.2975	10.3190	10.1022
CaO	0.0382	0.0268	0.0469	0.0475	0.0279	0.0335	0.0284	0.0377	0.0211	bd
MnO	0.1882	0.1881	0.1731	0.1524	0.1468	0.1843	0.1562	0.1467	0.1768	0.1543
FeO	19.9171	19.7869	19.6185	19.8656	19.6638	19.5681	19.5245	20.1802	20.4078	20.1099
Na2O	0.1087	0.0603	0.0641	0.0685	0.1301	0.1608	0.0911	0.1431	0.1761	0.1260
K2O	9.4052	9.6632	9.7001	9.2227	9.7740	9.3520	9.4925	9.2799	9.3460	9.5625
Total	94.9431	95.1310	94.6526	94.1469	95.0090	94.4370	94.2738	94.4742	94.6886	94.4943
Si	2.779	2.760	2.746	2.742	2.751	2.736	2.739	2.760	2.751	2.763
Ti	0.140	0.137	0.146	0.168	0.168	0.157	0.144	0.133	0.135	0.144
Al	1.433	1.484	1.517	1.551	1.482	1.506	1.510	1.495	1.488	1.484
Mg	1.246	1.219	1.178	1.092	1.175	1.205	1.218	1.187	1.189	1.165
Ca	0.003	0.002	0.004	0.004	0.002	0.002	0.002	0.003	0.002	bd
Mn	0.012	0.012	0.011	0.010	0.010	0.012	0.010	0.010	0.012	0.010
Fe	1.280	1.270	1.265	1.286	1.264	1.264	1.263	1.305	1.319	1.302
Na	0.016	0.009	0.009	0.011	0.019	0.024	0.014	0.021	0.027	0.020
K	0.923	0.946	0.954	0.910	0.958	0.921	0.937	0.915	0.922	0.944
Total	7.834	7.839	7.831	7.775	7.830	7.827	7.837	7.828	7.845	7.832

	SS63 Pt 2.4	SS63 Pt 2.5	SS63 Pt 2.6	SS63 Pt 2.7	SS63 Pt 2.8	SS63 Pt 2.9	SS63 Pt 2.10
SiO2	35.5513	35.3888	35.2860	36.0005	35.6967	35.4720	35.4049
TiO2	2.3354	2.5415	2.4446	2.4177	2.5373	2.4839	2.2020
Al2O3	16.4425	16.3100	16.5174	16.1834	15.9464	15.9350	16.8362
MgO	10.3301	9.8455	10.0717	10.3615	10.2584	10.1879	10.0935
CaO	0.0309	0.0624	bd	0.0655	0.0608	0.0691	0.0284
MnO	0.1975	0.1373	0.1203	0.1430	0.1241	0.1712	0.1241
FeO	20.0258	20.1552	19.7486	20.1674	19.7191	19.9830	20.4580
Na2O	0.1887	0.1015	0.1167	0.1267	0.1653	0.1765	0.0789
K2O	9.2022	9.3893	9.3896	9.3011	8.9303	8.8371	9.8684
Total	94.3044	93.9315	93.6949	94.7668	93.4384	93.3157	95.0944
Si	2.752	2.756	2.749	2.773	2.780	2.771	2.732
Ti	0.136	0.149	0.143	0.140	0.149	0.146	0.128
Al	1.500	1.497	1.517	1.469	1.465	1.468	1.532
Mg	1.192	1.143	1.169	1.189	1.191	1.187	1.160
Ca	0.002	0.005	bd	0.006	0.005	0.006	0.002
Mn	0.013	0.009	0.008	0.009	0.008	0.011	0.008
Fe	1.297	1.313	1.287	1.299	1.284	1.306	1.320
Na	0.029	0.015	0.018	0.019	0.026	0.027	0.012
K	0.909	0.933	0.933	0.914	0.887	0.881	0.972
Total	7.830	7.821	7.825	7.819	7.795	7.803	7.866

Hornblende Analyses

	SN414 PT 1.1	SN414 PT 1.2	SN414 PT 1.3	SN414 PT 1.4	SN414 PT1.5	SN414 PT 1.6	SN414 PT 1.7	SN414 PT 1.8	SN414 PT 2.1	SN414 PT 2.2
SiO_2	44.2443	44.2829	44.3710	44.0155	40.7359	44.0181	44.1091	44.6893	39.2384	44.4757
TiO_2	1.9373	1.9577	1.9365	1.4983	0.5903	1.5151	1.6032	1.9616	0.2859	1.4058
Al_2O_3	12.1298	11.9530	11.9799	12.0896	18.3475	12.3426	11.9510	11.9709	20.4553	12.6619
MgO	10.8757	11.4967	11.3987	10.8072	7.3416	10.2251	10.7968	11.4352	6.4429	10.5506
CaO	11.8026	11.7205	11.6888	12.0495	11.9254	11.9956	12.1326	12.0034	11.8068	11.8937
MnO	0.1787	0.0630	0.1279	0.1483	0.2002	0.1585	0.2090	0.1646	0.2646	0.1380
FeO	13.8923	13.5725	13.3119	14.2341	15.9809	14.9332	14.4621	13.0966	16.3927	14.4955
Na_2O	1.1358	1.1552	1.2263	1.0412	1.1353	0.8716	0.9394	0.9280	1.1203	0.9813
K_2O	1.0528	1.0126	1.0040	1.0055	0.9218	0.9942	0.8977	1.0576	1.2545	0.8572
Total	97.2493	97.2141	97.0450	96.8892	97.1789	97.0540	97.1009	97.3072	97.2614	97.4597
Si	6.537	6.513	6.541	6.537	6.067	6.534	6.533	6.571	5.856	6.539
Ti	0.216	0.217	0.215	0.168	0.066	0.170	0.178	0.217	0.033	0.156
Al	2.113	2.072	2.082	2.117	3.222	2.159	2.087	2.075	3.600	2.194
Mg	2.396	2.521	2.505	2.392	1.629	2.263	2.384	2.507	1.432	2.311
Ca	1.868	1.847	1.847	1.917	1.904	1.909	1.925	1.891	1.889	1.873
Mn	0.023	0.007	0.016	0.019	0.025	0.020	0.026	0.020	0.033	0.017
Fe2+	1.595	1.416	1.468	1.619	1.791	1.676	1.592	1.506	1.763	1.552
Fe3+	0.122	0.253	0.173	0.148	0.200	0.178	0.200	0.105	0.283	0.231
Na	0.327	0.331	0.352	0.299	0.329	0.250	0.270	0.265	0.324	0.279
K	0.198	0.190	0.188	0.191	0.175	0.187	0.170	0.199	0.238	0.161
Total	15.393	15.368	15.386	15.408	15.408	15.346	15.365	15.355	15.451	15.313
Aliv :	1.463	1.487	1.459	1.463	1.933	1.466	1.467	1.429	2.144	1.461
Alvi:	0.650	0.585	0.623	0.654	1.289	0.694	0.620	0.646	1.456	0.733
Na in M4:	0.132	0.158	0.153	0.083	0.096	0.091	0.075	0.109	0.111	0.127
Na in Asite:	0.195	0.178	0.198	0.217	0.233	0.159	0.195	0.156	0.213	0.152

bd= Below limits of detection

	SN414 PT 2.3	SN414 PT 2.4	SN414 PT 2.5	SN414 PT 2.6	SN414 PT 2.7	SN414 PT 2.8	SN489 PT 1.1	SN489 PT 1.2	SN489 PT 1.3	SN489 PT 1.4
SiO2	44.3880	44.0970	40.7811	43.3826	44.0089	43.8897	42.2124	42.7707	43.2295	43.5458
TiO2	1.8952	1.9690	0.5587	1.1503	1.8610	2.0033	0.7438	1.1770	2.1326	2.0303
Al2O3	12.2174	12.0228	17.6046	13.8052	11.9613	11.9979	16.2942	14.5457	13.0549	12.7940
MgO	10.8896	11.0689	7.8639	9.9250	10.4709	11.1819	8.3335	9.6440	10.3900	10.4983
CaO	11.9315	11.7327	11.8421	11.9983	12.1776	11.7456	11.6995	11.4935	11.1860	11.3704
MnO	0.1991	0.1562	0.1821	0.2131	0.1196	0.1866	0.1012	0.1519	0.2130	0.1378
FeO	13.8861	13.6494	15.8295	14.8699	15.0037	13.7642	15.7796	15.2575	14.4592	14.4180
Na2O	0.9673	1.1371	1.2361	0.9819	0.9074	0.9894	1.4545	1.4198	1.3666	1.3293
K2O	0.9911	0.9644	1.0096	1.0116	1.0191	0.9981	0.5098	0.7397	0.9464	0.9316
Total	97.3653	96.7975	96.9077	97.3379	97.5295	96.7567	97.1285	97.1998	96.9782	97.0555
Si	6.540	6.529	6.090	6.413	6.519	6.493	6.259	6.313	6.388	6.435
Ti	0.211	0.219	0.063	0.128	0.207	0.223	0.083	0.131	0.237	0.226
Al	2.122	2.098	3.098	2.407	2.089	2.093	2.848	2.532	2.273	2.228
Mg	2.391	2.443	1.749	2.188	2.311	2.465	1.841	2.121	2.288	2.312
Ca	1.883	1.861	1.894	1.901	1.933	1.863	1.859	1.817	1.772	1.800
Mn	0.025	0.020	0.023	0.026	0.015	0.024	0.013	0.019	0.026	0.018
Fe2+	1.564	1.517	1.721	1.600	1.721	1.425	1.720	1.486	1.426	1.487
Fe3+	0.148	0.174	0.256	0.239	0.138	0.278	0.237	0.398	0.361	0.295
Na	0.277	0.327	0.359	0.281	0.261	0.284	0.417	0.406	0.393	0.381
K	0.186	0.181	0.192	0.190	0.193	0.189	0.096	0.139	0.179	0.175
Total	15.346	15.370	15.446	15.372	15.387	15.335	15.372	15.363	15.343	15.356
Aliv :	1.460	1.471	1.910	1.587	1.481	1.507	1.741	1.687	1.612	1.565
Alvi:	0.662	0.628	1.188	0.820	0.608	0.586	1.107	0.846	0.662	0.663
Na in M4:	0.117	0.139	0.106	0.099	0.067	0.137	0.141	0.183	0.228	0.200
Na in Asite:	0.160	0.188	0.254	0.182	0.195	0.147	0.276	0.224	0.164	0.181

195

	SN489 PT 1.5	SN489 PT 1.6	SN489 PT 1.7	SN489 PT 1.8	SN489 PT2.1	SN489 PT 2.2	SN489 PT 2.3	SN489 PT 2.4	SN489 PT 2.5	SN489 PT 2.6
SiO2	43.4444	43.4514	43.4770	43.5632	40.8873	42.7899	42.6277	43.8518	42.1961	43.9349
TiO2	2.0884	0.9618	1.6517	1.8926	0.3110	1.3059	1.3815	2.0708	0.7030	1.4355
Al2O3	12.7678	14.0958	13.3746	13.0268	18.0016	14.0499	14.6261	12.9507	16.1574	13.9127
MgO	10.5046	9.6589	10.1638	10.3952	7.5578	10.0232	9.4139	10.4229	8.4929	10.0906
CaO	11.3918	11.4507	11.7155	11.6937	11.6202	11.5883	11.4776	11.5758	11.6111	11.6979
MnO	0.1217	0.1722	0.1423	0.1378	0.1193	0.1967	0.1034	0.1299	0.1662	0.0974
FeO	14.3569	15.2545	14.9897	14.7715	16.3757	14.6516	15.1641	14.5529	15.6175	14.6368
Na2O	1.3594	1.4242	1.3153	1.3470	1.4207	1.4413	1.3636	1.2715	1.4306	1.3868
K2O	0.9511	0.6165	0.6841	0.7234	0.4727	0.6297	0.8203	0.8319	0.4769	0.6552
Total	96.9861	97.0860	97.5140	97.5512	96.7663	96.6765	96.9782	97.6582	96.8517	97.8478
Si	6.430	6.412	6.403	6.412	6.081	6.343	6.319	6.443	6.260	6.433
Ti	0.233	0.107	0.183	0.209	0.035	0.146	0.154	0.229	0.078	0.159
Al	2.228	2.453	2.321	2.261	3.156	2.455	2.557	2.243	2.826	2.401
Mg	2.316	2.125	2.230	2.282	1.676	2.214	2.079	2.282	1.877	2.202
Ca	1.806	1.811	1.849	1.844	1.852	1.841	1.823	1.823	1.845	1.836
Mn	0.015	0.021	0.017	0.017	0.015	0.025	0.013	0.016	0.021	0.012
Fe2+	1.514	1.517	1.542	1.531	1.627	1.466	1.574	1.537	1.632	1.567
Fe3+	0.264	0.365	0.305	0.288	0.410	0.351	0.305	0.251	0.305	0.226
Na	0.390	0.406	0.377	0.385	0.409	0.414	0.391	0.362	0.411	0.395
K	0.179	0.117	0.128	0.135	0.089	0.119	0.155	0.156	0.091	0.123
Total	15.376	15.334	15.354	15.364	15.350	15.374	15.369	15.340	15.347	15.354
Aliv :	1.570	1.588	1.597	1.588	1.919	1.657	1.681	1.557	1.740	1.567
Alvi:	0.658	0.865	0.724	0.673	1.237	0.799	0.876	0.686	1.086	0.834
Na in M4:	0.194	0.189	0.151	0.156	0.148	0.159	0.177	0.177	0.155	0.164
Na in Asite:	0.197	0.217	0.226	0.229	0.261	0.255	0.214	0.185	0.257	0.230

196

	SN408 PT 2.1	SN408 PT 2.2	SN408 PT 2.3	SN408 PT 2.4	SN408 PT 2.5	SN408 PT 2.6	SN408 PT 2.7	SN408 PT 2.8	SN408 PT 2.9	SN408 PT 2.10
SiO2	44.2873	44.6977	44.6120	44.2404	44.7717	44.4252	44.1649	44.4178	44.6297	42.9330
TiO2	0.3204	0.5663	0.5573	0.5927	0.4949	0.5255	0.5442	0.4900	0.4322	0.4178
Al2O3	12.9078	12.2739	12.2588	12.2814	12.1820	12.1797	12.2034	12.2312	12.2216	13.7505
Cr2O3	0.1746	0.1982	0.1702	0.1656	0.1330	0.1050	0.1585	0.1562	0.1656	0.1003
MgO	11.5316	12.0576	12.0994	12.1784	11.9157	11.6974	11.8249	11.8840	11.8600	10.7492
CaO	11.6497	11.4499	11.5008	11.4900	11.5556	11.4496	11.4118	11.4621	11.6052	11.6817
MnO	0.3613	0.3480	0.2605	0.3480	0.4375	0.4336	0.3479	0.3169	0.3772	0.3248
FeO	14.2120	13.7925	13.7665	13.8031	13.5702	13.7970	13.9361	13.6140	13.7783	14.6987
Na2O	1.4122	1.2500	1.3429	1.4018	1.2592	1.3031	1.3398	1.3463	1.2782	1.4409
K2O	0.4184	0.8213	0.8233	0.8508	0.6850	0.7164	0.7511	0.8109	0.6076	0.5648
Total	97.2753	97.4554	97.3917	97.3522	97.0048	96.6325	96.6826	96.7294	96.9556	96.6617
Si	6.451	6.489	6.488	6.441	6.533	6.518	6.476	6.511	6.518	6.333
Ti	0.035	0.062	0.061	0.065	0.054	0.058	0.060	0.054	0.047	0.047
Al	2.217	2.100	2.102	2.108	2.095	2.106	2.109	2.113	2.104	2.391
Cr	0.020	0.023	0.020	0.020	0.015	0.013	0.019	0.019	0.020	0.012
Mg	2.503	2.609	2.623	2.643	2.592	2.558	2.583	2.595	2.581	2.363
Ca	1.818	1.781	1.792	1.793	1.808	1.800	1.793	1.800	1.817	1.846
Mn	0.044	0.043	0.032	0.043	0.054	0.053	0.043	0.040	0.047	0.040
Fe2+	1.051	0.964	1.009	0.958	1.040	1.069	1.016	1.065	1.046	1.186
Fe3+	0.680	0.710	0.666	0.722	0.616	0.624	0.694	0.603	0.637	0.627
Na	0.398	0.352	0.378	0.395	0.357	0.370	0.381	0.384	0.362	0.412
K	0.078	0.152	0.152	0.158	0.128	0.135	0.140	0.151	0.114	0.105
Total	15.294	15.285	15.322	15.346	15.292	15.304	15.314	15.335	15.293	15.364
Aliv :	1.549	1.511	1.512	1.559	1.467	1.482	1.524	1.489	1.482	1.667
Alvi:	0.667	0.589	0.590	0.549	0.628	0.624	0.585	0.624	0.622	0.725
Na in M4:	0.182	0.219	0.208	0.207	0.192	0.200	0.207	0.200	0.183	0.154
Na in Asite:	0.216	0.133	0.170	0.188	0.164	0.170	0.174	0.184	0.179	0.258

	SS 63 PT 1.1	SS 63 PT 1.2	SS 63 PT 1.3
SiO2	42.5262	42.0508	42.0551
TiO2	0.7298	0.6133	0.6590
Al2O3	13.0040	14.0474	13.6041
Cr2O3	0.1139	0.1697	0.1488
MgO	8.6304	8.1817	8.4364
CaO	11.4956	11.6828	11.5067
MnO	0.3333	0.2462	0.2386
FeO	17.9425	17.9289	18.3937
Na2O	1.4707	1.5206	1.4355
K2O	0.6492	0.5724	0.6825
Total	96.8956	97.0138	97.1604
Si	6.382	6.312	6.294
Ti	0.082	0.069	0.074
Al	2.300	2.486	2.399
Cr	0.013	0.020	0.018
Mg	1.930	1.830	1.882
Ca	1.849	1.879	1.846
Mn	0.042	0.032	0.030
Fe2+	1.742	1.828	1.695
Fe3+	0.509	0.423	0.607
Na	0.428	0.442	0.418
K	0.124	0.109	0.130
Total	15.401	15.430	15.393
Aliv :	1.618	1.688	1.706
Alvi:	0.681	0.798	0.694
Na in M4:	0.151	0.121	0.154
Na in Asite:	0.277	0.321	0.263

Plagioclase Analyses

	SS454 Pt 1.1	SS454 Pt 1.2	SS454 Pt 1.3	SS454 Pt 1.4	SS454 Pt 3.1	SS454 Pt 3.2	SS454 Pt 3.3	SS454 Pt 3.4	SS454 Pt 3.5	SS454 Pt 3.6
SiO_2	60.4122	60.4776	60.1080	60.2476	60.3099	60.5209	60.1638	60.0853	59.3098	56.6565
Al_2O_3	25.3134	25.2458	25.7861	25.4767	25.0100	25.1872	25.4220	25.5279	26.1577	27.8357
CaO	6.6669	6.6920	6.8208	7.1277	6.6134	6.6893	7.1893	7.0143	7.8479	9.7662
FeO	0.0000	0.0547	0.1240	0.2317	0.1478	0.2006	0.0821	0.0365	0.1788	0.3026
Na_2O	7.6878	7.7932	7.7484	7.5652	7.8553	7.7967	7.4599	7.5024	7.2411	5.9971
K_2O	0.0800	0.0632	0.0615	0.0474	0.0664	0.0670	0.0436	0.0637	0.0741	0.0411
Total	100.1603	100.3265	100.6488	100.6963	100.0028	100.4617	100.3607	100.2301	100.8094	100.5992
Si	2.681	2.682	2.660	2.666	2.685	2.682	2.669	2.668	2.629	2.531
Al	1.324	1.320	1.345	1.329	1.312	1.316	1.330	1.336	1.367	1.466
Ca	0.317	0.318	0.323	0.338	0.315	0.318	0.342	0.333	0.373	0.468
Fe	0.000	0.002	0.004	0.009	0.006	0.007	0.003	0.001	0.007	0.011
Na	0.662	0.670	0.665	0.650	0.678	0.670	0.642	0.646	0.622	0.520
K	0.005	0.003	0.003	0.003	0.004	0.004	0.002	0.003	0.004	0.002
Total	4.990	4.995	5.002	4.995	5.000	4.997	4.988	4.988	5.001	4.997
Xan	0.32	0.32	0.33	0.34	0.32	0.32	0.35	0.34	0.37	0.47

bd= Below limits of detection

200

	SS313 Pt 1.1	SS313 Pt 1.2	SS313 Pt 1.3	SS313 Pt 1.4	SS313 Pt 1.5	SS313 Pt 1.6	SS349 Pt 1.1	SS349 Pt 1.2	SS349 Pt 1.3	SS349 Pt 2.1
SiO2	61.2125	61.4073	61.7721	62.1738	61.5969	61.4282	59.4100	57.9814	57.8557	58.7631
Al2O3	25.0403	24.7686	24.4818	24.7901	24.5480	24.6313	25.8912	25.7242	26.8563	26.4645
CaO	6.2360	6.0843	5.9109	5.8538	5.8333	5.8881	7.7877	7.7058	8.5878	8.3422
FeO	0.1282	0.0898	0.0330	0.1502	0.0458	bd	0.0767	0.0658	0.0457	0.0821
Na2O	8.0055	8.1045	8.2879	8.3110	8.4661	8.2563	7.0486	7.0558	6.6307	6.9916
K2O	0.0553	0.0728	0.0619	0.0542	0.0411	0.0854	0.0527	0.0424	0.0658	0.0690
Total	100.6778	100.5273	100.5476	101.3331	100.5312	100.2893	100.2669	98.5754	100.0420	100.7125
Si	2.701	2.713	2.726	2.723	2.721	2.718	2.642	2.626	2.587	2.610
Al	1.303	1.290	1.274	1.280	1.278	1.285	1.357	1.373	1.416	1.385
Ca	0.295	0.288	0.279	0.275	0.276	0.279	0.371	0.374	0.412	0.397
Fe	0.005	0.003	0.001	0.005	0.002	bd	0.003	0.003	0.002	0.003
Na	0.685	0.694	0.709	0.706	0.725	0.709	0.608	0.620	0.575	0.602
K	0.003	0.004	0.003	0.003	0.002	0.005	0.003	0.002	0.004	0.004
Total	4.992	4.992	4.992	4.992	5.004	4.996	4.985	4.998	4.995	5.001
Xan	0.300	0.292	0.282	0.279	0.275	0.281	0.38	0.38	0.42	0.40

	SS349 Pt 2.2	SS349 Pt 2.3	SS287 Pt 2.1	SS287 Pt 2.2	SS287 Pt 2.3	SS287 Pt 2.7	SS287 Pt 2.8	SN125 Pt 2.1	SN125 Pt 2.2	SN125 Pt 2.3
SiO2	59.2123	57.9529	60.5213	60.2544	59.7204	61.0807	60.6641	63.5235	62.9182	63.6226
Al2O3	26.1807	26.7767	25.5190	25.3388	25.2759	25.0967	25.4616	23.1454	24.2793	23.1826
CaO	7.8815	8.6288	6.8974	6.8632	6.8432	6.4315	6.6541	4.1703	5.0590	4.1937
FeO	0.1040	0.1223	0.0861	0.0531	0.0494	0.0788	bd	0.1737	0.0949	0.0860
Na2O	7.1509	6.8056	7.7392	7.9307	7.7914	7.9368	7.7201	9.2703	8.6771	9.2551
K2O	0.0961	0.0674	0.2071	0.2006	0.1487	0.1418	0.2402	0.0707	0.0548	0.0603
Total	100.6255	100.3537	100.9701	100.6408	99.8290	100.7663	100.7401	100.3539	101.0833	100.4003
Si	2.628	2.586	2.671	2.670	2.667	2.695	2.680	2.798	2.755	2.799
Al	1.370	1.409	1.328	1.324	1.331	1.306	1.326	1.202	1.253	1.202
Ca	0.375	0.413	0.326	0.326	0.327	0.304	0.315	0.197	0.237	0.198
Fe	0.004	0.004	0.003	0.002	0.002	0.003	bd	0.006	0.003	0.003
Na	0.615	0.589	0.662	0.681	0.674	0.679	0.661	0.792	0.737	0.790
K	0.006	0.004	0.012	0.011	0.009	0.008	0.014	0.004	0.003	0.003
Total	4.997	5.006	5.002	5.014	5.010	4.995	4.996	4.999	4.988	4.996
Xan	0.38	0.41	0.326	0.320	0.324	0.307	0.318	0.20	0.24	0.20

202

	SN125	SN34	SN34	SN34	SN34	SN408	SN408	SN408	SN408	SN487
	Pt 2.4	Pt 2.1	Pt 2.2	Pt 1.1	Pt 1.2	Pt 2.1	Pt 2.2	Pt 2.3	Pt 2.4	Pt 1.1
SiO2	63.1107	61.2298	60.7808	61.5535	61.9433	59.9296	59.9821	60.0812	59.2261	60.3241
Al2O3	23.1707	24.8141	24.5805	24.4468	24.4497	25.5679	25.5625	25.4229	25.8916	25.1533
CaO	4.2736	5.9322	5.8374	5.5999	5.6768	7.1185	6.8853	6.9244	7.4578	6.5909
FeO	0.0785	0.0765	0.1129	0.0200	0.0237	0.0528	0.1292	0.1237	0.1638	0.0164
Na2O	9.0934	8.3493	8.1290	8.3994	8.4945	7.6612	7.5898	7.6987	7.3518	7.9438
K2O	0.0635	0.0634	0.0827	0.1053	0.0769	0.0895	0.0740	0.0905	0.0858	0.1695
Total	99.7904	100.4653	99.5233	100.1249	100.6649	100.4195	100.2229	100.3414	100.1769	100.1980
Si	2.794	2.708	2.712	2.727	2.730	2.660	2.665	2.668	2.639	2.681
Al	1.209	1.294	1.293	1.277	1.271	1.338	1.339	1.331	1.360	1.318
Ca	0.203	0.281	0.279	0.266	0.268	0.339	0.328	0.329	0.356	0.314
Fe	0.003	0.003	0.004	0.001	0.001	0.002	0.005	0.004	0.006	0.001
Na	0.780	0.716	0.703	0.722	0.726	0.659	0.654	0.663	0.635	0.684
K	0.003	0.003	0.005	0.006	0.004	0.005	0.004	0.005	0.005	0.010
Total	4.993	5.005	4.996	4.998	5.000	5.003	4.995	5.001	5.001	5.007
Xan	0.21	0.281	0.283	0.268	0.269	0.338	0.333	0.330	0.357	0.311

	SN487 Pt 1.2	SN487 Pt 1.3	SN487 Pt 1.4	SN487 Pt 1.5	SS63 Pt 1.1	SS63 Pt 1.2	SS63 Pt 1.3	SS63 Pt 2.1	SS63 Pt 2.2	SN414 Pt 1.1
SiO2	60.4485	59.4670	59.8384	59.5901	61.5344	61.7334	61.4724	60.5293	61.6607	56.4210
Al2O3	25.1788	25.8766	25.5395	25.7791	24.5550	24.1940	24.2284	24.9749	24.2738	27.9175
CaO	6.5734	7.2708	6.9964	7.1385	5.7562	5.4689	5.4888	6.2014	5.4021	9.8736
FeO	0.0200	0.2038	0.1728	0.2020	0.2186	0.2094	0.0656	0.0437	0.0747	0.0587
Na2O	7.8167	7.2901	7.5633	7.4086	8.4255	8.4835	8.5262	8.0118	8.5306	5.7682
K2O	0.1881	0.1194	0.1487	0.1140	0.0822	0.0360	0.0704	0.0914	0.0747	0.0761
Total	100.2255	100.2277	100.2591	100.2323	100.5719	100.1252	99.8518	99.8525	100.0166	100.1151
Si	2.684	2.646	2.661	2.651	2.718	2.736	2.731	2.694	2.734	2.529
Al	1.318	1.357	1.339	1.352	1.279	1.264	1.269	1.310	1.269	1.475
Ca	0.313	0.347	0.334	0.340	0.273	0.260	0.261	0.296	0.257	0.474
Fe	0.001	0.007	0.006	0.007	0.008	0.008	0.003	0.001	0.003	0.002
Na	0.673	0.629	0.652	0.639	0.722	0.729	0.735	0.691	0.733	0.501
K	0.011	0.007	0.009	0.006	0.005	0.002	0.004	0.005	0.004	0.005
Total	4.999	4.993	5.000	4.996	5.005	4.998	5.003	4.999	5.000	4.986
Xan	0.314	0.353	0.336	0.345	0.273	0.262	0.261	0.298	0.258	0.48

	SN414 Pt 1.2	SN414 Pt 1.3	SN414 Pt 1.4	SN414 Pt 1.5	SN414 Pt 1.6	SN414 Pt 2.1	SN414 Pt 2.2	SN414 Pt 2.3	SN414 Pt 2.4	SN414 Pt 2.5
SiO2	56.3572	56.8144	56.1817	56.5560	56.5520	56.3698	56.2723	57.0119	56.1256	56.0900
Al2O3	27.9223	27.8199	28.0204	27.5873	27.6559	27.3174	27.2429	27.5062	28.0425	28.0576
CaO	10.1715	9.8436	10.3583	9.6635	9.7280	9.4621	9.6003	9.4297	10.2881	10.1809
FeO	0.0312	0.0293	0.0623	0.0238	0.0568	0.0532	0.1338	0.0843	0.0477	0.0495
Na2O	5.5804	5.8643	5.6951	5.9697	5.9086	6.1636	6.1222	6.1259	5.6647	5.8037
K2O	0.0772	0.0669	0.0554	0.0712	0.0679	0.0887	0.0778	0.0566	0.0538	0.0669
Total	100.1398	100.4384	100.3732	99.8715	99.9692	99.4548	99.4493	100.2146	100.2224	100.2486
Si	2.526	2.537	2.516	2.540	2.538	2.544	2.542	2.550	2.517	2.515
Al	1.475	1.465	1.479	1.461	1.463	1.454	1.451	1.451	1.482	1.483
Ca	0.488	0.471	0.497	0.465	0.468	0.457	0.465	0.452	0.494	0.489
Fe	0.001	0.001	0.002	0.001	0.002	0.002	0.005	0.003	0.002	0.002
Na	0.485	0.507	0.495	0.520	0.514	0.539	0.536	0.532	0.492	0.504
K	0.005	0.004	0.003	0.004	0.004	0.005	0.005	0.003	0.003	0.004
Total	4.981	4.986	4.993	4.991	4.990	5.001	5.003	4.992	4.990	4.997
Xan	0.50	0.48	0.50	0.47	0.47	0.46	0.46	0.46	0.50	0.49

	SN414 Pt 2.6	SN489 Pt 1.1	SN489 Pt 1.2	SN489 Pt 1.3	SN489 Pt 1.4	SN489 Pt 1.5	SN489 Pt 2.1	SN489 Pt 2.2	SN489 Pt 2.3	SN489 Pt 2.4
SiO_2	55.7614	58.7894	60.9063	60.0758	59.4115	59.3730	59.8257	60.3200	59.9423	60.0764
Al_2O_3	28.3791	26.3930	24.8887	25.3596	26.0386	25.5618	25.7725	25.4971	25.7939	25.9602
CaO	10.4343	8.1633	6.3396	7.0152	7.5765	7.4502	7.2246	6.8540	7.1589	7.5225
FeO	0.0220	0.0367	bd	0.0459	0.0550	bd	0.1155	0.0495	bd	0.0679
Na_2O	5.5098	6.7611	7.8184	7.4246	7.1378	7.3025	7.3611	7.4705	7.3264	7.2737
K_2O	0.0648	0.0344	0.0756	0.0519	0.0696	0.0568	0.0437	0.0591	0.0875	0.0602
Total	100.1714	100.1779	100.0286	99.9730	100.2890	99.7443	100.3431	100.2502	100.3090	100.9609
Si	2.502	2.619	2.703	2.673	2.640	2.653	2.656	2.675	2.659	2.652
Al	1.501	1.386	1.302	1.330	1.364	1.346	1.349	1.333	1.349	1.351
Ca	0.501	0.389	0.301	0.335	0.361	0.357	0.343	0.325	0.340	0.356
Fe	0.001	0.001	bd	0.002	0.002	bd	0.004	0.002	bd	0.003
Na	0.479	0.584	0.673	0.640	0.615	0.632	0.633	0.642	0.631	0.622
K	0.003	0.002	0.005	0.003	0.004	0.003	0.002	0.003	0.005	0.003
Total	4.989	4.981	4.984	4.983	4.987	4.992	4.988	4.981	4.984	4.986
Xan	0.51	0.40	0.31	0.34	0.37	0.36	0.35	0.34	0.35	0.36

APPENDIX B

X-Ray Fluorescence Analyses

Conditions of X-ray Fluorescence Analysis

Instrument:	EG&G ORTEC X-Ray Fluorescence Spectrometer with Energy Dispersive SiLi Detector (EDS)		

	Conditions		
	1	**2**	**3**
Spectral Region of Interest (kV):	1.00 - 6.01	4.37 - 7.59	13.14 - 16.81
Accelerating Voltage (kV):	10	35	45
Current (nA):	150	125	150
Counting Time (sec):	300	300	300
Filter:	open	Cu	In
Anode:	Rh	W	W

Standards Used

NORM 5	Glass
PCC 1	Dunite
SARM 6D	Dunite
GSP 1A	Granite
BCR 1F	Basalt
AGV 1F	Andesite

Standard: AGV 1F

								Average	Standard Deviation	Accepted Value	Standard Error of Calibration
Na2O	3.878	3.960	4.153	4.105	4.170	3.887	4.020	4.025	0.122	4.270	0.270
MgO	1.290	1.329	1.394	1.426	1.354	1.361	1.337	1.356	0.045	1.376	0.200
Al2O3	17.399	17.482	17.399	17.429	17.288	17.384	17.395	17.397	0.058	17.564	0.200
SiO2	59.972	60.105	60.255	60.418	60.044	60.143	59.968	60.129	0.162	59.855	0.370
P2O5	0.442	0.466	0.481	0.481	0.463	0.479	0.471	0.469	0.014	0.464	0.032
K2O	2.908	2.888	2.932	2.899	2.885	2.915	2.906	2.905	0.016	2.901	0.060
CaO	4.957	4.922	5.005	4.937	4.919	4.969	4.959	4.952	0.030	4.929	0.100
MnO	0.084	0.085	0.088	0.083	0.081	0.086	0.086	0.085	0.002	0.080	0.014
TiO2	1.023	1.013	1.035	1.036	1.020	1.027	1.011	1.024	0.010	1.057	0.033
V	0.0115	0.0106	0.0112	0.0103	0.0107	0.0107	0.0106	0.0108	0.0004	0.0107	0.0240
Cr	0.0000	0.0000	0.0000	0.0000	0.0000	0.0000	0.0000	0.0000	0.0000	0.0000	0.0051
Fe2O3	6.626	6.599	6.673	6.574	6.633	6.602	6.622	6.618	0.031	6.782	0.230
Ni	0.0000	0.0000	0.0000	0.0000	0.0000	0.0000	0.0000	0.0000	0.0000	0.0000	0.0023
Rb	0.0069	0.0067	0.0068	0.0064	0.0067	0.0065	0.0065	0.0066	0.0002	0.0066	0.0004
Sr	0.0648	0.0661	0.0658	0.0661	0.0702	0.0651	0.0661	0.0663	0.0018	0.0670	0.0017
Y	0.0020	0.0018	0.0018	0.0020	0.0021	0.0018	0.0020	0.0019	0.0001	0.0019	0.0005
Zr	0.0229	0.0224	0.0226	0.0227	0.0242	0.0222	0.0226	0.0228	0.0006	0.0228	0.0028
Nb	0.0012	0.0011	0.0011	0.0011	0.0013	0.0012	0.0011	0.0011	0.0001	0.0011	0.0003
Total	98.688	98.956	99.525	99.496	98.972	98.961	98.884	99.069		99.387	

209

Standard: BCR 1F

						Average	Standard Deviation	Accepted Value	Standard Error of Calibration
Na2O	3.164	3.239	3.331	3.423	3.544	3.340	0.150	3.650	0.270
MgO	3.204	3.111	3.123	3.134	3.138	3.142	0.036	3.252	0.200
Al2O3	13.779	13.779	13.765	13.693	13.822	13.767	0.047	13.806	0.200
SiO2	54.502	54.675	54.680	54.747	54.833	54.687	0.122	54.408	0.370
P2O5	0.288	0.297	0.295	0.291	0.301	0.294	0.005	0.279	0.032
K2O	1.703	1.718	1.712	1.704	1.711	1.710	0.006	1.718	0.060
CaO	6.798	6.844	6.809	6.776	6.798	6.805	0.025	6.785	0.100
MnO	0.195	0.192	0.187	0.187	0.196	0.191	0.004	0.185	0.014
TiO2	2.159	2.141	2.141	2.136	2.166	2.148	0.013	2.212	0.033
V	0.0209	0.0214	0.0210	0.0206	0.0207	0.0209	0.0003	0.0209	0.0240
Cr	0.0097	0.0086	0.0099	0.0121	0.0099	0.0100	0.0013	0.0136	0.0051
Fe2O3	13.240	13.260	13.162	13.162	13.415	13.248	0.104	13.602	0.230
Ni	0.0030	0.0020	0.0029	0.0036	0.0036	0.0030	0.0007	0.0034	0.0023
Rb	0.0037	0.0034	0.0037	0.0037	0.0034	0.0036	0.0001	0.0038	0.0004
Sr	0.0343	0.0348	0.0379	0.0348	0.0357	0.0355	0.0014	0.0359	0.0017
Y	0.0030	0.0032	0.0035	0.0031	0.0032	0.0032	0.0002	0.0030	0.0005
Zr	0.0137	0.0132	0.0145	0.0137	0.0138	0.0138	0.0005	0.0136	0.0028
Nb	0.0008	0.0010	0.0012	0.0009	0.0009	0.0010	0.0001	0.0009	0.0003
Total	99.120	99.343	99.301	99.346	100.016	99.425		99.993	

Standard: GSP 1A

								Average	Standard Deviation	Accepted Value	Standard Error of Calibration
Na2O	2.973	3.082	2.983	3.076	3.069	3.079	2.980	3.034	0.053	2.800	0.270
MgO	0.943	0.938	0.960	0.945	0.870	0.940	0.849	0.921	0.043	0.960	0.200
Al2O3	15.030	14.985	15.121	14.910	14.943	14.905	14.924	14.974	0.079	15.250	0.200
SiO2	66.982	66.709	67.273	66.813	66.980	66.792	66.469	66.860	0.253	67.320	0.370
P2O5	0.380	0.342	0.396	0.348	0.358	0.364	0.322	0.358	0.024	0.280	0.032
K2O	5.597	5.551	5.594	5.580	5.545	5.558	5.524	5.564	0.027	5.530	0.060
CaO	2.252	2.215	2.243	2.231	2.221	2.234	2.213	2.230	0.015	2.020	0.100
MnO	0.036	0.030	0.033	0.026	0.034	0.031	0.030	0.031	0.003	0.042	0.014
TiO2	0.645	0.598	0.627	0.636	0.608	0.618	0.643	0.625	0.018	0.660	0.033
V	0.0064	0.0064	0.0063	0.0064	0.0063	0.0064	0.0060	0.0063	0.0001	0.0053	0.0240
Cr	0.0008	0.0014	0.0023	0.0015	0.0020	0.0000	0.0012	0.0013	0.0008	0.0013	0.0051
Fe2O3	4.133	4.087	4.099	4.088	4.072	4.097	4.091	4.095	0.019	4.330	0.230
Ni	0.0000	0.0000	0.0000	0.0000	0.0000	0.0000	0.0000	0.0000	0.0000	0.0019	0.0023
Rb	0.0259	0.0257	0.0270	0.0261	0.0261	0.0277	0.0268	0.0265	0.0007	0.0254	0.0004
Sr	0.0224	0.0222	0.0230	0.0219	0.0225	0.0243	0.0233	0.0228	0.0008	0.0240	0.0017
Y	0.0027	0.0029	0.0027	0.0027	0.0026	0.0027	0.0030	0.0028	0.0001	0.0030	0.0005
Zr	0.0470	0.0477	0.0488	0.0470	0.0477	0.0514	0.0507	0.0486	0.0018	0.0500	0.0028
Nb	0.0024	0.0024	0.0025	0.0023	0.0024	0.0028	0.0028	0.0025	0.0002	0.0029	0.0003
Total	99.077	98.644	99.440	98.761	98.810	98.733	98.156	98.803		99.306	

Standard: PCC 1

				Average	Standard Deviation	Accepted Value	Standard Error of Calibration
Na2O	0.000	0.040	0.000	0.013	0.023	0.006	0.270
MgO	42.234	42.508	42.000	42.247	0.254	43.500	0.200
Al2O3	0.832	0.835	0.832	0.833	0.002	0.740	0.200
SiO2	42.631	42.922	42.569	42.708	0.189	42.100	0.370
P2O5	0.000	0.002	0.000	0.001	0.001	0.002	0.032
K2O	0.000	0.000	0.000	0.000	0.000	0.004	0.060
CaO	0.425	0.425	0.425	0.425	0.000	0.550	0.100
MnO	0.116	0.116	0.111	0.114	0.003	0.120	0.014
TiO2	0.000	0.000	0.000	0.000	0.000	0.015	0.033
V	0.0017	0.0020	0.0016	0.002	0.0002	0.0029	0.0240
Cr	0.2868	0.2877	0.2898	0.288	0.0015	0.2800	0.0051
Fe2O3	8.297	8.233	8.261	8.264	0.032	8.280	0.230
Ni	0.2458	0.2434	0.2505	0.247	0.0036	0.2400	0.0023
Rb	0.0001	0.0001	0.0001	0.000	0.0000	0.0000	0.0004
Sr	0.0001	0.0000	0.0000	0.000	0.0000	0.0000	0.0017
Y	0.0002	0.0003	0.0003	0.000	0.0001	0.0005	0.0005
Zr	0.0028	0.0028	0.0027	0.003	0.0001	0.0007	0.0028
Nb	0.0005	0.0006	0.0005	0.001	0.0000	0.0002	0.0003
Total	95.073	95.618	94.743	95.145		95.841	

				Average	Standard Deviation	Accepted Value	Standard Error of Calibration
Standard: SARM 6D							
Na2O	0.000	0.000	0.000	0.000	0.000	0.000	0.270
MgO	42.679	42.852	42.397	42.643	0.229	43.883	0.200
Al2O3	0.465	0.452	0.487	0.468	0.018	0.478	0.200
SiO2	38.654	38.716	38.626	38.665	0.046	38.379	0.370
P2O5	0.000	0.000	0.000	0.000	0.000	0.000	0.032
K2O	0.031	0.025	0.027	0.028	0.003	0.031	0.060
CaO	0.227	0.222	0.219	0.223	0.004	0.216	0.100
MnO	0.216	0.218	0.211	0.215	0.004	0.212	0.014
TiO2	0.053	0.049	0.053	0.051	0.002	0.052	0.033
V	0.0042	0.0039	0.0041	0.004	0.000	0.0047	0.0240
Cr	0.2901	0.2929	0.2881	0.290	0.002	0.2966	0.0051
Fe2O3	16.649	16.674	16.731	16.685	0.042	16.989	0.230
Ni	0.2032	0.2066	0.2028	0.204	0.002	0.2099	0.0023
Rb	0.0001	0.0000	0.0000	0.000	0.000	0.0000	0.0004
Sr	0.0010	0.0009	0.0010	0.001	0.000	0.0008	0.0017
Y	0.0002	0.0002	0.0002	0.000	0.000	0.0000	0.0005
Zr	0.0028	0.0028	0.0028	0.003	0.000	0.0028	0.0028
Nb	0.0007	0.0005	0.0006	0.001	0.000	0.0006	0.0003
Total	99.476	99.716	99.251	99.481		100.757	

Analyses of Amphibolite Samples

	SN595	SN604	SN181	SN135A	SN550	SN420	SN497	SS7	SN496	SN592
Na2O	2.151	2.886	2.121	2.554	2.555	2.438	2.469	1.279	2.289	2.881
MgO	6.860	5.938	7.978	5.474	9.009	6.297	7.802	8.735	7.293	6.929
Al2O3	14.721	15.664	14.954	14.139	13.740	13.890	14.683	15.939	13.924	15.308
SiO2	52.672	56.658	48.855	46.168	49.642	49.428	49.198	49.145	49.072	51.045
P2O5	0.148	0.077	0.152	0.400	0.152	0.139	0.135	0.200	0.173	0.089
K2O	0.935	0.511	0.657	2.411	0.460	1.293	0.810	0.528	0.887	2.001
CaO	9.329	8.241	11.821	8.583	10.619	9.197	10.940	10.541	10.334	7.438
MnO	0.173	0.134	0.184	0.184	0.253	0.177	0.189	0.189	0.232	0.164
TiO2	1.442	0.632	1.441	3.039	1.474	1.916	1.470	1.964	1.921	1.206
V	0.0228	0.0132	0.0310	0.0233	0.0272	0.0258	0.0276	0.0282	0.0287	0.0182
Cr	0.0152	0.0156	0.0185	0.0111	0.0341	0.0192	0.0199	0.0252	0.0239	0.0271
Fe2O3	10.892	7.532	11.933	15.506	11.795	13.552	11.881	12.811	13.556	10.865
Ni	0.0036	0.0049	0.0058	0.0030	0.0074	0.0064	0.0069	0.0098	0.0070	0.0069
Rb	0.0014	0.0009	0.0008	0.0046	0.0006	0.0023	0.0008	0.0006	0.0010	0.0048
Sr	0.0164	0.0293	0.0125	0.0194	0.0176	0.0193	0.0194	0.0142	0.0141	0.0262
Y	0.0036	0.0023	0.0030	0.0043	0.0033	0.0041	0.0032	0.0041	0.0044	0.0035
Zr	0.0092	0.0089	0.0075	0.0150	0.0083	0.0105	0.0088	0.0104	0.0098	0.0094
Nb	0.0005	0.0004	0.0003	0.0014	0.0005	0.0007	0.0002	0.0004	0.0005	0.0009
Total	99.396	98.347	100.176	98.539	99.797	98.415	99.664	101.422	99.772	98.021
CaO + MgO	16.189	14.178	19.799	14.056	19.628	15.493	18.742	19.275	17.627	14.366
MgO/(FeO+MgO)	0.412	0.467	0.426	0.282	0.459	0.340	0.422	0.431	0.374	0.415

	SN527	SN489A	SN95A	SN168	SN96A	SN501A	SS5A	SN169	SN849	SN593A
Na2O	2.284	2.580	1.914	2.700	2.252	2.344	2.306	2.667	2.471	2.787
MgO	6.601	7.486	8.199	6.606	6.829	7.863	7.471	7.220	6.144	7.866
Al2O3	14.257	15.099	13.895	15.192	15.878	13.589	15.462	14.873	15.145	15.865
SiO2	49.069	49.012	49.403	52.021	48.498	47.757	52.512	51.769	53.787	51.771
P2O5	0.244	0.230	0.288	0.117	0.394	0.184	0.119	0.139	0.131	0.144
K2O	1.311	0.620	0.997	1.470	0.946	0.577	0.561	0.652	0.947	0.761
CaO	9.196	9.566	10.388	8.254	10.881	9.739	9.560	10.093	7.905	9.665
MnO	0.205	0.164	0.205	0.154	0.188	0.240	0.147	0.154	0.128	0.160
TiO2	1.998	2.048	1.223	1.238	1.578	2.487	1.060	1.328	1.345	1.055
V	0.0257	0.0244	0.0257	0.0193	0.0281	0.0290	0.0199	0.0243	0.0184	0.0207
Cr	0.0217	0.0091	0.0209	0.0203	0.0119	0.0228	0.0204	0.0216	0.0145	0.0195
Fe2O3	13.859	13.433	13.176	10.560	12.941	15.759	9.850	10.152	10.357	9.858
Ni	0.0050	0.0040	0.0042	0.0056	0.0037	0.0090	0.0051	0.0036	0.0046	0.0060
Rb	0.0029	0.0010	0.0015	0.0030	0.0017	0.0009	0.0014	0.0009	0.0018	0.0011
Sr	0.0257	0.0471	0.0426	0.0240	0.0549	0.0288	0.0227	0.0212	0.0238	0.0250
Y	0.0040	0.0021	0.0032	0.0035	0.0028	0.0045	0.0030	0.0032	0.0037	0.0023
Zr	0.0139	0.0113	0.0093	0.0094	0.0150	0.0118	0.0087	0.0093	0.0093	0.0081
Nb	0.0011	0.0008	0.0006	0.0007	0.0009	0.0009	0.0005	0.0004	0.0007	0.0003
Total	99.125	100.338	99.796	98.397	100.503	100.648	99.129	99.131	98.437	100.016
CaO + MgO	15.798	17.052	18.587	14.859	17.710	17.602	17.030	17.313	14.049	17.531
MgO/(FeO+MgO)	0.346	0.382	0.409	0.410	0.370	0.357	0.457	0.441	0.397	0.470

	SS67	SS548	GC9	SN798	SN1	SN837	HZ33	SN802	SS587	SS553
Na2O	2.562	2.993	1.577	1.840	2.462	3.305	2.121	2.857	2.124	2.587
MgO	8.218	6.165	8.261	9.234	5.309	6.507	7.938	6.474	8.038	7.441
Al2O3	14.275	19.078	14.772	14.121	15.065	15.427	14.372	16.842	15.796	16.226
SiO2	49.921	49.045	50.018	50.712	53.435	55.402	51.763	51.902	50.129	52.863
P2O5	0.178	0.565	0.151	0.346	0.241	0.100	0.290	0.302	0.186	0.149
K2O	0.384	2.265	0.222	1.904	1.904	0.964	2.029	1.522	0.555	0.604
CaO	10.640	8.809	10.667	9.101	7.534	7.776	8.900	8.574	11.649	9.996
MnO	0.219	0.163	0.219	0.172	0.151	0.119	0.166	0.155	0.175	0.145
TiO2	1.442	0.869	1.466	0.790	1.484	0.695	1.242	0.890	1.287	0.922
V	0.0259	0.0173	0.0275	0.0185	0.0186	0.0128	0.0214	0.0174	0.0270	0.0194
Cr	0.0117	0.0114	0.0179	0.0533	0.0098	0.0174	0.0176	0.0064	0.0189	0.0183
Fe2O3	12.034	9.532	12.510	9.761	10.540	8.009	10.125	9.292	10.744	8.843
Ni	0.0029	0.0052	0.0051	0.0125	0.0032	0.0038	0.0063	0.0032	0.0052	0.0057
Rb	0.0005	0.0062	0.0006	0.0049	0.0049	0.0020	0.0060	0.0033	0.0013	0.0014
Sr	0.0153	0.0575	0.0131	0.0264	0.0274	0.0188	0.0447	0.0574	0.0137	0.0243
Y	0.0033	0.0028	0.0040	0.0030	0.0045	0.0022	0.0026	0.0020	0.0029	0.0021
Zr	0.0087	0.0168	0.0099	0.0154	0.0141	0.0082	0.0137	0.0150	0.0075	0.0078
Nb	0.0005	0.0006	0.0004	0.0010	0.0009	0.0003	0.0008	0.0005	0.0002	0.0002
Total	99.943	99.603	99.943	98.117	98.208	98.370	99.058	98.916	100.760	99.855
CaO + MgO	18.858	14.975	18.928	18.335	12.843	14.282	16.838	15.047	15.971	16.371
MgO/(FeO+MgO)	0.431	0.418	0.423	0.512	0.359	0.474	0.466	0.436	0.454	0.483

	SN35	HZ44	SN542	SS130	SS63	SS467	SN782	SS528	SS142	SS613
Na2O	1.834	2.408	1.963	2.321	2.752	1.926	2.486	2.919	2.078	1.948
MgO	8.033	7.705	7.281	8.079	5.559	7.976	4.534	4.657	8.607	7.420
Al2O3	14.447	15.094	14.630	14.537	14.999	14.283	13.858	15.014	14.006	14.859
SiO2	44.881	49.602	49.270	48.669	48.385	48.826	45.812	47.198	49.360	49.295
P2O5	0.465	0.185	0.168	0.173	0.409	0.156	0.339	0.419	0.153	0.173
K2O	2.583	1.070	0.691	0.303	1.302	1.169	2.707	0.795	0.198	0.862
CaO	9.463	9.818	10.626	10.907	7.766	8.498	8.241	8.891	11.198	10.656
MnO	0.230	0.149	0.214	0.204	0.201	0.141	0.188	0.196	0.177	0.234
TiO2	1.332	1.281	1.797	1.816	3.474	1.675	2.960	3.396	1.651	1.490
V	0.0242	0.0239	0.0296	0.0304	0.0213	0.0236	0.0227	0.0239	0.0304	0.0283
Cr	0.0306	0.0251	0.0176	0.0272	0.0126	0.0335	0.0111	0.0111	0.0250	0.0168
Fe2O3	15.023	11.551	13.116	13.195	15.223	13.879	15.750	16.371	12.467	12.225
Ni	0.0077	0.0052	0.0040	0.0059	0.0058	0.0045	0.0019	0.0028	0.0077	0.0054
Rb	0.0053	0.0021	0.0009	0.0004	0.0022	0.0023	0.0072	0.0009	0.0005	0.0009
Sr	0.0368	0.0205	0.0135	0.0170	0.0286	0.0145	0.0259	0.0540	0.0165	0.0244
Y	0.0031	0.0035	0.0041	0.0035	0.0043	0.0039	0.0039	0.0029	0.0036	0.0033
Zr	0.0196	0.0082	0.0088	0.0105	0.0154	0.0093	0.0151	0.0119	0.0084	0.0086
Nb	0.0006	0.0007	0.0003	0.0005	0.0016	0.0005	0.0014	0.0010	0.0004	0.0007
Total	98.418	98.954	99.836	100.297	100.162	98.620	96.964	99.965	99.986	99.250
CaO + MgO	17.496	17.523	17.907	18.985	13.326	16.474	12.776	13.548	19.805	18.076
MgO/(FeO+MgO)	0.373	0.426	0.381	0.405	0.289	0.390	0.242	0.240	0.434	0.403

	SS129A	SN811	SN120	GC4	SN418	SN135B	SS623	SS469	SS49	SS141
Na2O	2.574	2.612	2.509	1.562	2.319	2.156	2.499	1.298	2.014	1.622
MgO	8.083	6.283	8.022	6.882	7.771	7.847	8.062	7.702	11.472	9.069
Al2O3	15.527	16.760	14.956	12.475	15.047	13.890	15.898	15.981	15.361	11.945
SiO2	48.490	49.503	48.565	50.559	50.306	48.834	49.087	47.971	47.614	47.187
P2O5	0.142	0.377	0.127	0.237	0.180	0.180	0.183	0.198	0.140	0.183
K2O	0.438	2.108	0.904	1.812	0.556	0.754	0.838	0.450	0.239	0.324
CaO	11.012	8.074	10.757	6.654	10.520	11.357	11.222	12.878	10.700	11.801
MnO	0.201	0.140	0.203	0.159	0.174	0.197	0.159	0.207	0.144	0.264
TiO2	1.396	1.256	1.242	1.967	1.608	1.632	1.432	1.549	1.309	2.331
V	0.0287	0.0203	0.0267	0.0179	0.0266	0.0306	0.0285	0.0337	0.0265	0.0368
Cr	0.0278	0.0099	0.0245	0.0171	0.0233	0.0182	0.0186	0.0224	0.0446	0.0216
Fe2O3	11.559	10.138	11.707	13.794	11.095	12.031	11.602	12.221	11.816	16.384
Ni	0.0069	0.0044	0.0060	0.0058	0.0067	0.0060	0.0057	0.0037	0.0227	0.0069
Rb	0.0006	0.0059	0.0015	0.0030	0.0007	0.0016	0.0010	0.0005	0.0005	0.0005
Sr	0.0197	0.0522	0.0190	0.0424	0.0145	0.0143	0.0247	0.0255	0.0137	0.0089
Y	0.0033	0.0049	0.0033	0.0024	0.0036	0.0036	0.0028	0.0032	0.0026	0.0047
Zr	0.0095	0.0183	0.0079	0.0118	0.0095	0.0086	0.0090	0.0096	0.0085	0.0085
Nb	0.0003	0.0017	0.0004	0.0007	0.0003	0.0003	0.0002	0.0002	0.0002	0.0005
Total	99.518	97.368	99.111	96.203	99.662	98.962	101.071	100.557	100.928	101.198
CaO + MgO	19.094	14.357	18.779	13.536	18.291	19.204	19.284	20.581	22.172	20.870
MgO/(FeO+MgO)	0.437	0.408	0.432	0.357	0.438	0.420	0.436	0.412	0.519	0.381

218

	SS65	SS150	SS552	SS338	SS145	SS9	SN509	SN177	SS8	SN544
Na2O	2.324	1.285	2.214	1.253	2.190	1.317	2.574	1.212	1.864	1.297
MgO	9.057	9.088	9.075	10.276	9.092	9.802	9.137	10.002	9.224	8.334
Al2O3	14.354	15.560	14.836	15.096	13.683	15.400	17.648	14.651	14.458	17.495
SiO2	49.925	49.348	49.622	48.611	48.558	48.431	48.257	49.121	46.994	41.655
P2O5	0.170	0.261	0.166	0.176	0.205	0.200	0.115	0.230	0.172	0.516
K2O	0.675	0.301	0.551	0.302	0.284	0.284	0.678	0.308	0.308	0.405	0.341
CaO	11.349	11.324	11.569	11.413	12.071	11.547	11.252	12.341	11.490	12.278
MnO	0.184	0.191	0.181	0.218	0.262	0.196	0.154	0.178	0.249	0.144
TiO2	1.167	1.833	1.239	1.352	1.808	1.460	0.950	1.532	1.986	2.011
V	0.0262	0.0308	0.0271	0.0293	0.0349	0.0303	0.0241	0.0317	0.0328	0.0427
Cr	0.0245	0.0274	0.0251	0.0236	0.0188	0.0299	0.0198	0.0177	0.0276	0.0207
Fe2O3	10.394	11.907	11.023	12.208	13.239	11.830	10.220	11.854	13.946	18.565
Ni	0.0066	0.0063	0.0062	0.0062	0.0063	0.0087	0.0053	0.0062	0.0061	0.0070
Rb	0.0012	0.0005	0.0008	0.0006	0.0004	0.0009	0.0008	0.0007	0.0005	0.0007
Sr	0.0212	0.0109	0.0134	0.0074	0.0155	0.0139	0.0275	0.0138	0.0202	0.0396
Y	0.0025	0.0045	0.0030	0.0035	0.0037	0.0038	0.0025	0.0035	0.0043	0.0012
Zr	0.0081	0.0101	0.0074	0.0063	0.0076	0.0082	0.0092	0.0085	0.0100	0.0051
Nb	0.0002	0.0004	0.0002	0.0002	0.0003	0.0006	0.0003	0.0004	0.0006	0.0002
Total	99.690	101.190	100.558	100.982	101.480	100.958	100.703	101.511	100.892	102.752
CaO + MgO	20.406	20.412	20.644	21.688	21.164	21.349	20.388	22.343	20.714	20.612
MgO/(FeO+MgO)	0.492	0.459	0.478	0.483	0.433	0.479	0.498	0.484	0.424	0.333

	SN504	SN525B	SN105	SN135	SN414	SN548	SS170A	SS457	SN850	SN552
Na2O	1.334	1.957	0.914	2.104	1.512	1.895	1.061	1.857	1.933	1.707
MgO	9.264	8.649	14.453	9.225	8.748	8.665	8.105	8.029	8.382	6.815
Al2O3	13.546	14.039	7.667	14.275	13.917	15.019	13.830	14.633	15.044	16.479
SiO2	48.446	49.181	49.079	50.362	50.947	49.702	50.618	50.891	49.705	50.724
P2O5	0.148	0.234	0.240	0.156	0.203	0.140	0.246	0.270	0.241	0.258
K2O	0.340	0.601	0.546	0.578	0.502	0.552	0.805	1.093	0.392	0.401
CaO	12.664	11.448	11.323	11.639	11.573	11.369	11.674	10.706	10.964	10.298
MnO	0.222	0.198	0.225	0.187	0.165	0.179	0.168	0.251	0.201	0.186
TiO2	1.419	1.969	1.066	1.141	1.512	1.251	2.039	1.671	1.797	1.958
V	0.0349	0.0308	0.0284	0.0272	0.0286	0.0269	0.0329	0.0273	0.0302	0.0267
Cr	0.0358	0.0242	0.0344	0.0266	0.0181	0.0244	0.0248	0.0202	0.0246	0.0188
Fe2O3	12.714	12.123	14.228	10.492	11.298	11.282	12.741	11.437	11.922	11.679
Ni	0.0067	0.0060	0.0067	0.0055	0.0080	0.0050	0.0060	0.0057	0.0073	0.0072
Rb	0.0007	0.0008	0.0010	0.0007	0.0007	0.0008	0.0019	0.0040	0.0006	0.0007
Sr	0.0184	0.0130	0.0052	0.0180	0.0189	0.0160	0.0289	0.0144	0.0127	0.0138
Y	0.0033	0.0041	0.0033	0.0024	0.0034	0.0030	0.0034	0.0044	0.0045	0.0046
Zr	0.0083	0.0111	0.0061	0.0072	0.0089	0.0074	0.0113	0.0081	0.0104	0.0125
Nb	0.0003	0.0005	0.0005	0.0002	0.0004	0.0003	0.0005	0.0008	0.0005	0.0005
Total	100.205	100.491	99.827	100.246	100.464	100.139	101.396	100.923	100.673	100.590
CaO + MgO	21.927	20.097	25.776	20.864	20.321	20.034	19.779	18.735	19.346	17.113
MgO/(FeO+MgO)	0.447	0.442	0.530	0.494	0.462	0.460	0.414	0.438	0.439	0.393

	SS501	SS522A	SS500	SS363	SS593	SS487	SS600	SS522	SS186	SS358
Na2O	0.774	2.640	0.406	2.012	2.561	1.650	0.994	1.897	1.041	2.222
MgO	6.943	8.222	7.572	7.635	7.893	10.129	9.214	9.539	10.324	10.268
Al2O3	14.630	15.730	12.529	18.582	16.827	13.387	15.370	16.327	15.279	16.855
SiO2	51.955	48.973	53.069	49.513	48.707	49.440	47.704	50.058	49.553	49.388
P2O5	0.188	0.024	0.149	0.167	0.132	0.160	0.234	0.170	0.241	0.165
K2O	0.532	0.545	0.430	0.397	0.593	0.303	0.462	0.512	0.301	0.233
CaO	9.306	7.655	9.126	11.779	9.764	11.109	13.117	11.796	13.108	10.888
MnO	0.199	0.178	0.234	0.132	0.098	0.156	0.188	0.162	0.202	0.149
TiO2	1.768	1.472	2.004	1.220	1.339	1.393	1.824	1.102	1.168	0.933
V	0.0269	0.0210	0.0262	0.0261	0.0228	0.0279	0.0379	0.0260	0.0311	0.0232
Cr	0.0209	0.0285	0.0224	0.0282	0.0207	0.0375	0.0251	0.0340	0.0150	0.0419
Fe2O3	13.031	12.766	15.369	8.882	11.349	11.477	13.169	9.477	10.947	9.574
Ni	0.0031	0.0060	0.0065	0.0031	0.0046	0.0067	0.0057	0.0053	0.0042	0.0153
Rb	0.0012	0.0008	0.0008	0.0009	0.0011	0.0006	0.0008	0.0011	0.0007	0.0005
Sr	0.0187	0.0216	0.0177	0.0175	0.0345	0.0208	0.0291	0.0275	0.0162	0.0241
Y	0.0042	0.0036	0.0045	0.0030	0.0029	0.0030	0.0032	0.0027	0.0028	0.0026
Zr	0.0114	0.0102	0.0107	0.0083	0.0106	0.0080	0.0094	0.0085	0.0068	0.0069
Nb	0.0005	0.0006	0.0006	0.0002	0.0005	0.0003	0.0003	0.0003	0.0002	0.0002
Total	99.414	98.299	100.979	100.406	99.361	99.310	102.388	101.145	102.240	100.790
CaO + MgO	16.250	15.877	16.698	19.414	17.656	21.239	22.331	21.334	23.432	21.157
MgO/(FeO+MgO)	0.372	0.417	0.354	0.489	0.436	0.495	0.437	0.528	0.512	0.544

|	SS594	SS310	SS822	HZ30	SN719A	HZ1	SN558
Na2O	1.851	1.364	2.585	1.836	3.368	3.051	2.633
MgO	9.412	10.312	4.619	7.525	4.142	4.441	4.244
Al2O3	13.869	15.660	18.079	14.909	17.832	15.852	14.785
SiO2	48.648	47.469	50.260	49.473	52.109	46.416	57.457
P2O5	0.069	0.185	0.330	0.103	1.075	1.596	0.162
K2O	0.485	0.786	3.665	0.410	0.752	2.858	2.057
CaO	11.189	12.534	6.228	9.810	11.522	9.416	5.825
MnO	0.206	0.251	13.053	0.171	0.155	0.121	0.169
TiO2	1.004	1.377	1.137	1.496	2.412	3.100	0.956
V	0.0277	0.0321	0.0146	0.0247	0.0292	0.0273	0.0120
Cr	0.0342	0.0265	0.0009	0.0226	0.0034	0.0152	0.0096
Fe2O3	12.938	11.333	9.639	12.817	8.974	13.149	9.000
Ni	0.0129	0.0081	0.0000	0.0076	0.0004	0.0002	0.0000
Rb	0.0007	0.0014	0.0101	0.0005	0.0014	0.0060	0.0052
Sr	0.0154	0.0241	0.0568	0.0227	0.1219	0.0620	0.0354
Y	0.0027	0.0029	0.0025	0.0038	0.0022	0.0085	0.0036
Zr	0.0071	0.0088	0.0168	0.0086	0.0529	0.0883	0.0208
Nb	0.0004	0.0003	0.0008	0.0068	0.0022	0.0055	0.0010
Total	99.772	101.376	109.698	98.647	102.555	100.212	97.374
CaO + MgO	20.602	22.846	10.847	17.335	15.664	13.857	10.068
MgO/(FeO+MgO)	0.447	0.503	0.348	0.395	0.339	0.273	0.344

VITA

Michael Joseph Quinn was born April 29, 1964 in Washington, D. C., the youngest of 10 children born to George and Linda Quinn. Michael grew up in rural Maryland until the age of 12 when he moved with his parents to New Hampshire. At the age of 14 Michael went away to a Catholic preparatory high school, Mount Assumption Institute (MAI), in Plattsburgh, N. Y. Boarding school had more than its share of negative points but it was here, in the eastern Addirondacks, that Michael developed a love for hiking, and the outdoors. He graduated from MAI in 1982.

After spending a year as an engineering major at Albright College in Reading PA, Michael returned to New Hampshire to be closer to home and the seashore. He enrolled in the University of New Hampshire in Durham and decided to focus his studies in geology. Michael received a B.S. in geology in 1986. Drs. Jo Laird and Wally Bothner, who were instrumental in guiding Michael successfully through his undergraduate studies, encouraged him to go on to graduate school. After two years of indecision (and hard labor) Michael finally packed his belongings and moved to Tennessee to enter graduate school at the University of Tennessee, Knoxville in the fall of 1988. He received a M.S. degree in Geology in May, 1991.

Michael plans to continue his graduate studies in the field of geology and will enroll in the graduate program at Rice University, Houston, Texas in the fall of 1991.

PLATE I

GEOLOGIC MAP OF A PORTION OF JACKSON COUNTY SURROUNDING SYLVA, NORTH CAROLINA

by

Michael J. Quinn
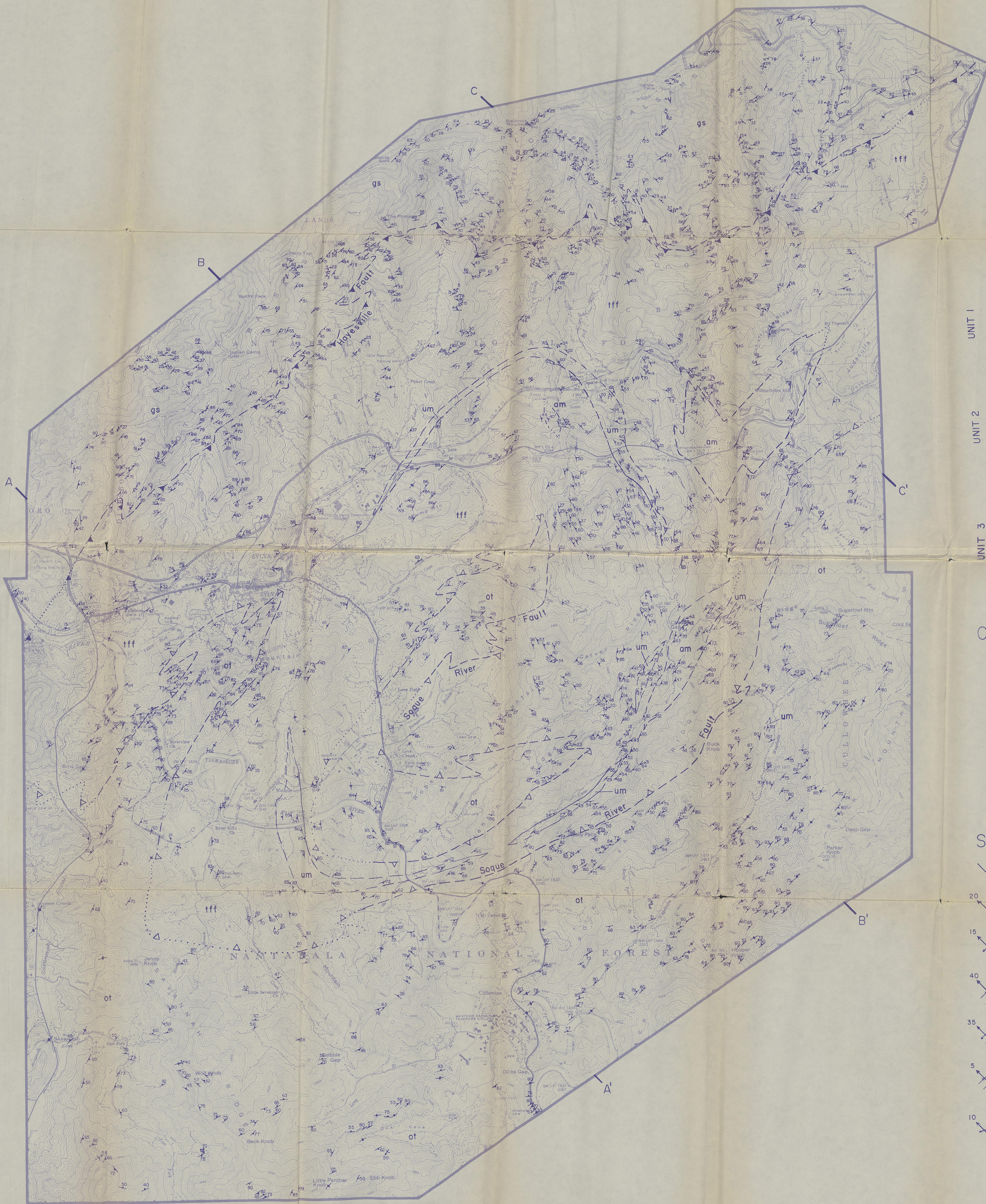
EXPLANATION

UNIT 1 — Upper Precambrian

gs — Great Smoky Group (undivided)

UNIT 2 — Upper Precambrian or Lower Paleozic

tff — Tallulah Falls Formation (?)

am — Amphibolite

um — Ultramafic Rocks

UNIT 3 — Upper Precambrian?
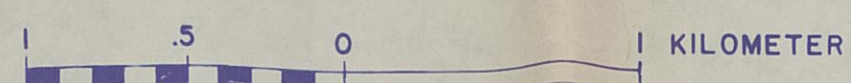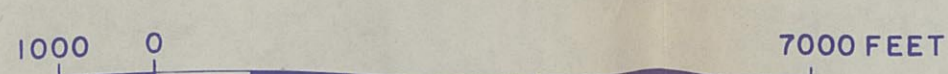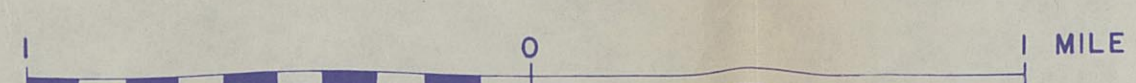
ot — Otto Formation

um — Ultramafic Rocks

CONTACTS

Lithologic — exact — approximate — inferred

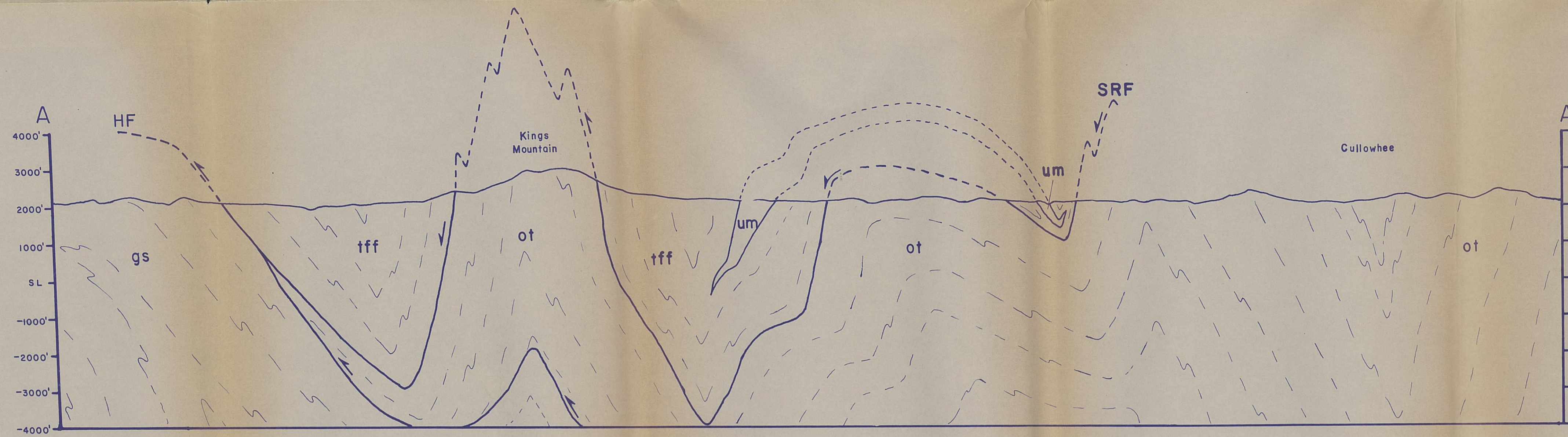Thrust Faults — exact — approximate — inferred

teeth on hanging wall

STRUCTURAL SYMBOLS

60 — Strike and dip of foliation

20 — Trend and plunge of lineation

15 — Trend and plunge of mesoscopic, upright antiform

40 — Trend and plunge of mesoscopic, upright synform

35 — Trend and plunge of mesoscopic, overturned antiform

5 — Trend and plunge of mesoscopic, overturned synform

10 — Trend and plunge of crenulation microfolds
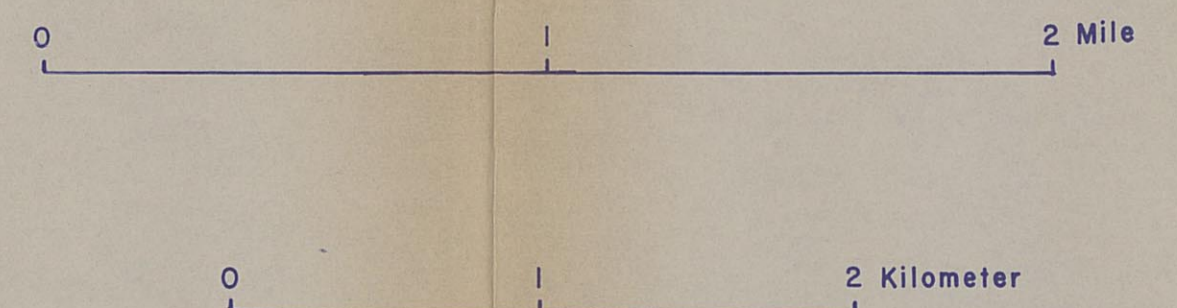
SCALE 1:24,000

1 MILE

1000 0 7000 FEET

3 0 KILOMETER

CONTOUR INTERVAL 40 FEET

PLATE 2   CROSS SECTIONS ALONG LINES A-A', B-B', AND C-C' ON PLATE I
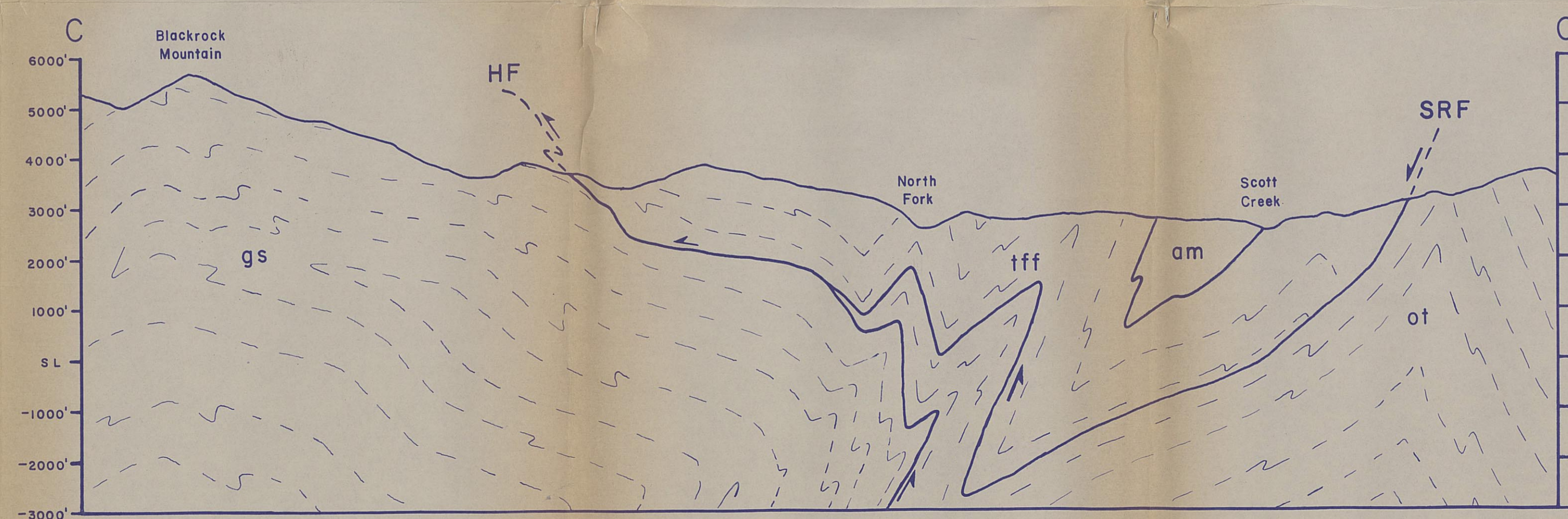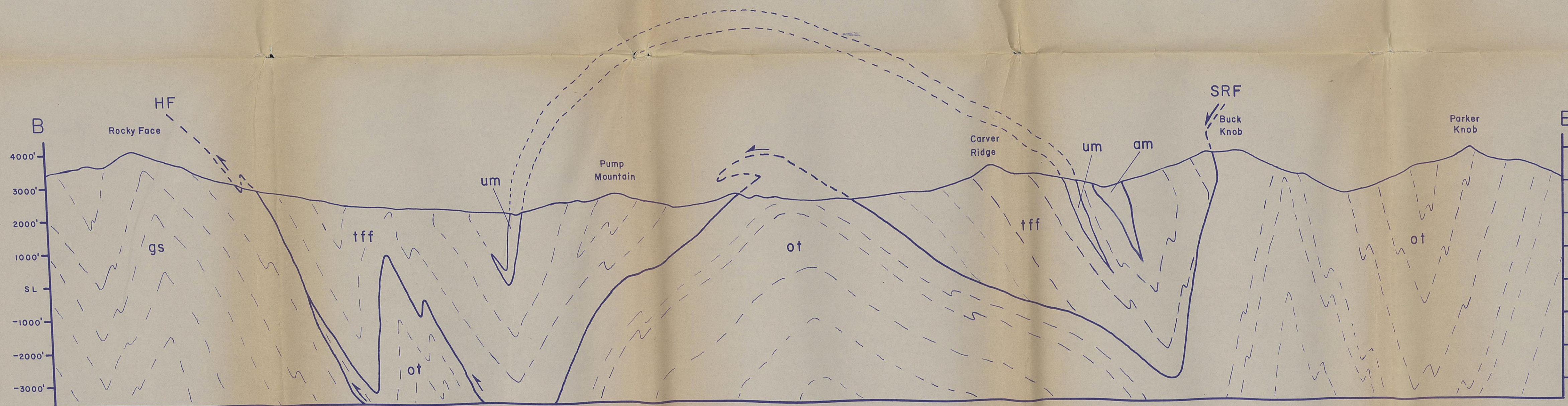
ABBREVIATIONS

HF = Hayesville fault
SRF = Soque River fault
gs = Great Smoky Group
tff = Tallulah Falls Formation
ot = Otto Formation
um = ultramafic rocks
am = amphibolite

SCALE

0   1   2 Mile

0   1   2 Kilometer

NO VERTICAL EXAGGERATION

PLATE 3

REGIONAL GEOLOGIC MAP OF THE WESTERN AND EASTERN BLUE RIDGE IN GEORGIA, NORTH CAROLINA, AND SOUTH CAROLINA

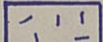(Modified after Gillon, 1989)

Rock Units

P€m = Murphy Group

P€o = Ocoee Supergroup

P€tf = Tallulah Falls Formation

P€cw = Coweeta Group

P€ot = Otto Formation

P€a = Ashe Formation

= P€ Basement Units

= Mafic and/or Ultramafic Units